PEOPLE'S DEMOCRATIC REPUBLIC OF ALGERIA MINISTERE DE
MINISTRY OF HIGHER EDUCATION AND SCIENTIFIC RESEARCH

Order N°:
Serial N°:

THESIS

In order to obtain the degree of

DOCTOR

UNIVERSITY OF TECHNOLOGY OF TROYES

IN SCIENCE FOR THE ENGINEER

Specialty: MATERIALS, MECHANICS, OPTICS, NANOTECHNOLOGY

and

UNIVERSITY OF LARBI BEN M'HIDI OUM EL BOUAGHI

IN PHYSICS

Specialty: PHYSICS OF SEMICONDUCTORS AND MATERIALS

As part of an international joint supervision of Franco-Algerian thesis

presented by

Ahlam BELGROUNE

11/07/2023

Wear and corrosion resistance of titanium based coatings deposited on cold spray 316l stainless steel

JURY

Mr. Faycal GOUMEIDANE	PROFESSOR	President
Mr. Akram ALHUSSEIN	ASSOCIATE PROFESSOR UTT	Supervisor
Mr. Mourad ZAABAT	PROFESSOR	Supervisor
Mrs Linda AISSANI	PROFESSOR	Co- Supervisor
Mr. Nicolas MARTIN	FULL PROFESSOR	Reviewer
Mr. Abdelouahad CHALA	PROFESSOR	Reviewer
Mr. Régis BARILLE	FULL PROFESSOR	Reviewer
Mr. Albano CAVALEIRO	FULL PROFESSOR	Reviewer

REPUBLIQUE ALGERIENNE DEMOCRATIQUE ET POPULAIRE
MINISTERE DE L'ENSEIGNEMENT SUPERIEUR ET DE LA RECHERCHE SCIENTIFIQUE

N° d'ordre:
N° de Série:

THESE

En vue de l'obtention du grade de

DOCTEUR

de l'UNIVERSITE DE TECHNOLOGIE DE TROYES

en SCIENCES POUR L'INGENIEUR

Spécialité : MATERIAUX, MECANIQUE, OPTIQUE, NANOTECHNOLOGIE

et

de L'UNIVERSITE LARBI BEN M'HIDI DE OUM EL BOUAGHI

en PHYSIQUE

Spécialité : PHYSIQUE DES SEMI-CONDUCTEURS ET MATERIAUX

Dans le cadre d'une cotutelle internationale de thèse franco-Algérienne

présentée par

Ahlam BELGROUNE

Le 11/07/2023

Tenue à l'usure et à la corrosion des revêtements à base de titane déposés sur des acier inoxydable 316L

JURY

M. Faycal GOUMEIDANE	PROFESSEUR	Président
M. Akram ALHUSSEIN	PROFESSEUR ASSOCIE UTT	Directeur de thèse
M. Mourad ZAABAT	PROFESSEUR	Directeur de thèse
Mme Linda AISSANI	PROFESSEURE	Co-encadrante
M. Nicolas MARTIN	PROFESSEUR DES UNIVERSITES	Examinateur
M. Abdelouahad CHALA	PROFESSEUR	Examinateur
M. Régis BARILLE	PROFESSEUR DES UNIVERSITES	Examinateur
M. Albano CAVALEIRO	PROFESSOR	Examinateur

I'm determined to reach my goal

Either I'll succeed or I'll succeed

Dale Carnegie

To the soul of my mother

To my father

To my sisters

To my brothers

To my husband

To my son

Acknowledgments

First I would like to express my special appreciation and thanks to my supervisors, **Mr. Akram Alhussein**, Associate Professor at the University of Technology of Troyes, **Mrs. Linda Aissani**, Professor at the University of Abbes Laghrour and **Mr**. **Mourad Zaabat**, Professor at Oum El Bouaghi University. I would like to thank them for encouraging my research, for believing in my potential and using my talents and curiosity to grow as a research scientist.

Moreover, I would like to profoundly thank **Mrs. Linda Aissani** for being as supervisor friend and sister, thanks for sharing her competences and experiences, for **Mr. Akram Alhussein** for being as a second family in France.

My sincere thanks to **Mr. Sami Rtimi**, **Mr. Christophe Verdy** and **Mme. Cecile Langlande** for their support in some experiments, scientific consultations and discussions.

I would like to thank **Mr. Nicolas Martin,** Professor at Franche-Comté university in France, **Mr. Régis Barille**, Professor at Angers university in France, **Mr**. **Albano Cavaleiro**, Professor at Coimbra university in Portugal, **Mr**. **Abdelouahad Chala**, Professor at Khenchela university in Algeria, and **Mr**. **Faycal Goumeidane**, Professor at Oum El Bouaghi university in Algeria, for accepting to be members of my Ph.D. committee.

I am deeply indebted to the University of Technology of Troyes (UTT) and the University of Oum El Bouaghi (UOEB) for giving me the opportunity to do my PhD. I am grateful to be a part of these two academic institutions, where I started my steps towards achieving my dreams. I thank also the Profas B+ Algerian-French program and GIP52 for their funding support.

My special thanks go to **Marie Lecomte** (UTT), **Pascale Denis** (UTT), **Isabelle Leclercq** (UTT), **Assia Sid** (UOEB), **Ziar Aissaoui** (UOEB), **Amir Baaloul** (UOEB), and **Abdelhakim Haddoun** (UOEB) for their administrative efforts and advice.

I am grateful to my LASMIS and LCAM colleagues at the UTT and UOEB, for the nice time spent together in the lab, especially to my sister and best friend **Nassima Bouaziz**, to **Maoxiang Zhu**, **Issam Lakdhar, Elia Zgheib, Abdelhakim Boussil, Kamel Ouari, Djellel Eddine Touaibia, Amel Mazbeche, Nadia Touzari, Yamina Zaidi, Mohamed Boukhalfa, Daniel Laurent, Fabrice Parent, Sofiane Achache, Mohamed El Garah, Frédéric Sanchette, Sandrine Sanchette and Sébastien Remy.** Many thanks to **Regis Deturche**, **Anna Rumyantseva** and **Serguei Kochtcheev**.

My special thanks to **Elias Kaady** as a colleague friend and brother, I shared with him amazing moments of laughter, tears, suffering, and joy in different circumstances during the thesis period, I will never forget you.

Thanks to **Fatna Sibari**, **Mina Bachiri**, **Idrisia Bachiri** and **Zbida** for making me a family member, for their help and supporting me especially during the covid-19 pandemic and my sickness in the special "Nogent city".

My appreciation goes to my family, my father, **Ben Djeddou Belgroune**, to the soul of my mother, **Malika Belgroune,** to my sisters and brothers; this achievement stands as a testament to your love and encouragement.

At the end I would like to thank my dear husband **Ibrahim Al-Mobarak**, thanks for giving me love and happiness that making my thesis work easier. Finally, for the piece of my heart our precious baby **Eilan Al-Mobarak** born last December.

Ahlam Belgroune

List of abbreviations

AE Auxiliary Electrode

AFM Atomic Force Microscopy

AISI American Iron and Steel Institute

Ag Silver

Al Aluminum

Ar Argon

BWR Boiling water reactor

CA contact angle

CC Centered Cubic

CFU Colony-Forming Unit

CGDS Cold-Gas Dynamic Spraying

CS Cold Spray

CSM Continuous stiffness measurement

DC Direct Current

DED Directed energy deposition

$\mathbf{d}_{hkl}$ Distance between two consecutive reticular planes of Miller index h, k, l

EDS Energy Dispersive Spectroscopy

E (GPa) Young's modulus of the film

eV Electron-volt

H (GPa) Hardness

He Helium

hkl Miller index

HTS Heat transport system

HVOF High Velocity Oxy-Fuel

IRInfrared radiation

KSS Kinetics Spray Solutions

LDMD Laser direct metal deposition

min Minutes

mm Millimeters

Mo Molybdenum

$\mathbf{N_2}$ Nitrogen

O Oxygen

OP Optical microscopy

RE Reference Electrode

PEMFC Proton Exchange Membrane Fuel Cell

RF Radio Frequency

PVD Physical Vapor Deposition

rpm Rotation Per Minute

sccm Standard Cubic Centimeter per Minute

SCE Saturated Calomel Electrode

SEM Scanning Electron Microscopy

Si Silicon

SS Stainless steel

SZM Structure Zone Model

TEM Transmission electron microscopy

Ti Titanium

TiN Titanium Nitride

TiAlN Titanium-Aluminum-Nitrogen

TiAlMoN Titanium-Aluminum-Molybdenum-Nitrogen

TiMoONAg Titanium- Molybdenum- Oxygen-Nitrogen-Silver

UVA Ultraviolet-A

UVB Ultraviolet-B

UVC Ultraviolet-C

UV-VIS Ultraviolet-Visible

Vcrit Critical velocity

Vp Particles speed

WAAM Wire Arc Additive Manufacturing

WE Working electrode

XPS Xray Photoelectron Spectroscopy

XRD X-Ray Diffraction

σ(GPa) Residual stress

Summary

Chapter II: Elaboration and characterization techniques

II. Elaboration techniques

II. Characterization techniques

GENERAL INTRODUCTION

GENERAL INTRODUCTION

The main challenges in the industrial field are to design and produce components coated with hard films for using in severe environments [1, 2]. These coatings should have low coefficient of friction (COF) and high wear and corrosion resistance. Cold spray (CS) is one of the coatings processes that rapidly progressed presenting a novel and emerging future technology consecutive to the thermal spray techniques. It has a high flexibility in materials combination that offers a wide range of applications.

The prior studies on stainless steel (SS) coatings elaborated by cold spray are very limited. Many researchers carried out works to understand the variation of austenitic stainless steel properties and microstructure. The effects of cold-spray conditions (e.g. particle velocity, temperature …etc) using a nitrogen propellant gas on AISI 316L stainless steel coatings were evaluated [3, 4]. It was found that a higher nitrogen propellant gas temperature and pressure produce dense coatings. The successful deposition of stainless steel by CS has a strong potential in biomedical field due to its characteristics such as ease of fabrication, good mechanical strength and corrosion resistance, biocompatibility and low cost [5, 6].

However, the SS316L surface hardness and the wear resistance are still low in slippery environments. The SS hip prostheses must be changed after 10 to 15 years because of the localized corrosion and wear, resulting from the high concentration of Cl^- ions in physiological fluids. Furthermore, poor antimicrobial property is one of the major limitations for stainless steel316 L (SS 316 L) that is mainly utilized in manufacturing of surgical instruments [7, 8].

In order to improve several properties such as mechanical, tribological, anticorrosion and antibacterial performance, it is necessary to enhance the surface features of SS 316L by applying protective coatings. In our work, the protective coatings were performed by magnetron sputtering technique. This later has rapidly developed and today it is one of the recommended techniques used for depositing various industrial coatings. This technique is used to deposit high quality coatings by controlling the thermodynamic and the kinetic conditions of growing films. It is used to deposit hard, anticorrosion, wear resistant and antibacterial coatings, as well as decorative coatings with specific optical and electrical properties [9, 10].

For many years, transition metal nitride films have shown a good corrosion resistance, high hardness and excellent electrical conductivity. Among them, titanium nitride (TiN) is widely used in the manufacturing of cutting tools and medical parts used for orthopedic

implants. TiN was also used in stamping tools, bearings, and as a decorative material. TiN coating is characterized by high tribological properties during friction due to the formation of a solid lubricant. The demand for biomedical and green manufacturing like high-speed machining or dry cutting along with the environmental protection legislation and the increase of its associated cost make an enormous pressure on the industry [11, 12]. Therefore, the combination of the TiN coatings with other elements (e.i. Al, O, Mo, Ag …etc) is usually considered as an effective approach to improve the hardness, wear resistance, anticorrosion behavior and antibacterial performance.

TiAlN is one of the most attractive coatings, which is characterized by its abrasion resistance at high temperature with a good thermoelectric conductivity and oxidation resistance. TiAlN coating exhibits better wear resistance and longer lifetime used for metals machining such as aluminum alloys and austenite stainless steel thanks to the formation of titanium and aluminum oxides [13].

More recently, TiON thin films have shown an effective performance against many pathogenic bacteria. N-doped titanium oxide films improve the visible light absorption range of TiO_2 since N-atoms occupy O-atom sites in the TiO_2 lattice forming ionic Ti-O-N bond red shifting the TiO_2 light absorption range towards the visible region.

Much attention has been paid to the development of the so-called adaptive materials, which means that they have to work successfully under different conditions and adapt to changing external factors [14].

On the other hand, molybdenum (Mo) is a good element in thin films or bulk materials, and functions similarly to vanadium (V). Due to its high temperature resistance, high thermal and electrical conductivities, it has been widely used in nuclear, defense and electronics industries. Low COF and good wear resistance were observed in various molybdenum-based nitride coatings, such as TiN/MoN and TiMoN [15]. This is due to the formation of a lubricious molybdenum oxide on the film surface that improves the wear resistance. Therefore, the magnéli-phase is a good lubricant in the Mo-based films where the existence of oxygen vacancies leads to the formation of easy shear planes with low friction properties.

Furthermore, Mo-based films were tested on Gram-positive and Gram-negative bacteria and showed antibacterial activity. It has been found that TiO_2 doped with Mo showed antimicrobial

performance on industrial surfaces. On the other side, Ag-nanoparticles were found to enhance the photocatalytic activity of TiON [16].

The aim of this thesis is to enhance the properties of coatings composed of two layers: The first layer of SS316L deposited by cold spray technique. Simulation and experimental study was done to identify the best process parameters used for high quality stainless steel coating (about 2 mm thick). Then a second layer of TiN(Al, Mo) quaternary coating was prepared by reactive R.F. magnetron sputtering. The purpose of this work is to improve the wear and corrosion resistance of coating. In this work, an innovative coating (TiMoONAg) was developed to enhance its antibacterial performance under solar light.

This thesis manuscript is divided into five chapters:

The first chapter focuses on the state of art where the stainless steels and their applications as well as the properties of cold-sprayed SS316L are presented. We present a global literature review on the binary TiN, ternary TiAlN and quaternary TiAlMoN systems, and finally, the novel TiMoONAg alloy coating.

In the second chapter, we presented the different techniques used for producing coatings, namely the cold spray of SS316L and magnetron sputtering techniques. This later was used for the preparation of TiN, TiAlN, TiAlMoN with different molybdenum contents, TiOMoN and TiMoONAg films with different silver contents. The different characterization methods used to determine the microstructural, mechanical, tribological and anti-corrosion behavior of our samples are also presented in this chapter.

In the third chapter, we first presented the optimal parameters of cold spray technique used to elaborate a good SS316L coating. The effect of both helium and nitrogen gases used was investigated. The tribological behavior was evaluated under different loads in dry conditions and the electrochemical corrosion performance was investigated in a 3.5 wt.% NaCl solution.

In the fourth chapter, we presented the hybrid coating developed and elaborated by both cold spray (CS) and magnetron sputtering (MS) techniques. In this chapter, we present the quaternary TiN(Al, Mo) coatings deposited by magnetron sputtering in a mixture gas (Ar and N_2). The physicochemical, tribological, mechanical and electrochemical properties of coatings were evaluated.

The fifth chapter presents the innovative TiMoON and TiMoON-Ag films prepared by RF-magnetron sputtering in (N_2/O_2) gas atmosphere. The physico-chemical properties of these coatings were evaluated. These coatings were annealed under vacuum at 400 °C to investigate their bacterial inactivation under simulated solar light irradiation. All results were given in details with adequate analysis and explanation.

Finally, the thesis is ended with general conclusions and perspectives for future works.

References

[1] L. Wang, D.O. Northwood, X. Niea, J. Housden, E. Spain, A. Leyland, A. Matthews, Corrosion properties and contact resistance of TiN, TiAlN and CrN coatings in simulated proton exchange membrane fuel cell environments, Journal of Power Sources, 195 (2010) pp. 3814–3821.

[2] K. Taube, K. Bewilogua, Encyclopedia of Materials: Science and Technology. (2001) pp. 9286–9293.

[3] S. Yoon, H. Kim, C. Lee, Fabrication of automotive heat exchanger using kinetic spraying process, Surface and Coatings Technology, 201(24) (2007) pp 9524-9532.

[4] J. Cizek, O. Kovarik, F. Siska, J. Bensch, J. Cupera, M. Matejkova, J. Siegl, T. Chraska, K. A. Kho, Increasing Fatigue Endurance of Hydroxyapatite and Rutile Plasma Sprayed Biocomponents by Controlling Deposition In-Flight Properties, ACS Biomater. Sci. Eng, 5 (2019) pp 1703-1714.

[5] G. Sundararajan, P.S. Phani , A. Jyothirmayi, R.C. Gundakaram, The influence of heat treatment on the microstructural, mechanical and corrosion behaviour of cold sprayed SS 316L coatings, Journal of materials science, 44(2009), pp. 2320–2326.

[6] T. Schmidt, F. Gartner, H. Assadi, H. Kreye, Development of a generalized parameter window for cold spray deposition. Actamaterialia, 54(3)(2006), pp. 729-742.

[7] M. Guemmaz, A. Moser, J. Grob, R. Stuck, Sub-surface modifications induced by nitrogen ion implantation in stainless steel (SS 316L) correlation between microstructure and nanoindentation results, Surf. Coat. Technol, 100-101 (1998) pp. 353-357.

[8] P. Wei, S.Lein, S. Chin, S. Jinn. Boron- ϕ doped Si grown by ultra-high vacuum chemical vapor deposition, Mater Chem&Phy, 767 (2002) pp. 426–429.

[9] D.M. Mattox, Handbook of Physical Vapor Deposition (PVD) Processing Noyes Publications, Westwood (1998).

[10] A.V. Ingle, V.S. Raja, J. Rangarajan, P. Mishr, Corrosion resistant quaternary Al-Cr-Mo-N coating on type 316L stainless steel bipolar plates for proton exchange membrane fuel cells, international journal of hydrogen energy, 45 (2020) pp. 3094 -3107.

[11] D. Zhang, L. Duan, L. Guo, Z. Wang, J. Zhao, W.-H. Tuan, K. Niihara,TiN-coatedtitaniumasthe bipolar platefor PEMFC by multi-arcionplating, Int. J. Hydrogen Energy, 36 (2011) pp. 9155–9161.

[12] C.J. Tavares, L. Rebouta, M. Andritschky, S. Ramos, Mechanical characterization of TiN/ZrN multi-layered coatings, J. Mater. Process. Technol. 92–93 (1999) pp. 177–183.

[13] H.A. Zaman, S. Sharif, M.H. Idris, A. Kamarudin, Metallic biomaterials for medical implant applications: A Review, Applied Mechanics and Materials 735 (2015) pp. 19−25.

[14] R. Franz, C. Mitterer, Vanadium containing self-adaptive low friction hard coatings for high-temperature applications: a review. Surf Coat Technol, 228 (2013) pp. 1–13.

[15] B. Tabernig, N. Reheis, joining of molybdenum and its application, Int. J. Refract. Metals Hard Mater. 28 (2010) pp. 728–733.

[16] M. Guemmaz, A. Moser, J. Grob, R. Stuck, Sub-surface modifications induced by nitrogen ion implantation in stainless steel (SS 316L) correlation between microstructure and nanoindentation results, Surf. Coat. Technol, 100-101 (1998) pp. 3

Chapter I

State of the art

Introduction

The increasing demand on stainless steel (SS) is more and more important due to its remarkable properties. However, it has some limits related to its low hardness, anticorrosion performance and anti-bacterial activity. One of the solutions used to protect stainless steels and to provide more functionality to the surface is to coat the manufactured SS pieces. In our work, we focus on the SS elaborated by cold spray and coatings deposited by magnetron sputtering technique. In the first step, the optimization of processes parameters is indispensable in order to get a high quality coating. Then, the physico-chemical and mechanical properties, anticorrosion behavior and bacterial activity of thin films are investigated.

In this chapter, we presented a literature survey on the stainless steels and their applications and we concentrate on the SS316L elaborated by cold spray. We present large literature reviews on titanium, titanium nitride, ternary TiAlN, quaternary TiAlMoN and (TiOMoN)Ag coating systems.

Part I. 1: Stainless steel

I.1.1 what is a stainless steel?

The stainless steel term is used to describe a family of about 200 alloys of steels with remarkable properties which in general are iron-based metal alloys containing carbon in the 0.03% - 1.2% range (Fig. I. 1). The SS is characterized by the high amount of chromium (≥ 10.5%) that improves its corrosion resistance and strength. The so-called “stainless” character is not due to the not oxidization of steel material. In fact, it oxidizes and forms some passive film rich in chromium that can protect the material. This mechanism allows retaining good appearance for long periods under normal working conditions.

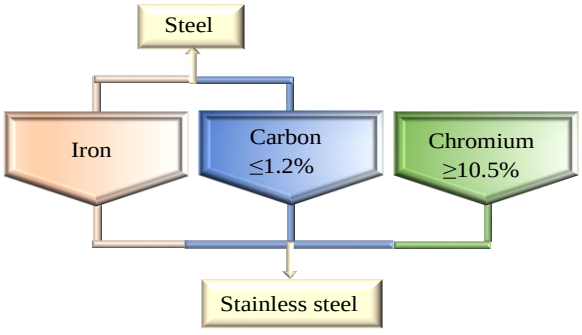

Fig. I.1. The basic elemental composition of stainless steel.

I.1.2 History of stainless steels

Stainless steel followed a series of scientific developments. The chromium content in steel was mentioned for the first time in the work of the French chemist *Nicolas-Louis Vauquelin* (1763). The first observations of the "stainless" properties of iron alloyed with chromium were performed by *Berthie*r, who showed in 1821 that the iron-chromium alloy was more resistant to certain acids. Its corrosion resistance was found enhanced with increasing the Cr content [1].

In 1840, both of British *Sheffield steelmakers* and then German *Krupp* (1850) were producing chromium steel. In 1861, *Robert Forester Mushet*gota patent on chromium steel in Britain. The first American production of chromium-containing steel was performed by *J. Baur* (*Chrome Steel Works of Brooklyn*) for the construction of bridges [2].

In 1904s in France, *Leon Guillet* prepared some alloys called today “stainless steel” and he published a study on chromium-nickel stainless steels (austenitic stainless steels) [2]. The German Philipp Monnartz reported on the relationship between chromium content and corrosion resistance by analyzing the passivity of stainless steels. In the early 1930s, *J. Hochmann* [1] discovered the austenitic-ferritic mixture phases that called duplex stainless steels. They are able to protect themselves from the surrounding environment by the spontaneous formation of a passive film on their surface in contact with air or an aqueous medium. The passive film of 1 to 10 nm thick is essentially composed of iron and chromium oxy-hydroxides [3-4]. The formation of this film leads to interesting mechanical characteristics such as mechanical strength, ductility and toughness. This enhances the material lifespan in the various environments.

I.1.3 Classification of stainless steels

The stainless steel family has several types of structures, which are differentiated by the alloying elements and their percentages. They can modify the iron-carbon equilibrium diagram and they can be grouped into two families: α-gene and γ-gene. The α-gene elements favor the preponderance at room temperature of the structure (cc) such as Cr, Mo, Si, V, Ti, and Nb. The γ-gene elements such as C, N, Ni, Cu, Co, and Mn promote the preponderance at room temperature of the crystallographic structure (fcc). We can distinguish four main types of stainless steels [3-5]:

- *Austenitic structure: It presents the largest family of stainless steels with a face-centered cubic crystal structure.*
- *Ferritic stainless steel with a BCC-crystal structure.*
- *Martensitic stainless steel with a metastable structure close to ferrite and a composition close to austenite.*
- *Austenitic-ferritic stainless steels (commonly called duplex steels) having a two-phase structure composed of ferrite and austenite.*

I.1.4 Applications and use of stainless steels:

Stainless steel is used in many fields including (Fig. I. 2):

- ***Construction and architecture***: Application of stainless steel in construction dates back over 90 years [6]. Thanks to its desirable durability and structural properties, it was used for many landmark buildings such as the cladding on the *Chrysler Building* in New York, the Atomism building in Brussels, Plaza Decoration Large Outdoor Sculpture Garden Statues, towers, domes, footbridges and road bridges.
- ***Medical application***: medical equipment needs to be in top condition and provides a high level of cleanliness. Stainless steel is used for the manufacturing of surgical instruments and implants [7] including calipers, scissors, scalpels, tweezers, and dental and orthopedic implants.
- ***Defense and nuclear industry***: Stainless steels are extensively used in heat transport system (HTS) of cooled water reactors like boiling water reactor (BWR) or pressurized water reactor (PWR)for nuclear application[8], artillery guns, missiles, etc.
- ***Industrial applications***: hygienic and durable alloy is required in food industries [9] and domestic kitchens like washing machines, knives, ovens and hot food containers, etc. It is also used in chemical and petrochemical industries. In addition, in order to provide a better internal anti-corrosion resistance, stainless steel has been increasingly used in submarine pipeline applications [10] as well as for power generation and electrical engineering. This type of steel fulfills most of the requirements as bipolar plates in Proton Exchange Membrane Fuel Cell [11].
- Due to its aesthetic appearance (silver shine), stainless steel is widely used in decoration, doors, jewelry, watches, neckpieces, anklets and rings.

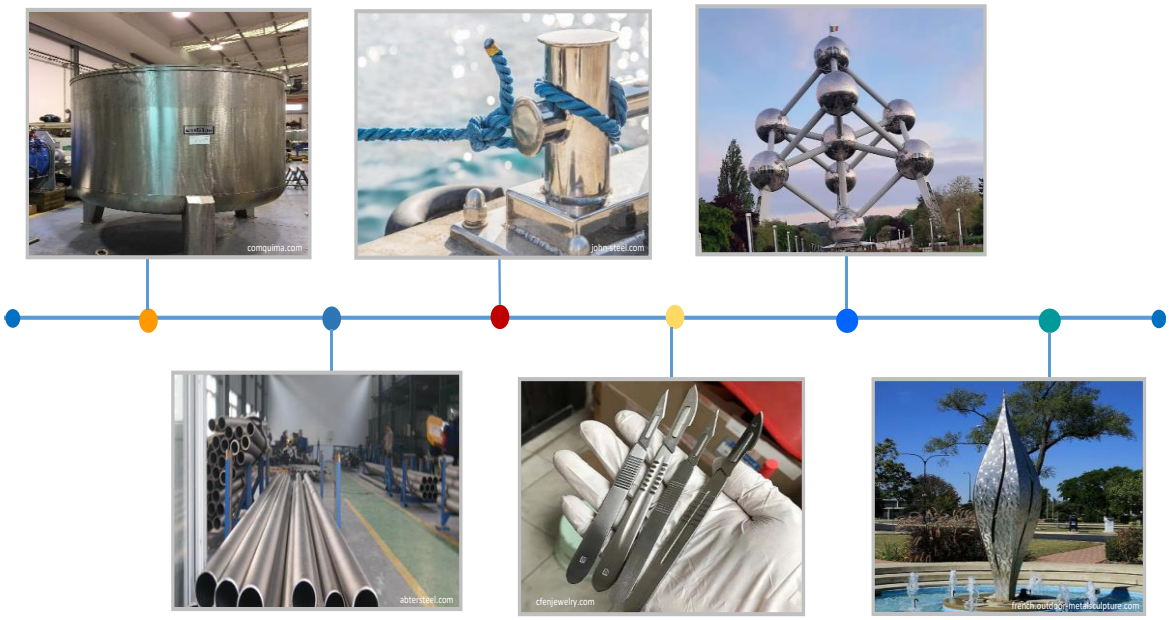

Fig. I.2. Different applications of stainless steels.

I.1.5 316L stainless steel

In this study, we will focus on the austenitic steels, in particular the 316L grade. It is classified under the Cr-Ni-Mo austenitic steel category with low carbon, which includes special alloys.In this family, we find steels 316, 321, 347 and 304. They have a low yield strength of less than 300 MPa, a fracture toughness of 100-278 MPa $m^{0.5}$.and a hardness of 250-400 HV as well asa low elongation[5]. However, 316L steel appears to be the most resistant to cracking after holding at high temperature, even under stress. Its ductility remains much higher than that of the steels mentioned above [12]. It is easily distinguishable from the rest because of its excellent corrosion resistance, in particular against sulfuric, hydrochloric, acetic and formic acids; acid sulphates and alkaline chlorides. This is due to the formation of a passive layer generally described as being composed mainly of chromium oxide in its internal part and iron oxy-hydroxides in its external part [13-14]. In welding applications, we can also remark the useof this material, which is due to thelow carbon content-minimal carbide precipitation.

I.1.6 Fabrication of 316L stainless steel by cold spray

316L stainless steel is elaborated by different techniques such as directed energy deposition (DED)[15], wire arc additive manufacturing (WAAM) process[16] and the laser direct metal deposition (LDMD) [17], etc. It was also previously obtained by thermal spraying, which contains a relatively high amount of oxides [18-20].The recent progress in the cold spray technique has been a great development for the deposition of metallic coatings containing little oxide [21]. There are several studies on this steel deposited by cold spray [22-24]. It is well known as a good corrosion resistant which has widely used in biomedical and food industries.To this date, a certain number of works have been carried out to study the manufacturing parameters, microstructures and properties of 316L coatings [25-27]. Many reserchers have shown that the quality of the cold spray coating depends on the gas used, the temperature, the pressure, the nozzle type ans its distance to the subsrtae.

In cold spray, the used gas is conventionally air, helium, nitrogen and their mixtures.*Dikici et al*. [28] deposited 316L using helium and nitrogen as the carrier gases with thickness of ~ 900 µm. The cross sectional SEM images (*Fig. I.3*) show a denser microstructure with lower volume porosity of 4.9 (±1.18) vol. % and 6.3 (±2.16) vol. % for 316L-He and 316L-N_2 coatings, respectively.

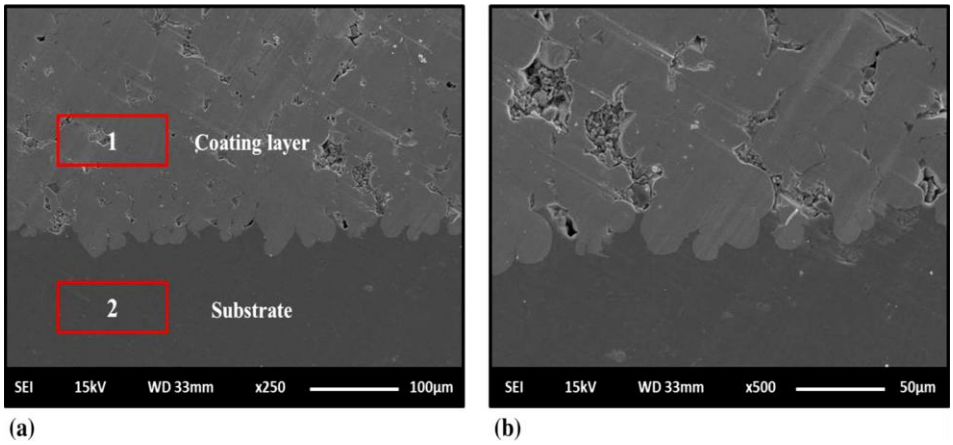

Fig. I.3. Cross-sectional SEM images of 316L coatings deposited with (a) He and (b) N_2 [28].

According to *Al-Mangour et al*. [29], the cold sprayed 316L deposited by using either N_2 or He propellants has been successfully employed to produce dense coatings with stable phase. Low porosity (≤0.3%) was obtained in He-sprayed coatings in the as-sprayed condition, while a heat treatment up to 800 °C allowed enhancing the density of the N_2-sprayed coating.

Adachi et al. [30] found that deposition of the AISI 316L powders of (5–20) µmat a higher nitrogen propellant gas temperature (700-800) °C, a 3-3.5 MPa pressure and a 40 mm standoff (distance between the nozzle and the substrate) presented the densest microstructure. They indicated that the sprayed coating, using air as accelerating gas, presented a relatively porous structure with about 3% of porosity. A dense coating with high micro hardness was obtained using an optimized nozzle (*Fig. I.4*) [26].

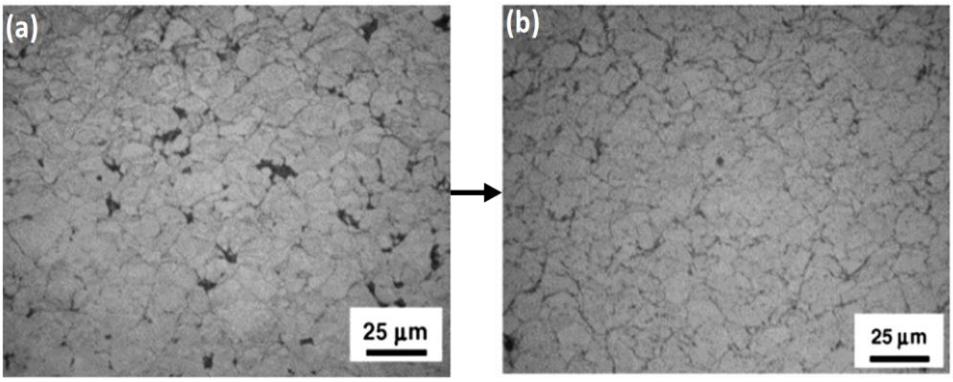

Fig. I.4. OM micrographs of the sprayed 316L stainless steel coating using air deposited with the (a) supplied and (b) optimized nozzle [26].

As mentioned by *Villa et al.* [22] the optimal cold sprayed coating of 316L steel is obtained at the highest temperature and pressure. The hardness value of 358 ± 36 HV was almost double than that of the initial powder.

The study of the tribological properties of the cold sprayed 316L steel is very limited. In order to improve the corrosion and wear resistance in dry conditions of commonly used alloys, 316L stainless steel coating is deposited using cold spray technology. *Chen et al* [31] improved the wear resistance of 316L steel-coated magnesium alloys tested against GCr15 and Si_3N_4. They found high friction coefficients of 0.7 and 0.65 and wear rates of 5.5. 10^{-4} mm^3/Nm and $9.6.10^{-5}$ mm^3/Nm, respectively. For the corrosion behavior in a3.5 wt.% NaCl solution, the 316L coating shifted the polarization curve of magnesium alloy substrate to a lower current density value and a more positive potential value: from 2.6×10^{-5} A/cm^2 and -1.27 V_{SCE} to $2.9\times10^{-7}A/cm^2$ and -0.26 V_{SCE}. Moreover, the stainless steel coatings evidently reduce the corrosion current density with no galvanic corrosion sign of the magnesium substrate. Corrosion tests performed by *Sova et al.* [23] showed that the 316L coatings of 1-3 mm thick deposited on aluminum substrate using nitrogen as a carrier gas with coarse powder have the

lowest potential and the highest corrosion current. The decrease in particle size leads to slight decrease in this current density.

Dikici et al. [28] found that the 316L coating sprayed using N_2 gas presented lower corrosion resistance than the material cold sprayed using He gas (tests performed in a 3.5% NaCl solution). From *Fig. I.5*, we can see the presence of small round pits on the 316L-He coating and the elongated pits on the 316L-N_2 coating. This behavior may be related to their higher porosity values, which act as preferential areas to Cl^- ions in the solution that facilitate the electrolyte penetration. This rapidly reaches the substrate and increases the corrosion of coatings.

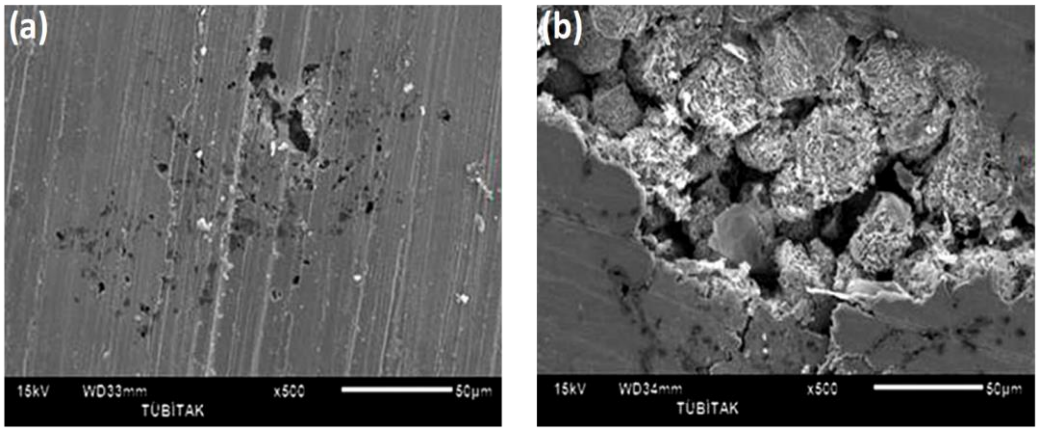

Fig. I.5. Corrosion and pits morphologies of 316L coating cold-sprayed using (a) He and (b) N_2 [28].

Austenitic stainless steels have an important use in the biomaterials field (especially the 316L stainless steel grade). This is utilized as an implant material to make devices like artificial joints, bone plates, and prosthesis. It is also used in food industry which is due to its excellent mechanical properties, availability, good biological and chemical properties as well as its low cost as compared to other implants metals [32-35].

However, they do not possess antibacterial properties. Inflammation and infection, which are usually due to the adherence and colonization of bacteria on biomaterials, are one of the major limitations of 316 L stainless steel. The surface of metallic implant and surgical site infection associated with surgical instruments which are a part of 316L medical devices are susceptible to initial adhesion of pathogenic bacteria including *Staphylococcus aureus, Pseudomonas aeruginosa, and Escherichia coli* [36]. The viability of bacteria attached to the 316L surface was tested by *Jin et al* [37] using the spread plate method for Escherichia coli.

They observed that the surface of stainless steel was almost completely covered by bacterial colonies due to its poor antimicrobial property. This phase becomes more virulent when they form a bio-film on the surface that is later hard to be eradicated. Therefore, an ideal device surface should be able to combat bacterial adhesion and colonization to prevent post-operative infections [38].

Part I.2: Titanium-based thin films

I.2.1 Titanium(Ti)

Titanium (Ti) is a transition metal of Group 4 (IVb) of the periodic table and the ninth most abundant element on Earth [39]. A compound of titanium and oxygen was discovered in 1791 by the English chemist and mineralogist *William Gregor* and independently rediscovered in 1795 and named by the German chemist *Martin Heinrich Klaprothbut.* It could only be obtained in high purity with a silvery grey color(*Fig. I.6*). Only since 1920 its properties were discovered by *Van Arckel and De Boer* [40].

Fig. I.6. Pure titanium [41].

Titanium (Ti) is a rather abundant metal on Earth but expensive due to its complex extraction and purification process. This material is chosen for many applications mainly due to its excellent properties (*Table. I.1*).

Table. I.1. General Properties of Titanium [42-43].

Atomic number	22
Atomic weight ($g.mol^{-1}$)	47.9
density ($g.cm^{-3}$)	4.54
Thermal conductivity ($W.m^{-1}.K^{-1}$)	19.2
Melting point (°C)	1668
Young'smodulus(GPa)	116
Vickers hardness (MPa)	800~2700 MPa
Yield strength (MPa)	380

The unalloyed titanium is characterized in particular by the high strength, good oxidation and corrosion resistance, and excellent hardness. It has two allotropic varieties (*Fig. I.7*): The phase (hexagonal compact), stable under standard temperature and pressure conditions and the β phase (centered cubic), stable above the allotropic processing temperature of 882.5 °C [5]. The addition of some chemical elements influences the Ti equilibrium diagram differently. Some of them are alphagenic that promote the compactness of the hexagonal α phase (e.g, O, N, B, C, Al…). The other betagenic can promote the centered cubic β phase (e.g, Mo, Nb, Fe, Cr…). Zn and Zr are neutral elements [43-47].

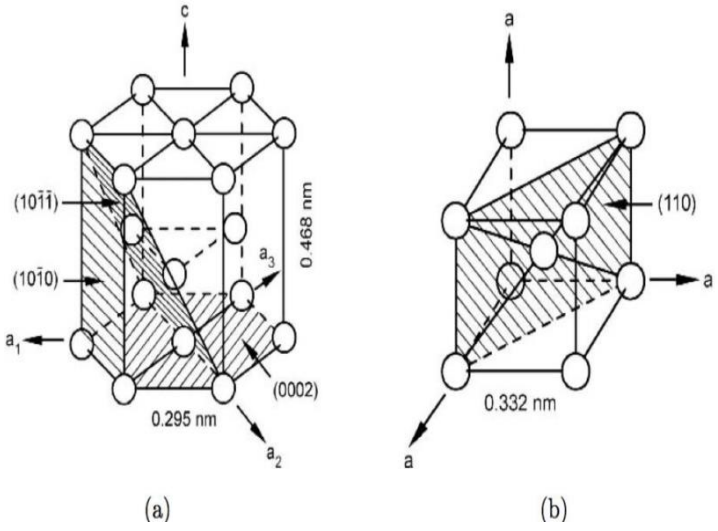

Fig. I.7. Crystal structure of: a) α-titanium, and b) β-titanium [47].

Titanium films are widely used in microelectronics: Very-Large-Scale Integration (VLSI) technology and Micro Electro Mechanical System (MEMS) based devices [48-49]. They are used as bolometers in infrared sensors [48], superconducting surface sensors in micro-

calorimeters and light detectors [5]. Its special properties make it a good choice for different applications such as aerospace and aeronautics, chemical, electrochemical, petrochemical and nuclear industries. It is well known for its high corrosion resistance, where it is used in the offshore oil and gas industry. This material presents also a great potential for the medical and aeronautic application [45-46]. It is intensively used in medicine and more particularly to develop cardiovascular (stents) and orthopedic prostheses [43]. Its mechanical properties and biocompatibility allow designing light and resistant prostheses [50]. Moreover, being non-magnetic material, titanium is compatible with current medical imaging techniques [51-52].

I.2.2 Ti-N coating

I.2.2.1 Structure et morphology

Titanium nitride TiN is one of the first industrial PVD nitride coatings [53]. Since 1980, it has been the subject of various studies due to its particular properties. TiN has a rock-salt structure (NaCl-structure) compound made up of titanium atoms in a face-centered cubic (fcc) based lattice with nitrogen atoms filling all octahedral positions (*Fig. I. 8*). It is a refractory material with a strong covalent Ti-N bonding energy [54].

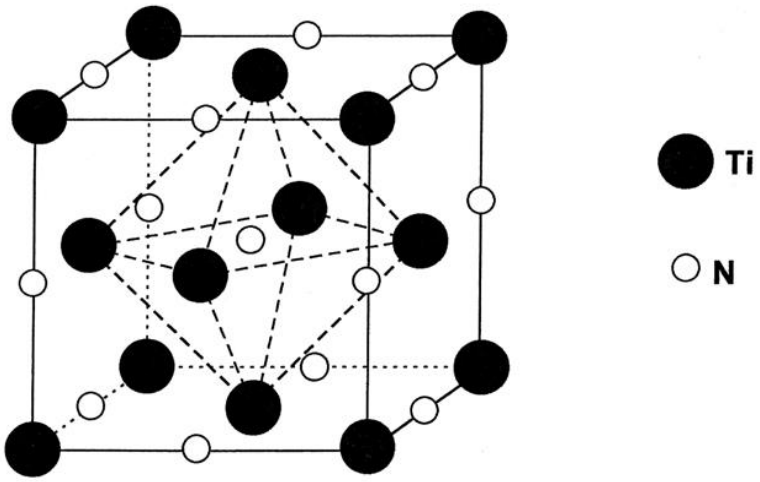

Fig. I.8. Lattice structure of TiN [55].

The equilibrium phase diagram of the Ti-N system is shown in *Fig. I.9*. several stable phases exist at low temperature depending on the nitrogen fraction. The solubility of nitrogen in α-titanium at low temperature is about 3 at. %. Beyond that, the Ti_2N compound is formed as well as the δ' compound up to 41 at.% of nitrogen. TiN is a stable phase and has a large

domain, ranging from 30 at. % (at 1000°C) up to 55 at. %, which corresponds to a stoichiometry variation from $TiN_{0.4}$ to $TiN_{1.2}$ [56]. However, *Hulten* noticed that for strongly over-stoichiometric coating, with N/Ti ratio> 1.2, the nitrogen is not integrated into the crystallographic structure but rather in the form of N_2 bubbles at the grain boundaries [57].

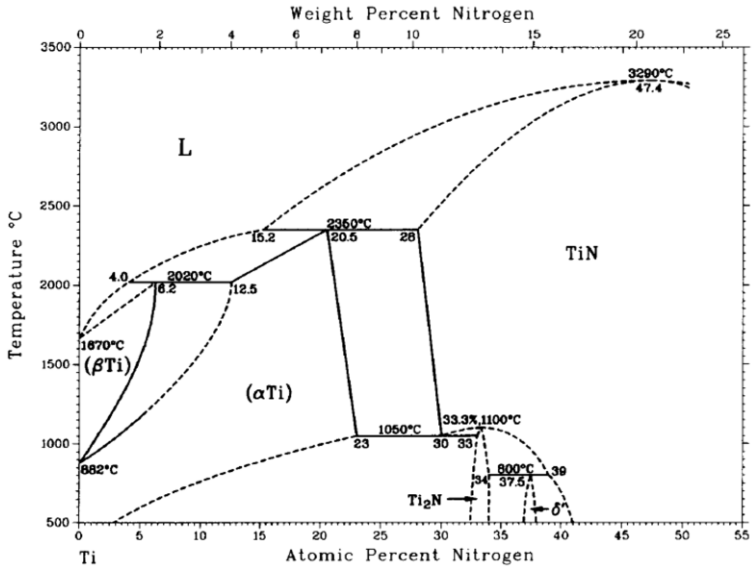

Fig. I. 9. Equilibrium phase diagram of Ti-N binary system [57].

The cathodic magnetron sputtering technique is an interesting alternative, in particular for deposition of nitrides such as TiN which are known to have a columnar structure (*Fig. I.10.a*). This is uniform and textured and exhibits a preferential crystallographic orientation [58-59]. The<111> orientation is most often observed [60] (*Fig. I.10b*), although the orientation in the <200> and <220> directions are also reported [61].

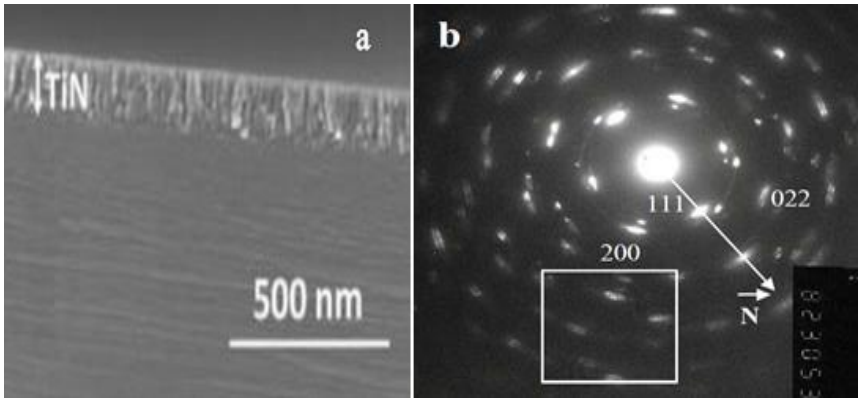

Fig. I.10.a) Cross sectional SEM image and b) selected area electron diffraction pattern of TiN coating [62-63].

Pelleg et al. [64] reported that for this material which crystallizes in NaCl type structure, the (200) plane has the lowest surface energy. The privileged (111) plane orientation is due to the minimization of the energy of the internal stresses which translate the presence of strong residual stresses within the coating. More recently, *Jones et al*. [65] and *Aissani et al.* [66] deposited TiN coatings by magnetron sputtering technique and confirmed that their preferential orientation was along the <111> direction.

I.2.2.2 Mechanical properties

In recent years, an important interest has been given to the titanium nitride thin films due to the superficial hardening generated by these films. The TiN coating deposited by PVD has high mechanical properties [67-68], which provide an improvement in the hardness and Young's module of SS316L substrates [69-70]. In the literature, we found that the hardness value of this coating is varied between 15 and 29 GPa [71-72]. *Łępickaet al* [73] performed nanoindentation tests and they found that the hardness and the elastic modulus of the coating increased from (7.5 ± 0.7) to (27.4 ± 4.0) GPa and from (231.7 ± 21.4) to (417.9 ± 65) GPa, respectively. According to *I. Saravanan et al*. [74] the microhardness was increased by approximately 9 times compared to the uncoated substrate with a fine grain structure and a higher resistance to plastic deformation. The residual stress generated in the sputtered TiN film can be either compressive or tensile. Its tendency observed in literature depends on the film thickness, crystal size, number of defects, adhesive layer and the deposition temperature [75-77].

I.2.2.3 Tribological properties

Many researchers have studied the tribological performance of the TiN-coated 316L stainless steel [78-79]. *Quan et al*. [80] found that the TiN film improves the wear resistance of 316L in a Simulated Body Fluid (SBF solution). *Wang et al.* [81] found that TiN tested against Al_2O_3 counterpart under 2N applied load and a 0.2 m/s speed presented low friction coefficient of 0.36 and wear rate of $3.19\times10^{-6}mm^3/nm$. In addition, *Saravanan et al.* [74] confirmed that the TiN coating on the SS 316L surface exhibited a superior wear resistance. These investigations demonstrate that the TiN oxidizes to TiO_2, which is less resistant to abrasion and reduces the friction with increasing temperature during sliding [82].

I.2.2.4 Corrosion behavior and wettability

Many studies on corrosion behavior have shown that TiN coatings can improve the corrosion response in certain solutions for extensive applications [83-85]. It is a material known for its good corrosion resistance, due to the high abandonment potential. In the corrosion phenomenon, the oxidation reaction of the TiN takes place in three stages: first, oxygen diffuses within the TiN lattice, which leads to the replacement of N by O, leading to the formation of titanium oxynitride as a protective film [5]. *Hentall et al.* [86] found that stainless steel 316L coated with TiN presented low contact resistance similar to gold and graphite coatings. *Lang et al*. [87] and *Omrani et al*. [88] reported that steel with low carbon content coated withTiNshowed critical and passive current densities lower than those of the substrate in a 1 M H_2SO_4 solution. *Hsu et al.* [89] found that by using 3.5 wt. % NaCl solution and with comparison to the uncoated substrate (SS316L), the TiN-coated SS316L samples exhibited an increase in Ecorr (-0.242 vs. -0.196 V_{SCE}) with a lower corrosion current density value (Icorr. = 22.4±1.1 and 19.5±0.1) $\times 10^{-9}$ A/cm^2, respectively. They characterized atypical morphology of localized corrosion occurred on the surface (*Fig. I.11*). *Wang et al.* [90] revealed that Ti and TiN coatings enhance the corrosion resistance and lead to relatively stable corrosion potential in an SBF solution. These results revealed that TiN coatings clearly improve the corrosion resistance of the SS316L.

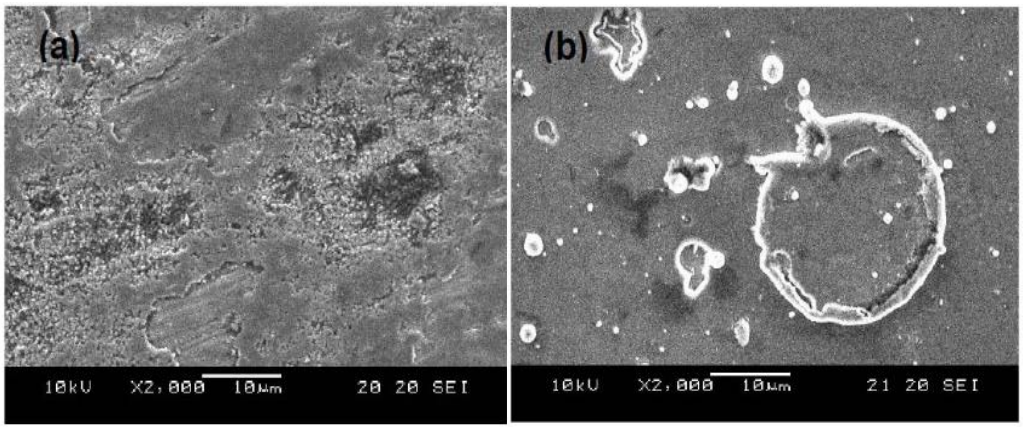

Fig. I.11. Surface morphology of (a) uncoated and (b) TiN-coated SS316L samples after polarization tests in a 3.5 wt.% NaCl solution [89].

Generally, a surface is considered hydrophilic with a contact angle <90 °, while it is considered hydrophobic if the contact angle is> 90° [49-50]. The spreading properties of lubricants become another key factor in the performance of PVD coated tools and therefore

the understanding of wettability has become crucial for optimizing the application field. In order to evaluate this ability [91-93], the measurement of different wetting parameters (contact angle, surface tension, spreading parameter…) is a good starting approach [94].The hydrophilic surface is harmful and prevents combustible gases from accessing the electrode [95]. In addition, accumulated water can also accelerate the degradation of corrosion resistance of bipolar plates. According to *Yi et al*. [96] the measured contact angles on 316L stainless steel substrate and TiN/316L using deionized water were approximately 81° and 101°, respectively, which confirms that the TiN-coated SS316L has a hydrophobic character.

I.2.3Ti-Al-N Ternary Coating

Aluminum (Al) is the 13th element in the periodic table distinguished with a light weight and a white color (*Fig. I.12*) [97]. Aluminum is the most abundant metallic element in Earth's crust. It is also the third most common chemical element on our planet after oxygen and silicon and the most widely used nonferrous metal. It normally exists in combination with oxygen, silicon, fluorine, and other elements [98-99].

Fig. I. 12. Pure Aluminum [97].

The main properties of aluminum are:

- *Excellent conductor of heat and electricity. Its thermal conductivity is about one-half that of copper and its electrical conductivity is about two-thirds.*
- *It is crystallized in an fcc-structure.*
- *Ductile and highly malleable with a low density: 2700 kg/m^3.*
- *Fusion point of 658 °C and Vickers Hardness of 167 MPa.*
- *Low Young's modulus (70 GPa) and yield strength (11 MPa for a pure Al)*

- *Highly oxidizable element; it is immediately passivated by a thin layer of alumina which protects the metal from corrosion and often used in maritime applications.*
- *Theoretically, this metal can be 100% recyclable with no quality loss.*
- *Re-melting of aluminum doesn't require a lot of energy, making it a more sustainable metal than others [98-102].*

TiN coatings have some limitations when used on high-speed machines in dry machining conditions, under high temperature [103], which causes the deterioration of the properties of the TiN coating. In order to improve the properties of TiN/316L many efforts have been made to overcome these limitations by the development of ternary compounds (Ti, X) N [104-105]. The titanium-aluminum-nitride is one of the most attractive coating materials that are well-studied as a ternary system in the 1980s. The first reported phase was Ti_2AlN in 1963, which is characterized by its resistance to high temperature abrasion and its good thermoelectric conductivity [106]. The TiAlN coatings can also be an alternative because they have a great improvement in the resistance to oxidation compared to the TiN coatings, being possible to use them at high temperature up to 800 °C. In recent years, the TiAlN has attracted a lot of interests because it has much better resistance to wear and a longer lifetime compared to the TiN coating [107].

Yang et al. [108] studied the effects of Al addition on microstructure and mechanical properties of TiN coating. They observed that TiAlN coatings showed columnar structure with fine grains, indicating that the increase in hardness results from grain size refinement, solution hardening and/or second-phase precipitation as shown in (*Fig. I.13*).

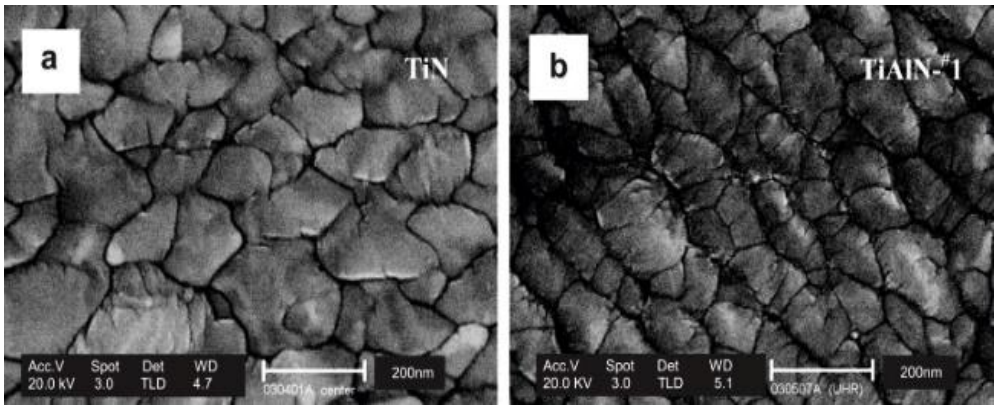

Fig. I.13. Surface morphology of a)TiN and b) TiAlN coatings [108].

Knotek et al. [109] and *Königet al*. [110] reported that Al has a higher activity than the Timoving through the parent phase, titanium and aluminum oxides. The formation of Al_2O_3 protection layer can also reduce the friction coefficient and the atomic diffusion in the film. In fact, this layer prevents the penetration of oxygen and therefore prolongs its lifetime compared to the pure TiN [108,111, 112].

The insertion of Al atoms into the TiN structure generally gives a polar interphase causing metallic (Ti-Al) and covalent (Ti-N et Al-N) bonds, which directly influence the electrical resistance of the TiN and TiAlN coatings [113-115]. *Yeung et al.* [116] fabricated ternary nitride coatings (TiAlN) using reactive magnetron sputtering at working pressures of 0.053 and 0.128 Pa. They found that increasing the nitrogen pressure led to reduce the film hardness from 18.6 GPato 13.6 GPa, respectively. Chu *et al.* [117] studied the mechanical properties of (Ti, Al)N films as a function of negative bias voltage, prepared at room temperature by a reactive closed field unbalanced magnetron sputtering in argon and nitrogen gas mixture. It was found that the variation of hardness and residual stress was clearly related to the negative bias voltages (U_b). At higher values of U_b, the enhanced hardness was more significant when comparing with TiN. The compressive stress in (Ti, Al) N films, deposited on SS, increased significantly with increasing U_b and reached a maximum value of 6.6 GPa. This high value of compressive stress was obtained in the film having a dense microstructure.

In general, the wear behavior of the coatings is evaluated in terms of wear rates and friction coefficients during the sliding processes against different counterparts. Wear and friction are complicated phenomena because it could be influenced by many parameters such as applied load, contact geometry, surface roughness and the existence of transferred layers between the counterpart materials, etc. *Zhang et al*. [118] investigated the performance of TiAlN-coated cutting tools in dry cutting. This coating showed an excellent wear resistance during machining of basic materials such as aluminum alloys and austenitic stainless steels [119]. In addition, according to [120-121], AlCrN and TiAlN coatings were confirmed to be also good wear resistant. Therefore, TiAlN coatings were suggested to be more advantageous than TiN coatings for high speed machining with respect to machining efficiency aside from the importance of TiAlN coatings that could be used at high temperature. *Man et al.* [122] revealed that adding 40 at.% of Al in the coating is the best choice to obtain the best oxidation resistance and the best hydrogen permeation barrier performance. The microstructural, electrical and corrosion properties of TiAlN/316L coatings were investigated by *Yun et al.*

[123]. The TiAlN film presented a smooth surface with an amorphous structure that resulted an excellent corrosion resistance (0.12 µA/cm^2) compared to uncoated 316L (1.5 µA/cm^2) and coated with TiN (0.35µA/cm^2).

The corrosion resistance of TiAlN is better than TiN, which is related to the addition of Al as a third transition element [124]. During the chemical attack, Al easily forms Al_2O_3 layer on the surface of the coating, which passivates the surface and prevents further corrosion [125].*William Grips et al.* [126] confirmed that the TiAlN coating exhibits better corrosion behavior as compared to the TiN and the CrN coatings tested in a 3.5 wt. % NaCl solution.

Ananthakumar et al. [127] evaluated the influence of TiN and TiAlN coatings on the 316L stainless steel after corrosion test performed in a 3.5wt. % NaCl solution. From the SEM images, more defects and corrosion products were observed in the bare SS316L with fine pits distributed throughout the surface (*Fig. I.14a*). For TiN coating, the surface exhibited several pinholes morphologies (*Fig. I.14b*).Thiscan be attributed to the columnar microstructure of the sputtered TiN coatings containing a lot of micropores which lead to accelerate the corrosion phenomenon. In the case of TiAlN coating, a low corrosion can be observed because of the formation of a stable layer ofAl_2O_3 on the surface of the coating (*Fig. I.14c*).

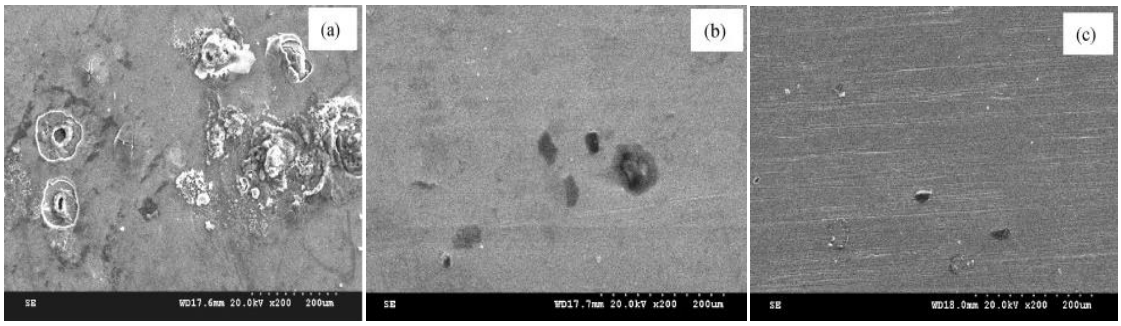

Fig. I.14. SEM surface morphology of (a) SS316L, (b) TiN, and (c) TiAlN coatings after corrosion tests in a 3.5wt.% NaCl solution [127].

Wettability can be described as the better spreading of a liquid on a tested surface [128]. According to *Mani et al.* [129] the contact angle measurements of uncoated SS316L, TiN, and TiAlN coatings are shown in *Fig. I.15*. The measured values were found 65°, 87° and 93°, respectively. All the coatings exhibited higher water contact angle values than that of the uncoated substrates, which indicate a low surface energy of coatings.

Fig. I.15. Contact angles of a) uncoated, b) TiN andc) TiAlN samples [129].

Zhang et al. [130] investigated the wettability of polished and multi-scale laser treated substrate surfaces and their impact on the adhesive strength of a PVD TiAlN coating. The results indicated that adhesion was enhanced by laser surface texturing due to the presence of micro/nano-scale grooves on the surface, which increased the hydrophilicity and hence the surface reactivity. On the other hand, it is known that if the surface roughness of a material increases, its surface will have low contact angle with water and as a result will exhibit high hydrophilicity due to the liquid filling the air pockets in the surface gaps [131]. This was confirmed by *Çomaklı et al.* [132] where the contact angles measured on TiN and TiAlN coatings were 65° and 67° that correspond to the surface roughness values of 0.41 µm and 0.38 µm, respectively.

I.2.4 Ti-Al-Mo-N Quaternary Coating

Molybdenum (Mo) is a lustrous and silvery metal (*Fig. I.16*). It is the 42th element in the periodic table and it is one of the elements of the second transition series, in Group 6B between chromium and tungsten. This element was discovered in 1778 by Carl Wilhelm Scheele as a new entity from the mineral salts of other metals, and then the metal was first extracted and isolated in 1781 by *Peter Jacob Hjelm* [133].

Fig. I.16. Pure Molybdenum [134].

The main properties of molybdenum are [135-139]:

- It has the sixth highest melting point (2620 °C) of all elements. It readily forms hard and stable carbides in alloys and for this reason the world most production of this element (about 80 %) is used in steel alloys, including high-strength alloys and super alloys.

- *Excellent thermal conductivity and a low degree of thermal expansion.*
- *The crystal structure of molybdenum is body-centered cubic structure. Its Vickers hardness is approximately 1530 MPa.*
- *In Industry, molybdenum compounds (about 14% of the world production) are used in high-pressure and high-temperature applications as pigments and catalysts.*
-*Molybdenum is less toxic than Cr, Co, and Ni.*
-*Mo-based films show good biomedical properties (they were tested on Gram-positive and Gram-negative bacteria).*

Important attention has been paid to the development of the so-called adaptive materials, which imply to work successfully under various conditions and adapt to changing external factors [140-141]. Several researchers demonstrated that the hard coatings are usually characterized by good tribological properties through oxidation during friction by the formation of a solid lubricant [142-143]. The demand for green manufacturing like high-speed machining or dry cutting along with environmental protection legislation and the increase in its associated cost has put huge pressure on the industry [144].

In fact, the combination of TiN coating with other elements (Al, Mo, Cr, etc) improves the hardness and wear resistance of the product. TiAlMoN films with different Mo contents were deposited by *Yang et al*. [145] using magnetron sputtering after depositing a Ti underlayer. They observed that both the TiAlMoN film and the Ti underlayer exhibited columnar growth perpendicular to the substrate-interface. It has been found that increasing the Mo content led to change the structure of TiAlMoN film. At 8.3 at. %, the columnar grains of TiAlMoN film disappeared and the film exhibited a good uniformity. With a further increase inMo content (12.1 at. %), the film morphology changed again to a columnar-granular structure (*Fig. I.17*).

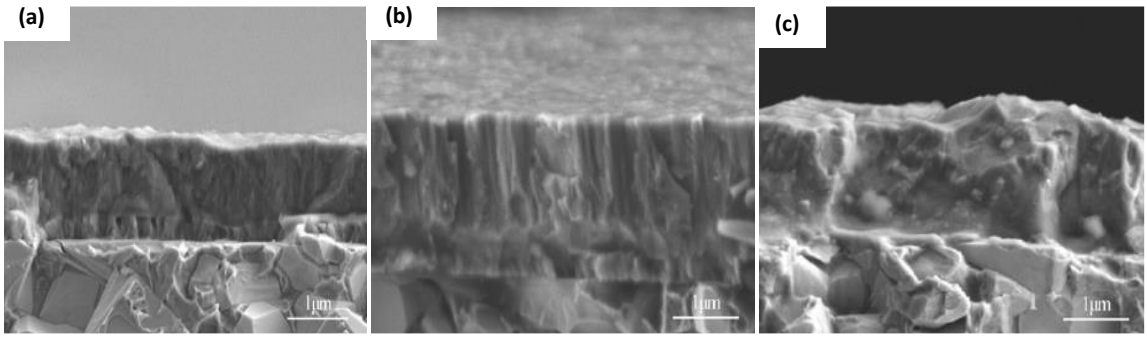

Fig. I.17. SEM cross-sectional structure of TiAlMoN films with different Mo contents: (a) 2.8 at.%; (b) 8.3 at.% and (c) 12.1 at.%[145].

From the literature, we can notice that the TiAlMoN films mainly present the TiN withother phases of Ti_2N, AlN, Mo_2N and MoN[146-145]. The presence of these phases suggests that Al and Mo atoms incorporate within the TiN crystalline lattice resulting in solid solution. It was observed that the molybdenum addition to TiAlN led to enhance the hardness and the elastic modulus of film. The improvement of mechanical properties is due to the increased solution strengthening [147-148]. According to *Qi et al*. [149], for the fcc structure nitride films, the TiN(111) preferred orientation has the lowest Schmid factor compared to (220) and (200) planes, which explains its high hardness. Otherwise, the enhanced mechanical properties can also be explained from XRD analysis by the increasing of intensity of TiN (111) peak with increasing the Mo content.

Low friction coefficient and excellent wear resistance were observed in various works investigating Mo-alloyed nitride coatings, such as TiN/MoN [150], TiMoN [151-152] and Mo–Si–N [153]. Molybdenum is considered as a potential alloying element in films which form a series of oxides that belong to the group of so-called Magnéli phases, depending on the specific order of oxygen vacancies leading to the formation of easy shear planes with low friction properties [154-155]. It is well accepted that the low friction of Mo-containing coatings is attributed to the formation of a lubricious MoO_3 layer through tribo-oxidation [146]. *Yang* [156] compared the friction and wear behaviors (in dry condition) of Mo-containing coatings (MoTiN, MoAlTiN, MoCrN and MoZrN) with their corresponding Mo-free TiN, AlTiN, CrN and ZrN coatings. It has been found that coatings doped with Mo had relatively lower friction coefficients. However, limited studies were carried out on quaternary nitride coatings doped with molybdenum such as TiAlMoN [157] and TiMoCN [158]. Regarding the previous works,

molybdenum is expected to be a good candidate for enhancing the wear and corrosion resistance.

Sergevnin et al [146] explained the decrease of friction coefficient of TiAlMoN films from 0.5 to 0.35 tested against Al_2O_3 balls in dry conditions by the formation of MoO_3 that acts as a solid lubricant. *Tomaszewski et al* [155] confirmed the improvement of tribological properties by the addition of molybdenum in TiAlN coatings. *Yang et al* [145] indicated that the best wear resistance was found for the TiAlMoN film containing 8.3 at. % of Mo, resulting from the highest toughness and the formation of molybdenum trioxide on the wear track surface. There are no previous studies on the wettability and pitting corrosion of the TiAlMoN coating.

I.2.5 Ti-O-Mo-N-Ag Quinary Coating

Pure silver (Ag) is nearly white and lustrous transition metal (*Fig. I.18*). It has an atomic number of 47 and it is located in Group 11 (Ib) and Period 5 in the periodic table, between copper (Period 4) and gold (Period 6). Its physical and chemical properties are intermediate between those Cu and Au metals. Silver is found in the Earth's crust in a pure form, free elemental form "native silver", or as an alloy with gold and other metals, and in minerals such as argentite and chlorargyrite [159].

Fig. I.18. Pure Silver [160].

The main properties of Silver are:

- *Silver is soft, very ductile and malleable metal. It has the highest electrical conductivity of all metals, but it is not widely used for electrical purposes as it is very expensive. It also has the highest thermal conductivity and reflectivityand it is used in fabricating*

printed electrical circuits and as a vapour-deposited coating for electronic conductors. It isoften alloyed with such elements as nickel or palladium for use in electrical contacts.

- *Silver is one of the noblest and lowest chemical reactive element among the transition elements. It is a highly inactive metal (it does not react with oxygen in air under normal conditions).*
- *Silver has an fcc crystalline structure and its Vickers hardness and Young's modulus are approximately 251 MPa and 8.3 GPa respectively.*
- *Silver is a natural element that has been used for currency and jewelry, for food serving, for water purification and more recently for industrial applications.*
- *It was perhaps the most important antimicrobial compound before the production of antibiotics in the 1940s. It is still used today in a wide range of medical applications because of its antibacterial effects and low toxicity to human cells.*
- *Silver is also widely used as a (co-) disinfectant of water systems such as swimming pool water, hospital hot water systems and potable water systems. It does not cause any undesirable effect on the color, taste and odor of water [159-164*].

There are no previous studies on the TiOMoNAg coating. We are the first who elaborate this coating by magnetron sputtering and investigate its antibacterial performance under solar simulated light with different conditions. This type of components can be designed as an advanced antibacterial TiOMoNAg coating. In this section, we introduce the important role, influence and effectiveness of this component on the antibacterial performance.

Infections due to bacteria are still unfortunately a major issue worldwide. It is reported by World Health Organization that approximately 1.4 million people suffer from serious infections by human pathogen in healthcare environments (nosocomial infections), which are considered as the fourth leading cause of disease in developed countries [165]. The number of patients that are affected by healthcare-associated infections is in the order of 10^8 each year, leading to significant mortality and financial losses for health services across the world [166-168].

The ability to sterilize these surfaces is a key to human comfort and health. However, the use of antibiotics to treat these infections implies high costs and induces bacterial resistance when administered for an extended time. Environmental pollution has been detected due to

furtive emissions from hospitals and health care facilities because of the use of antibiotics, antiseptics, and related drugs to eradicate pathogens [169]. For instance, titanium and its alloys have attracted considerable attention in biomedical applications (e.g. dental implants, artificial joints and surgical tools). One of the limitations associated with the use of biomedical devices is represented by bacterial infection resulting morbidity and implantation failure [170]. Since the contaminated medical device, surface serves as potential microbial reservoirs causing nosocomial infections. In fact, different surface modification methods have been attempted to prevent bacterial infection to the surfaces by means of surface engineering techniques to introduce antibacterial coating.

Recent research has explored the use of binary metal oxides, as an advanced infection process by the generation of reactive oxygen species (ROS) from photoactivated semiconductors which can effectively kill bacteria [168-170].

Among all the semiconductors, titanium dioxide (TiO_2) is the most popular photocatalyst and has exhibited great potential in water purification considering its non-toxicity, low cost and strong oxidizing [171]. A faster bacterial and viral inactivation by TiO_2-based compounds was observed when additives such as N, Zr, Mo, Ag or Cu modified the TiO_2 surfaces [172-174]. The antibacterial efficiency of silver coatings mainly depends on the release rate of silver ions from the coatings [175], while the TiO_2 photocatalysts generate strong oxidizing power of holes (h^+) and electrons (e^-) leading to hydroxyl radicals (·OH), singlet oxygen (O^{-}·) and hydrogen peroxide (H_2O_2) that cause cells damaging under UV light [176]. TiO_2 can only respond in the ultraviolet (UV) region, which limits its utilization under solar light [177]. More recently, TiON thin films have shown to be effective against many pathogenic bacteria. N-doped titanium oxide films also improve the visible light absorption range of TiO_2 since N-atoms occupy the O-atom sites in the TiO_2 lattice forming ionic Ti-O-N bond red-shifting the TiO_2 light absorption range towards the visible region [178].

Furthermore, Mo-based films tested on Gram-positive and Gram-negative bacteria presented beneficial properties. *Krishnamoorthy et al*. [179] investigated the antibacterial efficiency of MoO_3 nanoplates against pathogenic bacteria (E. Coli, Salmonella typhimurium, Enterococcus faecalis, and Bacillus subtilis) and confirmed their antibacterial activity similarly comparable with the antibiotic Kanamycin. *Zollfrank et al.* [180] and *Tétault et al.* [181] found that the antimicrobial activity of MoO_3 particles or sol–gel derived coatings is due to the in-situ formation of (H_3O^+) ions. The diffusion of H_3O^+ ions into the cell membranes destroys the pH-

equilibrium and enzymatic transport systems, thus deteriorating proliferation of bacteria. *Fisher et al.* [182] reported that TiO_2 doped with Mo enhanced the antimicrobial behavior of industrial surfaces.

However, the widespread usage of TiO_2 and MoO_3 semiconductors are limited by their large band gap (e.g. 3.2 eV for anatase and 3 eV for rutile) and (h-MoO_3 and a-MoO_3 are estimated to be 2.98 and 2.84 eV) with fast recombination of photo-induced electron-hole pairs [183-184].

Advanced works have been carried out to solve the above problems and suggest the combination of semiconductors to form a heterostructure that provides a promising way to enhance the visible light responsive compound. Recently, Ag_2O is found to be a self-stable and highly efficient visible-light photocatalyst with a narrow energy band-gap of ~1.2 eV [185]. It has been demonstrated that the heterojunction of Ag_2O with other semiconductors could efficiently enhance the visible-light induced photocatalytic activity, such as Ag_2O/TiO_2 [186] and $MoO_3/SiO_2/Ag_2O$[187].The semiconductors combination seems extremely good for improving the photo degradation ability and antibacterial capability under visible light irradiation by its strong visible-light absorption and effective inhibition of the recombination of photo-induced electron-hole pairs. Also *Adlhart et al.* [188] reported that the higher hydrophobicity of films led to a higher capability to inhibit bacterial adhesion which is similarly confirmed by *Zhao et al.* [187].

Conclusion

In this chapter, we presented detailed literature data on the materials and elaboration techniques used in our work. The most recent research findings were presented.

First, we presented the general properties of stainless steels and in particular the 316L elaborated by the cold spray technique. The main characteristics of stainless steels and limits were well introduced.

In the second part, we gave a resume on the different titanium-based thin films previously studied and the main approaches used for improving the surface properties. Several systems have been developed basedon the TiN binary system then the ternary (TiAlN) and the quaternary (TiAlMoN) systems. The doping effects with different elements as well as the magnetron sputtering parameters used to ameliorate the physicochemical, mechanical, tribological and anticorrosion properties of coatings were presented.

Finally, we introduced our novel coating TiOMoNAg developed in this thesis by adding literature data on relatively close components evaluated in previous works destined to the enhancement of antibacterial performance.

References

[1] P.J.Cunat, Aciers inoxydables: Critères de choix et structure, Tech. L'Ingénieur. 33 (2000) 18. http://cat.inist.fr/?aModele=afficheN&cpsidt=16028346.

[2] N. Chezeau, Léon Alexandre Guillet (1873-1946). *Revue de Métallurgie*, *94*(5) (1997), pp.592-596.

[3] J.M. Olive, V. Vignal, Scanning tunneling microscopic study of passive film formed on austenitic stainless steels in ambient air and in chloride media. Microscopy Microanalysis Microstructures, 5(4-6)(1994), pp. 301-311.

[4] C.O.D. Olsson, D. Landolt, Passive Films on Stainless Steels Chemistry, Structure and Growth. ElectrochimicaActa, 48(2003), pp. 1093-1104.

[5] S. Grosso, Revêtements architecturés de Ti, TiN et TiO élaborés par pulvérisation cathodique au défilé sur des fils en acier inoxydable : relation entre la composition chimique, la microstructure et les propriétés d'usage. Energieélectrique. Université Grenoble Alpes, 2017. Français. NNT : 2017GREAI083. tel-01725382.

[6] L. Gardner, Stability and design of stainless steel structures – Review and outlook, Thin-Walled Structures, 141(2019), pp. 208-216,

[7] D.M. Costa, L.K.O. Lopes, A.F.V. Tipple, K. Johani, H. Hu, A.K. Deva, E. Watanabe, K. Vickery, Evaluation of stainless steel surgical instruments subjected to multiple use/processing, Infection, Disease & Health, 23(2018), pp. 3-9.

[8] C. Palogi, S.M. Parthasarathy, R. Srinivasan, Use of dissolved ozone for chemical dissolution of chromium containing oxide and its application for stainless steel surface decontamination, Progress in Nuclear Energy, 133(2021)103634.

[9] J. Tao, S. Yan, H. Wang, L. Zhao, H. Zhu, Z. Wen, Antimicrobial and antibiofilm effects of total flavonoids from Potentillakleiniana Wight et Arn on Pseudomonas aeruginosa and its potential application to stainless steel surfaces, LWT,154(2022)112631.

[10] F.C. Wang, L.H. Han, Analytical behavior of carbon steel-concrete-stainless steel double-skin tube (DST) used in submarine pipeline structure, Marine Structures, 63(2019), pp.99-116,

[11] S. Akula, P. Kalaiselvi, A.K. Sahu, S. Chellammal, Electrodeposition of conductive PAMT/PPY bilayer composite coatings on 316L stainless steel plate for PEMFC application, International Journal of Hydrogen Energy, 46(2021), pp. 17909-17921,

[12] R. Castro, J.J. Cadenet, Métallurgie du soudage des aciers inoxydables et résistants à chaud, Paris, Dunod, 1968.

[13] P.J. Doherty, Biomater. -Tissue Interfaces, Advances in Biomaterials 10 International Conference Proceedings Book, Elsevier, Amsterdam (1992).

[14] K. D. Jandt, Evolutions, Revolutions and Trends in Biomaterials Science – A Perspective. Advanced Engineering Materials, 9-12 (2007), pp. 1035-1050.

[15] P.Y. Lin, F.C. Shen, K.T. Wu, S.J. Hwang, H.H. Lee, Process optimization for directed energy deposition of SS316L components. The International Journal of Advanced Manufacturing Technology, 111(2020), pp.1387–1400.

[16] T.S. Senthil, S. Ramesh Babu, M. Puviyarasan, V. Dhinakaran, Mechanical and microstructural characterization of functionally graded Inconel 825 - SS316L fabricated using wire arc additive manufacturing, Journal of Materials Research and Technology, 15(2021), pp. 661-669,

[17] K. Shah, I.u. Haq, A. Khan, S.A. Shah, M. Khan, A.J. Pinkerton, Parametric study of development of Inconel-steel functionally graded materials by laser direct metal deposition, Materials & Design,54(2014), pp. 531-538,

[18] M. Torrell, S. Dosta, J.R. Miguel, J.M. Guilemany, Optimisation of HVOF thermal spray coatings for their implementation as MSWI superheater protectors. Corrosion engineering, science and technology, 45(1)(2010), pp. 84–93.

[19] L. Zhao, E. Lugscheider, Influence of the spraying processes on the properties of 316L stainless steel coatings. Surface and coatings technology, 162 (2002), pp. 6–10.

[20] K. Dobler, H. Kreye, R. Schwetzke, Oxidation of stainless steel in the high velocity oxy-fuel process. Journal of Thermal Spray Technology, 9 (2000), pp. 407–413.

[21] T. Schmidt, F. Gartner, H. Kreye, New Developments in Cold Spray Based on Higher Gas and Particle Temperatures. Journal of Thermal Spray Technology, 155(2006), pp. 488–494.

[22] M. Villa, S. Dosta, J.M. Guilemany, Optimization of 316L stainless steel coatings on light alloys using Cold Gas Spray, Surface and Coatings Technology, 235(2013), pp.220-225.

[23] A. Sova, S. Grigoriev, A. Okunkova, I. Smurov, Cold spray deposition of 316L stainless steel coatings on aluminium surface with following laser post-treatment, Surface and Coatings Technology, 235(2013), pp.283-289.

[24] S. Yin, J.Cizek, X. Yan, R. Lupoi, Annealing strategies for enhancing mechanical properties of additively manufactured 316L stainless steel deposited by cold spray, Surface & Coatings Technology 370 (2019) 353–361, doi.org/10.1016/j.surfcoat.2019.04.012

[25] D. Kotoban, S.Grigoriev, A.Okunkova, A. Sova, Influence of a Shape of Single Track on Deposition Efficiency of 316L Stainless Steel Powder in Cold Spray. Surface & Coatings Technology, 309(2017), pp. 951–958.

[26] W.Y. Li, H. Liao, G.Douchy, C.Coddet, Optimal Design of a Cold Spray Nozzle by Numerical Analysis of Particle Velocity and Experimental Validation with 316L Stainless Steel Powder. Materials & design, 28(2007), pp. 2129–2137.

[27] A.M. Ralls, M. Daroonparvar, S. Sikdar, M.H. Rahman, M. Monwar, K. Watson, C.M. Kay, P.L. Menezes, Tribological and Corrosion Behavior of High Pressure Cold Sprayed Duplex 316 L Stainless Steel, Tribology International,169(2022),107471.

[28] B. Dikici, H.Yilmazer, I.Ozdemir, M. Isik, The effect of post-heat treatment on microstructure of 316L cold-sprayed coatings and their corrosion performance. *Journal of Thermal Spray Technology, 25*(4) (2016), pp.704-714.

[29] B. AL. Mangour, P. Vo, R. Mongrain, E. Irissou, S.Yue, Effect of Heat Treatment on the Microstructure and Mechanical Properties of Stainless Steel 316L Coatings Produced by Cold Spray for Biomedical Applications. Journal of Thermal Spray Technology, 23 (2014) pp 641–652.

[30] S. Adachi, N. Ueda, Effect of Cold-Spray Conditions Using a Nitrogen Propellant Gas on AISI 316L Stainless Steel-Coating Microstructures. Coatings, 7(7)(2017), pp.87.

[31] J. Chen, B. Ma, G. Liu, H. Song, J. Wu, L. Cui, Z. Zheng, Wear and Corrosion Properties of 316L-SiC Composite Coating Deposited by Cold Spray on Magnesium Alloy, Journal of Thermal Spray Technology, 26(6)(2017), 1381-1392.

[32] V. Azar, B. Hashemi, Mahboobeh Rezaee Yazdi, The effect of shot peening on fatigue and corrosion behavior of 316L stainless steel in Ringer's solution, Surface and Coatings Technology, 204(2010), pp. 3546-3551.

[33] H. Yang, K. Yang, B. Zhang, Pitting corrosion resistance of La added 316L stainless steel in simulated body fluids, Materials Letters, 61(2007), pp. 1154-1157,

[34] J.A. Disegi, L. Eschbach, Stainless steel in bone surgery, Injury, 31(2000), pp. D2-D6.

[35] D. Gopi, S. Ramya, D. Rajeswari, L. Kavitha, Corrosion protection performance of porous strontium hydroxyapatite coating on polypyrrole coated 316L stainless steel, Colloids and Surfaces B: Biointerfaces, 107(2013), pp. 130-136.

[36] W.J. Leong, H. Hasan, Z. Zakaria, M.Z.H. Ghazali, S.A. Ab Hamid, S.A. Hassan Risk factors and etiologies of clean and clean contaminated surgical site infections at a tertiary care center in Malaysia, Southeast Asian Journal of Tropical Medicine and Public Health, 48 (6) (2017), pp. 1299-1307.

[37] X. Jin, L. Gao, E. Liu, F. Yu, X. Shu, H. Wang, Microstructure, corrosion and tribological and antibacterial properties of Ti–Cu coated stainless steel, Journal of the Mechanical Behavior of Biomedical Materials, 50(2015), pp. 23-32.

[38] G. Jin, H. Qin, H. Cao, Y. Qiao, Y. Zhao, X. Peng, X. Zhang, X. Liu, P.K. Chu Zn/Ag micro-galvanic couples formed on titanium and osseointegration effects in the presence of S. aureus, Biomaterials, 65 (2015), pp. 22-31.

[39] W. W. Minkler et E. F. Baroch, The production of titanium, zirconium and hafnium. Metallurgical Treatises, (1981)pp. 171–189.

[40] A.E. Van Arkel, J.H. de Boer, Darstellung von reinem Titanium-, Zirkonium-, Hafnium- und Thoriummetall, Zeitschriftfüranorganische und allgemeineChemie. 148 (1925), pp. 345–350.

[41] Procédé Van-Arkel-de-Boer, Wikipédia, l'encyclopédie libre, https://fr.wikipedia.org/w/index.php?title=Proc%C3%A9d%C3%A9_Van-Arkel-de-Boer&oldid=121740618#/media/Fichier:Titan-crystal_bar.JPG, page consulted on 30 December 2015.

[42] F. Hilario. Synthèse et caractérisations de nanotubes de TiO_2 pour applications biomédicales : propriétés électrochimiques et bioactivité. Géniechimique. Université Grenoble Alpes (2017).

[43] X. Liu, P.K. Chu, C. Ding, Surface modification of titanium, titanium alloys, and related materials for biomedical applications, Materials Science and Engineering: R: Reports, 47(2004), pp. 49–121.

[44] M. Geetha, A. K. Singh, R. Asokamani and A. K. Gogia, Ti Based Biomaterials, the Ultimate Choice for Orthopaedic Implants—A Review, Progress in Materials Science, 54(2009), pp. 397-425.

[45] R. R. Boyer, An overview on the use of titanium in the aerospace industry, Materials Science and Engineering, 213(1–2)(1996), pp. 103-114.

[46] C. Leyens, M. Peters, Titanium and Titanium Alloys: fundamentals and applications. John Wiley & Sons (2003).

[47] G. Lütjering, J.C. Williams, Titanium matrix composites, Springer, (2007), pp. 367-382.

[48] M.V.S. Ramakrishna, G. Karunasiri, P. Neuzil, U. Sridhar, W.J. Zeng, Highly sensitive infrared temperature sensor using self-heating compensated microbolometers, Sensors and Actuators A: Physical,79 (2000), pp. 122–127.

[49] N. Fujitsuka, J. Sakata, Y. Miyachi, K. Mizuno, K. Ohtsuka, Y. Taga, O. Tabata, Monolithic pyroelectric infrared image sensor using PVDF thin film, Sensors Actuators A: Physical. 66 (1998), pp. 237–243.

[50] M. Long, H. J. Rack, Titanium alloys in total joint replacement--a materials science perspective. Biomaterials, 19 (18)(1998), pp. 1621-1639.

[51] A. D. Martin, C. L. W. Driscoll, C. P. Wood et J. P. Felmlee, Safety evaluation of titanium middle ear prostheses at 3.0 tesla. Otolaryngology - Head and Neck Surgery, 132 (4)(2005), pp. 537-542.

[52] H. von Tengg-Kobligk, T. F. Weber, F. Rengier, D. Kotelis, P. Geisbüsch, D. Böckler, H. Schumacher et S. Ley, Imaging modalities for the thoracic aorta. Journal of Cardiovascular Surgery, 49 (4)(2008), pp. 429-447.

[53] A. Schulz, H.R. Stock, P. Mayer, J. Staeves, D. Schmoeckel, Deposition of TiN PVD coatings on cast steel forming tools. Surface and Coatings Technology, 94-95(1997), pp. 446-450.

[54] H.O. Pierson, Handbook of refractory carbides and nitrides, Noyes Publications,USA (1996).

[55] L. Wang, Investigation of PVD and CVD Coatings for Manufacturing, Fuel Cell and Biomedical Applications, Doctoral dissertation, Ph. D. thesis, University of Windsor (2010).

[56] H.A. Wriedt, J.L. Murray, The N-Ti (Nitrogen-Titanium) system, Bull. Alloy Phase Diagrams. 8 (1987), pp. 378–388.

[57] L. Hultman, J. Sundgren, TiN(100) films formation of polyhedral N2 bubbles during reactive sputter deposition of epitaxial TiN (100) films, Journal of applied physics. 66(1989), pp. 536–544.

[58] J.P. Zhao, X. Wang, Z.Y. Chen, S.Q. Yang, T.S. Shi, X. Liu, Effect of film thickness on preferred growth of TiN films during filtered arc deposition. Journal of materials science letters, 16(12)(1997), pp. 974-976.

[59] F. Richter, H.Kupfer, H. Giegengack, G.Schaarschmidt, F. Scholze, F. Elstner, F., G. Hecht, Fundamental mechanisms of titanium nitride formation by dc magnetron sputtering. Surface and Coatings Technology, 54(1992), pp. 338-342.

[60] J.E. Sundgren, Structure and properties of TiN coatings. Thin solid films, 128(1985), pp. 21-44.

[61] J. Laimer, H. Störi, P. Rödhammer, Plasma-assisted chemical vapor deposition of titanium nitride in a capacitively coupled radio-frequency discharge. Journal of Vacuum Science & Technology A: Vacuum, Surfaces and Films, 7(5)(1989), pp. 2952-2959.

[62] N. White, A.L. Campbell, J.T. Grant, R. Pachter, K. Eyink, R. Jakubiak, G. Martinez, C. V. Ramana, Surface/interface analysis and optical properties of RF sputter-deposited nanocrystalline titanium nitride thin films, Applied surface science. 292(2014), pp. 74–85.

[63] C. Mendibide, Caractérisation de revêtements PVD nanostructurés à base de nitrures de métaux de transition pour application mécanique, Lyon(2003).

[64] J. Pelleg, L.Z. Zevin, S. Lungo, N. Croitoru, Reactive-sputter-deposited TiN films on glass substrates, Thin solid films, 197(1-2)(1991), 117-128.

[65] M.I. Jones, I.R. McColl, D.M. Grant. Effect of substrate preparation and deposition conditions on the preferred orientation of TiN coatings deposited by RF reactive sputtering. Surface and CoatingsTechnology, 132(1991) (2000), pp. 143-151.

[66] L. Aissani, A. Alhussein, A.A. Ayad, C. Nouveau, E. Zgheib, A. Belgroune, M. Zaabat, R. Barille, Relationship between structure, surface topography and tribo-mechanical behavior of Ti-N thin films elaborated at different N_2 flow rates. Thin Solid Films, 724(2021), 138598.

[67] M. Yoshitake, A. Thananan, T. Aizawaki, K. Yoshihara, Micro-XPS analysis of slide-tested TiN films with/without Cl^+ implantation. Surface and Interface Analysis, 34(1)(2002), pp. 698–702.

[68] W.J. Chou, G.P. Yu, J.H. Huang, Mechanical properties of TiN thin film coatings on 304 stainless steel substrates, Surface and Coatings Technology. 149 (2002), pp. 7–13.

[69] M.Li,S. Luo, C. Zeng, J. Shen, H. Lin, C. Cao, Corrosion behavior of TiN coated type 316 stainless steel in simulated PEMFC environments, Corrosion Science 46 (2004), pp. 1369–1380.

[70] B.Tiana, W.Yuea, Z.Fua, Y.Gu, C. Wang, J. Liu,Microstructure and tribological properties of W-implanted PVD TiN coatings on 316L stainless steel, Vacuum, 99 (2014), pp. 68-75.

[71] M.B. Daia, P. Aubert, S. Labdi, C. Sant, F.A. Sadi, P. Houdy,Nanoindentation investigation of Ti/TiN multilayers films,Journal of Applied Physics, 87(2000), pp.7753-7757.

[72] Y. Massiani, A. Medjahed, P. Gravier, J. P. Crousier, Effect of a titanium underlayer on the corrosion behaviour of physically vapour deposited titanium nitride films, Thin Solid Films, 217 (1992), pp. 31-37

[73] M. Łępicka, M.G. Dahlke, D. Pieniak, K. Pasierbiewicz, K. Kryńska, A. Niewczas,Tribological performance of titanium nitride coatings: A comparative study on TiN-coated stainless steel and titanium alloy, Wear, 422–423(2019), pp. 68–80.

[74] I. Saravanan, A. ElayaPerumal, S.C. Vettivel, N. Selvakumar, A. Baradeswaran. Optimizing wear behavior of TiN coated SS 316L against Ti alloy using Response Surface Methodology, Materials and Design, 67 (2015), pp. 469–482.

[75] L. Zhang, H. Yang, X. Pang, K. Gao, A.A. Volinsky, Microstructure, residual stress, and fracture of sputtered TiN films, Surface and Coatings Technology, 224(2013), pp. 120-125,

[76] R. Machunze, G.C.A.M. Janssen, Stress gradients in titanium nitride thin films, Surface and Coatings Technology, 203(2008), pp. 550-553.

[77] H. Köstenbauer, G.A. Fontalvo, M. Kapp, J. Keckes, C. Mitterer, Annealing of intrinsic stresses in sputtered TiN films: The role of thickness-dependent gradients of point defect density, Surface and Coatings Technology, 201(2007), pp. 4777-4780.

[78] J. Zuo, Y. Xie, J. Zhang, Q. Wei, B. Zhou, J. Luo, Y. Wang, Z.M. Yu, Z.G. Tang,TiN coated stainless steel bracket: tribological, corrosion resistance, biocompatibility and mechanical performance, Surface and Coatings Technology. 277 (2015), pp. 227–233.

[79] L. Wang, J.F. Su, X. Nie, Corrosion and tribological properties and impact fatigue behaviors of TiN- and DLC-coated stainless steels in a simulated body fluid environment, Surface and Coatings Technology. 205 (2010), pp. 1599-1605

[80] Z. Quan, P. Qiang Wu, L. Tang, J.P. Celis, Corrosion-wear monitoring of TiN coated AISI 316 stainless steel by electrochemical noise measurements, Applied Surface Science,253 (2006), pp. 1194-1197.

[81] Q. Wang, F. Zhou, C. Wang, M.F. Yuen, M. Wang,T.Qian, M. Matsumoto, J. Yan, J. Comparison of tribological and electrochemical properties of TiN, CrN, TiAlN and a-C:H coatings in simulated body fluid. Materials Chemistry and Physics, 158(2015), pp.74–81.

[82] Y.M. Zhou, R. Asaki, K. Higashi, W. H. Soe, R. Yamamoto, Sliding wear behavior of polycrystalline TiN/CrN multilayers against an alumina ball, Surface and Coatings Technology,130 (2000), pp. 9-14.

[83] Y. Massiani, A. Medjahed, P.Gravier, L. Argème, L.Fedrizzi, Electrochemical study of titanium nitride films obtained by reactive sputtering. Thin Solid Films, 191(2) (1990), pp. 305-316.

[84] C. Liu, Q. Bi, A.E.I.S. Matthews, EIS comparison on corrosion performance of PVD TiN and CrN coated mild steel in 0.5 N NaCl aqueous solution. Corrosion Science, 43(10) (2001), pp. 1953-1961.

[85]F.S. Shieu, Y.C. Sung, L.H. Cheng, J. Huang, G.P. Yu, Control of the corrosion resistance of TiNcoated AISI 304 stainless steel, Corrosion science, 39 (5) (1997), pp. 893-899.

[86] P.L. Hentall, J.B.Lakeman, G.O.Mepsted, P.L. Adcock, J.M. Moore, New materials for polymer electrolyte membrane fuel cell current collectors. Journal of Power Sources, 80(1999), pp.235-241.

[87] F. Lang, Z. Yu, The corrosion resistance and wear resistance of thick TiN coatings deposited by arc ion plating. Surface and Coatings Technology, 145(2001), pp. 80-87.

[88] M. Omrani, M. Habibi, R. Amrollahi, A. Khosravi, Improvement of corrosion and electrical conductivity of 316L stainless steel as bipolar plate by TiN nanoparticle implantation using plasma focus, international journal of hydrogen energy,37 (2012), pp.14676-14686.

[89] C.H. Hsu, H.T. Liu, W.C. Huang, M.R. Lin, Effect of post heated TiN coating on pitting corrosion of austenitic stainless steel, *Journal of Coating Science and Technology*, *2*(3) (2015), pp. 93-99.

[90] H. Wang, R. Zhang, Z. Yuan, X. Shu, E. Liu, Z. Han, A comparative study of the corrosion performance of titanium (Ti), titanium nitride (TiN), titanium dioxide (TiO_2) and nitrogen-

doped titanium oxides ($N–TiO_2$), as coatings for biomedical applications,Ceramics International 41 (2015),pp. 11844–11851.

[91] X. Zhang, F. Huo, X. Liu, K. Dong, H. He, X. Yao, S. Zhang, Influence of microstructure and interaction on viscosity of ionic liquids, Industrial & Engineering Chemistry Research, 54 (2015), pp. 3505-3514,

[92] M. Hua, H.Y. Tam, H.Y. Ma, C.K. Mok, Patterned PVD TiN spot coatings on M2 steel: tribological behaviors under different sliding speeds Wear, 260 (2006), pp. 1153-1165,

[93] M. Kalin, M. Polajnar The correlation between the surface free energy, the contact angle and the spreading parameter, and their relevance for the wetting behaviour of DLC with lubricating oils, Tribology International,66 (2013), pp. 225-233,

[94] D. Blanco, J.L. Viesca, M.T. Mallada, B. Ramajo, R. González, A. Hernández Battez, Wettability and corrosion of [NTf2] anion-based ionic liquids on steel and PVD (TiN, CrN, ZrN) coatings, Surface and Coatings Technology, 302(2016), pp. 13-21.

[95] Y. Fu, G. Lin, M. Hou, B. Wu, H. Li, L. Hao, Z. Shao, B. Yi, Optimized Cr-nitride film on 316L stainless steel as proton exchange membrane fuel cell bipolar plate International Journal of Hydrogen Energy,34 (2009), pp. 453–458.

[96] P. Yi, L. Zhu, C. Dong, K. Xiao, Corrosion and interfacial contact resistance of 316L stainless steel coated with magnetron sputtered ZrN and TiN in the simulated cathodic environment of a proton-exchange membrane fuel cell, Surface & Coatings Technology 363 (2019), pp. 198–202.

[97] Wikipédia, http://images-of-elements.com/aluminium.php, Page last changed on March 05. 2016

[98] A. Becaria, A. Campbell& S.C. Bondy. Aluminum as a toxicant. Toxicology and Industrial Health, 18(7)(2002), 309-320.

[99] W.B. Frank, W.E. Haupin, H.Vogt,M. Bruno, J.Thonstad, R.K. Dawless, H. Kvande,O.A. Taiwo, Aluminum. Ullmann's Encyclopedia of Industrial Chemistry, 2000.

[100] A.C. Alfrey, Aluminum, Advances in ClinicalChemistry,Elsevier, 23(1983), pp. 69-91,

[101] https://www.morecambemetals.co.uk/metals-and-their-properties-aluminium/, Morecambemetals, 20 June 2018.

[102] https://almet-metal.com/informations-techniques/donnees-aluminium, ALMET Métal 2012-2020.

[103] S.Y. Yoon, J.K. Kim, K.H. Kim, A comparative study on tribological behavior of TiN and TiAlN coatings prepared by arc ion plating technique, Surface and Coatings Technology, 161 (2002), pp. 237-242,

[104] D.E. Wolfe, B.M. Gabriel, M.W. Reedy, Nanolayer (Ti,Cr)N coatings for hard particle erosion resistance, Surface & Coatings Technology, 205 (2011), pp. 4569–4576.

[105] S.C. Vettivel, R. Jegan, J. Vignesh, S. Suresh, Surface characteristics and wear depth profile of the TiN, TiAlN and AlCrN coated stainless steel in dry sliding wear condition, Surfaces and Interfaces, 6 (2017), pp1–10.

[106] D. Amari, H. Khireddine, Y. Khelfaoui, N. Saoula, Adhesion and Corrosion of Ti, TiN and TiCrN Films Deposits on AISI 316L in SBF Solution, Defect and Diffusion Forum397(2019), pp. 39-50.

[107] C.C. Lai. Growth and Phase Stability of Titanium Aluminum Nitride Deposited by High Power Impulse Magnetron Sputtering. Department of Physics, Chemistry and Biology Linköping University (2011).

[108] Q. Yang, D.Y. Seo, L.R. Zhao, X.T. Zeng, Erosion resistance performance of magnetron sputtering deposited TiAlN coatings, Surface and Coatings Technology, 188–189(2004), pp. 168-173,

[109] O. Knotekand T. Leyendecker, On the structure of (Ti, Al)N-PVD coatings. Journal of Solid State Chemistry, 70(2)(1987), pp. 318-322.

[110] W. König, D. Kammermeier, New ways towards better exploitation of physical vapour deposition coatings, Surface and Coatings Technology, 54(1992), pp. 470-475.

[111] A. Mitsuo, S. Uchida, N. Nihira, M. Iwaki, Improvement of high-temperature oxidation resistance of titanium nitride and titanium carbide films by aluminum ion implantation, Surface and Coatings technology, 103(1998), pp. 98-103.

[112] L.A. Donohue, I.J. Smith, W.D. Munz, I. Petrov, J.E. Greene, Microstructure and oxidation-resistance of $Ti_{1-x-y-z}Al_xCr_yY_zN$ layers grown by combined steered-arc/unbalanced-magnetron-sputter deposition. Surface and Coatings Technology, 94(1997), pp. 226-231.

[113] L.M. Liu, S.Q. Wang, H.Q. Ye, First-principles study of polar Al/TiN (111) interfaces, ActaMaterialia 52 (2004), pp. 3681–3688.

[114] Y.H. Cheng, B.K. Tay, S.P. Lau, Electrical properties of TiN films deposited by filtered cathodic vacuum arc, Journal of Vacuum Science & Technology B 20 (2002), pp. 2000–2006.

[115] A.A. Irudayaraj, P. Kuppusami, S. Kalainathan, Structural properties and electrical resistivity of TiNx and Ti1−xAlxN films prepared by reactive dc magnetron sputtering: effect of nitrogen flowrate, Surface Engineering, 24 (2008), pp. 28–35.

[116] W.Y. Yeung, S.N. Dub, R. Wuhrer,Y.V. Milman, A Nanoindentation Study of Magnetron Co-Sputtered Nanocrystalline Ternary Nitride Coatings. Science of Sintering, 38(2006), pp. 211-221.

[117] K. Chu,P.W. Shum,Y.G. Shen, Substrate bias effects on mechanical and tribological properties of substitutional solid solution (Ti,Al)N films prepared by reactive magnetron sputtering. Materials Science and Engineering, 131(2006), pp. 62–71.

[118] K. Zhang, J. Deng, R. Meng, P. Gao, H. Yue, Effect of nano-scale textures on cutting performance of WC/Co-based $Ti_{55}Al_{45}N$ coated tools in dry cutting, International Journal of Refractory Metals and Hard Materials, 51(2015), pp. 35-49

[119] Q. Luo, Temperature dependent friction and wear of magnetron sputtered coating TiAlN/VN, Wear,271(2011), pp. 2058–2066.

[120] J.P. Celis, J.R. Roos, E. Vancoille, S. Boelens, J. Ebberink, The Development of (Ti,Al)N and (Ti,Nb)N Ceramic Coatings Produced by Steered Arc Ion-Plating, Materials Science Forum, 102-104(1992), pp. 599 – 614.

[121] U. Konig, Deposition and properties of multicomponent hard coatings,Surface and Coatings Technology, 33(1987), pp.91-103.

[122] B.Y. Man, L. Guzman, A. Miotello, M. Adami, Microstructure, oxidation and H - permeation resistance of TiAlN films deposited by DC magnetron sputtering technique, Surface and Coatings Technology, 180–181 (2004), pp. 9–14.

[123] E.Y. Yun, W.J. Lee, Q.M. Wang, S.H. Kwon, Electrical and Corrosion Properties of Titanium Aluminum Nitride Thin Films Prepared by Plasma-Enhanced Atomic Layer Deposition, Journal of Materials Science & Technology, 33 (2017), pp. 295–299.

[124] H. Alanyani, R.M. Souto, Research on the corrosion behavior of TiN–TiAlN multilayer coatings deposited by cathodic-arc ion plating, Corrosion, 59 (2003), pp. 851-854.

[125] L. Cunha, M. Andritschky, L. Rebouta, K. Pischow, Corrosion of CrN and TiAlN coatings in chloride-containing atmospheres, Surface and Coating Technology, 116 (1999), pp. 1152-1160.

[126] V.K. William Grips, V. EzhilSelvi, Harish C. Barshilia, K.S. Rajam, Effect of electroless nickel interlayer on the electrochemical behavior of single layer CrN, TiN, TiAlN coatings and nanolayeredTiAlN/CrN multilayer coatings prepared by reactive dc magnetron sputtering, ElectrochimicaActa, 51(2006), pp. 3461-3468.

[127] R. Ananthakumar, B. Subramanian, Akira Kobayashi, M. Jayachandran, Electrochemical corrosion and materials properties of reactively sputtered TiN/TiAlN multilayer coatings, Ceramics International, 38(2012), pp. 477-485.

[128] J.J. Narbon, C. Moreno-Diaz, J.M. Arenas, Influence of surface treatment on the surface energy of an aluminium substrate, Colloids and Surfaces A: Physicochemical and Engineering Aspects, 560 (2019), pp. 323-329.

[129] S. Pugal Mani, M. Kalaiarasan, K. Ravichandran, N. Rajendran, and Y. Meng, Corrosion resistant and conductive TiN/TiAlN multilayer coating on 316L SS: a promising metallic bipolar plate for proton exchange membrane fuel cell, Journal of Materials Science, 56(2021),pp. 10575–10596.

[130] K. Zhang, J. Deng, X. Guo, L. Sun, S. Lei, Study on the adhesion and tribological behavior of PVD TiAlN coatings with a multi-scale textured substrate surface,International Journal of Refractory Metals and Hard Materials, 72 (2018), pp. 292-305.

[131] F. Rupp, L. Scheideler, N. Olshanska, M. Wild, M. Wieland, J. Geis-Gerstorfer, Enhancing surface free energy and hydrophilicity through chemical modification of microstructured titanium implant surfaces,Journal of Biomedical Materials Research A, 76 (2015), pp. 323-334.

[132] O. Çomaklı, Improved structural, mechanical, corrosion and tribocorrosion properties of Ti45Nb alloys by TiN, TiAlN monolayers, and TiAlN/TiN multilayer ceramic films, Ceramics International, 7(2021), pp. 4149-4156.

[133] R.L. Hamlin, Molybdenum. In: Handbook of plant nutrition. CRC Press, (2016), pp. 391-410.

[134] Alchemist hp, Wikipedia, https://en.wikipedia.org/wiki/Molybdenum#/media/File:Molybdenum_crystaline_fragment_and_1cm3_cube.jpg, 22 May 2010.

[135] Y. L. Jeng, E.J. Lavernia, Processing of molybdenum disilicide. journal of materials science, 29(1994), pp. 2557–2571.

[136] J.A. Novotny, C.A. Peterson, Molybdenum, Advances in Nutrition, Vol. 9, Issue 3(2018), pp. 272–273

[137] M. Nordberg, G. F. Nordberg, Toxicology and biological monitoring of metals, General, Applied and Systems Toxicology, (2009).

[138] M. Curzon, J. Kubota, and B. Bibby, Environmental effects of molybdenum on caries, Journal of Dental Research, 50(1971), pp. 74-77.

[139] K. Krishnamoorthy, M. Veerapandian, K. Yun, S.J. Kim, New function of molybdenum trioxide nanoplates: Toxicity towards pathogenic bacteria through membrane stress, Colloids and Surfaces B: Biointerfaces, 112(2013), pp. 521-524.

[140] R. Franz, C. Mitterer, Vanadium containing self-adaptive lowfriction hard coatings for high-temperature applications: a review. Surface and Coatings Technology, 228(2013), pp. 1–13.

[141] S. Aouadi, Y. Paudel, B. Luster, S. Stadler, P. Kohli, C. Muratore, C.J. Hager, A. Voevodin, Adaptive Mo_2N/MoS_2/Ag tribological nanocomposite coatings for aerospace applications, Tribology Letters, 29(2008), pp. 95–103.

[142] L. Tomaszewski, W. Gulbinski, A. Urbanowicz, T. Suszko, A. Lewandowski, W. Gulbinski, TiAlN based wear resistant coatings modified by molybdenum addition. Vac. 121(2015), pp. 223–229

[143] T. Suszko, W. Gulbinski, J. Jagielski, The role of surface oxidation in friction processes on molybdenum nitride thin films. Surface and Coatings Technology, 194(2005), pp. 319–324.

[144] M. Ghufran, G. Moeen Uddin,S. Muhammad Arafat, M. Jawad, A. Rehman, Development and tribo-mechanical properties of functional ternary nitride coatings: Applications-based comprehensive review, J Engineering Tribology, (2020), pp. 1–37.

[145] K. Yang, G. Xian, H. Zhao, H. Fan, J. Wang, H. Wang, H. Du, Effect of Mo content on the structure and mechanical properties of TiAlMoN films deposited on WC–Co cemented carbide substrate by magnetron sputtering, Int. Journal of Refractory Metals and Hard Materials, 52 (2015), pp. 29–35.

[146] V.S. Sergevnin, I.V. Blinkov, A.O. Volkhonskii, D.S. Belov, D.V. Kuznetsov, M.V. Gorshenkov, E.A. Skryleva, Wear behaviour of wear-resistant adaptive nano-multilayeredTi-Al-Mo-N coatings, Applied Surface Science, 388 (2016), pp. 13–23.

[147] F. Regent, J.Musil,Magnetron sputtered Cr–Ni–Nand Ti–Mo–N films: comparison of mechanical properties, Surface and Coatings Technology. 142–144 (2001), pp. 146–151.

[148] Q. Yang, L.R. Zhao, P.C. Patnaik, X.T. Zeng, Wear resistant TiMoN coatings deposited by magnetron sputtering, Wear, 261 (2006),pp. 119–125.

[149] Z.B. Qi, P. Sun, F.P. Zhu, Z.C.Wang, D.L. Peng, C.H.Wu, The inverse Hall–Petch effect in nanocrystallineZrN coatings, Surface and Coatings Technology. 205 (2011), pp. 3692–3697.

[150] V. M. Beresnev, O. V. Bondar, B. O. Postolnyi, M. O. Lisovenko, G. Abadias, P. Chartier, D. A. Kolesnikov, V. N. Borisyuk, B. A. Mukushev, B. R. Zhollybekov, A. A. Andreev Comparison of tribological characteristics of nanostructured TiN, MoN, and TiN/MoN Arc-PVD coatings. Journal of Friction and Wear, 35(2014), pp. 374–382.

[151] J. Xu, H. Ju, L. Yu, Effects of Mo content on the microstructure and friction and wear properties of TiMoN films, ActaMetall Sin. 48 (2012), pp. 1132–1138.

[152] S. Komiyama, Y. Sutou, K. Oikawa, J. Koike, M. Wang, M. Sakurai, Wear and oxidation behavior of reactive sputtered δ-(Ti,Mo)N films deposited at different nitrogen gas flow rates, TribologyInternational, 87 (2015), pp. 32–39.

[153] Y.C. Liu,B.H.Liang,C.R. Huang, F.B. Wu, Microstructure Evolution and Mechanical Behavior of Mo–Si–N Films, Coatings,10(2020), pp. 1-13.

[154] M. Woydt, A. Skopp, I. Doerfel, K. Witke, Wear engineering oxides/anti-wear oxides, Wear, 218 (1998), pp. 84-95.

[155] Ł.Tomaszewski, Wo. Gulbinski, A. Urbanowicz, T. Suszko, A. Lewandowski, W. Gulbinski, TiAlN based wear resistant coatings modified by molybdenum addition, Vacuum, 121 (2015), pp. 223-229.

[156] Q.Yang, Wear resistance and solid lubricity of molybdenum-containing nitride coatings deposited by cathodic arc evaporation, Surface and Coatings Technology, 332 (2017), pp. 283–295.

[157] V. S. Sergevnin, I. V. Blinkov, D. S. Belov, N. I. Smirnov, A. O. Volkhonskii, K. A. Kuptsov, Wear and erosion of arc-PVD multilayer Ti-Al-Mo-N coatings under various conditions of friction and loading, The International Journal of Advanced Manufacturing Technology, 98 (2018), pp. 593–601.

[158] B. Yi, S. Zhou, Z. Qiu, D.C. Zeng, The influences of pulsed bias duty cycle on tribological properties of solid lubricating TiMoCN coatings, Vacuum, 180 (2020)109552.

[159] B.A. Rogers, I.C. Schoonover, L. Jordan, Silver: its properties and industrial uses. US National Bureau of Standards, (1936).

[160] Alchemist-hp, https://en.wikipedia.org/wiki/Silver#/media/File:Silver_crystal.jpg, 25 July 2009.

[161] K.Mijnendonckx, N. Leys, J.Mahillon, S. Silver, R.V. Houdt, Antimicrobial silver: uses, toxicity and potential for resistance. Biometals, 26(4)(2013), pp. 609-621.

[162] D.J. Barillo, D.E. Marx, Silver in medicine: A brief history BC 335 to present, Burns, 40 (2014), pp. S3-S8.

[163] S. Medici, M.Peana, V.M.Nurchi, M.A.Zoroddu, Medical uses of silver: history, myths, and scientific evidence. Journal of medicinal chemistry, 62(13) (2019), pp. 5923-5943.

[164] M.T. Yahya, L.K.Landeen, M.C. Messina, S.M.Kutz, R. Schulze, C.P.Gerba, Disinfection of bacteria in water systems by using electrolytically generated copper: silver and reduced levels of free chlorine. Canadian Journal of Microbiology, 36(2) (1990), pp. 109-116.

[165] C. Zollfrank, K. Gutbrod, P. Wechsler, J.P. Guggenbichler, Antimicrobial activity of transition metal acid MoO_3 prevents microbial growth on material surfaces, Materials Science and Engineering: C, 32 (1) (2012), pp. 47–54.

[166] World Health Organization HAI Fact Sheet; World Health Organization, (2014).

[167] S. Rtimi, Indoor Light Enhanced Photocatalytic Ultra-Thin Films on Flexible Non-Heat Resistant Substrates Reducing Bacterial Infection Risks. Catalysts,7(2017), pp. 57.

[168] S. Rtimi, C.Pulgarin, M.Robyr, A. Aybush, I.Shelaev, F.Gostev, V.Nadtochenko, J. Kiwi, Insight into the Catalyst/Photocatalyst Microstructure Presenting the Same Composition but Leading to a Variance in Bacterial Reduction under Indoor Visible Light,Applied Catalysis B: Environmental,208(2017), pp. 135−147.

[169] S. Rtimi, S.Konstantinidis, N.Britun, V.Nadtochenko, I.Khmel, J. Kiwi, New Evidence for Ag-Sputtered Materials Inactivating Bacteria by Surface Contact without the Release of Ag Ions: End of a Long Controversy?, ACS applied materials & interfaces, 12(4) (2020), pp. 4998-5007.

[170] X. Zhang, R. Hang, H. Wu, X. Huang, Y. Ma, N. Lin, X. Yao, L. Tian, B. Tang, Synthesis and antibacterial property of Ag-containing TiO_2 coatings by combining magnetron sputtering with micro-arc oxidation, Surface and Coatings Technology, 235(2013), pp. 748-754.

[171] M.D. Hernández-Alonso, F. Fresno, S. Suárez, J.M. Coronado, Development of alternative photocatalysts to TiO_2: challenges and opportunities. Energy & Environmental Science, 2(12)(2009), pp. 1231-1257.

[172] A.S. Breathnach, Nosocomial infections and infection control. Medicine, 41(2013), pp. 649-653.

[173] O. Baghriche, S. Rtimi, C. Pulgarin, R. Sanjines, J. Kiwi, Effect of the spectral properties of TiO_2, Cu, TiO_2/Cu sputtered films on the bacterial inactivation under low intensity actinic light, Journal of Photochemistry and Photobiology A: Chemistry, 251(2013), pp. 50-56,

[174] S. Rtimi, C. Pulgarin, R. Sanjines, J. Kiwi, Innovative semi-transparent nanocomposite films presenting photo-switchable behavior and leading to a reduction of the risk of infection under sunlight. RSC advances, 3(37)(2013), pp. 16345-16348.

[175] W.R. Fordham, S. Redmond, A. Westerland, E.G. Cortes, C. Walker, C. Gallagher, C.J. Medina, F. Waecther, C. Lunk, R.F. Ostrum, C.A. Caputo, J.D. Hettinger, R.R. Krchnavek, Silver as a bactericidal coating for biomedical implants, Surface and Coatings Technology, 253 (2014), pp. 52–57.

[176] R. Aminedi, G. Wadhwa, N. Das, B. Pal, Shape-dependent bactericidal activity of TiO_2 for the killing of Gram-negative bacteria Agrobacterium Tumefaciens under UV torch irradiation, Environmental Science and Pollution Research, 20 (2013), pp. 6521–6530.

[177] R. Levinson, P. Berdahl, H. Akbari, Solar spectral optical properties of pigments— part I: model for deriving scattering and absorption coefficients from transmittance and reflectance measurements, Solar energy materials and solar cells, 89 (2005), pp. 319–349.

[178] S. Lee, E. Yamasue, H. Okumura, K. Ishihara, Effect of oxygen and nitrogen concentration of nitrogen doped TiOx film as photocatalyst prepared by reactive sputtering, Applied Catalysis A-General, 371(2009), pp. 179–190.

[179] K. Krishnamoorthy, M. Veerapandian, K. Yun, S.J. Kim, New function of molybdenum trioxide nanoplates: Toxicity towards pathogenic bacteria through membrane stress, Colloids and Surfaces B: Biointerfaces, 112(2013), pp. 521-524.

[180] C. Zollfrank, K. Gutbrod, P. Wechsler, J.P. Guggenbichler, Antimicrobial activity of transition metal acid MoO_3 prevents microbial growth on material surfaces, Materials Science and Engineering: C, 32 (1) (2012), pp. 47–54.

[181] N. Tetault, H. Gbaguidi-Haore, X. Bertrand, R. Quentin, N. van der Mee-Marquet, Biocidal activity of metalloacid-coated surfaces against multidrug-resistant microorganisms, Antimicrobial resistance and infection control,1(1)(2012), pp.1-6.

[182] L. Fisher, S. Ostovapour, P. Kelly, K.A. Whitehead, K. Cooke, E. Storgårds, J. Verran show less Molybdenum doped titanium dioxide photocatalytic coatings for use as hygienic surfaces: the effect of soiling on antimicrobial activity, Biofouling, 30(2014), pp. 911-919.

[183] J. Du, X. Lai, N. Yang, J. Zhai, D. Kisailus, F. Su, D. Wang, L. Jiang, Hierarchically ordered macro− mesoporous TiO_2− graphene composite films: improved mass transfer, reduced charge recombination, and their enhanced photocatalytic activities. ACS nano, 5(2011), pp. 590-596.

[184] Q.Qu, W-B. Zhang, K. Huang, H-M. Chen, Electronic structure, optical properties and band edges of layered MoO_3: A first-principles investigation, Computational Materials Science, 130(2017), pp. 242-248.

[185] Y. Du, D. Tang, G. Zhang, X. Wu, Facile synthesis of Ag_2O-TiO_2/sepiolite composites with enhanced visible-light photocatalytic properties. Chinese Journal of Catalysis, 36 (2015), pp. 2219-2228.

[186] B. Liu, L. Mu, B. Han, J. Zhang, H. Shi, Fabrication of TiO_2/Ag_2O heterostructure with enhanced photocatalytic and antibacterial activities under visible light irradiation, Applied Surface Science, 396(2017), pp. 1596-1603.

[187] Y. Zhao, J. Xu, Z. Li, T. Fu, S. Jiang, In vitro antibacterial properties of MoO_3/SiO_2/Ag_2O nanocomposite coating prepared by double cathode glow discharge technique. Surface and Coatings Technology, 397(2020), 125992.

[188] C. Adlhart, J. Verran, N.F. Azevedo, H. Olmez, M.M. Keinanen-Toivola, I. Gouveia, L.F. Melo, F. Crijns, Surface modifications for antimicrobial effects in the healthcare setting: a critical overview, Journal of Hospital Infection, 99 (3) (2018), pp. 239–249.

Chapter II

Elaboration and characterization techniques

Introduction

This chapter presents the different techniques used for producing coatings developed in this study. Cold Spray (CS) technique was used to elaborate 316L stainless steel using helium and nitrogen. Kinetic Spray Solutions (KSS) software was used to simulate the process before cold spraying. We will also explain the Magnetron Sputtering (MS) technique used to perform thin films. The MS technique was used for the preparation of the following thin films: TiN, TiAlN, TiAlN-Mo with different molybdenum contents, TiMoON and TiMoON-Ag with different silver contents. The different characterization methods used to determine the microstructural, mechanical, tribological, anticorrosion behaviors and antibacterial performance of the developed coatings are also presented in this chapter.

II. Elaboration techniques

II. 1 Cold spray technology

II. 1.1 Scientific background

The Dynamic Gas Projection Procedure (CGDS*: Cold-Gas Dynamic Spraying*) is a new coating technology, initially developed by *Alkimov et al*. [1] in the mid-1980s at the institute of theoretical and applied Mechanics of the Siberian division in the Russian Academy of Sciences of Novosibirsk. The basic idea behind the cold spray is quite simple and the concept was already patented at the beginning of the 20th century. The invention of the cold spray process dates back to the time of the invention of thermal projection process by Schoop [2]. However, the idea of using the impact energy of particles to produce the coating using a gas vector jet to accelerate the solid particles was studied on diphasic supersonic flows (gaseous compound associated with solid particles). With the use of particles as trackers in the gas flows with different impact angles, they can adhere to various materials when the impact speed is higher than a certain critical value [2]. A wide range of materials (metals, alloys or even composite) can be projected on a wide variety of substrates for multiple applications.

After being patented in the United States [3] and in Europe [4], the Cold Spray process was born in 1994 by *Papyrin* who defines it as follows [5]: “Dynamic gas projection more commonly known as Cold Spray is a process for making deposits by exposing a metal or dielectric substrate to a high speed jet (from 300 to 1200 m.s^{-1}) small particles (1 to 50 µm) accelerated by means of a supersonic flow of a compressed gas.”

The difference between the cold projection process and other thermal projection procedures (arc plasma projection, flame spraying, HVOF (*High Velocity Oxy-Fuel*)) is

illustrated in *Fig. II.1*. These processes are distinguished between them in particular by their gas temperature and projection yield as a function of the particles speed and the deposition rate, respectively. In the thermal spray process, a coating is formed by melting the material then dipping the melted droplets. Consequently, thermally projected coatings generally have microstructures with various degrees of porosity, oxides and other inclusions, and low corrosion resistance [6]. However, in the cold spray, gas heating only gives the flow of injected particles a higher speed [5] (supersonic speed) by kinetic energy and not to use this heat to melt the particles which plays a role on their physical conditions of the impact of particles.

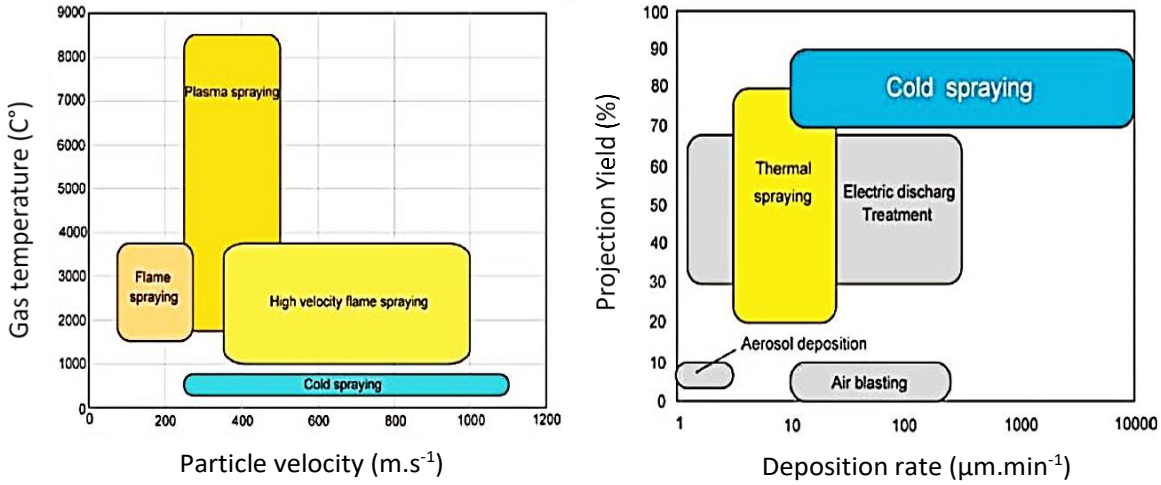

Fig. II.1. Comparison between different thermal spray processes [7-8].

II. 1.2 Principle of cold spray

Fig. II.2.a shows a typical CS system using nitrogen (N_2), helium (He) or air as a propellant gas and also sent to the powder feeder (carrier gas) to drive the powders into the nozzle [9].

During a spraying process the propellant gas can be heated up to 900 °C under high pressure generally set in 1.5-3.5 MPa range. This will accelerate the metal powders with a particle size distribution between 1 and 50 µm through a convergent-divergent de-Laval nozzle to reach a high velocity (500–1200 m/s) [10]. The heated particles at a temperature lower than the melting point impact the substrate and form a coating. So the cold spray process is based on the transformation of the kinetic energy of particles into plastic deformation and thermal energy when impacting with the substrate [11].

Cold spraying was performed using a CGTK3000 cold spray system. *Fig. II. 2b* presents the de-Laval type converging–diverging nozzle where nitrogen and helium as process gases

were used for powders spraying via SiC-OUT4 and SiC-OUT1 nozzles, respectively. The industrial robot arm is used to perform the motion of the spray gun in order to achieve controllable, safe and accurate spraying path.

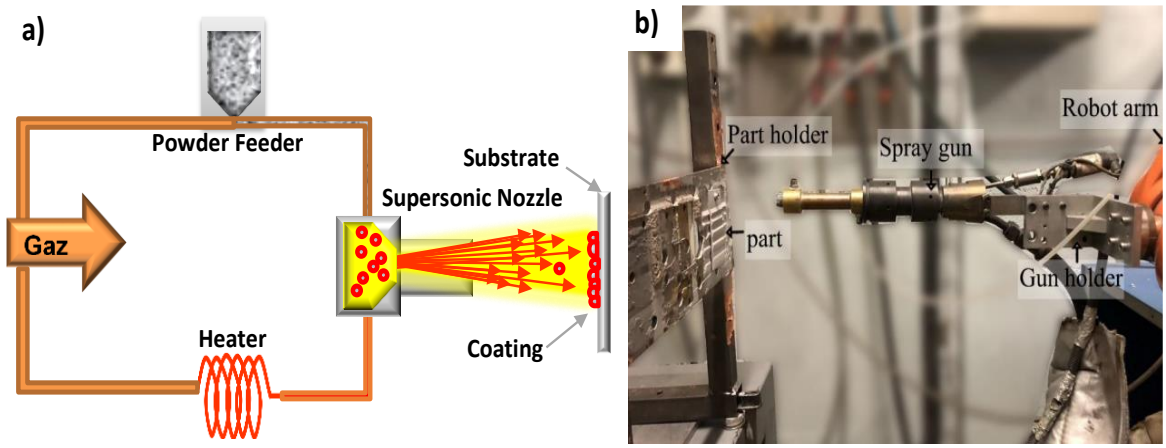

Fig. II.2. (a)Schematic diagram of the CS system, and(b)the cold spraying deposition machine [12].

II. 1.3 The main spraying parameters in cold spray

Many works described the relationship between the spraying parameters and the coating characteristics as well as the coating applications [11-12].

II. 1.3.1 Particle speed

The particles speed (Vp) is an essential parameter in the projection carried out during the cold spray process [13]. The adhesion of particles to the substrate depends on a critical speed, which influences the adhesion force and the film surface [14]. Only particles reaching this speed can likely adhere to the substrate by a complex phenomenon involving large deformations by the accumulation of successive layers. In the case that particles speed is low and cannot achieve the requested critical value, they will rebound and can erode the substrate surface (*Fig. II.3*) [15].

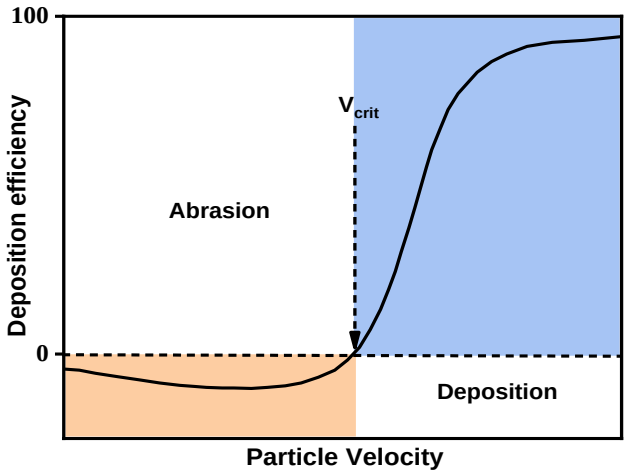

Fig. II.3. Diagram illustrating the effect of particle velocity on deposition efficiency [15].

The critical velocity (V_{crit}) of the projected particle was evaluated by Schmidt [16] as follows (*Eq. II.1*):

$$V_{crit} = 667 - 0.014\rho + 0.08(T_f - T_r) + 10^{-7}R_e - 0.4(T_i - T_r) \qquad (II.\ 1)$$

Where ρ is the density of the projected particle, T_f its melting temperature, T_r the reference temperature (20°C), Ti the impact temperature and Re the yield stress of particle material.

This velocity directly depends on the projection conditions such as the characteristics of the carrier gas (nature, pressure, temperature) and particles (chemical composition, density, size, and shape) as well as the parameters of the machine (type of nozzle, distance from the nozzle to the substrate, projection angle).

II. 1.3.2 Spray distance

The distance between the nozzle and the substrate surface is known as the spray distance or standoff distance. It has an impact on the final states of particles that reach the substrate and consequently the coating thickness and deposition efficiency [17] (*Fig. II. 4*).

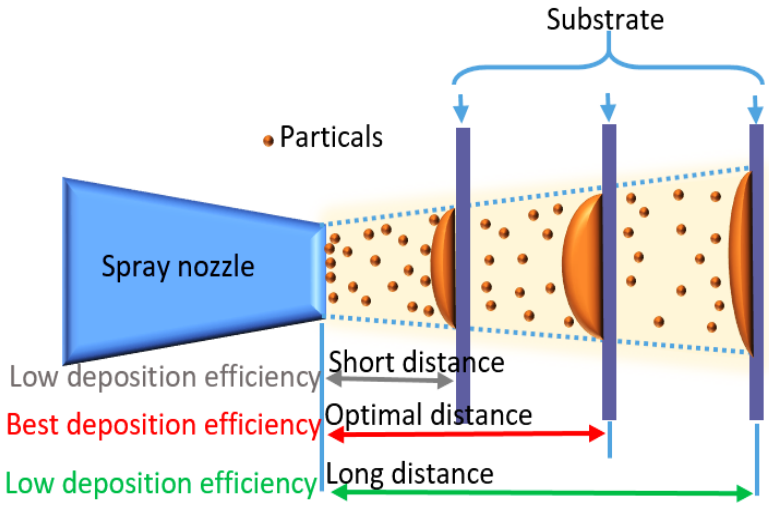

Fig. II.4. Effect of the spray distance on the deposition efficiency.

The increase in the standoff distance generally results a lower particle speed due to the applied drag force as shown in *Eq. II.2*[18].

$$F = \frac{C_d A_p \rho_g (V_g - V_p)^2}{2} \qquad \text{(II. 2)}$$

Where C_d is the drag coefficient, A_p is the cross-section of the particles (in m^2), ρ_g is the gas density (in $kg.m^{-3}$), $(V_g\text{-}V_p)$ is the relative velocity between gas and particle (in $m.s^{-1}$).

Computational and experimental studies were performed by *Pattison et al.* [19] to understand the effect of standoff distance. They reported that a small standoff distance (<6 cm) can reduce the particle velocity and deposition efficiency. This is due to the bow shock phenomenon occurring near the substrate surface caused by the free gas jet impingement, which decreases the particle velocity before impact. They reported that the standoff distance should be optimized to achieve high particle velocity and deposition efficiency. The optimum distance should be defined and kept constant during the deposition process.

II. 1.3.3 Projection gas

For the type of vector gas, it is conventionally air, helium, nitrogen or their mixtures. The use of nitrogen reduces the oxidation of the projected material (unlike air) but the hard materials cannot be deposited with nitrogen gas because higher speed is required. Therefore, helium is a good solution thanks to its inert reactivity and smallest molecular mass to reach the highest particle speed. *Yoon et al.* [20] reported the improvement in deposit efficiency obtained when

the processing gas changed from nitrogen to helium during projection. Helium velocity is much higher but more expensive than nitrogen, however, as a solution a helium recovery system (HRS) is usually installed to recover it [21].

The other important parameter is the temperature and pressure of the vector gas. The increase in the deposition efficiency was reported by *Li et al.* [22] during the study of sprayed titanium powder as a function of propellant gas temperature. They found that there was no particle deposition occurred at a low nitrogen gas temperature less than 155 °C. Increasing the temperature led to enhancing the deposition efficiency, in particular, when the nitrogen temperature exceeded 215 °C. The effect of gas temperature on morphology and properties of 304 stainless steel coatings was studied by *Meng et al.* [23]. They found that the increase in the gas temperature from 450 to 550 °C reduced the porosity of the coating from 6% ± 0.5% to 2% ± 0.3% with the formation of a denser morphological structure with a better corrosion resistance. The propellant gas pressure is also an important factor that influences the speed of particles. The results obtained by *Li et al.* [24] showed that the particles velocity increases with the increasing of gas pressure whatever the type of gas and the speed remains higher with helium than with nitrogen.

II. 1.3.4 Projection angle

The angle between the nozzle and the substrate surface is known as the spray angle. The ideal conditions, as reported by *Karthikeyan et al.* [6], the CS nozzle should be oriented perpendicularly to the substrate throughout the deposition to obtain the highest particle impact energy against the substrate, which would give high-quality coatings. *Yin et al.* [25] noticed that the particles sprayed with an angle less than 90° deformed locally on one side owing to the tangential momentum. This one-sided localized deformation increased with a further decrease in spray angle, leading to poorer particle deposition. As well, adhesion strength, coating thickness, density and mechanical properties deteriorate with respect to decreasing the CS angle.

In general, the inclined spray angle causes the particle rebounds during the impact on the substrate which increase particle loss and reduce deposition efficiency. Therefore, the most active manner is that the spray angle should be maintained perpendicular (at 90°), which is easy for a plane surface. However, according to *Singh et al.* [26], it is not feasible to consistently carryout CS at an orthogonal angle with respect to the substrate surface since the majority of

engineering components have complex geometries. Therefore, it is pertinent to investigate the effect of spray angle on deposition mechanism and the associated coating properties.

II. 1.3.5 Projected Feedstock (powder)

The choice of powders used in cold spray is based on their ability to deform plastically during the impact on substrate. In practice, the class of materials most usable in cold spraying corresponds to ductile metals and alloys. Soft particles deform more severely than hard particles and result better adhesion strength. Hard particles cause erosion of the substrate, while soft particles deform over the substrate without causing erosion [27].The majority of studies on the cold spray process focus on the deposition of ductile metals such as aluminum [28], copper [29], stainless steels [30], nickel-based alloys [31], etc.

The spherical morphology is preferred to achieve better adhesion strength and denser coating microstructures [32]. Spherical particles penetrate deeper inside the substrate and undergo the phenomenon of jet formation, which leads to higher adhesion strength. Additionally, smaller particles attain higher velocity at the nozzle exit than the larger particles owing to their lower mass. However, the bow-shock effect is stronger for smaller particles that reduce their impact energy [33].

II. 1.3.6 Substrate

In cold spray, substrate deformation promotes the jet formation [25]. Soft substrates, such as aluminum and copper, are more susceptible to deformation than hard substrates, such as ceramics and steel, which improves adhesion strength [34]. *Wang et al.* [35, 36] found that a hard steel substrate induced high deformation onto the striking Al particles, which improved the cohesive strength in the coating nearer to the substrate. They found that softer substrates resulted in higher deposition efficiency, better cohesion strength, higher hardness and lower porosity [36].

There are contradicting reports on the effect of substrate roughness concerning adhesion. For instance, *Hussain* [37] reported that smoother substrate surfaces are best for good adhesion strength. *Kumar et al.* [38] found that semi-polished substrates were ideal for achieving the best adhesion for a copper-steel combination. *Singh et al.* [33] obtained better adhesion for mirror-finished substrates than semi-polished and as-received substrates for the same material combinations. It is also reported by *Ghelichi et al.* [39] that with a higher roughness of substrate

surface, the deposition efficiency of metal powders increases because the impacting particles deform more severely on a rough surface compared to a smooth one.

The substrate pre-heating results in the softness of the substrate surface, which facilitates deformation of the substrate during the impact of the particles, resulting in jet formation and better bonding strength [40]. *Fukumoto et al.* [41] found that for high substrate temperature, higher deposition efficiency was obtained with Cu particles. *Perton et al*. [42] applied laser heat treatment prior to CS to improve the adhesion strength by reducing the substrate hardness.

II. 1.4 Advantages and limitations of cold spray

As with any other material processing technique, the cold spray process has its own advantages and disadvantages. The main advantage over thermal spray techniques is the low temperature involved which minimizes any probable phase change and maintains the particles in their unmodified solid state. The other advantages can be summarized in the following points [13, 16, and 43]:

- *Avoid oxidation and undesirable phase changes;*
- *Deposition of thicker coatings thanks to the elimination of solidification stresses;*
- *Provide a high-density, high-strength, and high-hardness microstructure;*
- *Spraying of fine-grained powders (<5–10 μm);*
- *Achieve high deposition efficiency and high deposition rate;*
- *Produce substrate-coating couple with different materials;*
- *Minimal substrate preparation with surface preparation/masking;*
- *Recycling of particles and spray gases (e.g. helium);*
- *Increase operational safety due to the absence of high temperature gas jets, radiation and explosive gases;*
- *The gas temperature being low, no melting of the material being sprayed.*

Some disadvantages of the cold spray process can be listed by:

- *Hard materials such as pure ceramics and some alloys (such as hard hardened alloys) are difficult to be deposited;*
- *Cold spray coatings on ceramic substrates have limited bond strength, as the process requires some substrate ductility to produce well-bonded coatings;*
- *Gas flow rates under high pressure leading to high gas consumption that results a high cost (problem with helium for example).*

II. 1.5. Numerical simulation

In order to evaluate the cold spraying and try to estimate the optimum spray conditions, numerical simulation using the commercially available Kinetics Spray Solutions (KSS) software was done to simulate the CS process before our experimental work. Thus, the software of fluid dynamic modeling was employed to determine the effect of different parameters; it is able to calculate the particle velocities and gas temperature at the set process conditions. The simulation can describe also the influence of particle size, nozzle geometry and all significant process parameters [44-45].

In our work, 316L stainless steel was elaborated by CS process on aluminum substrates considering the ideal parameters mentioned above and the values obtained by the numerical simulation. All CS process details and results are presented in next chapter, *Chapter III*.

II.2 Magnetron sputtering technique

II. 2.1 Sputtering mechanisms

Sputtering is one of the oldest techniques used for forming thin films discovered by William *Robert Grove in* 1852 [46]. It showed later the appearance of a thin film at the anode during an electric discharge between two conductive electrodes under a reduced pressure of inert gas. Sputtering systems allow the deposition of any type of solid materials at room temperature for many publications.

The most important physical phenomenon in sputtering technology is the momentum transfer between energetic atomic-sized particles (usually ions of gases) and the atoms of the surface of the material (Target). During the interchange of momentum, many effects can be produced through the elastic and inelastic collisions. During the first collisions, mainly reflected particles can be found (neutrals, ions of target and gas). In the second step, the collisions can result in secondary electrons, X-rays and implanted particles. *Fig. II.5* shows the different processes that may occur during the interaction between the charged particles and the surface of the material [47, 48].

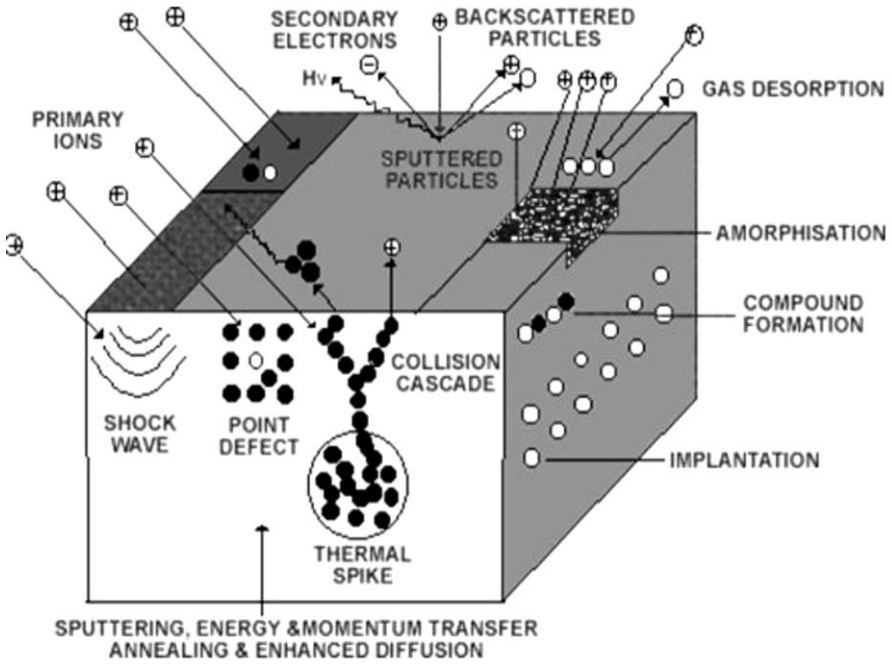

Fig. II. 5. The main physical processes produced in sputtering technique [49].

Sputtering is considered as a simple erosion of the surface, namely target, by the energetic particles, which is a sort of atomistic sandblasting [50]. The mechanism of the conventional sputter deposition is based on the ejection of atoms from a solid material by bombarding its surface with energetic species. A simplified schematic illustration of the sputtering process is shown in *Fig. II.6*.

In practice, target acts as a cathode and substrate acts as an anode and an inert gas is used as a sputtering medium such as Ar^+ to reduce the reactions with any component in the chamber. By applying a potential difference, the positively charged gas ions (Ar^+) are accelerated towards the cathode and sputter out electrons and target species from the target surface [51]. This ionization process can be described as follows (*Eq. II. 3*):

$$Ar + e^- \rightarrow Ar^+ + 2e^- \qquad \text{(II. 3)}$$

Electrons emitted from the surface, also known as secondary electrons, are repelled from the cathode and generate more sputtering gas ions through collisions which create plasma maintaining the density of gas ions. When an ion collides with the target, the kinetic energy of the ion is transferred to the atom of the target. This collision may lead to the sputter ejection of an atom from the target surface depending on the energy of the impinging ions. If the energy of incoming ions is sufficient, the atomic bonds are broken and atoms are ejected from the surface

[52-53]. The ejected target species are transferred through the gas phase to be deposited on a substrate and eventually form a film.

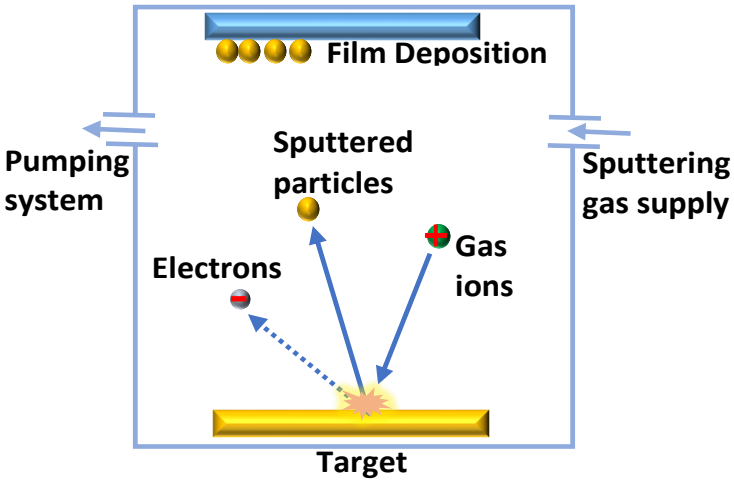

Fig. II.6. Schematic illustration of a simplified sputtering process.

A useful parameter of the sputtering process is the sputtering yield (S) which is defined as the number of atoms ejected per incident ion [53]. The sputtering yield depends on various parameters, such as masses of the incident and target atoms, surface binding energy of the target material and the energy of the incident atoms/ions [51]. It is sensitive also to the angle of incidence of the bombarding particle. For ion energies from 100 eV to 1000 eV the sputtering yield can be calculated as follows (*Eq. II. 4*):

$$Y = \frac{3\alpha}{4\pi^2} \frac{4m_i m_t}{(m_i + m_t)^2} \frac{E}{U} \qquad (II.\ 4)$$

Where m_i is the atomic mass of the bombarding incident ion, m_t is the atomic mass of the target material (g.cm-^{3}), U the binding energy of the target surface atoms (eV), E the energy of the incident ion (eV), and α depends on the ratio of the masses of the target atom and the incident ion (monotonically increased with m_i/m_t; for a ratio 0.1 α = 0.17, for a ratio 10 α =1.4) [54].

The target can be powered in different ways using D.C (*Direct Current*) for conductive targets and R.F (*Radio Frequency*) for non- conductive targets:

- *In the D.C sputtering process, the voltage applied is a direct voltage. This process is used exclusively for the preparation of thin metallic layers. The main disadvantage of*

DC magnetron sputtering which has a deposition rate of (~10-20 nm/min), and the high pressure required reduces the film quality [55].

- *In R.F sputtering process, it is possible to deposit different types of films such as ceramics, insulators e.g. silica as well as the metallic materials [56]. The idea is to alternate the plasma excitation voltage; during the negative alternation, the Ar^+ ions attracted to pulverize the target and during the positive alternation, the electrons precipitating on the target neutralize and restore the balance leading to enhancing the deposition efficiency compared with the D.C process.*

II. 2.2. Magnetron sputtering mechanism

The conventional sputtering technique has some limitations, such as low ionization efficiency and low deposition rate. Emitted secondary electrons during the sputtering process can recombine with ions, and some of them are drained from the plasma through the chamber walls. Also to maintain a constant plasma density, the cathode must be fed continuously with high voltage under high sputtering gas pressure. The magnetron sputtering process presents a solution to overcome this problem by placing a set of well-designed permanent magnets below the target; the plasma is confined to the near-target region. According to the Lorentz force formula (*Eq. II. 5*), the magnetic fields confine the secondary electrons in the spiral trajectories in the vicinity of the target surface (*Fig. II.7*) [57]. Confining the electrons not only leads to a higher density of plasma and increased deposition rate, but also prevents damage which would be caused by direct impact of these electrons with the substrate or growing film.

$$\vec{F} = q\left[\vec{E} + (\vec{V} \perp\times \vec{B})\right] \quad \text{(II. 5)}$$

Where q (C) is the charge of the particle, $\vec{E}$ (V/m) is the electric field, $\vec{V}\perp$ (m/s) is the velocity of the charged particle perpendicular to the magnetic field $\vec{B}$ (T), $\vec{F}$ (N) is the force experienced by the particle.

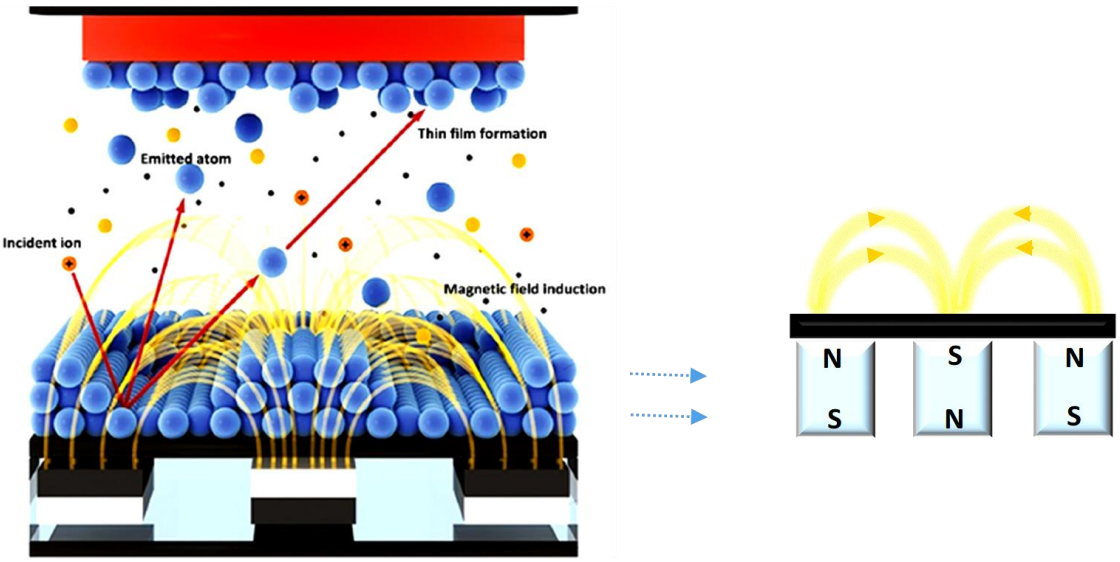

Fig. II.7. Schematic illustration of the magnetron sputtering with a balanced field [58].

II. 2.3 Unbalanced magnetron sputtering

In the conventional or balanced magnetron sputtering, the emitted electrons cannot escape easily from the magnetic trap, and the plasma will be confined close to the target (*Fig. II. 7*) [59]. In this case, the energy of the ejected target particles is low with a weak bonding strength. In the case of low-energy deposition, atoms have a low mobility on the surface of the substrate and easily generate film with a porous and rough columnar structure. On the other hand, if the center magnets are week, all the magnetic field lines will not be caught up and the shape of the resultant magnetic field will change allowing some electrons from plasma to escape easily towards the substrate [59]. This condition of magnetron arrangement is called unbalanced magnetron as shown in *Fig. II.8*.

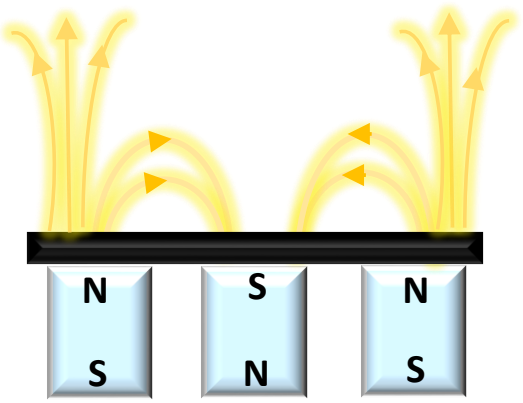

Fig. II. 8. Schema of magnetic field lines in an unbalanced magnetron sputtering.

II. 2.4 Reactive magnetron sputtering

Reactive sputtering is a sputtering process which allows compounds to be deposited by adding a reactive gas (e.g. O_2 and N_2). During the reactive sputtering process, the reactive gas is activated by the plasma and chemically reacts with the target materials. While the formation and accumulation of compound molecules at target surface is referred as the target poisoning [60], without sufficient incorporation of reactive gas atoms, non-stoichiometric films will be produced. These regimes are known as a metallic mode. The increasing of reactive gas content in the sputtering atmosphere leads to the growth of stoichiometric films. In this process, a wide range of compounds (oxides, nitrides, carbides …) thin films can be produced [60-61].

II. 2.5 Pulsed magnetron sputtering

Oxide coatings can be produced by the reactive magnetron sputtering of a metallic target in a controlled oxygen atmosphere. It can also be deposited by the RF sputtering of an oxide target usually with ~ 13.56MHz frequency [62]. However, both of these processes are problematic and have limitations. RF sputtering can produce high-quality films but deposition rates are very low. Other problem can be also associated with the reactive magnetron sputtering where the target poisoning leads to the formation of arcs causing defects in the growing film. These later affect its performance and can also lead to damage the magnetron power supplier [63-64].

Many of these issues have been solved by the development of the pulsed magnetron sputtering process (PMS). In fact, during the deposition of insulating films, the pulsed magnetron discharge in a medium frequency range (10-200 kHz) can largely reduce the creation of arcs and, as a result, reduce the number of defects in the deposited film [62-65]. In addition, the deposition rate in pulse mode is good which is close to those obtained for the deposition of pure metal films [66].

In our work, a magnetron sputtering deposition machine (*DEPHIS, France*) was used (*Fig.II.9*). The choice of this technique for the growth of our different coatings has been made due to its many advantages over other vacuum coating techniques such as high deposition rate, sputtering ease, high purity, good density, good film uniformity, etc.

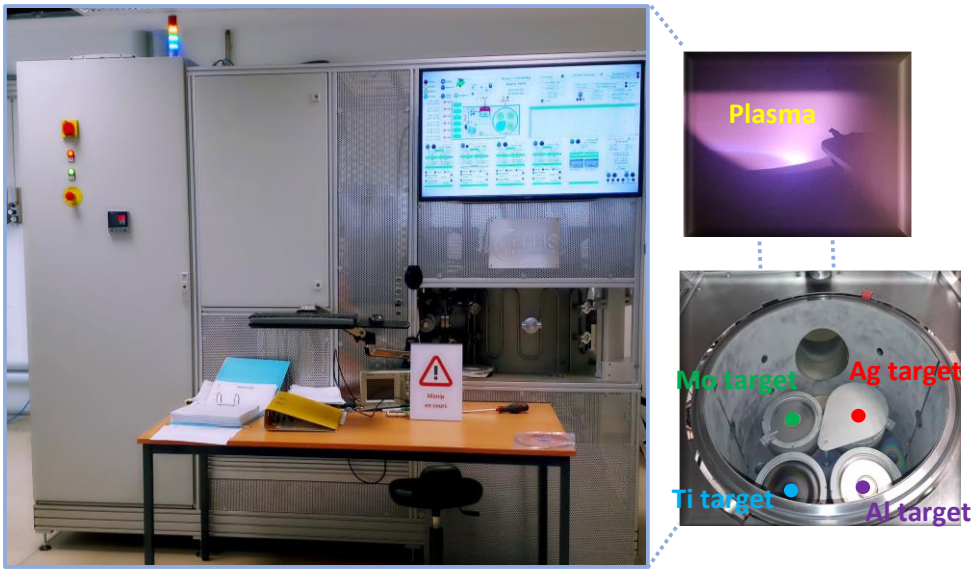

Fig. II.9. The magnetron sputtering deposition machine (DEPHIS, France).

II. Characterization techniques

II. 3 X-Ray Diffraction (XRD)

X-ray diffraction (XRD) is a nondestructive technique for materials characterization. It can be used for any solid sample without any special preparation. It provides information on structures, phases, preferred crystal orientations (texture), and other structural parameters, such as grain size, crystallinity, and strain. The X-rays are generated by a cathode ray tube, filtered to produce a monochromatic radiation, collimated to be concentrated, and directed toward the sample (*Fig.II.10*) [67]. The interaction of the incident X-rays with the sample produces constructive interference which can be determined by Bragg's law (*Eq. II.6*):

$$n\lambda = 2d_{hkl}\sin\theta \qquad (II.\ 6)$$

Where λ (Å) is the wavelength of X-rays, d_{hkl} (Å) is the distance between crystalline planes (hkl), θ (°)is the scattering angle and n is the order of reflection.

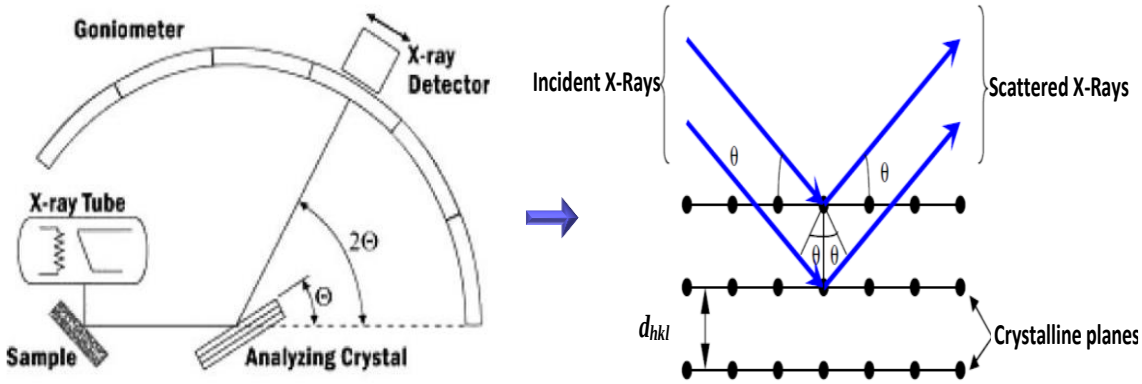

Fig. II.10. A schematic representation of the principle of X-ray diffraction [67].

In our work, the X-ray diffraction analyses were carried out using a *Bruker D8 Advance diffractometer, (Karlsuhe, Germany)* operated at 40 kV/40 mA, using a Cu–Kα radiation tube,with a scan step of 0.02°s^{-1}, 2θ was varied in the 30°-100° range for SS316L, in the 30°-80° range for TiAlMoN and in the 20°-80° range for TiMoONAg coatings. All the XRD patterns were equated with the standards gathered by the Joint Committee on Powder Diffraction and Standards (JCPDS, card No. 00-038-1420 for TiN, No. 01-084-8748 for Mo_2N, No. 01-087-0633 for TiON and No. 04–0783 for Ag).

The average crystallite size was determined by using Scherrer equation (*Eq. II. 7*):

$$D = \frac{0.9\lambda}{\beta\cos\theta} \qquad \text{(II. 7)}$$

Where λ is the X-ray wavelength ($\lambda_{Cu} = 0.154$ Å), β is the full width at half maximum intensity (FWHM) and θ is the angle of Bragg.

The lattice parameter was calculated for fcc-crystal structure using the following equation:

$$a^2 = \left(\frac{\lambda^2}{4\sin^2\theta}\right)(h^2 + k^2 + l^2) \qquad \text{(II. 8)}$$

The lattice distortion (ε) was calculated using the following equation:

$$\varepsilon = \left(1 - \frac{a}{a_0}\right) \qquad \text{(II. 9)}$$

Where, (a) is the lattice constant produced in different conditions, and(a_0) is the lattice parameter of bulk structure.

The coefficient of texture (T_C)of coating was calculated as follows:

$$T_{C(hkl)} = \frac{I\,(hkl)}{I_0\,(hkl)}\left\{\frac{1}{n}\sum\frac{I\,(hkl)}{I_0\,(hkl)}\right\}^{-1} \qquad (II.\ 10)$$

Where $I_{(hkl)}$ is the measured peak intensity and $I_{0(hkl)}$ is the integrated intensity of the corresponding diffraction peak (in our study, TiN (200) and TiN (111)).

II. 4X-ray Photoelectron Spectroscopy (XPS)

X-ray photoelectron spectroscopy (XPS), also known as electron spectroscopy for chemical analysis (ESCA), is a quantitative technique for measuring the elemental composition of the surface of a material, and it also determines the binding states of the elements. XPS spectra are obtained by irradiating a solid surface with a beam of X-rays and measuring the kinetic energy E_k(*Eq. II. 11*) of electrons that are emitted from the top 1-10 nm of the material [68]. A photoelectron spectrum is recorded by counting ejected electrons over a range of kinetic energies. The energies and intensities of the photoelectron peaks enable identification and quantification of all surface elements.

$$E_k = h\upsilon - E_B - \Phi \quad (II.\ 11)$$

Where $h\nu$ is the X-ray photon energy, E_B is the electron binding energy, and Φ the work function that is the energy needed for the electron to free itself from the surface.

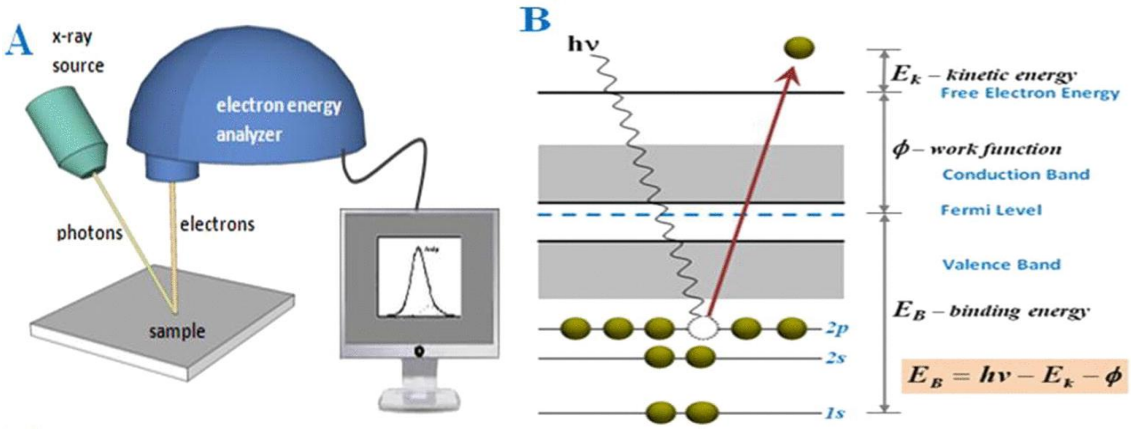

Fig. II.11.A schematic drawing of the principle of X-ray photoelectron spectroscopy (XPS) [69].

An ES300 KRATOS spectrometer (*Kratos Analytical, Manchester*, UK, $Al_{K\alpha}$, 1486.6 eV, 300 W, 5×10^{-9} mbar) was used for the XPS tests to determine the binding energy of our TiON(Mo, Ag) thin films.Prior to the XPS analysis, the ion bombardment (Ar^+) with 3 keV of primary energy was sputtered on the sample for 5 min at 1 keV and 20 mA was applied for 30 min to remove the topmost contaminated layers and to increase the reliability of chemical analysis. The electron analyzer was calibrated against $Au4f_{7/2}$ (84 eV) and $Cu2p_{2/3}$ (932.7 eV) photoelectron line positions obtained from cleaned metallic surfaces of gold and copper, respectively. Non-monochromatic Mg K_α radiation was used for analysis without calibration because of the conductivity of the samples. The corresponding Ti2p, Mo3d, Ag3d, N1s and O1s spectra were fitted using a multi-peak fitting method using XPS-Calc software (*Boreskov Institute of catalysis, Novosibirsk, Russia*).

II. 5 Raman spectroscopy

Raman spectroscopy is an important technique to identify several materials which can be solids, liquids or gases. It is simple and non-destructive technique and no sample preparation needs. Raman technique is based on exciting a sample using a high-intensity laser beam, with the resulting scattered light being passed through a spectrometer (*Fig. II.12*). This technique works on inelastic scattering of the monochromatic light of frequency υ_0. A part of the light is absorbed and a part is diffused either with the same frequency (it is the elastic or Rayleigh diffusion) or with a different frequency vshifted up or down in respect to the primary monochromatic frequency which is termed as Raman effect. Stokes scattering is observed in the lower wave number (longer wavelength) region and anti-Stokes scattering in the higher wave number (shorter wavelength) region. These shifts give valuable information on the vibrational, rotational and low frequency transitions of the sample molecules [70-71].

Raman spectroscopy (*Bruker Senterra spectrometer*) was used for identification of the TiAlMoN film phases with exciting laser radiation wavelength of 600 nm.

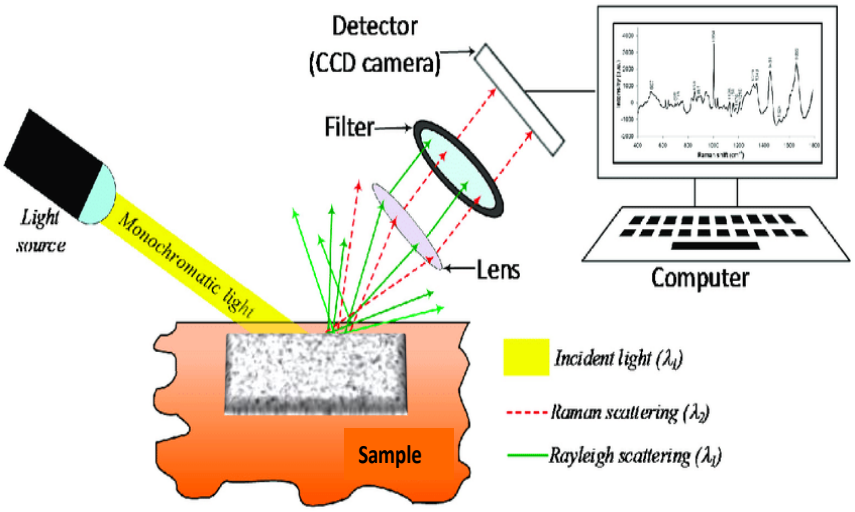

Fig. II.12. Schematic representation of a basic Raman spectroscopy instrument [72].

II. 6 Ultraviolet-Visible Spectroscopy (UV-VIS)

UV-Vis spectroscopy is an analytical technique that measures the amount of discrete wavelengths of UV or visible light that are absorbed or transmitted through a sample in comparison to a reference or blank sample (*Fig. II.13*). It ranges from the light level ultraviolet region i.e. 180 nm to the visible region i.e. 780 nm. UV spectrum extends from 180 nm to 400 nm whereas the visible region ranges from 400 nm to 780 nm. It is used to observe the optical behavior of chemical compounds, identification of various species, and quantification of specific analyses [73]. Using the Beer Lambert law, the absorption of spectra generated from these samples at given wavelengths can be related directly to the concentration of the sample.

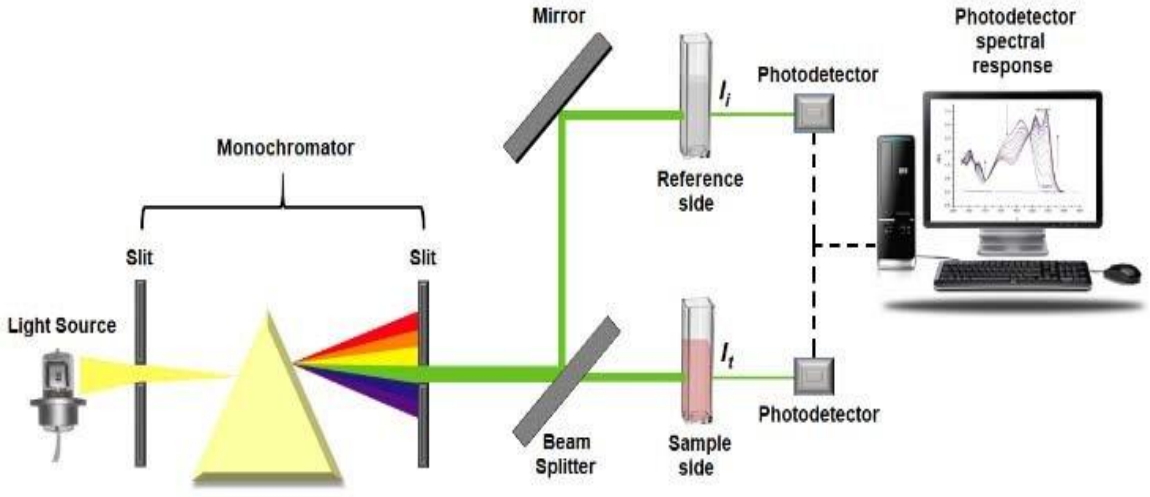

Fig. II.13. Schematic representation of the dual-beam UV-VIS spectrometer [74].

The absorption of the optimized TiOMoN(7.4 at. % Ag) coating was performed using an UV-VIS spectroscopy to examine the impact of Ag doping into TiOMoN on the light absorbance capacity of the photocatalyst samples. The absorption spectra were obtained along the 250-800 nm wavelengths to determine their band gap values using Tauc equation (*Eq. II. 12*):

$$(\alpha h\nu)^n = K(h\nu - Eg) \qquad (II.\ 12)$$

Where *K*, α, and h*ν* present the constant value, absorbance coefficient, and photon energy, respectively, n is the transition category (n = 0.5 for indirect and n = 2 for direct transition). The intercept from the extrapolation of the linear portion of the $(\alpha h\nu)^{1/2}$ versus hν gives the bandgap (E_g).

II. 7. Scanning electron microscopy (SEM)

Fig II. 14 presents a schematic representation of a scanning electron microscope. Accelerated electrons generated normally from a tungsten filament in an SEM carry significant amounts of kinetic energy, and this energy is dissipated as a variety of signals produced bby electron when the incident electrons are decelerated in the solid sample. These signals include secondary electrons (SE which are most valuable for showing morphology and topography of samples), backscattered electrons (BSE for illustrating contrasts in composition in multiphase), diffracted backscattered electrons (EBSD that are used to determine crystal structures and orientations of minerals), and photons (characteristic X-rays that are used for elemental analysis and continuum X-rays are carried out with the EDS or WDS [75]).

When a cathode emits electrons under a very high electric field, it is also known as a field emitter-FE-SEM, less electrostatically distorted images with best spatial resolution will be obtained [76].

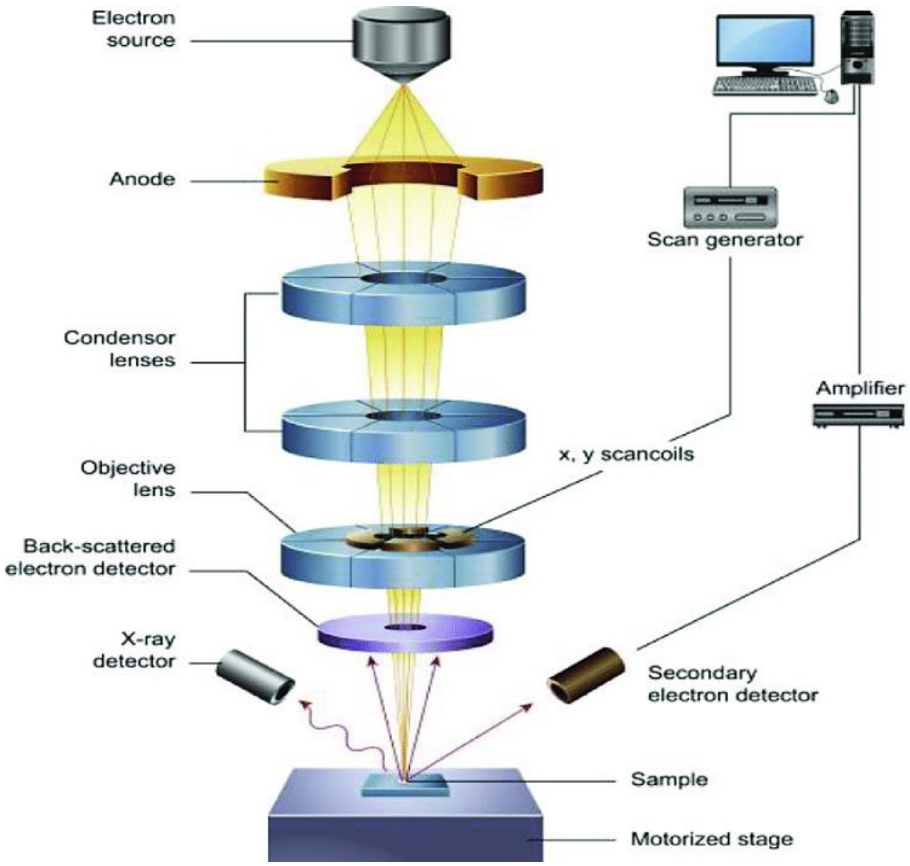

Fig. II.14. Schematic representation of a Scanning Electron Microscope (SEM) [77].

In our work, the surface and cross-section morphology of the coatings were examined using a field emission scanning electron microscope (*FE-SEM, Hitachi S3500 N, USA*). Chemical compositions of thin films were analyzed with energy (EDS) and wavelength dispersive X-ray spectroscopy (WDS) techniques (*Oxford INCA x-act, 15 kV, USA*).

II. 8 Transmission electron microscopy (TEM)

The transmission electron microscopy (TEM) is a good microscopy technique used for material observations in which a beam of electrons is transmitted through a sample (*Fig II.15*). It is a quantitative method to determine the particle size, shape and distribution. The interactions between electrons and atoms allow the observation of important features such as the crystal structure, dislocations and grain boundaries. Chemical analysis can also be performed. The TEM can be used to study the growth of layers, their composition and defects. It has a higher resolution than an SEM. The main TEM advantages are better spatial resolution with the additional capability of analytical measurements [78].

This technique has few limitations concerning the high vacuumrequirement and the sample preparation which is extremely important for getting high-quality images. The samples observed using an TEM should be thin and less than 200 nm thick [79].

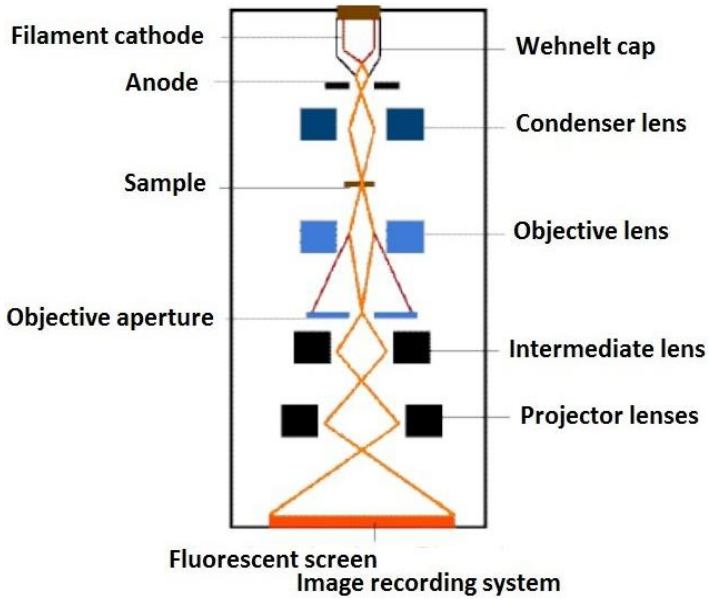

Fig. II.15. Basic components of a transmission electron microscope (TEM) [80].

Transmission electron microscopy (TEM) images of thin films were obtained using a JEM-2100 transmission electron microscope (*JEOL, Tokyo, Japan*) at an accelerated voltage of 200 Kv to analyze the TiAlN(16.09 at.% Mo) and TiMoON(7.4 at. % Ag) films.

II. 9 Optical microscopy (OM)

The optical microscope uses a visible light and a system of lenses to magnify images of small samples. *Fig. II.16* presents the basic components of an optical microscope. If the sample is transparent or at least exhibits a high light transmission; the light is then projected through the sample and collected by the objective lens onto the eyepiece. However, if the sample is translucent or opaque, the light is reflected off the surface to the viewing eyepiece. Therefore, the optical microscope is useful for observing morphology, crystallization, multiphase structures, and fracture surfaces [82].

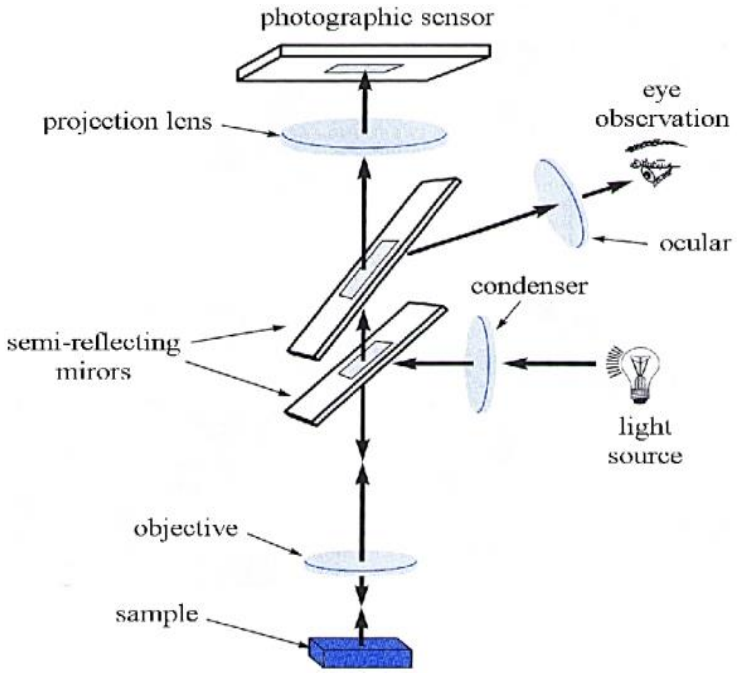

Fig. II.16. Basic components of an optical microscope (OM) [83].

In our work, after corrosion tests of TiAlMoN coatings, the surface morphology was examined by using an optical microscope (*KEYENCE digital microscope system*).

II. 10 Stereomicroscopy

Stereo microscope or Dissecting microscope is a variant of optical microscope that typically uses the light reflected from the surface for examination in 3-Dimension. The instrument uses two separate optical paths with two objectives and eyepieces to provide slightly different viewing angles to the left and right eyes [84] (*Fig. II.17*). It also consists of a digital camera that is used for viewing the images of the samples in the computer for a close observation. The produced image is little larger than normal and is recorded. The dissecting microscope has two magnifications known as fixed magnification and Zoom magnification. Fixed mode is used in eyepiece to provide a degree of magnification while Zoom mode offers different magnifications at different ranges.

Dissecting microscope is used widely in various fields and has a lot of applications. It is a good technique that provides accurate information concerning the morphology of paint traces, surface characteristics, number of layers, colors …etc [85].

We used a stereomicroscope (*Leica MZ16 FA, Leica Microsystems GmbH Wetzlar, Germany*) to monitor the sample fluorescence and images were processed using an LAS V.1.7.0 software on the coatings tested for bacterial inactivation.

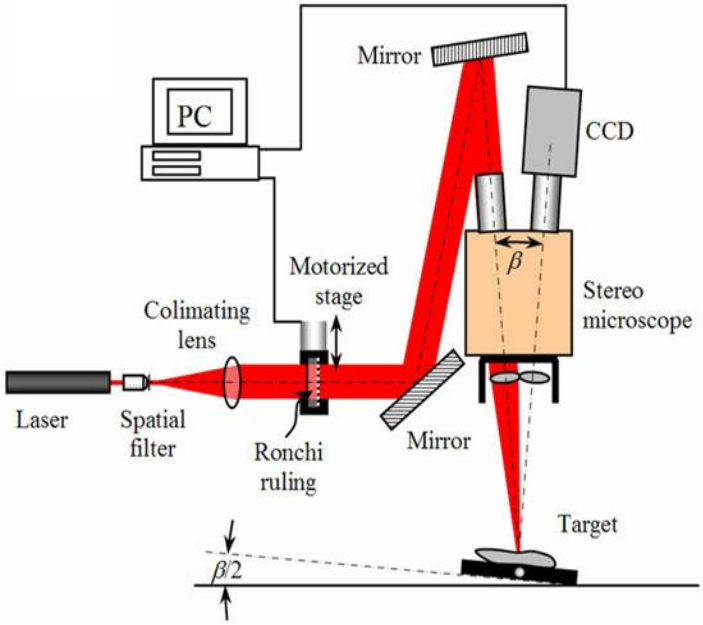

Fig. II.17. Basic components of a stereomicroscope [86].

II. 11 Atomic force microscopy (AFM)

Atomic force microscopy (AFM) can be used for any type of surface, including polymers, ceramics, composites, glass, and biological samples. AFM is used to measure and localize many forces, including adhesion strength, magnetic forces, and mechanical properties. AFM force measurements are performed using a sharp tip of about 10-20 nm diameter attached to a cantilever. AFM tips and cantilevers are micro fabricated from Si or Si_3N_4. The tip moves in response to tip–surface interactions, and this movement is measured by focusing a laser beam on the tip with a photodiode [87] (*Fig. II.18*).

The AFM is operated in two basic modes: contact and tapping. In the contact mode, the AFM tip is continuously in contact with the surface, while in the tapping mode, the AFM cantilever is vibrated above the sample surface so that the tip is in contact with the surface only intermittently. The AFM maps/images are suitable for further investigation of the surface such as measurement of surface roughness, analysis of particle and grain size. The AFM can also be used to measure magnetic and electrical properties of the material [88]. In comparison to the electron microscope, which provides a two-dimensional projection or a two-dimensional image

of a sample, the AFM provides a true three-dimensional surface profile. Additionally, samples used for AFM experiments do not require any special treatment [89].

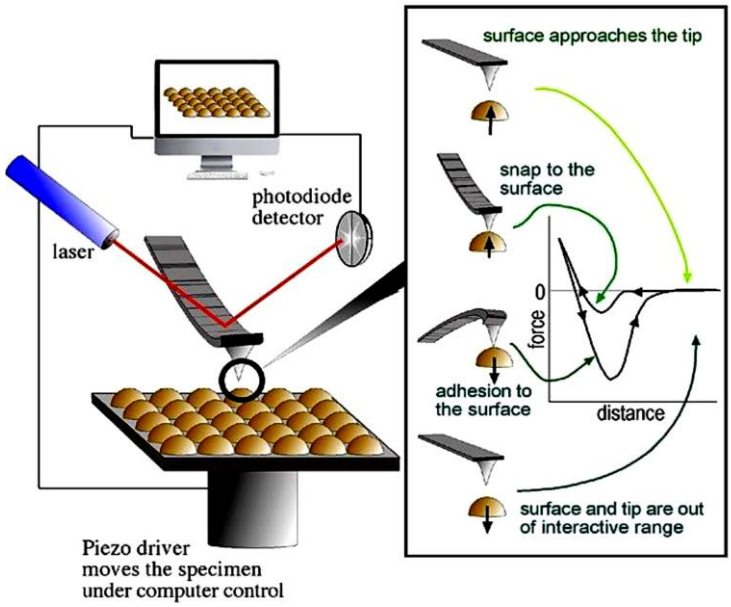

Fig. II.18. Schematic representation of an atomic force microscope (AFM) [90].

In our study, the surface roughness was analyzed by an atomic force microscope (*AFM-Veeco Bioscope II*) and determined from three different locations using a NanoScope Analysis software. The scanned images were (2×2 μm^2), and line profiles werecentrally measured along 2 µm.

II. 12 Optical profilometry

Optical profilometry is a non-destructive and non-contact surface analysis technique. The optical profilometer is a type of microscope in which the light source is used to measure the surface profile, in order to quantify its roughness (*Fig. II. 19*). Critical features such as step, curvature, and flatness are computed from the surface topography. The light from the profiler lamp splits into two paths by a beam splitter where one path is directed towards the sample surface and the other path is directed towards the reference mirror. The reflections from these two paths are recombined and projected onto an array detector. The difference in the path of recombined beams is in the order of few wavelengths which lead to less interference [91].

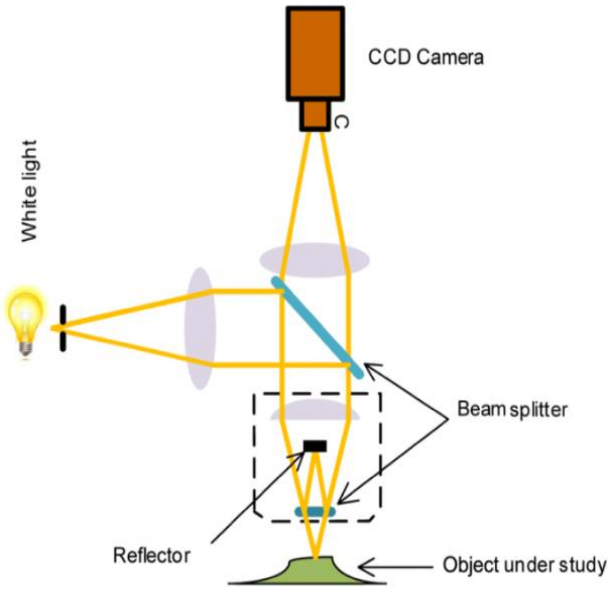

Fig. II.19. The working principle of an optical profilometer [92].

During the thin film deposition, the deposited layers are subjected to residual tensile or compressive stresses. The Optical profilometry is also a method that can be used to determine the residual stresses using *Stoney's* formula (*Eq. II.13*):

$$\sigma = \frac{E_S}{6(1-\upsilon_s)} x \frac{e_s^2}{e_f}\left(\frac{1}{R} - \frac{1}{R_0}\right) \qquad (II.\ 13)$$

Where Es and νs are the Young's modulus (181 GPa) and Poisson's ratio (0.28) of iron substrate used in our work. es and ef are the thicknesses of the iron substrate and deposited film (m), while R_0 and R are the curvature radius before and after film deposition (m), respectively.

In our study, we used an optical profilometer (*Altisurf 500VEECO*) to determine the surface roughness and profile depth of SS316Lcold-sprayed substrates with a scanning range of (2×2)mm^2. The film thickness, wear volume loss, the depth and width of corrosion pits of coatings were measured using this optical profilometer. The residual stresses were calculated using the curvature method (*Stoney's formula*, *Eq. II. 13*) using an iron sample (50×4×0.2)mm^3 where its curvature radius was measured before and after film deposition.

II. 13 Nanoindentation technique

Nanoindentation technique is used to measure the mechanical properties, elastic modulus and hardness of different types of materials at a very small scale. It can provide accurate information on the properties of various samples including thin films, polymers, biological materials, etc.

In nanoindentation, the mechanical properties are characterized by driving an indenter, made of a hard material usually diamond, into the material surface under certain pressure. This later maintains for a short time before unloading of the sample (*Fig. II.20*). The system measures the load applied to the tip as well as the depth of indentation during the whole process. Over time, the force applied to the probe and the indenter penetration distance are both measured. In the case of thin films and in order to avoid the substrate stiffness, the indenter penetration depth must be limited to < 10% of the film thickness [93, 94].

The hardness and Young's modulus are given by the following formulas:

$$H = \frac{P_{max}}{A(h_c)} \qquad \text{(II. 14)}$$

$$E = \frac{1-\upsilon_s^2}{\frac{1}{E_r}-\frac{1-\upsilon_i^2}{E_i}} \qquad \text{(II. 15)}$$

Where P_{max} is the maximum load, A(hc) is the projected contact area; vs is the Poisson's ratio of the sample, vi is the Poisson's ratio of the indenter, Er is the reduced modulus and Ei is the Young's modulus of the indenter.

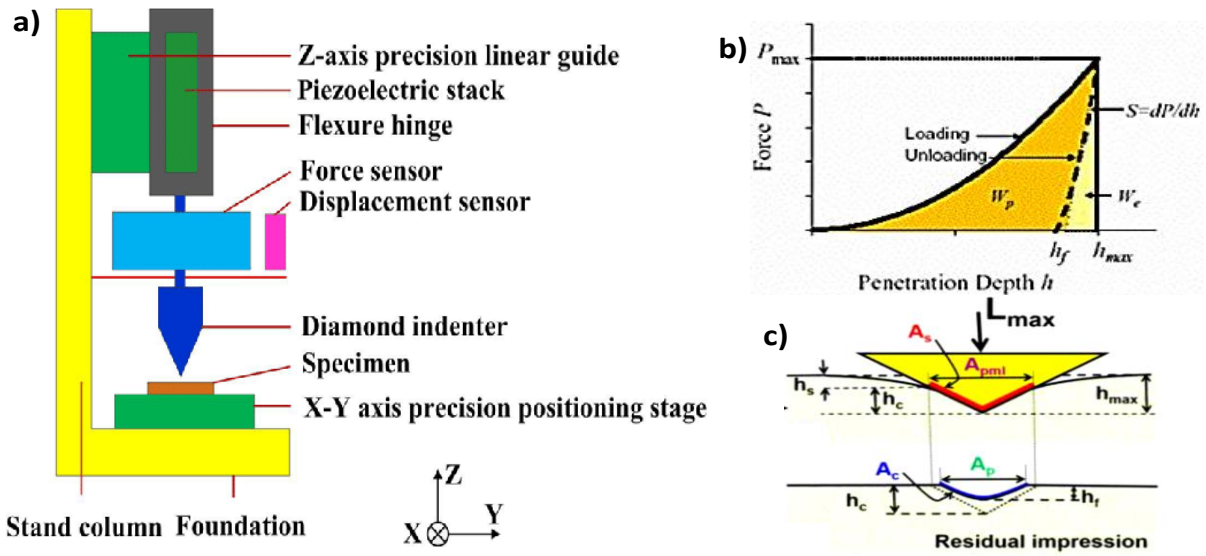

Fig. II.20.a) Schematic diagram of the nanoindentation instrument, b) Indentation load–displacement curve, c) Elasto-plastic deformation at the maximum applied load and after load releasing [92-94].

The hardness and Young's modulus values of the coatings were measured using nanoindentation technique. A *TI 980 Triboindenter* machine was used with a Berkovich

diamond indenter and tests were performed following the method described by Oliver and Pharr [98]. Nanoindentation tests were carried out by applying a maximum load of 50 mN. For each sample, 20 indents were performed during 36 s of loading.

In order to avoid the effect of substrate stiffness on the mechanical properties of coatings, the maximum indentation depth was limited to not exceed 10 % of the coating thickness and the average values were calculated for twenty indentations for each sample.

II. 14 Wettability

Wettability is the ability of interaction of liquids with other fluids and/or solid surface. Wettability measures the level of wetting when solid and liquid phases interact with each other [99]. It has attracted enormous research interests due to its influence in wide range of applications such as enhancing heat flux for thermal energy conversion, energy saving through self-cleaning, antifogging, atmospheric water collection, oil–water separation and anti-bacterial activity [100].

The surface wetting behavior can be categorized with the help of contact angle measurement. The concept of contact angle was proposed by *Thomas-Young* [101], which provides information about three-phase contact point (*Fig. II.21*) given by *Eq. II. 16*:

$$\cos\theta_Y = (\gamma sg - \gamma sl) / \gamma lg \qquad (II.\ 16)$$

where θ_Y (deg)Young's equilibrium contact angle and γij (mJ/m^2) is the surface tension at the interface between the two different phases with s, l and g representing solid, liquid and gas, respectively. The sessile drop technique utilizes an optical tensiometer and is one option for wettability measuring. In this measurement, a drop of liquid is placed onto a surface and the contact angle is measured. Lower contact angle ($\leq 90°$) signifies hydrophilic behavior and greater wettability, whereas higher contact angle ($\geq 90°$) infers hydrophobic behavior and lower wettability.

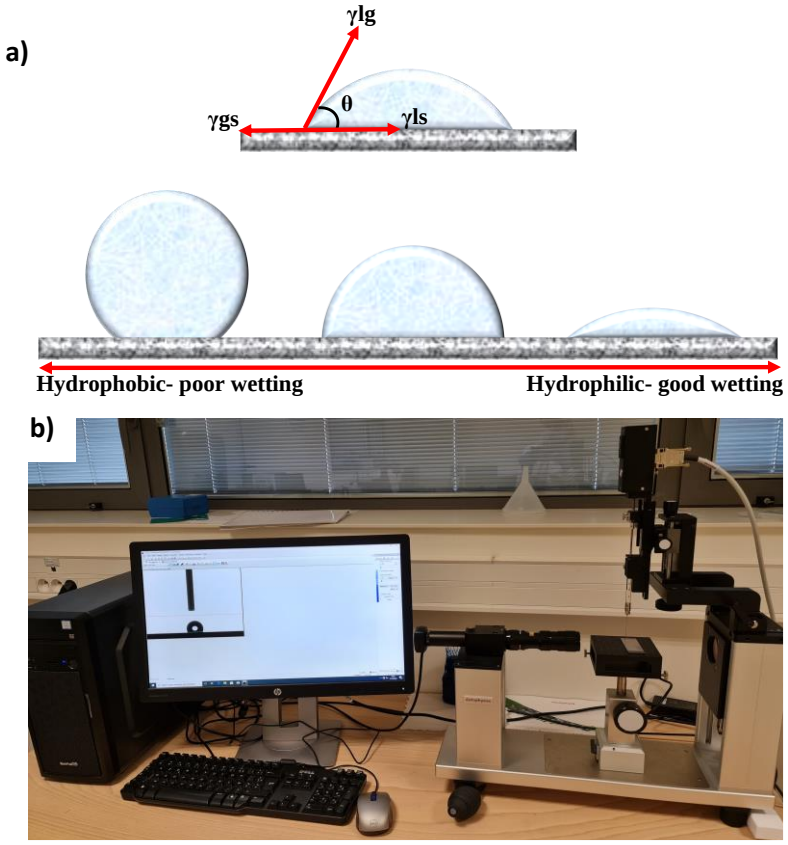

Fig. II.21.a) Representation of the Contact Angle, and b) optical goniometer (*Data Physics Model ESr-N*).

There are different factors that affect the contact angle: surface free energy, roughness, chemical composition, porosity, surface tension, surface chemistry, and surface charge. They are considered as the governing properties for wettability alteration [100]. Generally, surface free energy (SFE) or interfacial free energy or surface energy determines how the solid behaves in contact with other materials. It arises from molecular interactions at the liquid-solid interface. The most typical unit for SFE is mN/m which can be calculated with different theoretical approaches. *Owen-Wendt-Rabel-Kaelble* (OWRK) methodis the most used for calculating the surface free energy from the contact angle with several liquids. It separates the interactions at the liquid-solid interface into dispersive and polar by the following formula:

$$\gamma_T(1+\cos\theta) = 2\left(\sqrt{\gamma_S^D\gamma_L^D} + \sqrt{\gamma_S^P\gamma_L^P}\right) \qquad \text{(II. 17)}$$

Where: $\gamma_T$is the total surface tension (mN/m), θ is the contact angle (deg), γ_S^D is the dispersive component of surface energy (mJ/m^2), γ_L^D is the dispersive component of surface tension (mN/m), γ_S^P is the polar component of surface energy (mJ/m^2), and γ_L^P is the polar component of surface tension (mN/m).

The wettability of our films was investigated using a contact angle device with an optical goniometer (*Data Physics Model ESr-N, Germany*). Three liquids: water, thiodiglycol and diiodomethane were used to determine the contact angle by dropping 2.0025 µl of liquid on the films surfaces with a 1 $\mu l \cdot s^{-1}$rate. Due to its small weight, this is sufficient to ignore the impact of the fall effect [102]. Surface energy of TiAlMoN films was estimated using the *Owens-Wendt-Rabel-Kälble* (OWRK) method and the dynamic contact angles of TiMoON-Ag films were measured using water contact-angle recorded at room temperature for 100 s.

II. 15 Tribometry

Friction occurs when two bodies are moved in contact with each other (e.g. Machining). Therefore, wear is a consequence of friction defined as the progressive loss of surface material as a result of relative motion of two bodies in contact.

Ball-on-disk tribometer is one of the most widely used machines in the field of tribology (*Fig. II.22*). It is used to perform studies focused on bearings, brake systems, manufacturing industry, train wheel systems, etc. It consists of a pin (or ball) which, by means of an arm, applies a normal force on a rotating disk (sample). The tribological tests can be performed in dry conditions and with lubricants [103].

Friction and wear tests were carried out in our study using a continuous stiffness measurement (*CSM)* tribometer. Our coatings were tested against 100C6 steel balls with 6 mm diameter. The tests were performed at room temperature and relative humidity of approximately 25 ± 3% under two loads of 2 N and 5 N during 50 m of sliding distance. The friction coefficient curves were automatically recorded by the tribometer software.

On the other hand, the wear volume loss was measured using a profilometer (*Altisurf 500*) then the wear rates (W in $mm^3.N^{-1}\,m^{-1}$) of the coatings were calculated using *Eq. II. 18*:

$$W = \frac{V}{LF} \qquad \text{(II. 18)}$$

Where V is the wear volume loss in mm^3, L is the total sliding distance in m, and F is the applied load in N. After the sliding tests, the worn tracks were analyzed by an SEM, EDX and Raman spectroscopy.

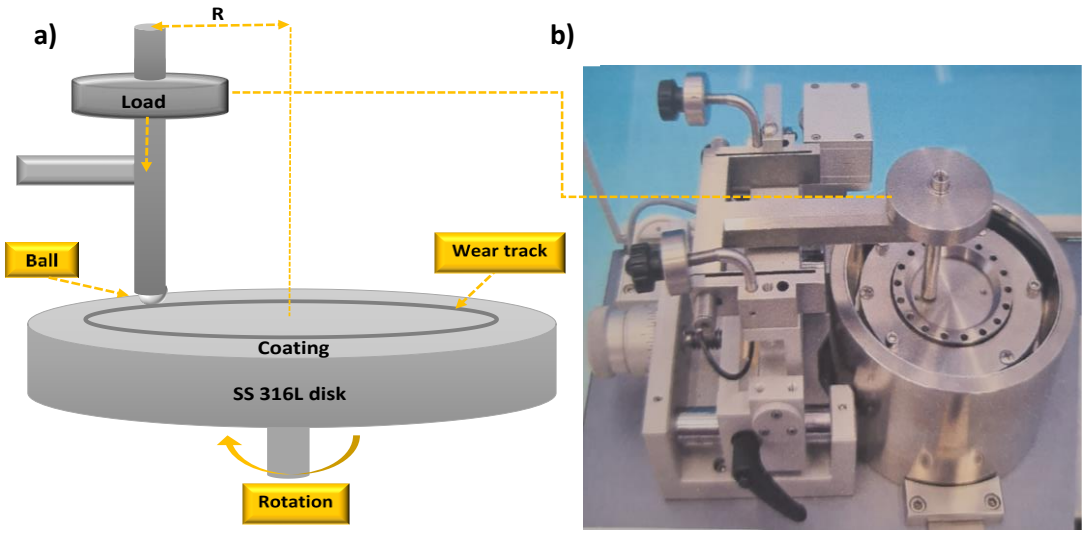

Fig. II.22. (a) Representation of the ball-on-disk tribologicaltest, and (b) a *tribometer (CSM, Anton Paar)*.

II. 16 Electrochemical measurements

Corrosion is based on the reaction of a metallic material with its environment. The metal (M) atoms of a component change from the metallic state into an oxidized state. The driving force of this process has the tendency to reduce the free energy of the system [104]. An anode (positive electrode) is oxidized and a cathode (negative electrode) is chemically reduced. The free electrons are consumed by H_2, O_2 and H_2O (*Eqs. II. 19-22*).

$$M \rightarrow Mn^{+} + ne^{-} \qquad \text{(II. 19)}$$

$$H^{+} + e^{-} \rightarrow H \qquad \text{(II. 20)}$$

$$2\,H \rightarrow H_2 \qquad \text{(II. 21)}$$

$$2\,H_2O + O_2 + 4e^{-} \rightarrow 4OH^{-} \qquad \text{(II. 22)}$$

Equations (19) and (20) represent a two-step process in which hydrogen gas is formed. The reaction presented by the *Eq. II.22* depends upon the level of dissolved oxygen in solution. When this level varies locally in the corrosion cell, differential-aeration corrosion may result [53,104].

When a sample is immersed in a corrosive solution in the absence of electrical connections, the natural electrode potential (corrosion potential → open circuit potential) can then be measured by measuring this potential against a reference electrode. It is possible to evaluate corrosion characteristics and corrosion behavior by performing electrochemical tests. Electrochemical measurement is an effective analytical technique for corrosion investigation.

Fig. II. 23 present the experimental setup used for our electrochemical corrosion tests. The sample constitutes the working electrode (WE). To measure the sample potential with respect to the electrolyte, a reference electrode (RE) is used (e.g saturated calomel electrode SCE). Using an external generator (potentiostat), the current is passed through the metal electrode; its surface takes a new potential value and this current can be measured using a counter-electrode (CE) (*generally platinum*) [105]. The obtained current intensity-potential curves (I=f(E)) constitute the polarization curves.

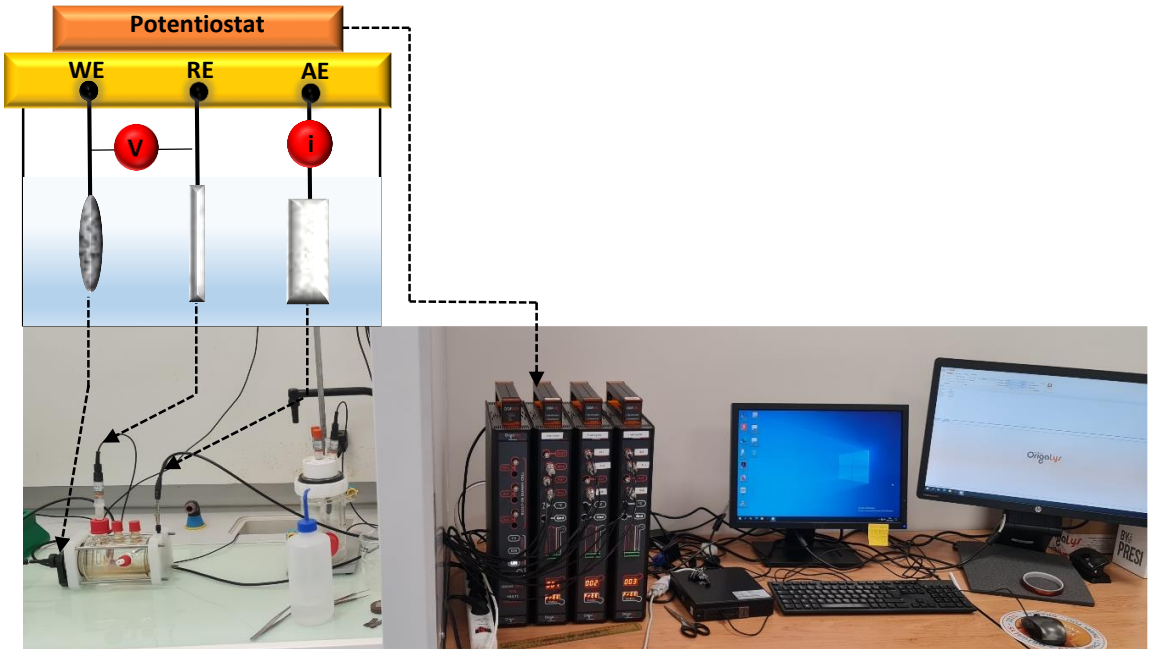

Fig. II.23. Experimental setup for electrochemical corrosion tests.

In our work, the corrosion tests of the cold-sprayed stainless steel 316L substrate and coatings were performed in a chlorinated medium NaCl. The polarization curves successively exhibited different behaviors. *Fig. II.24* presents a typical polarization curve. The critical potential at which the current density increases suddenly is termed as pitting potential (E_{pit}). At a low potential, a state of passivity is observed with a very low current where pitting can occur at a potential $<E_{pit}$ (metastable pits) [106]. At a higher potential, the current suddenly increases

and the pitting observed at a potential >E_{pit} is stable which continues to grow in a destructive way.

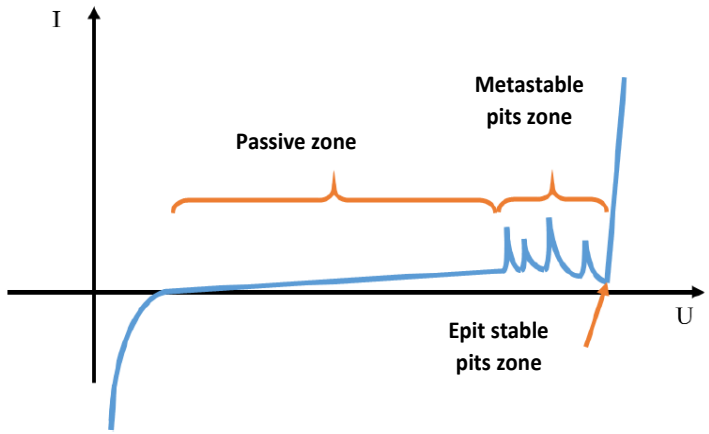

Fig. II.24.A typical polarization curve under pitting corrosion test in chloride medium [107].

The electrochemical properties of ours samples were evaluated using an Origalys potentiostat and a Biologic flat corrosion cell. Pitting corrosion tests were performed on a 1 cm^2 exposure surface at room temperature in a 3.5 wt.% NaCl solution (pH~6.3). Three electrodes were used: a saturated calomel electrode SCE (Hg/Hg_2Cl_2-Sat. KCl) as a reference electrode, a platinum mesh (counter electrode) and cold-sprayed SS316 L with or without coating (working electrode). In order to ensure system stability, the Open Circuit Potential (OCP) was measured for 60 min. Measurement range was fixed from -150 mV/free to 1.3 V/ref. The scan rate was fixed to 0.5 mV/sec and the current threshold to 3 mA. The extrapolation of the Tafel method was used to determine the main corrosion parameters.

II. 17 Antibacterial tests

The antibacterial behavior of the developed TiMoON and TiMoON-Ag thin films, as-deposited and annealed under vacuum at 400 °C against *Escherichia coli* bacteria (*E. coliK12*) was investigated by determining their inactivation kinetics, stability, efficiency and adhesive properties using the Deutsche Sammlung von Mikroorganismen und Zellkulturen (GmbH (DSMZ), Braunschweig, Germany). Tests were performed under solar simulated light (*CPS Suntest System, Atlas GmbH, Hanau, Germany*) with an emission between 320 and 800 nm with light dose of 50 mW/cm^2. Each sample was placed into a glass Petri dish then inoculated with bacteria. The 100 µL culture aliquots with an initial concentration of 4.3×10^6 colony-forming unit per milliliter (CFU mL^{-1}) in NaCl/KCl were placed on coated and uncoated (control) samples.

After preselected times, the samples were transferred into a sterile tube containing 900 µL autoclaved NaCl/KCl saline solution. This solution was subsequently mixed thoroughly using a Vortex for 2 min. Serial dilutions were made in NaCl/KCl solution. A 100 µL sample of each dilution was pipetted onto a nutrient agar plate and then spread over the surface of the plate using the standard plate method. Agar plates were incubated lid down to prevent evaporation for a period of 24 h before the colonies counting. Experiments were carried in triplicates and statistical analysis show standard deviation error bars (± SD, n = 5 %). Solutions and samples were autoclaved before use at 121 °C. The genetically modified *E. coli* mutant strains deficient in OmpF and OmpC porins was also used. This approach allowed comparing the bacterial inactivation kinetics induced by: (i) the ions able to penetrate inside the cell, or (ii) by contact of the bacteria with the coated/sputtered surface.

Stereomicroscopy imaging was carried out on samples inoculated with 10^8 CFU of *E. coli* and incubated for 2 hours in a humidification chamber. This method uses a fluorochrome based staining procedure from Film tracer™ LIVE⁄DEAD® Biofilm Viability Kit (Molecular Probes, Invitrogen). The kit contains a combination of the SYTO9® green fluorescent nucleic acid stain and propidium iodide (PI) fluorochromes for the staining of live and dead cells, respectively. The sample fluorescence was monitored in a stereomicroscope (*Leica MZ16 FA, Leica Microsystems GmbH Wetzlar, Germany*) and the images were processed using the LAS v.1.7.0 provided for with a 1240 software from Leica Microsystems CMS GmbH. Adhesion of bacteria on the samples was allowed for 5 min before washing the sample with sterile Milli-Q water to remove the non-adhered bacteria. Finally, the scavenging experiments by dimethyl-sulfoxide (DMSO, 2 mM), superoxide dismutase (SOD, 2 mM) and Ethylene tetra-acetic acid di-sodium salt (EDTA-2Na, 2 mM) were carried out to detect/identify the $^{\bullet}OH$, O_2^{-} and $vb(h^+)$ generated in solution during the bacterial inactivation process.

Conclusion

In this chapter, we presented the two deposition techniques and the experimental parameters used in our work; the cold spray for elaborating the 316L stainless steel and the magnetron sputtering used for elaborating different thin films (TiN,TiAlN,TiAlMoN, TiMoON and TiMoON-Ag).The various experimental techniques for structural, morphological, mechanical, tribological, antibacterial and anticorrosion characterizations were also presented in this chapter. *Table II. 1* summarizes the elaboration and characterization techniques used in our study.

Table II.1. Summary of the elaboration and characterization techniques used in our work.

Testing / Properties	**Techniques/ machines**
Elaboration of substrates	Cold spray technique
Elaboration of coatings	Reactive magnetron sputtering system
Structural analysis	XRD
Morphology observation	SEM, TEM, OM
Chemical Composition	EDS , XPS, RAMAN
Surface topography	AFM
Wetting and surface energy	Contact angle measurements
Residual stress and film thickness	Profilometer
Hardness and Young's modulus	Nanoindentation
Friction coefficient and Wear resistance	Ball on disk tribometer (CSM, HT)
Corrosion resistance	Electrochemical polarization measurements (Potentiostat and corrosion cell)
Antibacterial test	Stereomicroscopy

References

[1] A.P. Alkhimov, V.F. Kosarev, A.N. Papyrin, A method of "cold" gas-dynamic deposition, Soviet physics Doklady, 35 (1990), pp. 1047-1049.

[2] H. Singh, T.S. Sidhu, S.B.S. Kalsi, Cold spray technology: future of coating deposition processes, FratturaedIntegritàStrutturale, 22 (2012), pp. 69-84.

[3] A.P. Alkhimov, A.N. Papyrin, V.F. Kosarev, N.I. Nesterovich, M.M. Shushpanov, Gas-dynamic spraying method for applying a coating, US patnet, (1994)5302414.

[4] A.P. Alkhimov, A.N. Papyrin, V.F. Kosarev, N.I. Nesterovich, M. Mikhailovich, Shushpanov, Method and device for coating, European Patent, (1995)0484533B1.

[5]Q. Blochet, Influence de la rugosité de surface du substrat sur l'adhérence de revêtements à base d'aluminium élaborés par projection dynamique par gaz froid « cold spray », PhD Thesis, ParisTech France (2015).

[6] J. Karthikeyan, Cold spray technology:International status and USA efforts, report by ASB Industries, 44203(2004), pp. 1-14.

[7] T. Goyal, T. S. Sidhu, R. S. Walia, An overview on cold spray process over competitive technologies for electro-technical applications. In: National conference on advancements and futuristic trends in mechanical and materials engineering, (2010), pp. 364-368.

[8] K. Ichimura, Mechanical properties of aluminum deposition produced by low pressure type cold spray technique, PhD thesis, University of Sendai Japan (2007).

[9] M.I. Boulos, P.L. Fauchais, J.V.R. Heberlein, Thermal Spray Fundamentals – From Powder to Part, Springer International Publishing, (2014).

[10] V.K. Champagne, Repair of magnesium components by cold spray techniques. In: The Cold Spray Materials Deposition Process. Woodhead Publishing, (2007), pp. 327-352.

[11] A. Moridi, S.M. Hassani-Gangaraj, M. Guagliano, M. Dao, Cold spray coating: review of material systems and future perspectives, Surface Engineering. 30 (2014), pp. 369–395.

[12] H. Wu. Process Modeling and Planning for Robotic Cold Spray Based Additive Manufacturing. Material chemistry. University of Bourgogne Franche-Comté France (2020).

[13] H. Assadi, F.Gärtner, T. Stoltenhoff, H. Kreye, Bonding mechanism in cold gas spraying, ActaMaterialia, 51(2003), pp. 4379–4394.

[14] R.R. Chromik, D. Goldbaum, J.M. Shockley, S. Yue, E. Irissou, J.G. Legoux, N. X. Randall, N. X. Modified ball bond shear test for determination of adhesion strength of cold spray splats, Surface & Coatings Technology, 205(2010), pp. 1409–1414.

[15] A.N. Papyrin, S.V. Klinkov, V.F. Kosarev, Effect of the substrate surface activation on the process of cold spray coating formation, in: Proceedings of the International Thermal Spray Conference (ITSC) Switzerland, (2005), pp. 145-150.

[16] T. Schmidt, F. Gartner, H. Assadi, H. kreye, Development of a generalized parameter window for cold spray deposition, ActaMaterialia, 54(3)(2006), pp. 729-742

[17] Z. Cai, Programmation robotique en utilisant la méthode de maillage et la simulation thermique du procédé de la projection thermique, PhD Thesis, UTBM, Belfort-Montbéliard, France (2014).

[18] R. G. Neo, K. Wu, S.C. Tan, W. Zhou, Effect of spray distance and powder feed rate on particle velocity in cold spray processes, Metals, 12(1) (2022), pp. 75.

[19] J. Pattison, S. Celotto, A. Khan, W. O'neill, Standoff distance and bow shock phenomena in the Cold Spray process. Surface and Coatings Technology, 202(8)(2008), pp. 1443-1454.

[20] S. Yoon, C. Lee, H. Choi, H. Jo, Kinetic spraying deposition behavior of bulk amorphous NiTiZrSiSn feedstock. Materials Science and Engineering: A, 415(1-2)(2006), pp. 45-52.

[21] X. Suo, S. Yin, M.P. Planche, T. Liu, H. Liao, Strong effect of carrier gas species on particle velocity during cold spray processes, Surface & Coatings Technology, 268(2015), pp. 90-93.

[22] C.J. Li, W.Y. Li, Deposition characteristics of titanium coating in cold spraying. Surface and Coatings Technology, 167(2-3)(2003), pp. 278-283.

[23] X. Meng, J. Zhang, J. Zhao, Y. Liang, Y. Zhang, Influence of gas temperature on microstructure and properties of cold spray 304SS coating, Journal of Materials Science and Technology, 27(9)(2011), pp. 809-815

[24] C.J. Li, W.Y. Li, Optimization of Spray Conditions in Cold Spraying Based on Numerical Analysis of Particle Velocity, Transactions of Nonferrous Metals Society of China, 14(2)(2004), pp. 43-48.

[25] S. Yin, X. Suo, J. Su, Z. Guo, H. Liao, X. Wang, Effects of substrate hardness and spray angle on the deposition behavior of cold-sprayed Ti particles. Journal of thermal spray technology. 23(2014), pp. 76–83.

[26] S. Singh, R.S. Raman, C.C. Berndt, H. Singh, Influence of cold spray parameters on bonding mechanisms: a review. Metals, 11(12)(2021), pp. 2016.

[27] T. Go, Y.J. Sohn, G. Mauer, R. Vaßen, J. Gonzalez-Julian, Cold spray deposition of Cr2AlC MAX phase for coatings and bond-coat layers. Journal of the European Ceramic Society, 39(4) (2019), pp. 860-867.

[28] R. Morgan, P. Fox, J. Pattison, C. Sutcliffe, W. O'Neill, Analysis of cold gas dynamically sprayed aluminium deposits, Materials letters,58 (2004), pp. 1317–1320.

[29] T. Stoltenhoff, H. Kreye, H.J. Richter, An analysis of the cold spray process and its coatings, Journal of Thermal Spray Technology, 11(4)(2002), pp. 542-550.

[30]M. Villa, S. Dosta, J.M. Guilemany, Optimization of 316L stainless steel coatings on light alloys using Cold Gas Spray, Surface and Coatings Technology, 235(2013), pp. 220-225.

[31] N. Bala, H. Singh, J. Karthikeyan, S. Prakash, Performance of cold sprayed Ni-20Cr and Ni-50Cr coatings on SA 516 steel in actual industrial environment of a coal fired boiler, Materials and Corrosion, 64 (2013), pp. 783–793.

[32] H. Jami, A. Jabbarzadeh, Effect of particle shape on mechanics of impact in the deposition of titanium nanoparticles on a titanium substrate. Surface and Coatings Technology, 394(2020), 125880.

[33] S. Singh, H. Singh, R.K. Buddu, Microstructural investigations on bonding mechanisms of cold-sprayed copper with SS316L steel. Surface Engineering, 36(10)(2020), pp. 1067-1080.

[34] S. Singh, S. Chaudhary, H. Singh, Effect of electroplated interlayers on properties of cold-sprayed copper coatings on SS316L steel, Surface and Coatings Technology, 375(2019), pp. 54–65.

[35] L.S. Wang, H.F. Zhou, K.J. Zhang, Y.Y. Wang, C.X. Li, X.T. Luo, G.J. Yang, C.J. Li, Effect of the powder particle structure and substrate hardness during vacuum cold spraying of Al_2O_3, Ceramics International, 43(2017), pp. 4390–4398.

[36] O.Wang, N. Birbilis, M.X. Zhang, Interfacial Structure between Particles in an Aluminum Deposit Produced by Cold Spray. Materials Letters. 65(2011), pp. 1576–1578.

[37] T. Hussain, Cold spraying of titanium: A review of bonding mechanisms, microstructure and properties, Key engineering materials, 533(2012), pp. 53–90

[38] S. Kumar, G. Bae, C. Lee, Influence of substrate roughness on bonding mechanism in cold spray, Surface and Coatings Technology, 304(2016), pp.592–605.

[39] R. Ghelichi, M. Guagliano, Coating by the cold spray process: a state of the art. FratturaedIntegritàStrutturale, 3(8) (2009), pp.30-44.

[40] R.O. Fernandez, S. Imbriglio, R. Chromik, B. Jodoin, The Role of Substrate Preheating on the Adhesion Strength of Cold-Sprayed Soft Particles on Hard Substrates, Journal of Thermal Spray Technology, 30(2021), pp. 655–667.

[41] M. Fukumoto, H. Wada, K. Tanabe, M. Yamada, E. Yamaguchi, A. Niwa, M. Sugimoto and M. Izawa, Effect of Substrate Temperature on Deposition Behavior of Copper Particles on

Substrate Surfaces in the Cold Spray Process, Journal of Thermal Spray Technology, 16(5) (2007), pp. 643-650.

[42] M. Perton, S.Costil, W. Wong, D. Poirier, E. Irissou, J.-G.Legoux, A.Blouin, S. Yue, Effect of Pulsed Laser Ablation and Continuous Laser Heating on the Adhesion and Cohesion of Cold Sprayed Ti-6Al-4V Coatings, Journal of Thermal Spray Technology, 21(2012), pp. 1322–1333.

[43] Y. Wang, Electrochemical behavior of cold sprayed coatings dedicated to corrosion protection applications, PhD thesis, Lyon (2015).

[44] H. Che, P. Vo, S. Yue, Investigation of cold spray on polymers by single particle impact experiments. Journal of Thermal Spray Technology, 28(1)(2019), pp. 135-143.

[45] T. Schmidt, H. Assadi, F. Gärtner, H. Richter, T. Stoltenhoff, H. Kreye, T. Klassen, From particle acceleration to impact and bonding in cold spraying. Journal of thermal spray technology, 18(5) (2009), pp. 794-808.

[46] T. Tavsanoglu, Deposition and characterization of single and multilayered boron carbide and boron carbonitride thin films by different sputtering configurations, PhD thesis, EcoleNationaleSupérieure des Mines de Paris (2009).

[47] Y. R. Park, K. J. Kim, Sol–gel preparation and optical characterization of NiO and Ni1-xZnxO thin films, Journal of Crystal Growth, 258 (2003), pp. 380–384.

[48] E. Alfonso, J. Olaya, G. Cubillos, Thin film growth through sputtering technique and its applications. Crystallization-Science and technology, 23(2012), 11-12.

[49] C.R. Weissmantel, Deposition of Metastable Films by Ion Beam and Plasma Techniques, In: Proc. 9th Int. Vacuum Congress and 5th Int. Conf. on Solid Surfaces Madrid, (1983), pp 229-308.

[50] M. Henini, Handbook of Thin-Film Deposition Processes and Techniques, William Andrew Publishing, (2000).

[51] D. Depla, S. Mahieu, J. Greene, Sputter deposition processes, Handbook of Deposition Technologies for Films and Coatings, 281 (1991), pp. 253–296.

[52] B. Chapman, Glow discharge processes: sputtering and plasma etching, Wiley, (1980).

[53] B. Biswas, Growth Defects in CrN/NbN Coatings Deposited by HIPIMS/UBM technique, PhD thesis, UK at Sheffield Hallam University and Zimmer Biomet (2017).

[54] Y. Ochiai, K. Aso, M. Hayakawa, H. Matsuda, K. Hayashi, W. Ishikawa, On specimen preparation by radio frequency planar magnetron sputtering, Journal of Vacuum Science & Technology A: Vacuum, Surfaces and Films, 4(1986), pp. 19-25.

[55] S. Swann, Magnetron sputtering, Physics in technology, 19 (1988) 67.

[56] A. Behera, S. Aich, T. Theivasanthi, Magnetron sputtering for development of nanostructured materials. In Design, Fabrication, and Characterization of Multifunctional Nanomaterials, Elsevier, (2022), pp. 177-199

[57] M. Ohring, A Review of Material Science. In Materials Science of Thin Films: Deposition and Structure, Academic Press, San Diego, USA, (2002).

[58] M. Qadir, Y. Li, C. Wen, Ion-substituted calcium phosphate coatings by physical vapor deposition magnetron sputtering for biomedical applications: A review. ActaBiomaterialia, 89(2019), pp. 14-32.

[59] G. Shanker, P. Prathap, K.M.K. Srivatsa, P. Singh, Effect of balanced and unbalanced magnetron sputtering processes on the properties of SnO_2 thin films, Current Applied Physics, 19(2019), pp. 697-703.

[60] S. Berg, T. Nyberg, Fundamental understanding and modeling of reactive sputtering processes. Thin solid films, 476(2005), pp. 215-230.

[61] K. Koski, J. Hoelsae, P. Juliet, Surface defects and arc generation in reactive magnetron sputtering of aluminum oxide thin films, Surface and Coatings Technology, 115 (1999), pp. 163–171.

[62] P.J. Kelly, R.D.Arnell, Magnetron sputtering: a review of recent developments and applications, Vacuum, 56(2000), pp. 159-172,

[63] M. Scherer, J. Schmitt, R. Latz, M. Schanz, Reactive alternating current magnetron sputtering of dielectric layers. Journal of Vacuum Science & Technology A: Vacuum, Surfaces, and Films, 10(4) (1992), pp. 1772-1776.

[64] S. Schiller, K. Goedicke, J. Reschke, V. Kirchoff, S. Schneider, F. Milde, Pulsed magnetron sputter technology. Surface and Coatings Technology,61 (1993), pp. 331-337

[65] W.D. Sproul, M.E. Graham, M.S. Wong, S. Lopez, D. Li, R.A. Scholl, Reactive direct current magnetron sputtering of aluminum oxide coatings. Journal of Vacuum Science & Technology A: Vacuum, Surfaces, and Films, 13(3)(1995), pp. 1188-1191.

[66] W.D. Sproul, High-rate reactive DC magnetron sputtering of oxide and nitride superlattice coatings, Vacuum, 51 (4) (1998), pp. 641-646.

[67] A.A. Bunaciu, E.G. UdriŞTioiu, H.Y. Aboul-Enein, X-ray diffraction: instrumentation and applications. Critical reviews in analytical chemistry, 45(4) (2015), pp. 289-299.

[68] R.R. Mather, Surface modification of textiles by plasma treatments. In Surface modification of textiles, Woodhead Publishing, (2009), pp. 296-317.

[69] R. Gurwitz, R. Cohen, I. Shalish, Interaction of light with the ZnO surface: Photon induced oxygen "breathing," oxygen vacancies, persistent photoconductivity, and persistent photovoltage, Journal of Applied Physics, 115(3) (2014) 033701.

[70] M.T. Riosbaas, K.J. Loh, G. O'Bryan, B.R. Loyola, In situ phase change characterization of PVDF thin films using Raman spectroscopy, Sensors and Smart Structures Technologies for Civil, Mechanical, and Aerospace Systems, International Society for Optics and Photonics, 9061 (2014) 235-245.

[71] J. ÁlvarezGarcía, V. IzquierdoRoca, P. Pistor, T. Schmid, A. PérezRodríguez, Raman spectroscopy on thin films for solar cells, Advanced Characterization Techniques for Thin Film Solar Cells, 2 (2016) 469-499.

[72] V. Gonzales, A.T. Mobashsher, A. Abbosh, The progress of lucose monitoring—A review of invasive to minimally and non-invasive techniques, devices and sensors. Sensors, 19(4) (2019) 800.

[73] N. NicDaéid, Forensic Sciences, Systematic Drug Identification,Editor(s): P. Worsfold, C. Poole, A. Townshend, M. Miró, Encyclopedia of Analytical Science (Third Edition), Academic Press, (2019), pp. 75-80.

[74] M. S. Braga, O. F. Gomes, R. F. V. Jaimes, E. R. Braga, W. Borysow, W.J. Salcedo, Multispectral colorimetric portable system for detecting metal ions in liquid media. In 2019 4th International Symposium on Instrumentation Systems, Circuits and Transducers (INSCIT), IEEE, (2019), pp. 1-6.

[75] A. Zairi, Elaboration et Caractérisation de revêtements à base de nitrure de chrome par pulvérisation cathodique magnétron en condition réactive: propriétés mécaniques et tribologiques, Doctoral dissertation, PhD, Thesis, Paris ENSAM, (2013).

[76] T. Khare, U. Oak, V. Shriram, S.K. Verma, V. Kumar, Biologically synthesized nanomaterials and their antimicrobial potentials, In Comprehensive Analytical Chemistry Elsevier,87(2019), pp. 263-289.

[77] A.S. Ali, Application of nanomaterials in environmental improvement. Nanotechnology and the Environment (2020).

[78] S. Padhi, A. Behera, Biosynthesis of Silver Nanoparticles: Synthesis, mechanism, and characterization. In Agri-Waste and Microbes for Production of Sustainable Nanomaterials Elsevier, (2022), pp. 397-440

[79] S. Mohanta, Transmission electron microscopy, Indian Association for the Cultivation of Science, (2021).

[80] W. Demtroeder. Lehrbuch der Experimentalphysik 2, Springer LehrbuchVerlag, 4(2010).

[81] A.D. Gianfrancesco, Technologies for chemical analyses, microstructural and inspection investigations. In Materials for ultra-supercritical and advanced ultra-supercritical power plants,Woodhead Publishing, (2017), pp. 197-245.

[82] G. Youssef, Chapter 11 - Characterization of polymers, Applied Mechanics of Polymers, Elsevier, (2022), pp. 273-299,

[83] V. Le Houérou, Rayabilité des verres Silico-Sodo-Calciques Scratchability of Soda-Lime Silica Glasses, Université de Rennes 1, France, (2005).

[84] A.S. Stickley, Image and Imagination of the Life Sciences. N.T.M. 27(2019), pp.109–144

[85] C. Muehlethaler, L. Gueissaz, G. Massonnet, Forensic paint analysis, Encyclopedia of Forensic Sciences (2013), pp. 265-272.

[86] R.Rodriguez-Vera, K. Genovese, J.A. Rayas, F. Mendoza-Santoyo, Calibration of a micro-topographic measurement system based on Talbot fringe projection. In Proc. 2007 SEM Annual Conf. and Exposition on Experimental and Applied Mechanics, 83(2007).

[87] S.S. Ray, 4 - Techniques for characterizing the structure and properties of polymer nanocomposites, In Woodhead Publishing Series in Composites Science and Engineering, Environmentally Friendly Polymer Nanocomposites, Woodhead Publishing, (2013), pp. 74-88.

[88] P. Eaton, P. West, Atomic Force Microscopy, Oxford University Press, (2010).

[89] S.S. Ray, 3 - Structure and Morphology Characterization Techniques, Clay-Containing Polymer Nanocomposites, Elsevier, (2013), pp. 39-66.

[90] B.D. Ratner, D.G. Castner, Surface properties and surface characterization of biomaterials, Biomaterials science, Elsevier (2020), pp. 53-75.

[91] Q. Li, H. Gao, S. Xue, L. Li, Optical profilometer based on the principle of differential interference. Optical engineering, 40(2001), pp. 833-836.

[92] A. Bakhtazad, S. Chowdhury, An evaluation of optical profilometry techniques for CMUT characterization. Microsystem Technologies, 25(9) (2019), pp.3627-3642.

[93] S. Sasmal, M.B. Anoop, Nanoindentation for evaluation of properties of cement hydration products, In Nanotechnology in Eco-efficient Construction, Woodhead Publishing, (2019), pp. 141-161.

[94] H. Wang, L. Zhu, B. Xu, Principle and Methods of Nanoindentation Test. In Residual Stresses and Nanoindentation Testing of Films and Coatings, Springer, Singapore, (2018), pp. 21-36.

[95] X. Sun, L. Li, Y. Guo, H. Zhao, S. Zhang, Y. Yu, D.Wu, H. Liu, M.Yu, D. Shi, Z. Liu, M. Zhou, L. Ren, L. Fu, View AffiliationsView Contributors. Influences of organic component

on mechanical property of cortical bone with different water content by nanoindentation, AIP Advances, 8(3) (2018), 035003.

[96] H. M. Jennings, J.J.Thomas, J. S. Gevrenov, G. Constantinides, F.J. Ulm, Nanostructure of CSH gel in cement paste as a function of curing conditions and relative humidity. Creep, shrinkage and durability of concrete and concrete structures, proceedings of Concreep, 7(2005), pp. 19-37.

[97] E. Broitman, Indentation hardness measurements at macro-, micro-, and nanoscale: a critical overview, Tribology Letters, 65 (2017), pp. 1-18.

[98] W.C. Oliver, G.M. Pharr, An improved technique for determining hardness and elastic modulus using load and displacement sensing indentation experiments. Journal of materials research, 7(6)(1992), pp. 1564-1583.

[99] M. Sarkar, M. Hasanuzzaman, F. Gulshan, A. Rashid, Surface, mechanical and shape memory properties of biodegradable polymers and their applications,Encyclopedia of Materials: Plastics and Polymers, 2(2022), pp. 1092-1099.

[100] C. G. Jothi Prakash, R. Prasanth, Approaches to design a surface with tunable wettability: a review on surface properties, Journal of Materials Science, 56(1)(2021), pp. 108-135.

[101] T. Young, III. An essay on the cohesion of fluids. Philosophical transactions of the royal society of London, (95)(1805), pp. 65-87.

[102] G.W. Stachowiak, A.W. Batchelor, G.B. Stachowiak, 3 - Tribometers, Tribology Series, Elsevier, 44(2004), pp. 25-78.

[103] M. Valdes, J. Gonzalo, A. Marín, M. Rodriguez, J. Betancur, Tribometry: How is friction research quantified? A review. International Journal of Engineering Research and Technology, 13(2020), pp. 2596-2610.

[104] K.R. Trethewey, Corrosion for science and engineering, Longman, (1996).

[105] R.A. Buchanan, E.E. Stansbury, 4 - Electrochemical Corrosion, Handbook of Environmental Degradation of Materials (Second Edition), William Andrew Publishing, (2012), pp. 87-125

[106] J. Soltis, Passivity breakdown, pit initiation and propagation of pits in metallic materials - Review, Corrosion Science, 90 (2015), pp. 5–22.

[107] S. Grosso, Revêtements architecturés de Ti, TiN et TiO élaborés par pulvérisation cathodique au défilé sur des fils en acier inoxydable : Relation entre la composition chimique, la microstructure et les propriétés d'usage, Energie électrique, PhD Thesis, GrenobleAlpes Université, (2017).

Chapter III

Preparation and characterization of cold sprayed 316L stainless steel

Introduction

This chapter is dedicated firstly to identify the optimal parameters of cold spray process in order to elaborate a good 316L stainless steel coating. The effect of both helium and nitrogen gases used was investigated. The temperature, powder particles sizes, and distance from the nozzle throat to the impinging point were estimated by using the Kinetics Spray Solutions GmbH software.

After that, we deposited the 316L stainless steel coating using N_2 and He gases. The 316L stainless steel (SS) coatings were examined by X-ray diffraction, Scanning Electron Microscopy and Energy Dispersive X-Ray Microanalysis. The tribological behavior was evaluated under different loads (2 N and 5 N) in dry conditions. We also investigated the electrochemical corrosion performance in a 3.5 wt.% NaCl solution.

The results presented in this chapter were published as a research paper entitled "***Effect of He and N_2 gas on the mechanical and tribological assessment of SS316L coating deposited by cold spraying process***" in the Journal of Materials Science, 57(8) (2022), 5258-5274.https://doi.org/10.1007/s10853-022-06950-1.

III. 1 Numerical simulation and deposition conditions

- As a first approach in this part of study, one-dimensional model was performed for such a set of given gas velocities and temperatures, particle size and the distance between nozzle and substrate by using the Kinetics Spray Solutions GmbH software.
- 316L stainless steel coatings were deposited on aluminum substrates using cold spray technique (CS). A commercially powder of 316L H.C. Starck 0717-074 was used. 316L stainless steel coatings were obtained by spraying of spherical particles (Ø 15-35 µm diameter) in a helium and nitrogen atmosphere. *Fig. III.1* shows a scanning electron microscope (SEM) image of these particles. *Table. III.1* summarizes the chemical composition of these powders. The helium and nitrogen pressures were 21.8 and 30 bar corresponding to gas flow rates of 2200 and 100 m/s, respectively. These both conventional configurations were fixed by the industrial experience that led to get a dense structure. Prior to coating deposition, the surface of the aluminum substrate was grit blasted with alumina using compressed air, cleaned by acetone and ethanol (5 min for each one) and dried in air.

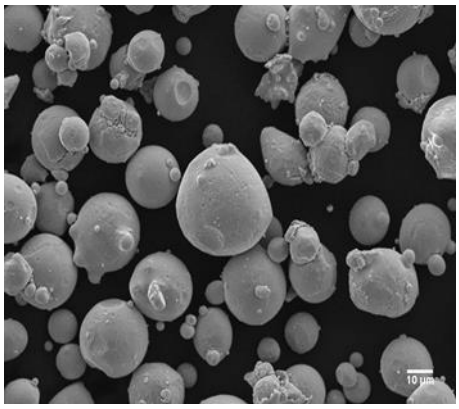

Fig. III. 1. Spraying powder free surface observed by a scanning electron microscopy.

Table III. 1. Chemical composition of 316L powders.

Elements wt.%	Cr	Ni	Mo	C	Mn	N	O	P	S	Si	Fe
Min	16.5	10.0	2.0								balance
Max	18.5	14.0	3.0	0.03	2.0	0.03	0.05	0.045	0.015	1.0	

The details of processing parameters used in this study are shown in *Table III. 2*.

Table III. 2. Spray conditions of SS 316L deposition.

	N_2	He
Powder mass flow rate (g/min)	40	75
Scanning speed (mm/s)	300	200
Standoff distance (mm)	25	25
Main gas pressure (bar)	30	21.8
Main gas temperature ° C	650	480
Injector- throat distance (mm)	-50	-18
scanning step (mm)	2	1

III. 2 Cold spray modeling by KSS software (Kinetics Spray Solutions GmbH)

The numerical simulation of the cold spray was performed to investigate the usefulness of the combination of the following parameters on the spraying speed: temperature, particle size of spraying powder and distance from the nozzle throat to the impinging point. The N_2 and He were used as process gases. The results are summarized as follows:

III. 2.1 For nitrogen (N_2) gas

The most important parameter in cold spraying is the particle velocity prior to impact. It is known that the sprayed particles in CS have to be accelerated to a sufficiently high velocity in order to be successfully deposited on the substrate. Generally, there is a critical velocity for a successful particle deposition with a given sprayed material. Only the particles moving at a velocity higher than the critical one can be deposited to produce a coating [1, 2].

Table III.3 and *Fig. III.2* present the modeling results obtained with KSS software using nitrogen. Three particle sizes were considered: 15, 28 and 35 µm. The velocity decreases with the increase of the particle diameter. The finest particles are more heated at the throat, but they are cooled faster in the diverging part of the nozzle [3] (*Fig. III.3*). The η factor is the ratio between the particle velocity and the critical velocity depending on the temperature and diameter of the stainless steel particles. This factor is a little more important for the biggest particles due to its highest temperature.

Table III.3. Spray modeling results using N_2.

Average particle size (µm)	15	28	35
V (m/s)	661	598	569
T °C	253	366	375
η	1.03	1.04	1.06

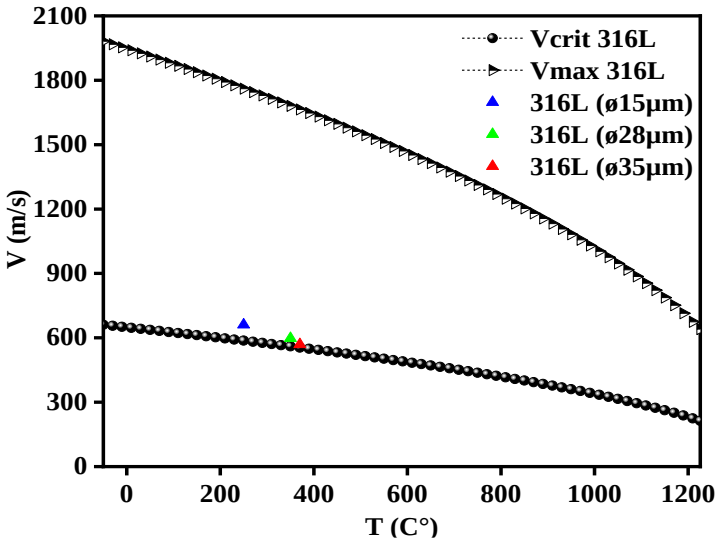

Fig. III. 2. Spraying speed of SS 316L powder as a function of temperature using N_2.

The temperature and velocity of particles are given along the entire length of the nozzle until the standoff distance (25 mm) (*Fig. III. 3*). The maximum temperature is reached at the throat and the maximum velocity at the impinging point [4], with a 650 °C nitrogen temperature.

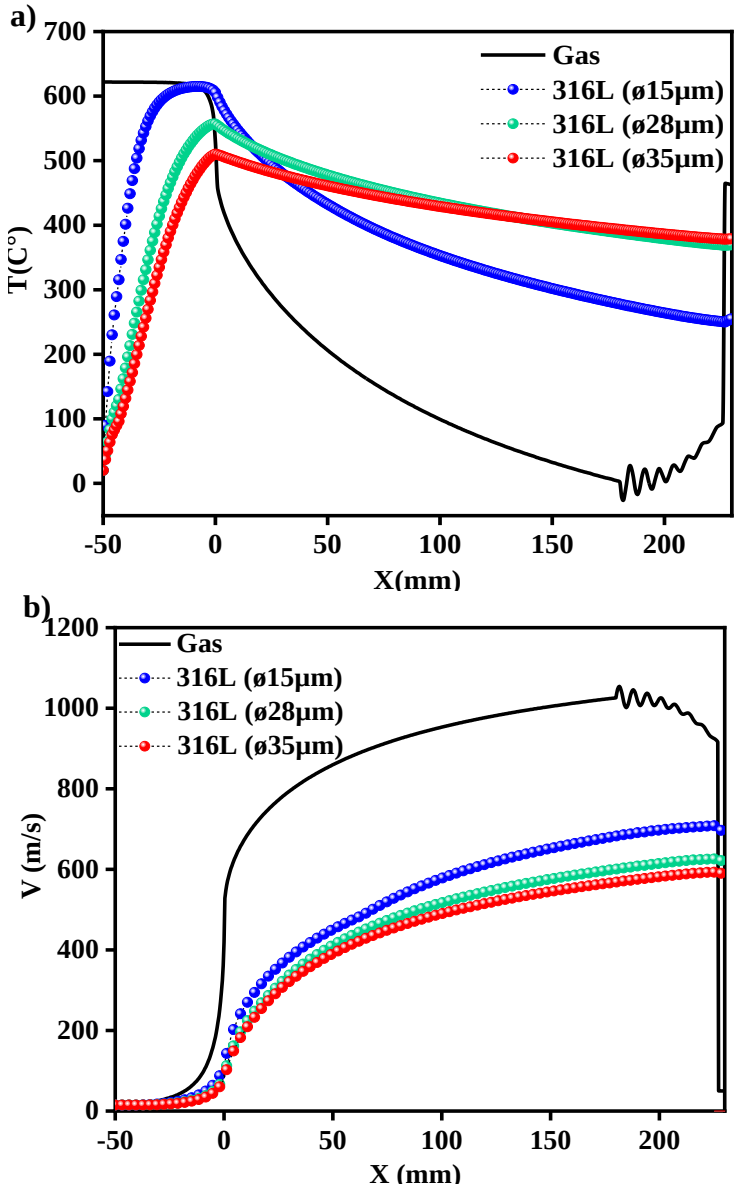

Fig. III. 3. Numerical modeling of SS 316L powder spraying using N_2 gas: temperature (**a**) and velocity (**b**) as a function of distance (0 mm at the nozzle throat).

III. 2.2 For helium (He) gas

Table III.4 and *Fig. III. 4* present the modeling results obtained with KSS software using Helium. The velocity decreases with the increase of particle diameter from 15 to 35 µm. *Katanoda et al*. [4] found that the particle velocity before the normal shock increases with decreasing the particle diameter using N_2 or He as a process gas. The powder particle size has also been confirmed to be an important factor influencing the particle acceleration [5-7]. *Li et al.* [2] confirmed that the particle size significantly influences the particle velocity. With the decrease in particle diameter, the particle velocity increases rapidly, especially when the particle diameter is less than ~20 µm and it was more important using He as a propellant gas. This can be simply explained using *Alkhimov* equations given below [8-9].

$$Vp = Vg / (1 + 0.85\ Vg\ (D\ \rho_p / X\ P_o)^{1/2}) \qquad (III.\ 1)$$

$$Vg = M\sqrt{\gamma R T_g} \qquad (III.\ 2)$$

Where Vp and Vg represent the particle and gas velocities, respectively, D is the particle diameter, $\rho_p$is the particle density, X is the length of diverging section, P_0 is the stagnation inlet pressure, γ is the specific heat ratio for N_2 and He, 1.4 and 1.667 respectively, M is the exit Mach number, R is the specific gas constant for N_2 and He, (0.2968 and 2.0769)kJ/kg. K respectively, Tg is the exit gas temperature.

According to *Eq. III. 2*, the gas velocity of helium will be much higher than that of nitrogen under the same conditions. Therefore, in *Eq. III. 1* the particles will be accelerated to a higher velocity when using He. On the other hand, the gas velocity will be increased as well as the particle velocity with the increase in gas temperature [2]. The comparison between the particle temperatures and velocities using nitrogen and helium shows that the η factor is more important with helium. However, the particle temperature is lower in the case of the He gas compared to its value with nitrogen.

Table III. 4. Spray modeling results using He gas.

Average particle size (µm)	15	28	35
V (m/s)	951	740	673
T °C	22	131	172
η	1.35	1.20	1.15

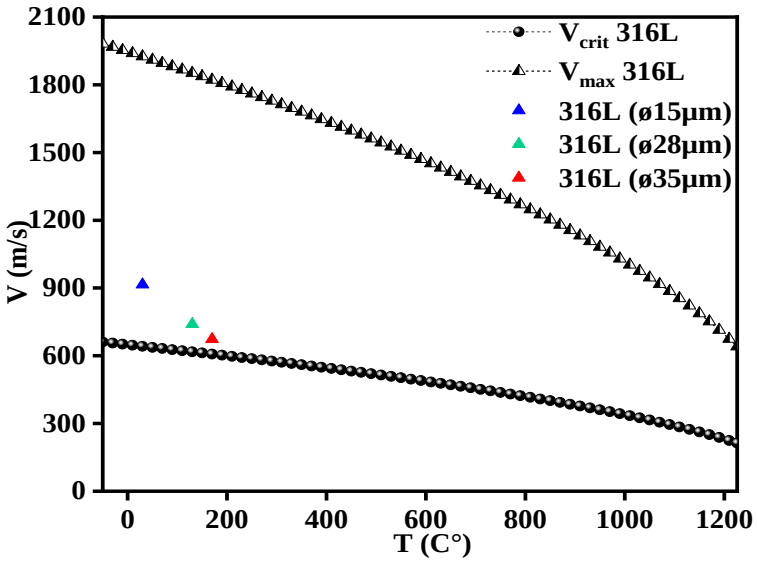

Fig. III. 4. Spraying speed of SS 316L powder as a function of temperature using He.

The velocity of helium gas is 2200 m/s which is more than twice than that of the nitrogen gas (1000 m/s) (*Figs. III. 3 and 5*). From *Fig. III. 5*, it is obvious that the temperature rapidly decreased with helium in the diverging nozzle part compared to the nitrogen gas. The cold work hardening is enhanced. Based on the simulation results for the diffrent cold spray parametres, we identified the main ideal ones to be used in the expermimental invesitigation. Afterwards the morphologies, tribomechanical behaviors and electrochedmical performance of the steel coatings elaborated under nitrogen and helium were compared.

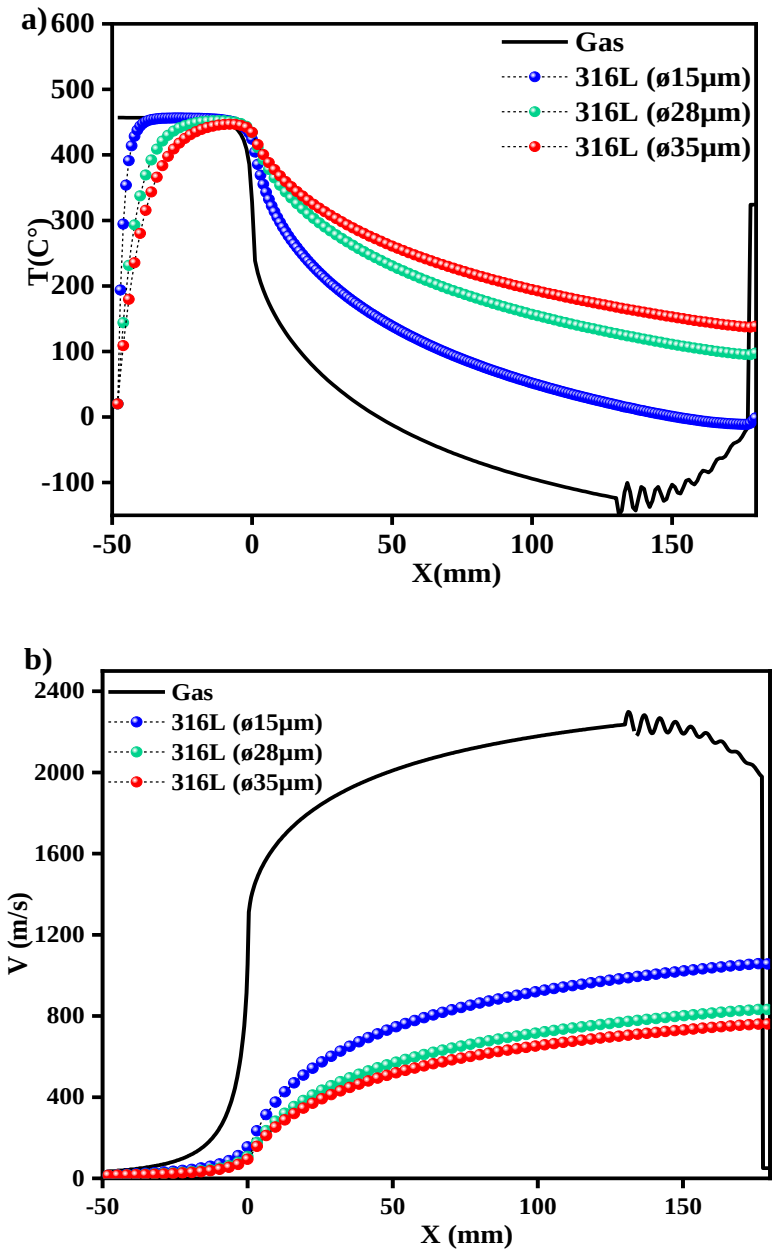

Fig. III.5. Numerical modeling of SS 316L spraying powder using He gas: temperature (**a**) and velocity (**b**) as a function of distance (0 mm at the nozzle throat).

III. 3 Structural and morphological characterization

Fig. III. 6 shows XRD patterns of cold-sprayed stainless steel coatings, using nitrogen and helium as propellant gases, deposited on Al substrates. It can be seen that only the austenite phase (γ) was detected presenting a fcc structure.

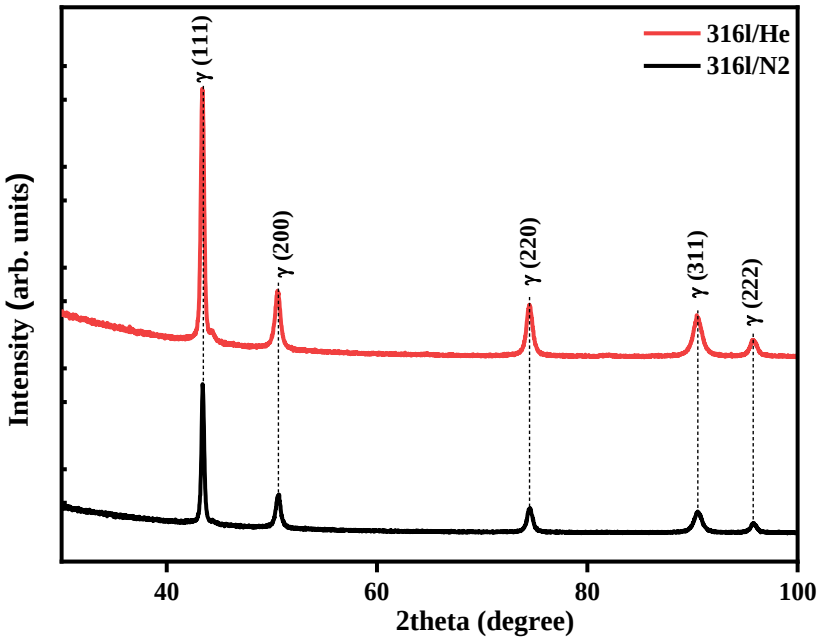

Fig. III. 6. XRD patterns of 316L coatings cold-sprayed with He and N_2 gases.

The influence of nitrogen and helium propellant gases on the surface topography and microstructure of cold-sprayed 316L coatings was investigated by using SEM images (*Figs. III.7 and 8*).

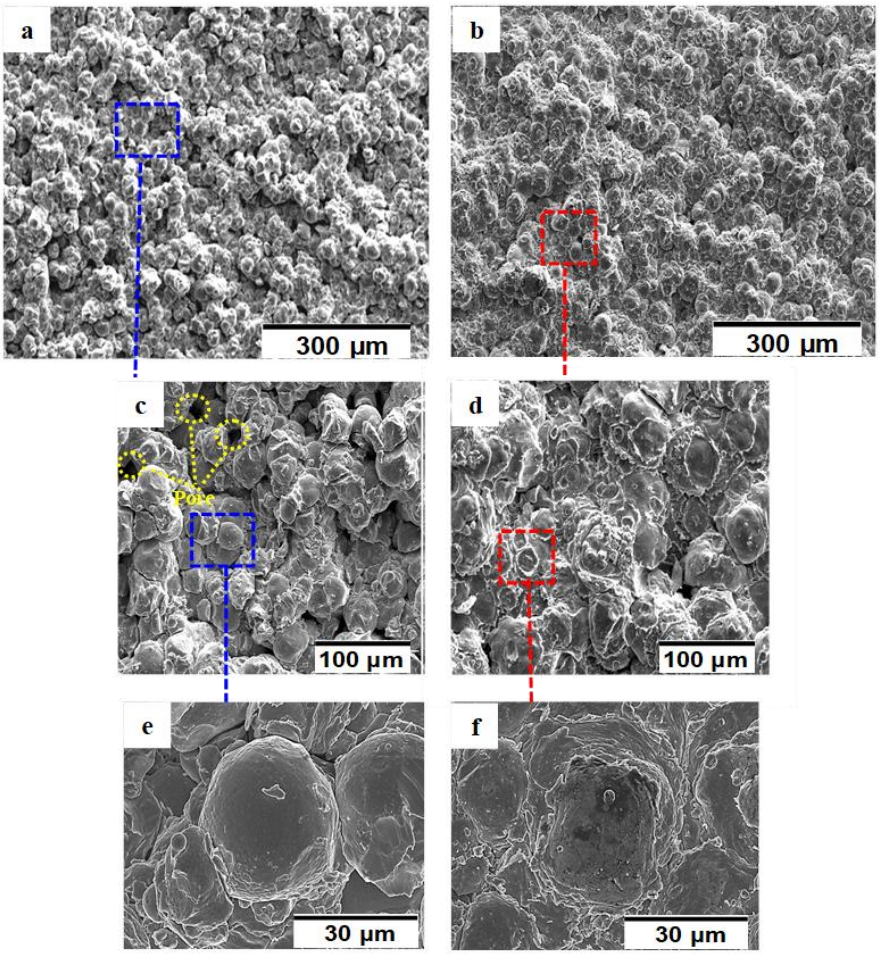

Fig. III. 7. SEM images of SS 316L coatings cold-sprayed with N_2 (a, c, e) and He (b, d, f).

The chemical compositions of coatings were measured by EDX (*Fig. III. 8*). Dense and thick (2 mm) 316L coatings had a similar chemical composition with small content of oxygen (3 and 1.9 at.%) using N_2 and He respectively. This indicates that no significant chemical interactions and no phase transformation occurred during spraying attributed to the low-temperature characterizing the CS process [10]. In addition, the evaluation of interface revealed that steel particles penetrated into the soft aluminum substrate resulted a strong coating bonding. Similar observation was obtained by *Sova et al.* [11] for the SS316L coating obtained by the same process performed on 1.5 mm thick non-sandblasted aluminum sheets with dimensions of 50 × 80 mm. However, it can be seen that the 316L coating deposited with He was denser with a lower oxygen content and homogeneous smooth surface confirmed by a lower roughness (Ra = 14.9µm) as compared to that deposited with N_2 (Ra = 15.8 µm) (*Fig. III. 8*) [12]. On the other hand, the porosity measurements confirm that the 316L coating sprayed with He exhibited a lower value (0.5 ± 0.01%) as compared to that sprayed with N_2 (1.06 ± 0.03 %), which is due to the higher particle impact velocity of He associated with a great plastic deformation resulting

a denser coating. Similar results were obtained by *Mangour et al.* [13]. The higher porosity of the 316L coating sprayed with N_2 is due to the incomplete bonding of particle-particle because of the nitrogen which is a reactive gas and has a weak effect to accelerate the deposition of 316L stainless steel powders and film formation as compared to helium.

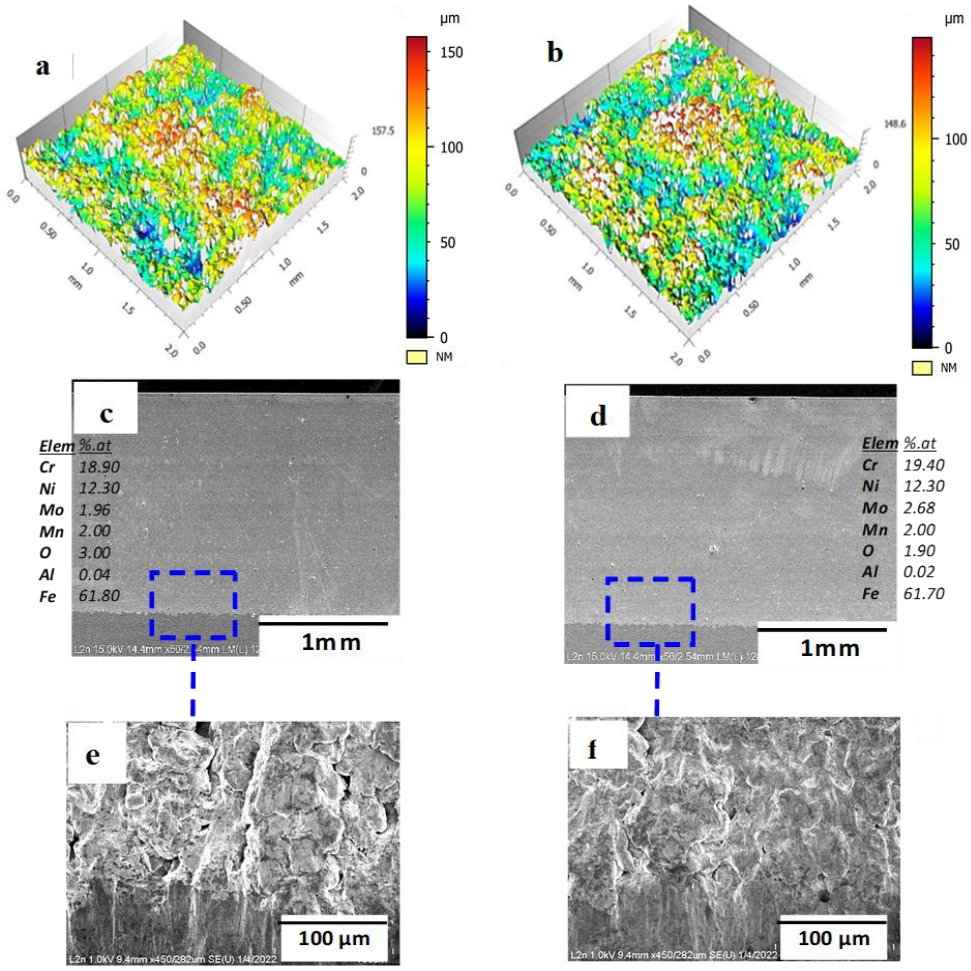

Fig. III. 8. Surface topography, SEM and optical microscopy images of cross-sectional SS 316L coatings cold-sprayed with N_2 (a, c, e) and He (b, d, f).

For determining the coating microstructure and properties, it is obvious that the particle morphology is an important parameter in the CS process that directly affects its velocity [14]. Generally, a higher particle velocity leads to obtain a denser coating and strong adhesion without porosity [12, 15]. *Borchers et al.* [16] evaluated the impact of particle velocity and temperature on the quality and performance of 316L coatings deposited with the following parameters: 850 m/s and -20 °C with helium and 600 m/s and 300 °C with nitrogen. *Codd et al.* [17] used MOC type 24 nozzle geometry at 550 °C inlet gas temperature, a 28 bar nozzle pressure and a 30 µm particle size. They reported that the impact velocity of cold sprayed

particles performed with He gas was found 847 m/s higher than that of the particles sprayed with N_2 (535 m/s) absolutely evident and due to the difference in the molecular weight of process gases (4 for He and 28 for N_2). *Fig. III.7c* shows the presence of many inter-splat voids (pores) and some cracks in the SS 316L-CS deposited with N_2. In contrast, using He gas led to obtain a good coating where the shape of SS316L-CS particles was significantly changed from spherical to slightly elongate (*Fig. III. 7f*). This evolution is due to the large plastic deformation resulting from the high particle velocity [16].

III. 4 Mechanical properties

Fig. III. 9 shows the evolutions of hardness (H) and elasticity modulus (E) of the SS 316L coatings deposited with He and N_2 propellant gases.

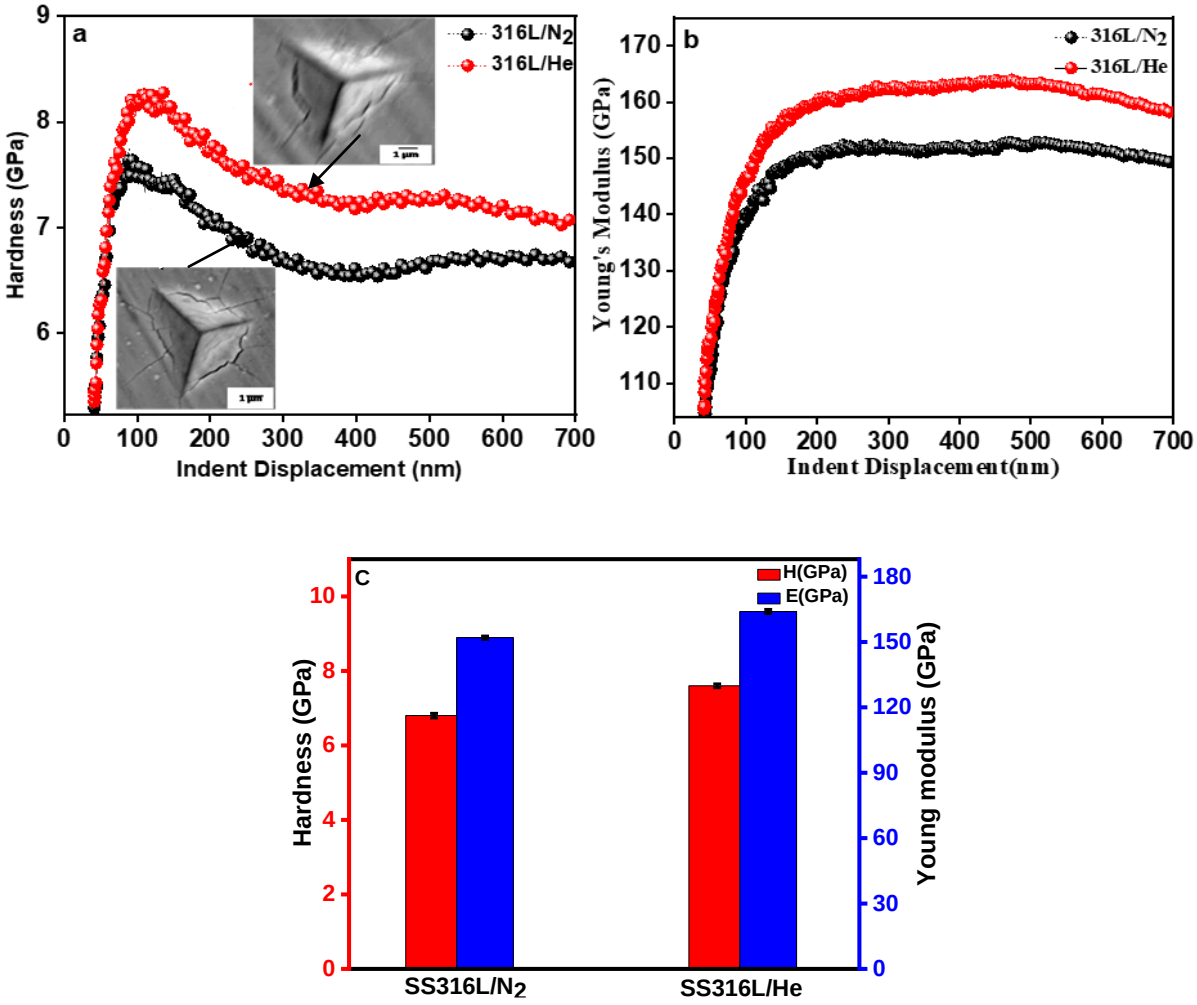

Fig. III. 9. Hardness (a, c) and Young's modulus (b, c) of SS 316L coatings cold-sprayed with He and N_2.

According to *Maestracci et al.* [18] the coating hardness was measured through its cross-section under 50 mN normal load. *Fig. III. 9* shows the dependence of the hardness and elastic modulus of 316L coatings obtained by nanoindentation. Hardness and elastic modulus of 316L coatings follow the same trend, which is consistent with the literature [19-22].

It is evident that there are significant changes in hardness and Young's modulus between the first 150 nm of indenter penetration (primary loading) and the stable following part of curves. Such behavior likely reflects the surface effects, such as surface roughness and surface oxides, on the mechanical behavior of materials. This makes it difficult to accurately measure and estimate the contact area [23-24]. From *Fig. III. 9* (stable part), the average H and E values for both steels cold sprayed with helium and nitrogen were (7.5 ± 0.5) and (6.8 ± 0.5) GPa, and (164 ± 10) and (152 ± 10) GPa, respectively, which is higher than that of aluminum (2017 A) substrate (E = 72.5 GPa, H = 1.12 GPa). It can be clearly seen that the deposition with He led to enhance the mechanical properties of SS 316L coatings. In both cases, coating hardness was twice the powder one (3 GPa), which is attributed to the finer microstructure obtained during the cold spray process with a strong work hardening effect. Due to the work hardening in the coating deposited with He, SS 316L had higher hardness and elasticity modulus. This is related to the strain hardening effect during the deposition process with a higher particle velocity using helium as reported by *Mangour et al.*[13]. Meanwhile, the decrease in the porosity could be associated to the absence of a significant number of defects produced during the film growth and to the decrease of the surface roughness [25].

III. 5 Tribological properties

After sample polishing, friction tests were carried out at room temperature in dry conditions under 2 and 5 N applied loads. *Fig. III. 10* shows the friction coefficients and wear rates of different samples. The wear rates of these coatings were calculated and the effect of He and N_2 propellant gases on the coating tribological behavior was evaluated. We notice that the friction coefficient rapidly increased and reached a maximum value (~ 0.83) in the initial sliding stage (***zone I***) then it stabilized after 10 m of sliding distance (***zone II***) at about (0.65 - 0.70) for 316L sprayed with He and (0.69 - 0.73) for 316L sprayed with N_2 under 2N and 5N normal loads, respectively. However, the SS 316L coating presents a relatively high friction coefficient, which could be related to the local softening of the sample with a severe abrasion of the ball during the friction test [25,26].

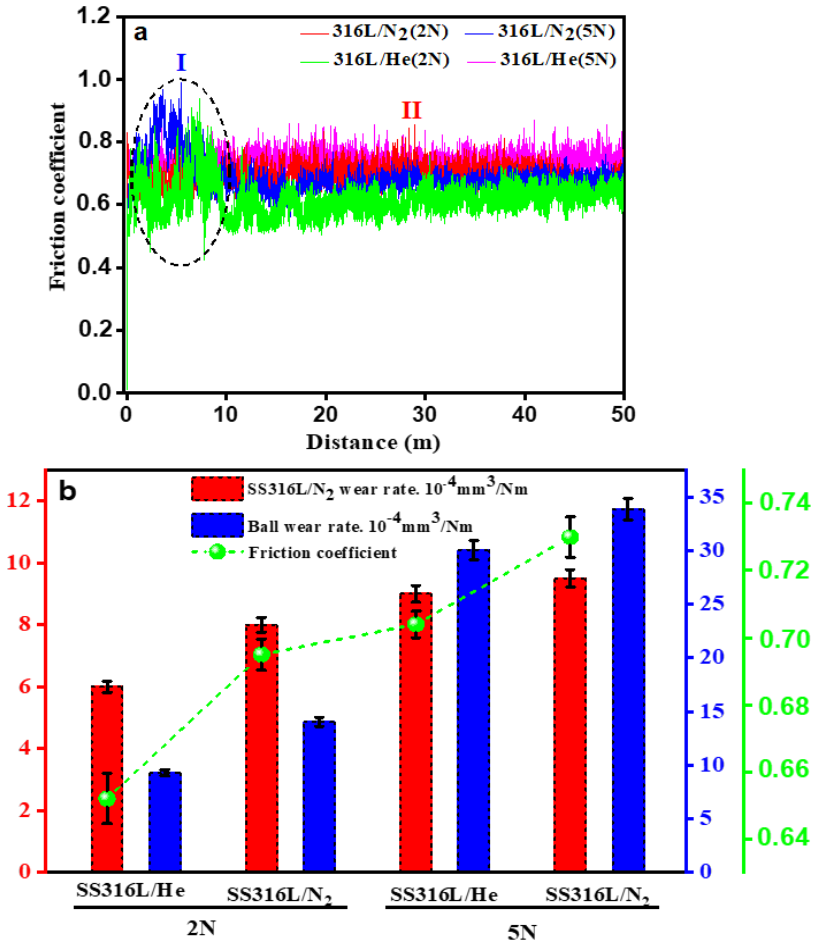

Fig. III. 10. Friction coefficients (a) and wear rates of SS 316L coatings and balls (b) tested under different normal loads (2 and 5 N).

The effect of the applied load on the wear rates of the SS 316L coatings and balls is shown in *Fig. III. 10 b*. The wear rates of coatings and balls increased with increasing the applied load from 2 to 5 N in both configurations. At a higher applied load (5N), the penetration depth in the 100C6 ball increased and reached 22.5 and 15 µm for coatings sprayed with nitrogen and helium, respectively (*Fig. III.11*). At the same time, due to the Fe transfer between the contact surfaces, a greater degree of surface softening led to the smoothening of the contact surfaces and the formation of grooves and severe patches [26]. The increase in wear rate consequently led to raise the coating friction coefficient, but it is comparatively lower for the SS 316L coating sprayed using helium, for the two loads, due to the improvement of surface hardness [27-29].

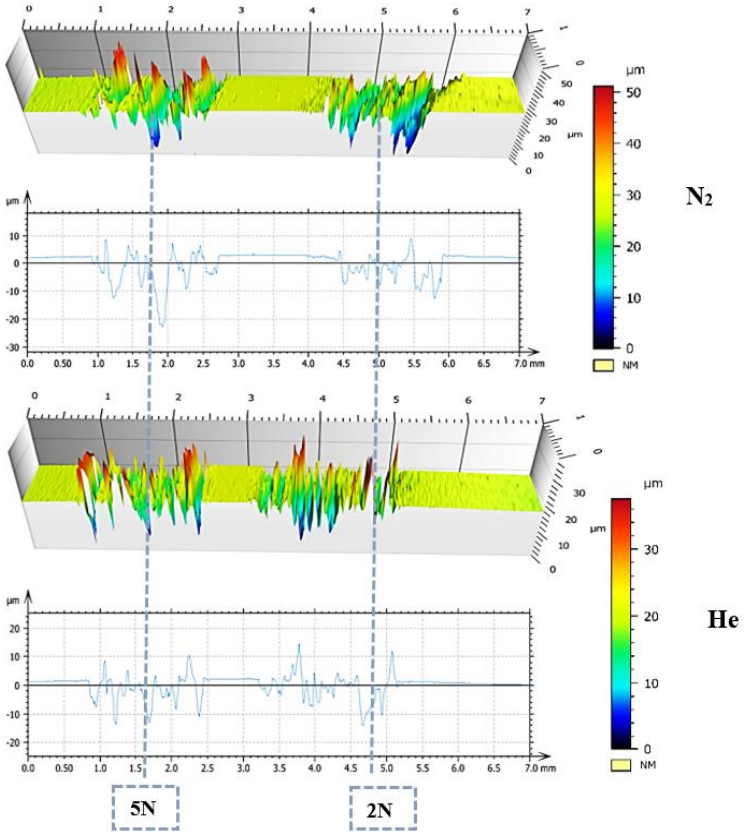

Fig. III. 11. 3D images and profiles of the wear tracks shown on the SS 316L cold-sprayed with N_2 and He tested under 2 and 5 N.

The tribological behavior and elements transferred during the friction tests were also investigated by a SEM and EDX. *Figs. III. 12* and *13* illustrate the different elements of wear tracks produced under 2 and 5 N applied loads. The wear tracks on the SS 316L coatings exhibit somehow a mixing of wear debris and plastically deformed with the appearance of many types of surface defects like micro pits, delamination, chunks and debris particles because of high contact stress formation especially at 5 N. Furthermore, the existence of oxygen resulted in increasing surface oxidation rate and formation of iron oxides [30-31].

The main reasons for the delamination are the propagation of micro-cracks in the coatings during the wear test [32]. It can be seen that there are observable furrows on the worn surface, indicating that abrasive wear occurring in the deep groove area [33]. This is more apparent on the coating surface tested at 5 N and found to be less smooth as compared to that tested at 2 N for the both coatings using helium and nitrogen. Furthermore, the 100C6 ball contact areas were increased with increasing the applied loads during the wear test which is caused by increasing

the temperature between the counter ball and the SS 316L coatings [34]. These worn zones presented higher contact diameters *Fig. III. 12 (e, f)*and *Fig. III. 13 (e, f)*).

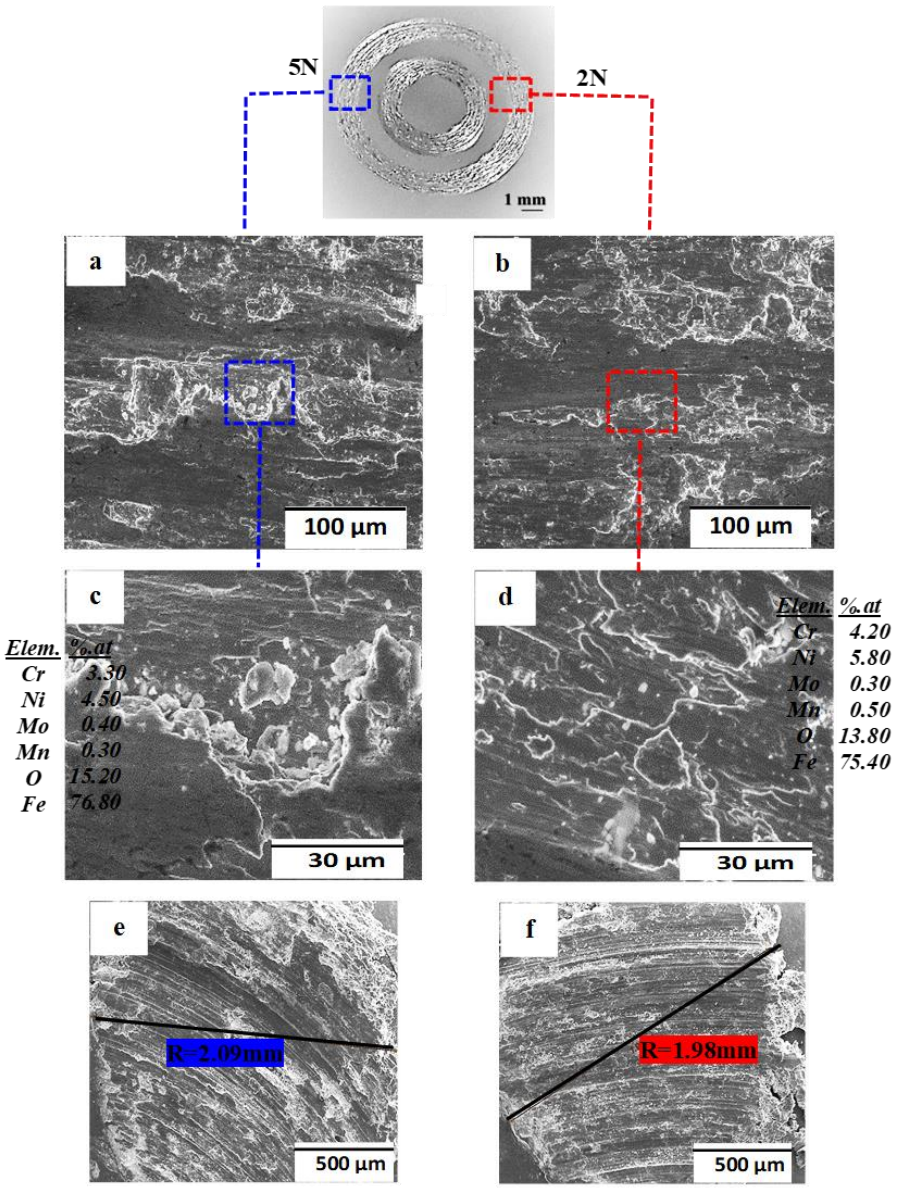

Fig. III. 12. EDX elemental compositions and SEM images of wear tracks on SS 316L cold-sprayed using N_2 (a, b, c and d) and worn size on 100C6 ball (e, f) after 50 m sliding distance (friction tests).

In friction tests conducted in dry conditions, a particular attention should be paid to the tribo-chemical reactivity. In order to investigate the delamination causes, EDX elemental analysis was performed on the worn surfaces (*Figs. III. 12(c, d)* and *Fig. III. 13(c, d)*). The results showed the presence of oxygen rich in those areas. This indicates that oxide on the 316L stainless steel coating surface is the main cause of delamination and grinding. According to

Kato et al. [35], the elemental analysis showed that crack propagation was due to the formation of Fe_2O_3 in the coating which is a brittle phase that accelerates the material wear.

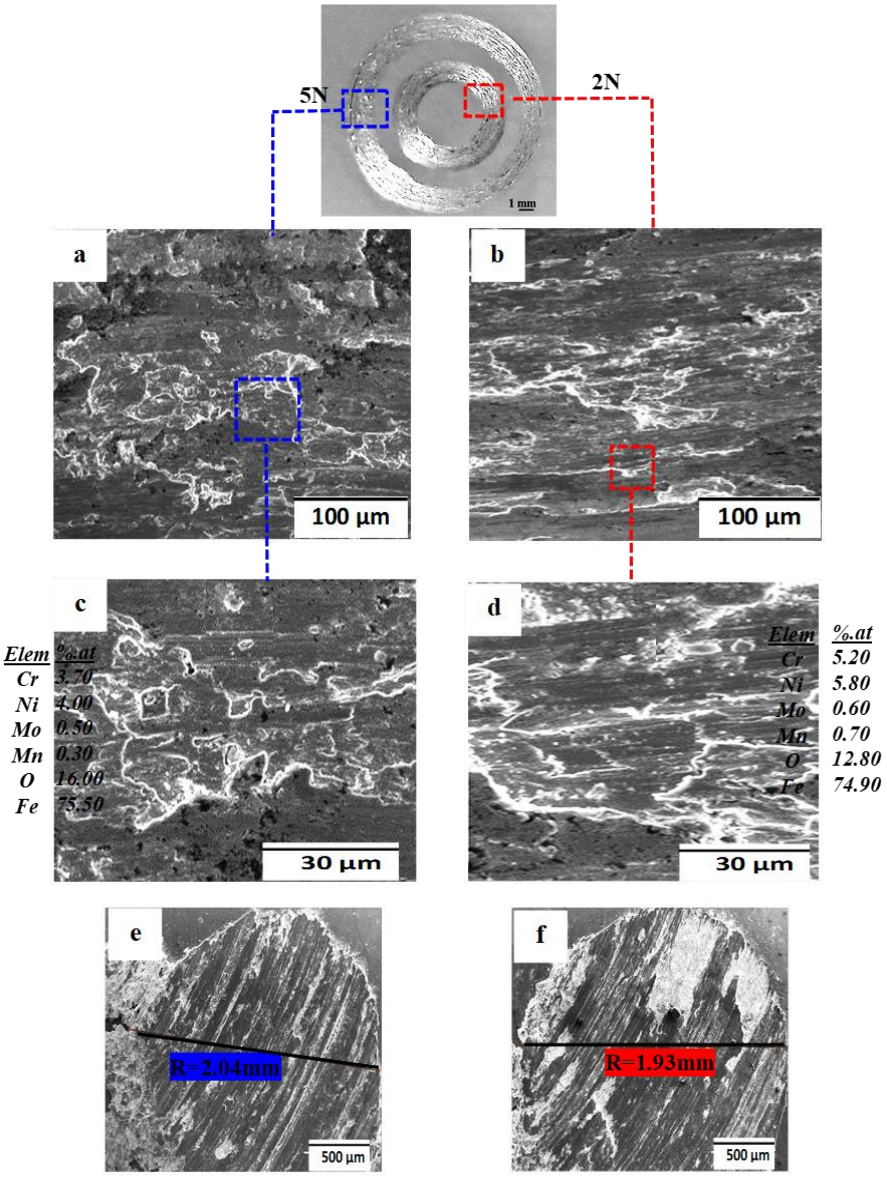

Fig. III. 13. EDX elemental compositions and SEM images of wear tracks on SS 316L cold-sprayed using He (a, b, c and d) and worn size on 100C6 ball (e, f) after 50 m sliding distance (friction tests).

III. 6 Corrosion resistance and electrochemical analysis

Open circuit potentials (OCP) of 316L stainless steel cold-sprayed with helium and nitrogen were registered for 60 min during the immersion of samples in a simulated sea water of 3.5 wt. % NaCl. The OCP curves are shown in *Fig. III. 14*.

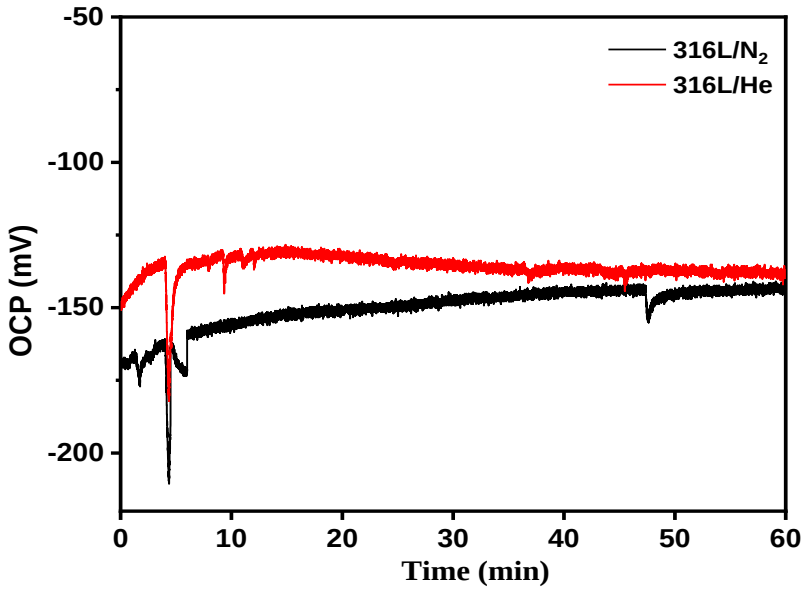

Fig. III. 14. Open circuit potential (OCP) of SS316L cold sprayed with He and N_2.

As shown in *Fig. III. 14*, the OCP values increased rapidly in the first 15 min then stabilized to a higher value. The Open circuit potential of the SS316L cold sprayed with nitrogen was -144 mV which increased to -137 mV for SS cold sprayed with helium.

The results of corrosion tests are shown in *Fig. III. 15*. The cold-sprayed 316L/N_2 stainless steel has the least noble potential (-170 mV) and the highest corrosion current density (1.20 µA.cm^{-2}). The corrosion potential and current density of SS316L sprayed with He improved to reach better values of (-157 mV and 0.74 µA.cm^{-2}, respectively), and better polarization resistance from (15.67 to 21.66) KΩ.cm^2. The polarization curves indicate that passive transition region was observed for the two tested samples, indicating that both SS316L cold sprayed samples spontaneously passivated in 3.5 wt.% NaCl solution. In general, a passive film on an austenitic stainless steel has been investigated largely and described as a film composed of distinct bilayers. The inner layer is enriched in chromium oxide while the outer layer is a mixture of iron oxide and a hydroxide film [36-37]. When the applied potential reached Epit value, a sharp increase in the current density occurred as shown in *Fig. III. 15*, indicating the initiation and growth of pitting corrosion [38].

Fig. III. 15 shows that the Epit = 413 mV for SS316L/He corresponding to a largest passivation region ΔE (393 mV) compared to (Epit = 146 mV, ΔE = 195 mV) for SS316L/N_2.This can be explained by the low oxidation, the dense surface with lowest

porosity and roughness which con contribute to the optimization of the good corrosion resistance [39].

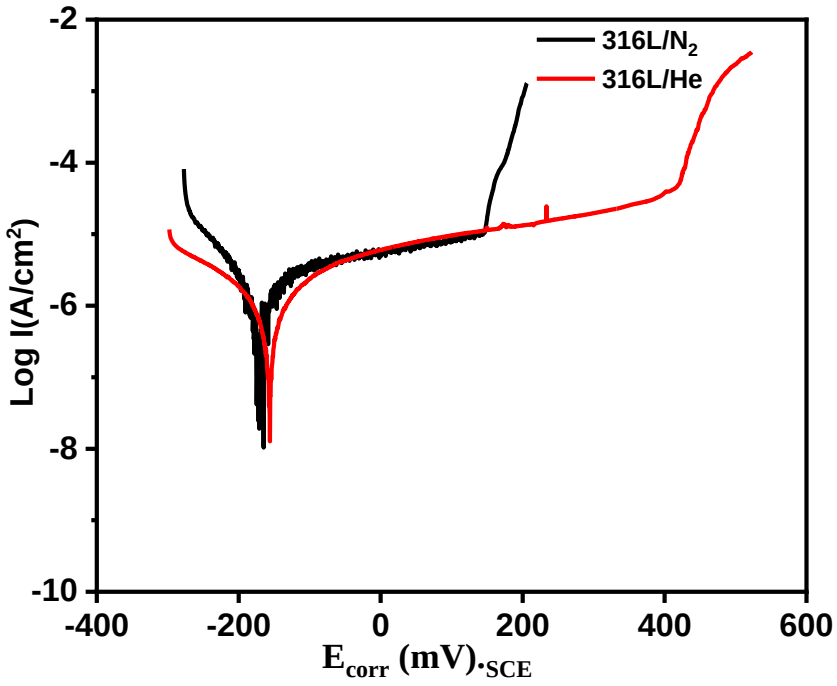

Fig. III. 15. Polarization curves of SS316L cold sprayed with He and N_2(immersion tests in a 3.5 wt % NaCl solution for 60 min).

Conclusion

In this chapter, we presented the 316L austenitic stainless steel coatings deposited on aluminum substrates by Cold Spray process under He and N_2 gases. Cold spray process parameters were simulated and many experiments were carried out to evaluate the effect of process parameters on the tribo-mechanical behavior and electrochemical corrosion performance of the cold-sprayed 316L coating.

- The One-dimensional model showed that the increase of carrier gas temperature with a fine size particle led to a larger particle velocity.
- The 316L coating cold-sprayed under He with high particle velocity presented a dense and smooth coating, leading to enhanced hardness and goodtribological performance.
- Nanoindentation showed that cold-sprayed 316L coating using He had the highest hardness and Young's modulus of (7.5 ± 0.5) and (164 ± 10) GPa compared to that of N_2 (6.8 ± 0.5) and (152 ± 10) GPa, respectively, and both were higher than aluminum substrate (H = 1.12 GPa, E = 72.5 GPa).
- The increase in wear rate consequently led to rise the coating friction coefficient, but it is comparatively lower for the SS 316L coating sprayed using helium, tested under the two loads (2 and 5N), due to the improvement of surface hardness
- The corrosion resistance of 316L stainless steel in sea water was ameliorated by using helium as a propellant gas during the cold spray process.

References

[1] A. Papyrin, Cold Spray Technology, Advanced Materials Processes,159 (2001), pp 49-51.

[2] W.Y. Li, C.J. Li, Optimal Design of a Novel Cold Spray Gun Nozzle at a Limited Space, Journal of Thermal Spray Technology, 14(3) (2005), pp. 391-396.

[3] P. Liebersbach, A. Foelsche1, V.K. Champagne, M. Siopis, A. Nardi, D.P. Schmidt, CFD Simulations of Feeder Tube Pressure Oscillations and Prediction of Clogging in Cold Spray Nozzles, Journal of thermal spray technology, 29(2020), pp. 400–412.

[4] H. Katanoda, M. Fukuhara, N. Iino, Numerical Study of Combination Parameters for Particle Impact Velocity and Temperature in Cold Spray, Journal of Thermal Spray Technology, 16(5-6) (2007), pp. 627-633.

[5] T. Stoltenhoff, H. Kreye, H.J. Richter, An Analysis of the Cold Spray Process and Its Coatings, Journal of thermal spray technology, 11 (2002), pp. 542-550.

[6] D.L. Gilmore, R.C. Dykhuizen, R.A. Neiser, T.J. Roemer, M.F. Smith, Particle Velocity and Deposition Efficiency in the Cold Spray Process, Journal of thermal spray technology, 8(1999,) pp. 576-582.

[7] B. Jodoin, Cold Spray Nozzle Mach Number Limitation, Journal of thermal spray technology,1(2002), pp. 496-507.

[8] L. Venkatesh, Naveen M. Chavan, G. Sundararajan, The Influence of Powder Particle Velocity and Microstructure on the Properties of Cold Sprayed Copper Coatings, Journal of Thermal Spray Technology, 20(5) (2011), pp. 1009-1021

[9] A.P. Alkhimov, V.F. Kosarev, S.V. Klinkov, The Features of Cold Spray Nozzle Design, Journal of thermal spray technology, 10(2) (2001), pp. 375-381.

[10] J. Chen, B. Ma, G. Liu, H. Song, J. Wu, L. Cui, Z. Zheng, Wear and Corrosion Properties of 316L-SiC Composite Coating Deposited by Cold Spray on Magnesium Alloy, Journal of thermal spray technology, 26 (2017), pp. 1381-1392.

[11] A. Sova, S. Grigoriev, A. Okunkova, I. Smurov, Cold spray deposition of 316L stainless steel coatings on aluminium surface with following laser post-treatment, Surface and Coatings Technology 235 (2013), pp. 283-289.

[12] M. Amiri, G.A. Crawford, J.C. Earthman, Quantitative percussion diagnostics for evaluating porosity and surface roughness of cold sprayed and laser deposited materials, Journal of materials research and technology, 14(2021), pp. 312-323.

[13] B. AL. Mangour, P. Vo, R. Mongrain, E. Irissou, S. Yue, Effect of Heat Treatment on the Microstructure and Mechanical Properties of Stainless Steel 316L Coatings Produced by Cold

Spray for Biomedical Applications, Journal of thermal spray technology,23 (2014), pp. 641-652.

[14] V.K. Champagne, The Cold Spray Materials Deposition Process: Fundamentals and Applications, Wood head Publishing Ltd., England, (2007).

[15] L. Venkatesh, N.M. Chavan, G. Sundararajan, The Influence of Powder Particle Velocity and Microstructure on the Properties of Cold Sprayed Copper Coatings, Journal of thermal spray technology, 20(5) (2011), pp. 1009-1021.

[16] C. Borchers, T. Schmidt, F. Gärtner, H. Kreye, High strain rate deformation microstructures of stainless steel 316L by cold spraying and explosive powder compaction, Applied Physics A, 90 (2008), pp. 517-526.

[17] P. Coddet, C. Verdy, C. Coddet, F. Debray, F. Lecouturier, Mechanical properties of thick304L stainless steel deposits processed by He cold spray, Surface and Coatings Technology, 277(15) (2015), pp. 74-80.

[18] R. Maestracci, A. Sova, M. Jeandin, J.M. Malhaire, I. Movchan, P. Bertrand, I. Smurov, Deposition of Composite Coatings by Cold Spray Using Stainless Steel 316L, Copper and Tribaloy T-700 Powder Mixtures, Surface and Coatings Technology. 287(1) (2016), pp. 1-8.

[19] E. Duru, F. Doğan, M. Uysal, H. Akbulut, S. Aslan, Fabrication and characterization of graphene oxide reinforced NiB composite coating by pulsed electrodeposition technique, Diamond and Related Materials,120(2021)108688.

[20] S. Aslan, E. Duru, Microstructure and Wear Properties of Electrodeposited Ni-B-Al2O3 Composite Coating on Low Carbon Steel at Elevated Temperature. Journal of Materials Engineering and Performance, 31(2)(2022), pp. 1693-1704.

[21] D. Gültekin, E. Duru, H. Akbulut, Improved wear behaviors of lead-free electrolessNiB and Ni-B/CeO2 composite coatings, Surface and Coatings Technology, 422(2021),127525.

[22] E. Duru, F. Dogan, M. Uysal, H. Akbulut, S. Aslan, Optimization of Ni-B coating bath and effect of DMAB concentration on hardness and wear, Surface and Interfaces, 22(2021),100880.

[23] Y.F. Jia, Y.Y. Cui, F.Z. Xuan, F. Yang, Comparison between single loading–unloading indentation and continuous stiffness indentation, RSC Advances, 7(2017), pp. 35655-35665.

[24] R.W. Li, Z. Zhang, J.W. Li, K.X. Ma, Y.Y. Guo, Y.W. Zhou, F.Y. Wu, Surface modification of 316L stainless steel by diamond-like carbon films, Journal of Iron and Steel Research International, 27(2020), pp. 867–874.

[25] L. Aissani, A. Alhussein, C. Nouveau, L. Ghelani, M. Zaabat, Influence of film thickness and ArN_2 plasma gas on the structure and performance of sputtered vanadium nitride coatings, surface and Coatings Technology, 378(2019)124948.

[26] I. Saravanan, A. ElayaPerumal, S.C. Vettivel, N. Selvakumar, A. Baradeswaran, optimizing wear behavior of TiN coated SS 316L against Ti alloy using Response Surface Methodology, Materials and Design, 67 (2015), pp. 469-482.

[27] J. Zhou, K. Ma, C.X. Li, M. Yasir, X.T. Luo, C.J. Li, Microstructures of aluminum surfaces reinforced with 316L stainless steel particles via high-speed particle injection and the resulting double strengthening mechanism, Surface and Coatings Technology, 385 (2020) 125380.

[28] L. Aissani, A. Alhussein, A. Ayad, C. nouveau, E. Zgheib, A. Belgroune, M. Zaabat, R. Barille, Relationship between structure, surface topography and tribo-mechanical behavior of Ti-N thin films elaborated at different N2 flow rates, Thin Solid Films, 724(2021)138598.

[29] L. Aissani, A. Alhussein, A. Belgroune, C. Nouveau, E. Zgheib, R. Barille, A. Montagne, Effect of carbon content on structural, mechanical and tribological properties of Cr-V-C-N coatings, Thin Solid Films, 732(2021)138782.

[30] M. Uysal, H. Algül, E. Duru, Y. Kahraman, A. Alp, H. Akbulut,Tribological properties of Ni–W–TiO_2–GO composites produced by ultrasonically–assisted pulse electro co–deposition, Surface and Coatings Technology, 410(2021) 126942.

[31] Q. Li, P. Song, Q. Ji, Y. Huang, D. Lia, R. Zhaia, B. Zhenga, J. Lu, Microstructure and wear performance of arc-sprayed Al/316L stainless-steel composite coating, Surface and Coatings Technology, 374 (2019), pp. 189-200.

[32] F. Doğan, M. Uysal, E. Duru, H. Akbulut, S. Aslan, Pulsed electrodeposition of Ni-B/TiN composites: effect of current density on the structure, mechanical, tribological, and corrosion properties, Journal of Asian ceramic societies, 8(2021), pp. 1271-1284.

[33] Q. Li, H. Luo, P. Song, J. Zang, H. Zhou, Friction and wear properties of 316L stainless steel/aluminum composite coating, Heat Treat. Met., 42 (2017), pp. 6-12.

[34] Ş. Ürdem, E. Duru, H. Algül, M. Uysal, H. Akbulut, Evaluation of high temperature tribological behavior of electroless deposited NiB–Al2O3 coating,Wear, 482–483(2021), 203960.

[35] H. Kato, Effects of supply of fine oxide particles onto rubbing steel surfaces on severe–mild wear transition and oxide film formation, Tribology International, 41 (2008), pp. 735-742.

[36] C.O.A. Olsson, D. Landolt, Passive films on stainless steels − chemistry, structure and growth, Electrochimicaacta, 48 (2003), pp. 1093-1104

[37] Z. Feng, X. Cheng, C. Dong, L. Xu, X. Li, Passivity of 316L stainless steel in borate buffer solution studied by Mott-Schottky analysis, atomic absorption spectrometry and X-ray photoelectron spectroscopy, Corrosion Science, 52 (2010), pp. 3646-3653.

[38] X. Hao, Q. Fan, Y. Li, R.Miao, J. Ma, H. Chen,X. Zhao, C. Wang, Structural, mechanical and corrosion behaviors of the homogeneous and gradient CrAlSiN coatings in 3.5% NaCl solution. Journal of Materials Research and Technology, 15(2021), pp.2781-2791.

[39] S.G. Rodríguez, B. Torres, N.P. González, E. Otero, J. Rams, Corrosion behavior of 316L stainless steel coatings on ZE41 magnesium alloy in chloride environments. Surface and Coatings Technology, 378(2019), 124994.

Chapter IV

Elaboration and characterization of TiAlMoN coatings deposited by magnetron sputtering

Introduction

In this chapter we developed a hybrid coating of 316L stainless steel/ TiN(Al,Mo)N. The hybrid component was manufactured by depositing a thick 316L stainless steel by cold spray (CS) using helium as a process gas (*Chapter III*) followed by quaternary Ti(Al, Mo)N coatings deposited by magnetron sputtering (MS) in a gas mixture (Ar and N_2).

The obtained coatings were characterized by X-ray diffraction, Scanning Electron Microscopy, Raman, Energy Dispersive X-ray Microanalysis, and nanoindentation. The residual stress was determined using Stoney formula and the surface wettability was evaluated by the contact angle measurements and surface energy. The tribological behavior was evaluated under different loads (2 N and 5 N) in dry conditions. We also investigated the electrochemical behavior and anticorrosion performance in a 3.5 wt.% NaCl solution. The obtained results were analyzed and discussed. The results presented in this chapter are the subject of a research paper entitled "*Development of magnetron sputtered TiAlMoN coatings for enhancing the tribo-mechanical and anticorrosion behavior of cold sprayed stainless steel 316L*".

IV. 1 Coating deposition

Quaternary TiAlMoN films were deposited using a magnetron sputtering system (*Machine PVD DEPHIS 4, Etupes, France*) equipped with four cathodes. Three pure targets of titanium (99.99 %), aluminum (99.99 %) and molybdenum (99.95 %) were used. Coatings were deposited on Si wafers (100) (10 mm × 10 mm × 480 µm) and stainless steel substrates (SS 316L, Ø 15 mm × 2 mm). The SS316L samples were elaborated by cold spray using helium as a process gas (more details are explained in our work [1], *Chapter III*). These samples were polished to achieve an average roughness of about R_a = 0.03 µm. A schematic view of this equipment is presented in *Fig. IV.1*.

The SS 316L samples were ultrasonically cleaned with acetone and ethanol for 10 min, and dried in air. They were placed on the substrate-holder at 10 cm above the targets (*Fig. IV.1*). The vacuum pressure was reduced down to 6×10^{-4} Pa. Prior to film deposition, the targets and substrates were etched by Ar^+ ion bombardment for 20 min. The working pressure of 0.4 Pa was kept constant during the film deposition. The films were deposited in a mixture of Ar and N_2 with a N_2/Ar ratio of 1/4. Before depositing TiAlMoN film, a Ti underlayer was deposited for 10 min (about 50 nm) to improve its adhesion to the substrate. In order to evaluate the

influence of chemical composition in particular the Mo content on the film properties, many TiAlMoN films were deposited with applying constant currents of 2.5 A and 0.5 A respectively to Ti and Al targets and varying the Mo target current from 0.1 to 0.7 A. The deposition times of different films were adjusted to obtain films of 2 µm thick. *Table. IV.1* presents the deposition conditions of TiAlMoN coatings.

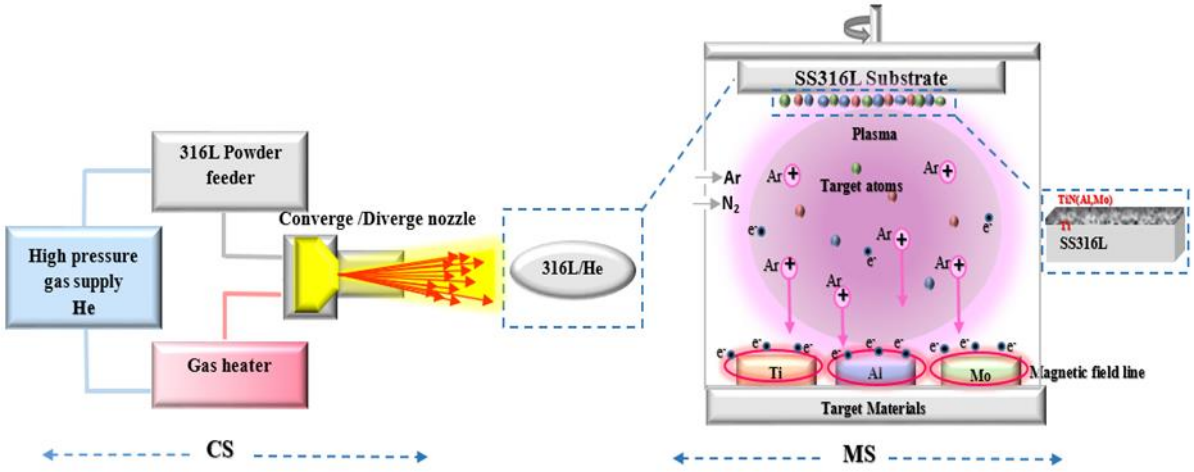

Fig. IV.1. A schematic view of the hybrid system of cold-sprayed SS 316L and TiAlMoN magnetron sputtered coatings.

Table IV.1. Deposition conditions of TiAlMoN thin films.

Substrate (elaborated by cold spray)	SS 316L
Vacuum pressure	6×10^{-4} Pa
Working pressure	0.4 Pa
N_2/Ar ratio	0.25
Sputter current for Ti and Al targets	Ti(2.5)A, Al(0.5)A
Sputter current for Mo target	0-0.7 A
Substrate temperature	Floating temperature
Rotation velocity of substrate-holder	10 rpm

IV. 2 Coating composition and structural analysis

The elemental composition of coatings (Ti, Mo, Al and N) is summarized in *Table. IV.2*. The N/(Ti+Al+Mo) ratio is close to 1, which was suitable to a stoichiometric of TiN, and TiAlN films. Nitrogen percentage in films was in the (46.95-49.28)at. % range and did not significantly change. Titanium concentration was balanced with the other elements, especially with Mo.

With increasing the current applied to the Mo target from 0 to 0.7 A, the Mo amount in TiAlMoN films increased linearly from 0 to 26.14 at. % and Ti and Al contents were decreased, respectively, from 48.02 to 22.66 at. % and from 6.40 to 1.33 at. %.

Table IV. 2. Chemical composition of TiAlMoN thin films.

Coatings	Chemical composition						Thickness
	Ti	**N**	**O**	**Al**	**Mo**	**N/(Ti+Al+Mo)**	
Ti underlayer	~100						50 nm
$Ti_{0.48}N_{0.47}$	48.02	46.95	5.03			0.98	
$Ti_{0.43}Al_{0.06}N_{0.48}$	42.66	47.94	4.60	6.40		0.98	
$Ti_{0.37}Al_{0.05}Mo_{0.4}N_{0.49}$	37.28	49.28	3.50	5.41	3.91	0.97	
$Ti_{0.35}Al_{0.04}Mo_{0.11}N_{0.49}$	34.38	47.81	2.50	4.13	11.18	0.96	~2 µm
$Ti_{0.30}Al_{0.03}Mo_{0.16}N_{0.48}$	30.60	47.85	2.40	3.06	16.09	0.96	
$Ti_{0.22}Al_{0.01}Mo_{0.26}N_{0.48}$	22.66	47.77	2.10	1.33	26.14	0.95	

Fig. IV.2 presents X-ray diffraction patterns of TiAlMoN films and *Fig. IV.3* presents the texture coefficient, microstrain, lattice constant and crystallite size. TiN coating presented a (200) preferential orientation with a lattice parameter a_{TiN} = 4.29 Å. The diffraction peaks of the TiAlN coating was identified to fcc-TiN (JCPDS No. 00-038-1420). The AlN phase was not observed as reported in a previous work [2]. The formation of a single fcc-TiN phase in TiAlN film with TiN (200) preferential orientation and a low value of $I_{(111)}/[I_{(111)} + I_{(200)}]$ of about 0.68 indicates that aluminum was fully incorporated into the TiN producing a crystalline structure rich in Al solid solution [3]. In addition, TiN (200) was shifted to a higher angle compared to the TiN powder diffraction data, revealing a decrease in the lattice constant from 4.29 to 4.25 Å (relaxing of crystalline structure). Simultaneously, the TiAlN lattice microstrain increased from 0.002 to 0.004, as shown in *Fig. IV.3a*, which can be associated with the tensile stress that leads to the formation of more structural defects.

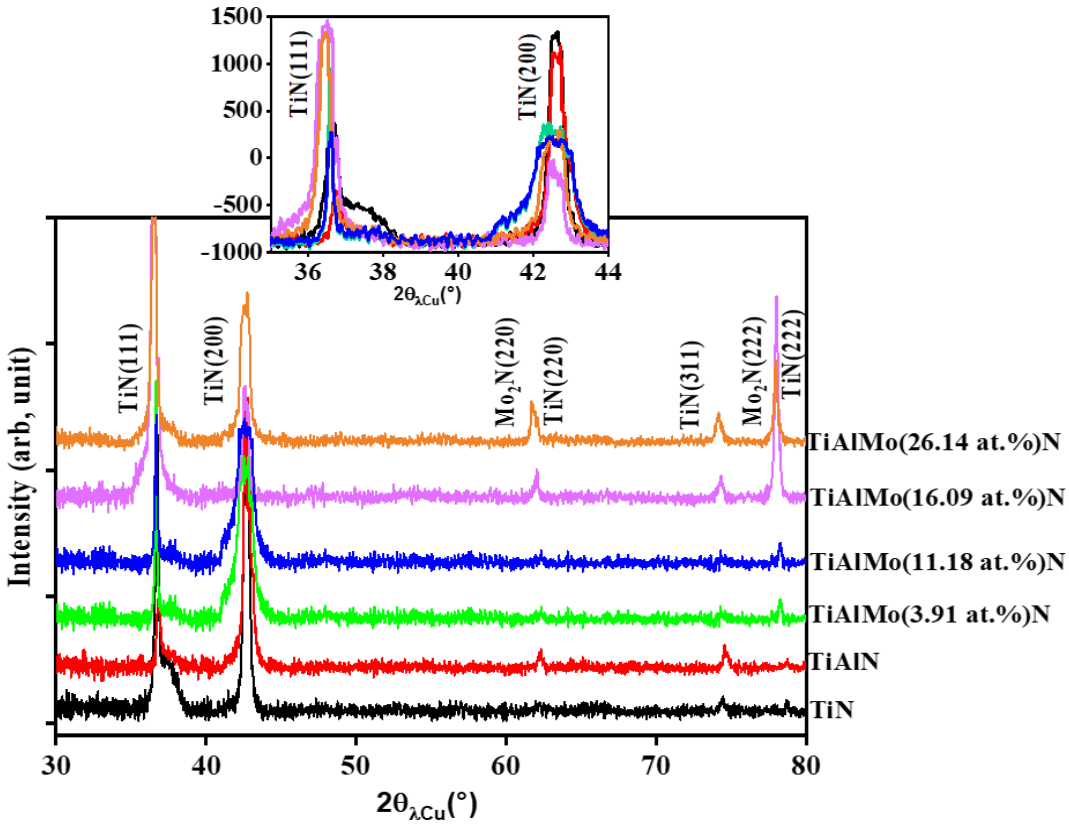

Fig. IV.2. XRD patterns of TiN, TiAlN and TiAlMoN coatings with different Mo contents.

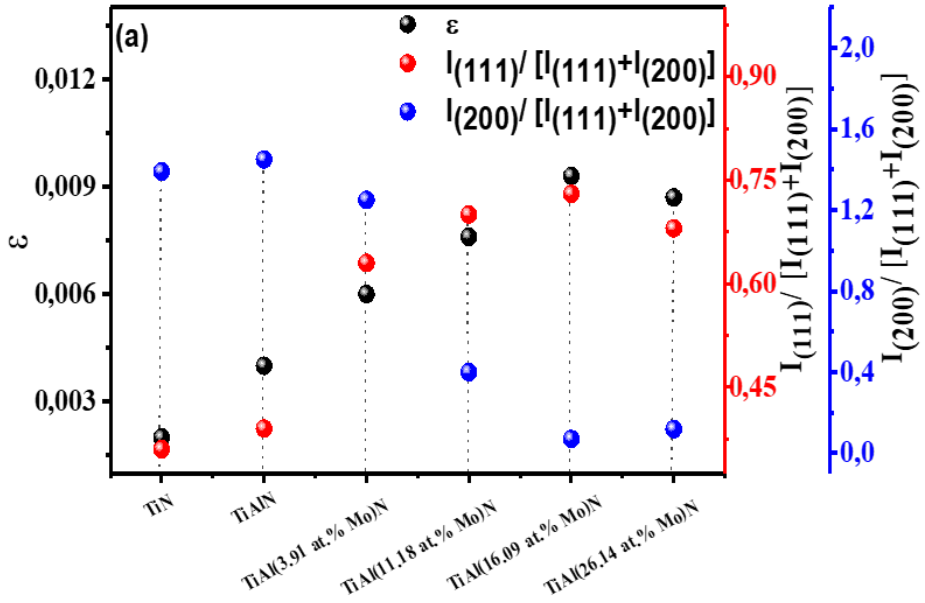

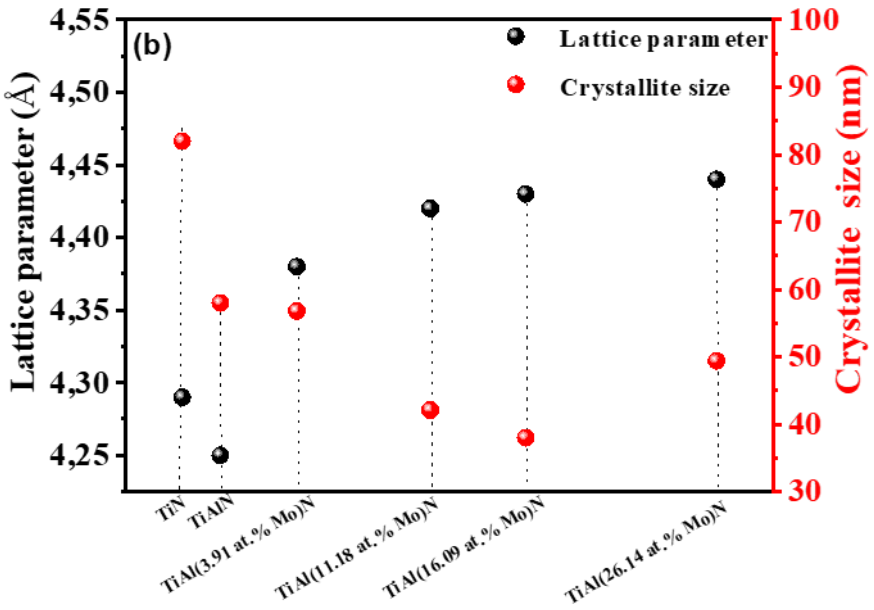

Fig. IV. 3. a) I(111) /[I(111)+I(200)], I(200) /[I(111)+I(200)] and lattice microstrain, b) Lattice constant and crystallite size of coatings.

For TiAlMoN films, it can be noticed the changes in XRD (200) and (111) peaks intensities with the variation of Mo quantity in films. We can also see the evolution of texture coefficient: increasing of $I_{(111)}/[I_{(111)} + I_{(200)}]$ and reduction of $I_{(200)}/[I_{(111)}+I_{(200)}]$ (*Fig. IV. 3a*). For the TiAlN-3.91 at.% Mo film, it can be noticed the (220) and (222) peaks position corresponding to the TiN ($2\theta = 61.81°$, $2\theta = 78.96°$) (JCPDS card No. 00-038-1420) and the Mo_2N phases ($2\theta = 62.64°$, $2\theta = 79.08°$) (JCPDS card No. 01-084-8748). The overlap of TiN and Mo_2N peaks suggests the formation of a two-phase mixture of TiN-Mo_2N. With increasing Mo content, the TiN(111) peak becomes border and shifts to a lower angle.

In fact, the insertion of Mo atoms results in the expansion of the lattice and the increase of microstrain to 0.0093 (for the film containing 16.09 at. % of Mo) (*Fig. IV.3a*). This is due to the Mo atoms having a large atomic radius (1.41 Å) and the formation of Mo_2N phase [4-5]. The increase of Mo content led to a relative increase in the lattice parameter and introducing compressive residual stress in the film, which can impede the dislocations mobility. In *Section IV.5.1*, we will give a detailed analysis on the residual stresses generated in films.

The variation of crystallite size is shown in *Fig. IV.3b*. TiN and TiAlN films had a crystallite size of about 82 and 58 nm, respectively. For the TiAlMoN coatings, increasing the Mo content to 16.09 at. % leds to gradually reduce the crystallite size to 38 nm.

Raman spectra of TiN(Al, Mo) films are presented in *Fig. IV.4*. TiN and TiAlN spectra show two large wavelengths at 178 and 534 cm^{-1} related to the optical and acoustic modes of TiN [6-7]. With increasing the Mo content in TiAlN film, the intensity of the peaks is gradually increased, and the wavelength divergence is clearly observed between the acoustic and optic regions. With a low Mo content, Mo-N vibration mode is very low which is due to the low intensity of the scattered Mo-N peaks and the high amounts of Ti and N in films that display a resolved signature dominating the spectrum. With increasing Mo content, a slight shift was noticed in the position of the TiN modulation wavelength with the increase of Mo-N bonds intensities to high intense Mo_2N peaks at 798, 871 and 1037 cm^{-1}. This indicates that more Ti atoms were replaced by Mo ones favoring the vibration of Mo-N bonds in the TiAlMoN films [8-9].

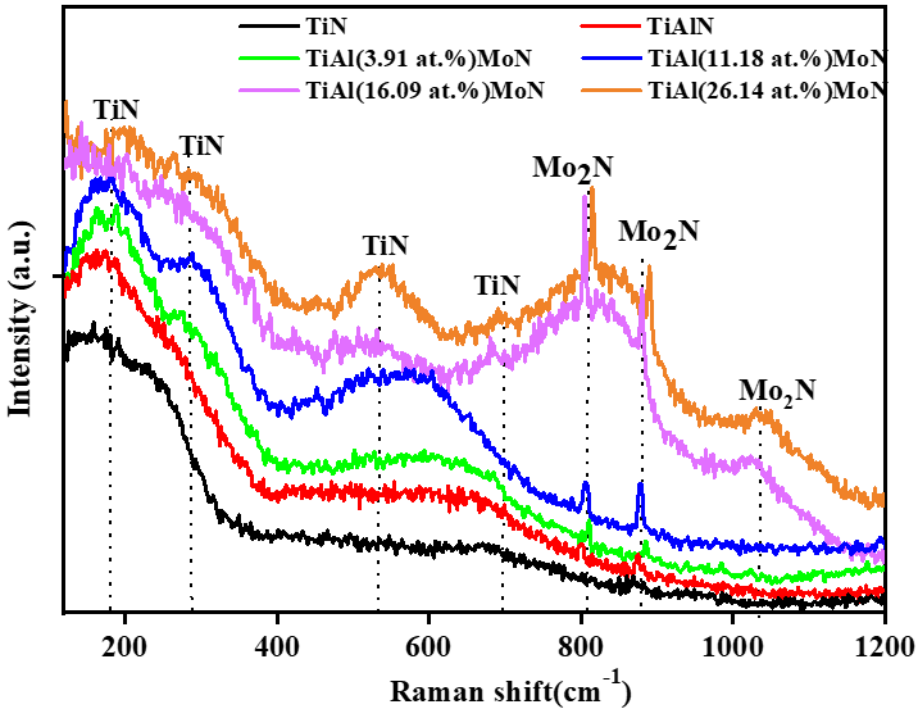

Fig. IV. 4. Raman spectra of TiN(Al, Mo) coatings.

IV. 3 Coating morphology and surface topography

Fig. IV.5 presents the SEM images of surfaces and cross-sections of TiN(Al, Mo) films. TiN and TiAlN coatings exhibited a columnar structure with some porosity between globular grains, which corresponds to the zone II of Anders's structural zone model (ASZM) (Fig. *IV.5 (a and b)*) [10].

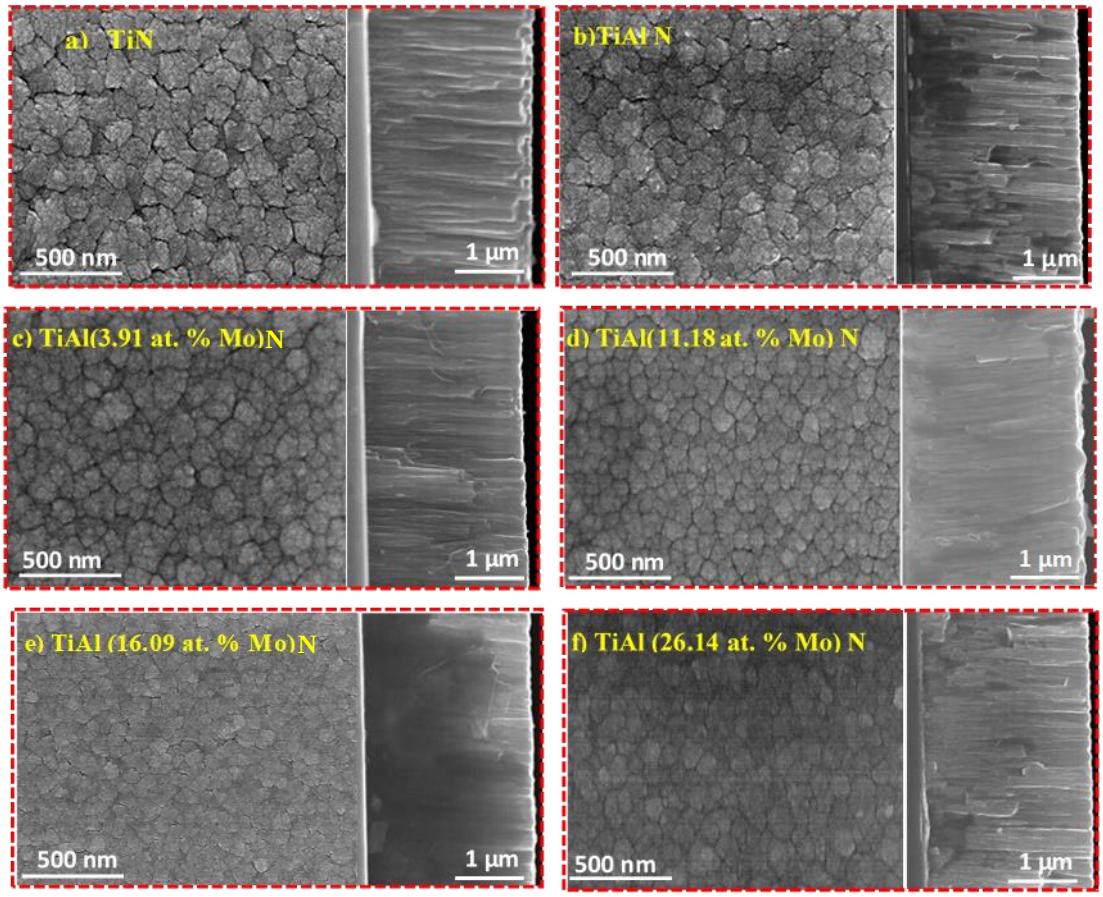

Fig. IV.5. Surface and cross-sectional SEM images of: a) TiN, b) TiAlN, and TiAlMoN coatings containing c) 3.91, d) 11.18, e) 16.09 and f) 26.14 at. % of Mo.

Increasing the Mo content in the coating (11.18 and 16.09 at. % of Mo) led to enhance the surface quality. The columnar grains gradually disappeared and the TiAlMoN coatings became denser with smooth and homogeneous surface corresponding to the zone T in ASZM [10]. This is attributed to the increasing of applied current that enhances the adatom mobility and leads to the densification of structure. In addition, the (111) crystal plane strongly plays an important role on the densification of film growth. With a high Mo content (26.14 at. %), the TiAlMoN coating presented large grains with columnar structure corresponding to the zone I in ASZM [10].

Fig. IV. 6 shows cross-section TEM images of TiAlN(16.09 at. % of Mo) coating. The bright field (BF-TEM) (*Fig. IV.6a*) shows bright and dark fields TEM images of different areas on the film surface, while *Fig. IV.6b* presents a high-resolution TEM image of the film and selected area electron diffraction (SAED) pattern. TEM images of the TiAlN(16.09 at.% of Mo) coating showed a mixed structure of dense and columnar grains . We noticed two different zones:

the zone (I) presenting a dense structure with (111) and (200) Bragg reflections of cubic TiN phase and the zone (II), rich on Mo, corresponding to Mo_2N with a dominant (111) orientation growth. These results are in agreement with those obtained by XRD and Raman.

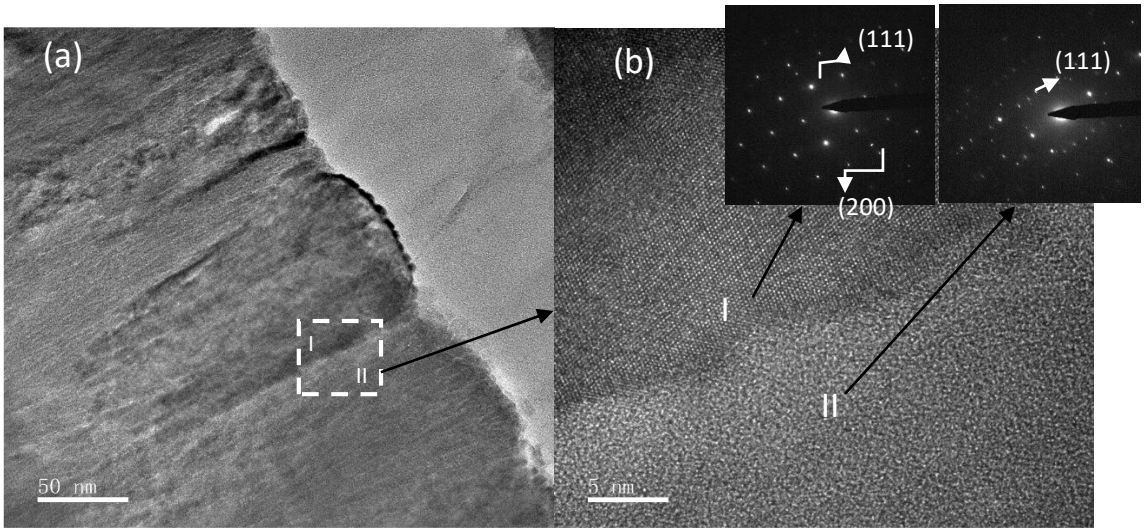

Fig. IV.6. a) BFTEM image, b) HRTEM and SAED images of TiAlN(16.09 at.% Mo) film.

Fig. IV.7 shows 2D and 3D AFM images and profiles of TiN, TiAlN and TiAlMoN films. The surface roughness (R_a) of TiN and TiAlN coatings was (10.2 ± 0.23)nm and (8.1 ± 0.37) nm, respectively. The surface topography of all TiN(Al, Mo) films showed a same variation in particles shape as observed in SEM images, which can be explained by the variation of grain size [11]. With increasing the Mo content, a significant change in the topography of the TiAlMoN films was observed and the R_a roughness gradually reduced to a low value of (3.4 ± 0.08) nm. This was oserved for the film containing 16.09 at.% of Mo presenting a fine microstructure (*Fig. IV. 7e*).

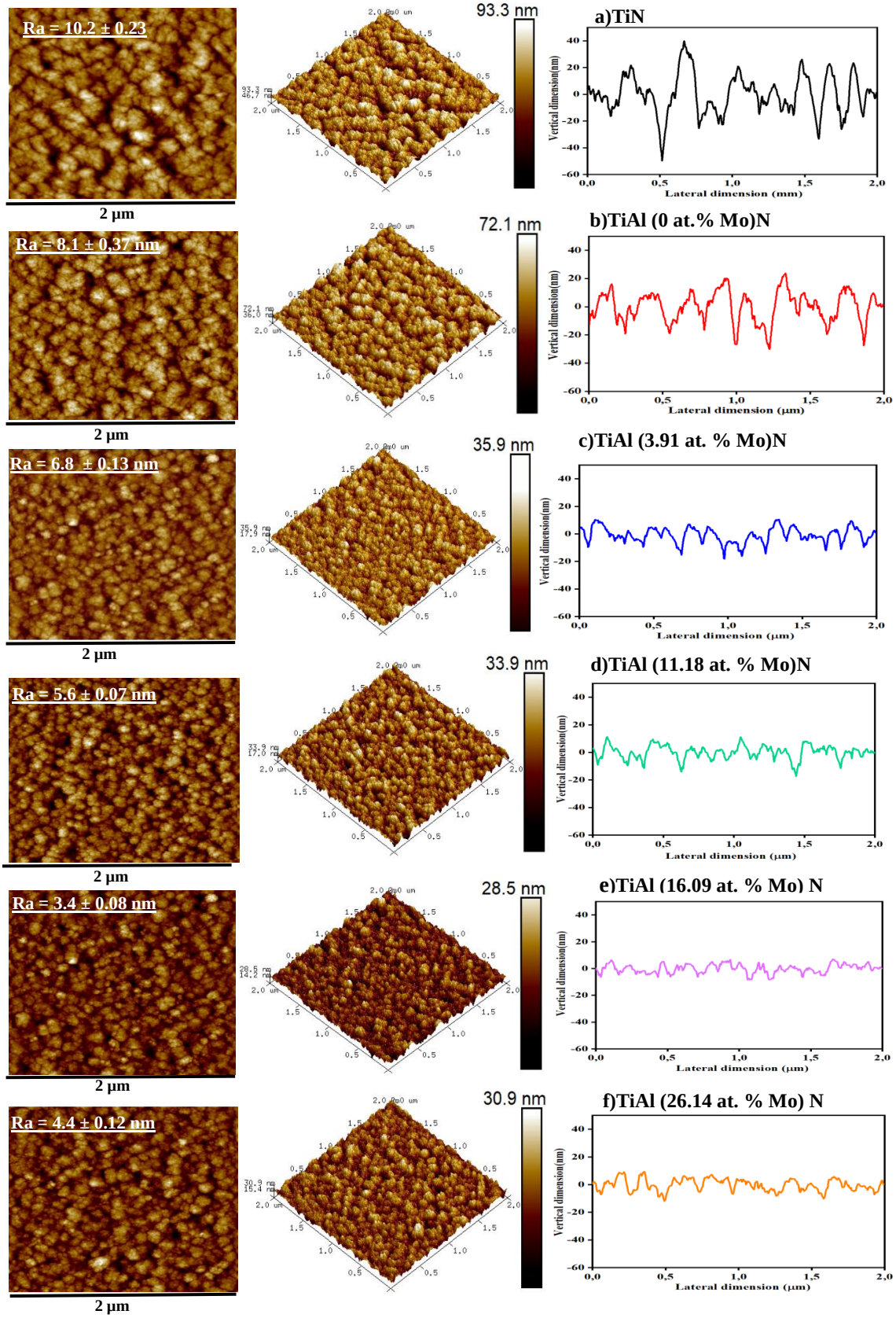

Fig. IV.7. 2D and 3D AFM images and profiles of a) TiN, b) TiAlN, and TiAlMoN coatings containing: c) 3.91, d) 11.18, e) 16.09 and f) 26.14 at. % of Mo.

IV. 4 Coating wettability

Coating wettability was evaluated by contact angle measurements at room temperature. Each film was tested using three liquids (water, thiodiglycol and diiodomethane) and the total surface energy values were calculated. *Fig. IV.8* presents the values of contact angle and surface energy of TiN(Al, Mo) coatings.

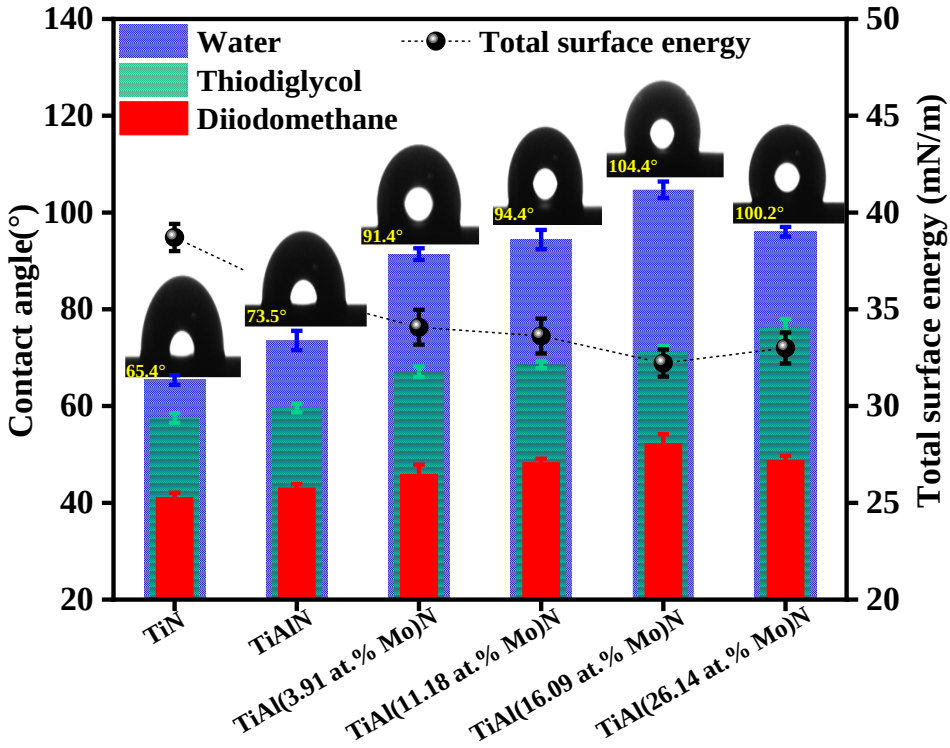

Fig. IV.8. Contact angle and total surface energy of TiN(Al, Mo) coatings.

We can notice that the water contact angles were generally higher than those measured with thiodiglycol and diiodomethane. This is due to the higher surface tension and the lower viscosity of water compared to thiodiglycol and diiodomethane [12-13]. *Tang et al.* reported similar results [14] where the water contact angle with various paint surfaces was consistently higher than that of ethylene glycol and diiodomethane. The average water contact angle values were 65.4°, 73.5°, 91.4°, 94.4°, 104.4° and 100.2° for TiN, TiAlN and TiAlMoN coatings containing 3.91, 11.18, 16.09, and 26.14 at. % of Mo, respectively. TiAlMoN coating containing 16.09 at. % Mo had the highest contact angle corresponding to the lowest wettability and the highest hydrophobicity compared to the other coatings as shown in *Fig. IV.8*. We can also notice that the total surface energy decreased with increasing the Mo content. The lowest value of 32.22 mN/m was obtained for the film containing 16.09 at.% of Mo. In general, the wettability of a surface depends on two main factors, namely the surface energy related to the

surface chemical composition, structure and surface roughness, which can make the surface more hydrophilic or hydrophobic [15-16]. In our study, the surface roughness had a direct impact on the contact angle and surface energy. Other factors affecting the surface energy have been mentioned such as the (111) preferred orientation resulting in a lower surface energy than that of the (200) orientation which is consistent with previous works [5, 17, 18].

IV. 5 Mechanical properties

IV. 5. 1 Residual stress

The variation of residual stresses generated in TiN(Al, Mo) films during the magnetron sputtering is presented in *Fig. IV.9*.

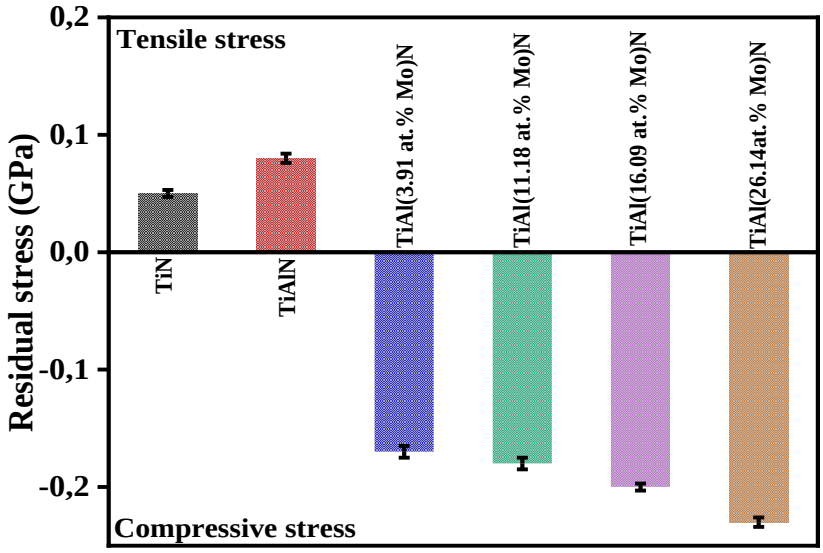

Fig. IV.9. Residual stress generated in the TiN(Al, Mo) films during the deposition process.

The TiN coating had a tensile residual stress of 0.05GPa, which is lower than that reported in the literature [73] due to the under stoichiometry of TiN film (N/Ti < 1). TiAlN coating had the highest tensile stress of 0.08 GPa due to the small incorporated Al (1.82 Å atomic radius) and the preferential (002)-oriented grains that are low compressive than (111) [19]. Mo addition led to change the generated stress state from tensile to compressive residual stress. The increase of Mo content up to 26.14 at. % led to gradually increase the compressive stress and its maximum value was found equal to -0.23 GPa. The variation of residual stress from tensile to compressive state is related to the film microstructure and its growth mechanism [20]. The evolution of residual stress of TiAlMoN film with increasing Mo content may be attributed to

the lattice distortion occurred by the insertion of Mo atoms within the TiAlN, which prevent the dislocations movement, resulting in improvement of mechanical properties [21]. In fact, the change in preferential orientation and grain refinement play an important role on the residual stress value. *Carvalho et al.* [22] found that the residual stress is directly dependent on the lattice defects and the formation of different phases in films.

IV. 5. 2 Nanoindentation measurements

Fig. IV. 10 shows typical load-displacement curves obtained from nanoindentation measurements. The maximum applied load was approximately 8000 µN, resulted in a maximum indentation depth in the 120-170 nm range, which guarantees a minimal substrate influence on the coating measured properties. For all films, the continuity in the loading curves was noticed suggesting that the material did not fracture or crack under the applied load [23]. TiN film had a maximum penetration depth with a large load-unload curve. The incorporation of Al and Mo in the TiN exhibited a lower indenter penetration indicating that films became more resilient to elastoplastic deformation. TiAlMoN coating containing a high Mo content (16.09 - 26.14 at. %) showed a narrower load-displacement curve and lower depth, signifying a high resistance to indenter penetration.

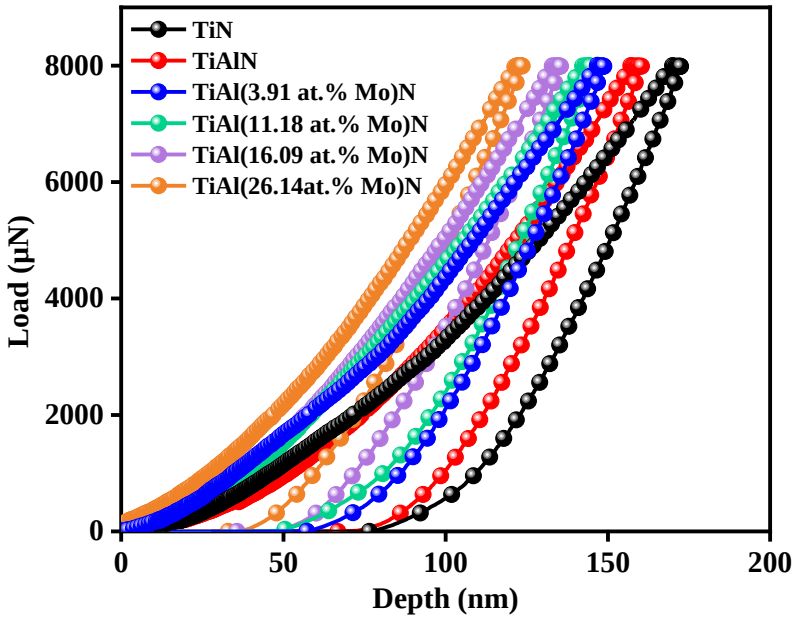

Fig. IV.10. Loading-displacement curves of TiN(Al, Mo) coatings.

Fig. IV.11 presents hardness (H), Young's modulus (E) and H/E ratio. The mechanical properties of sputtered TiN(Al, Mo) films can be influenced by several factors including phases,

preferential orientation and residual stress. From *Fig. IV.11*, we can notice that the hardness values of TiN and TiAlN coatings were 20.5 and 21.4GPa, respectively. With increasing Mo content from 3.91 to 26.14 at. %, a continuous raise in the hardness and Young's modulus values was observed, respectively from (23.4, 278.5) to (29.5, 334.5) GPa. This is due to the strengthening effect with the presence of Mo_2N phase, grain refinement and high compressive stress [24]. In addition, the high hardness of TiAlMoN films is also due to the dense TiN(111) plane [25-26].

H/E and H^3/E^2 ratio generally related to the plasticity index and plastic deformation resistance respectively that gives a good prediction on the tribological behavior of coating [27]. The maximum value of H/E and H^3/E^2 were of 0.092 and 0.237 respectively was obtained for the film containing 16.09 at. % of Mo that should present a high wear resistance.

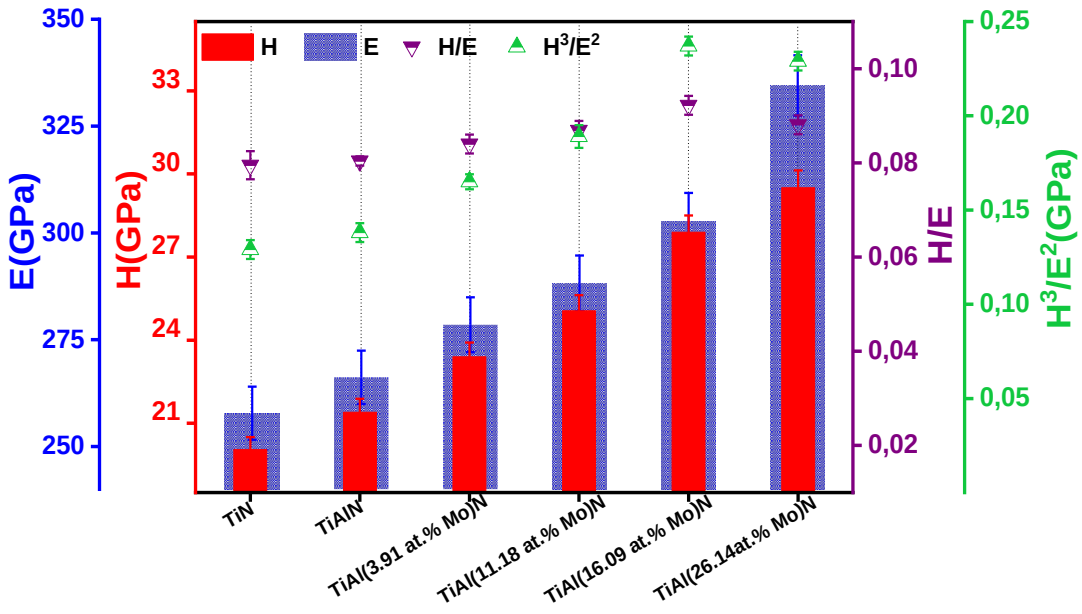

Fig. IV. 11. Hardness, Young's modulus and H/E ratio of TiN(Al, Mo) coatings.

IV. 6 Tribological properties

Fig. IV.12 shows the coefficients of friction (COF) of TiN(Al, Mo) films over the entire sliding distance, obtained under 2 and 5 N normal loads. The COF of films started from relatively high and instable values at the first contact. This initial stage can be attributed to the break-in period associated with the low contact area between the 100Cr6 ball and the film, where the wear debris occurs through cracking of rough tips between the two counterparts. After a short sliding distance (~ 3 m), the COF decreased to a stable value. The COF of

TiAl(16.09 at. % Mo)N coatings decreased with increasing the applied load from 2 to 5N and clearly enhanced by 17 % and 59.5 %, respectively, compared to the SS316L substrates deposited by cold spray presented *in Chapter III* [28].

TiN and TiAlN coatings had a high COF because of their low hardness. In addition, the intensity of the low packed TiN (200) orientation is higher than that of the TiN (111) orientation in TiN and TiAlN films. With increasing Mo content, the COF decreased to 0.3 for the film containing 16.09 at. %, then slightly increased as the Mo content further increased up to 26.14 at.%. This indicates that the tribological performance of TiAlMoN film significantly improved with the incorporation of Mo and the formation of strong mixed phases **(***Fig. IV. 2* and *Fig. IV.6*). Furthermore, the low friction can be due to the dense structure and the formation of a higher amount of fine molybdenum oxide particles that serve as a lubricant between the two counterparts [25, 29].

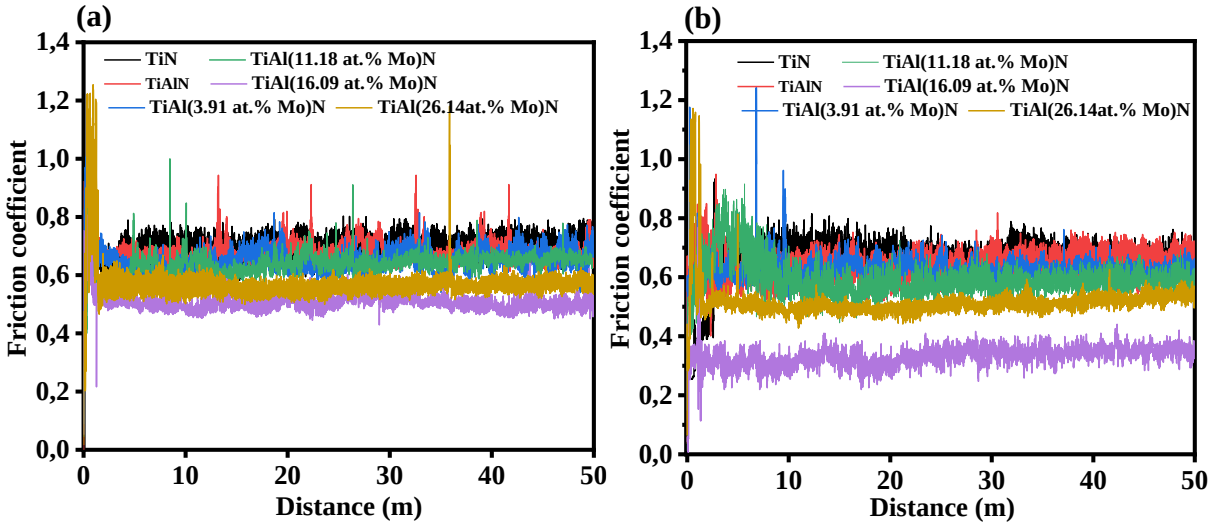

Fig. IV.12. Coefficients of friction of TiN(Mo, Al) coatings under: a) 2N and b) 5N normal loads.

The wear depth and width profiles of TiN(Al, Mo) films tested under 2 and 5N normal loads are illustrated in *Figs. IV. (13 and 14)*, respectively.

At 2N, TiN and TiAlN films had wear depth and width of about (1.7 and 1023) µm and (1.32 and 890) µm, respectively. The incorporation of Mo into TiAlN reduced the wear depth and width to (1.02 and 730) µm in the film containing 3.91 at. % Mo and reached the lowest values of (0.570 and 363) µm in the film containing 16.09 at. % Mo.

At a higher loading (5 N), TiN and TiAlN films showed wear depth and width of about (1.4 and 933) µm and (1.145 and 822) µm, respectively. The addition of Mo to TiAlN reduced the wear depth and width to (0.850 and 714) µm in the film containing 3.91 at. % Mo and reached the lowest values of (0.384 and 211) µm in the film containing 16.09 at. % Mo, which is consistent with the COF tendency. The COF reduction and enhancement in tribological characteristics can be attributed to the low roughness, grain refinement and the good adhesion between the film and substrate. *Yang et al.* [20] observed a similar phenomenon when Mo was incorporated into TiAlN coatings and attributed it to the dense structure, smooth surface and high hardness.

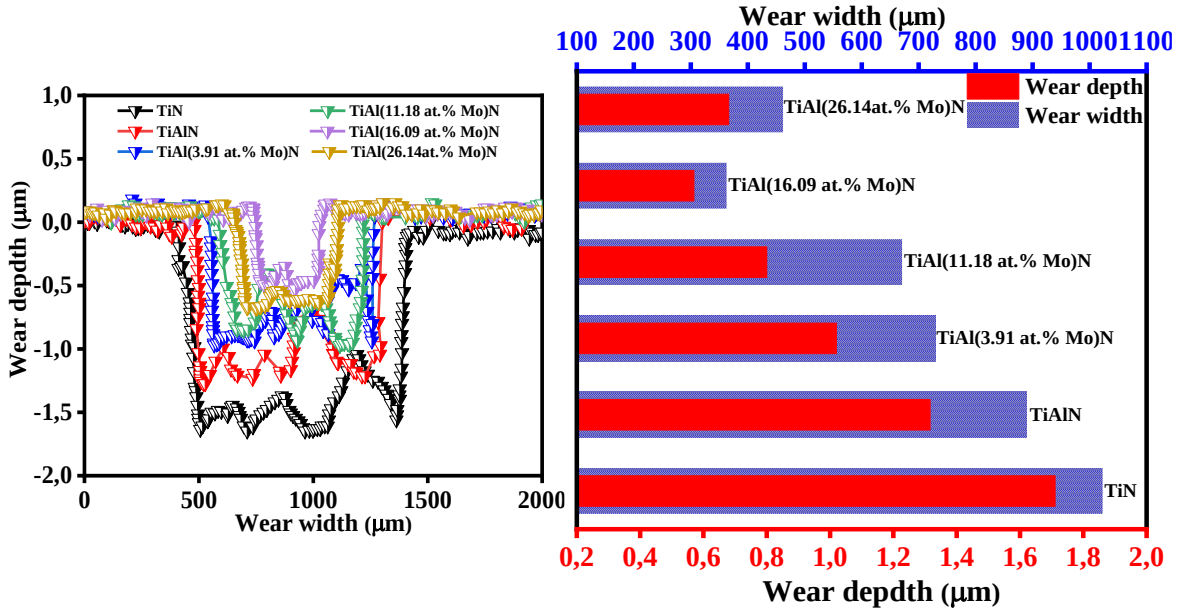

Fig. IV.13. Depth and width of wear tracks on TiN(Mo, Al) coatings tested under 2N normal load.

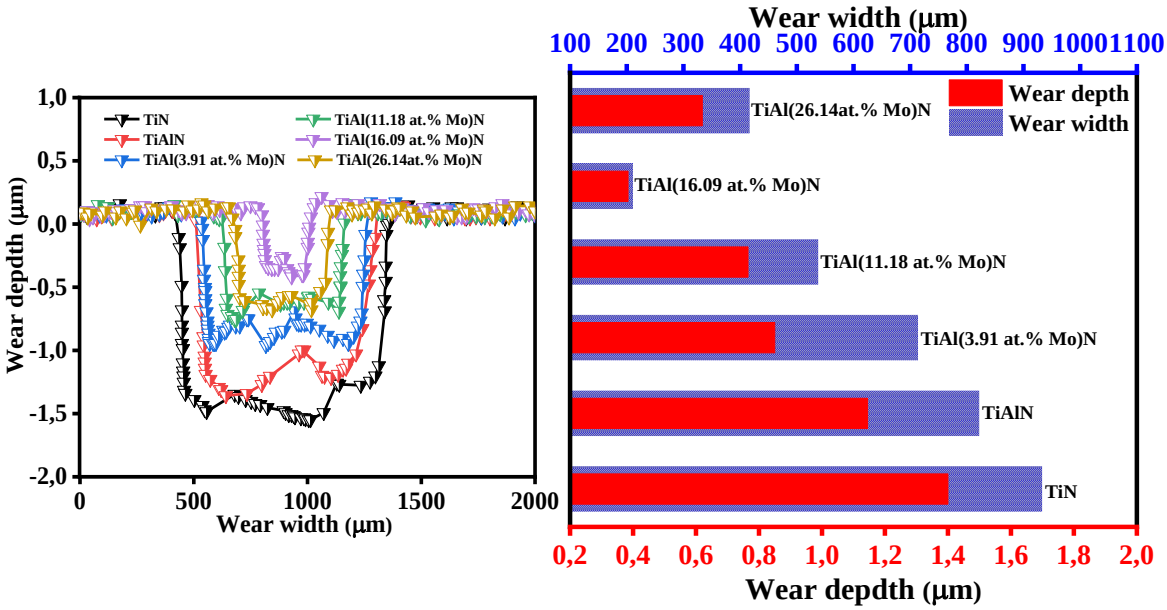

Fig. IV.14. Depth and width of wear tracks on TiN(Mo, Al) coatings tested under 5N normal load.

The wear rates of TiN(Al, Mo) coatings and counter 100C6 balls are presented in *Fig. IV.15*. *Figures IV. 16 and 17* show the EDS elemental compositions and SEM images of wear tracks of TiN(Mo, Al) coatings and balls tested under 2N and 5N normal loads, respectively.

The worn surfaces of TiN and TiAlN coatings show multiple signs of wear and prominent grooves. They are clearly visible with large worn areas on the coatings and 100Cr6 balls (1900 and 1750 µm diameter, respectively). They were slightly lower under a higher 5N load. According to *Du et al.* [30], the abrasive feature is due to the low hardness, rough surface and low film/substrate adhesion. The TiAlMoN film containing 16.09 at.% Mo presented the narrowest and the shallowest wear track. Its wear rate was found equal to 1.534×10^{-6} and 0.849×10^{-6} mm^3/N under 2 and 5N loads, respectively. The worn zones on the counter balls showed the lowest diameters of 760 and 633 µm under 2 and 5N applied loads, respectively. This indicates the positive effect of Mo addition to enhance the tribological properties of the TiAlN film. Thus, the good wear resistance of TiAlMoN films can be related to its low roughness and high H/E ratio as confirmed by *Xu et al.* [31].

The film containing 26.14 at.% Mo showed more wear debris formed on the worn surface that are due to the brittle fracture caused by the high stress generated in the film. The EDS results indicated the presence of high oxygen in the worn surface due to the oxidation of the film surface. We also detected some elements of the counter ball in worn track. *Yang et al.* [29]

confirmed that the dark area represents chemical changes on the film surface and high oxygen content indicates oxidation of the films during sliding test.

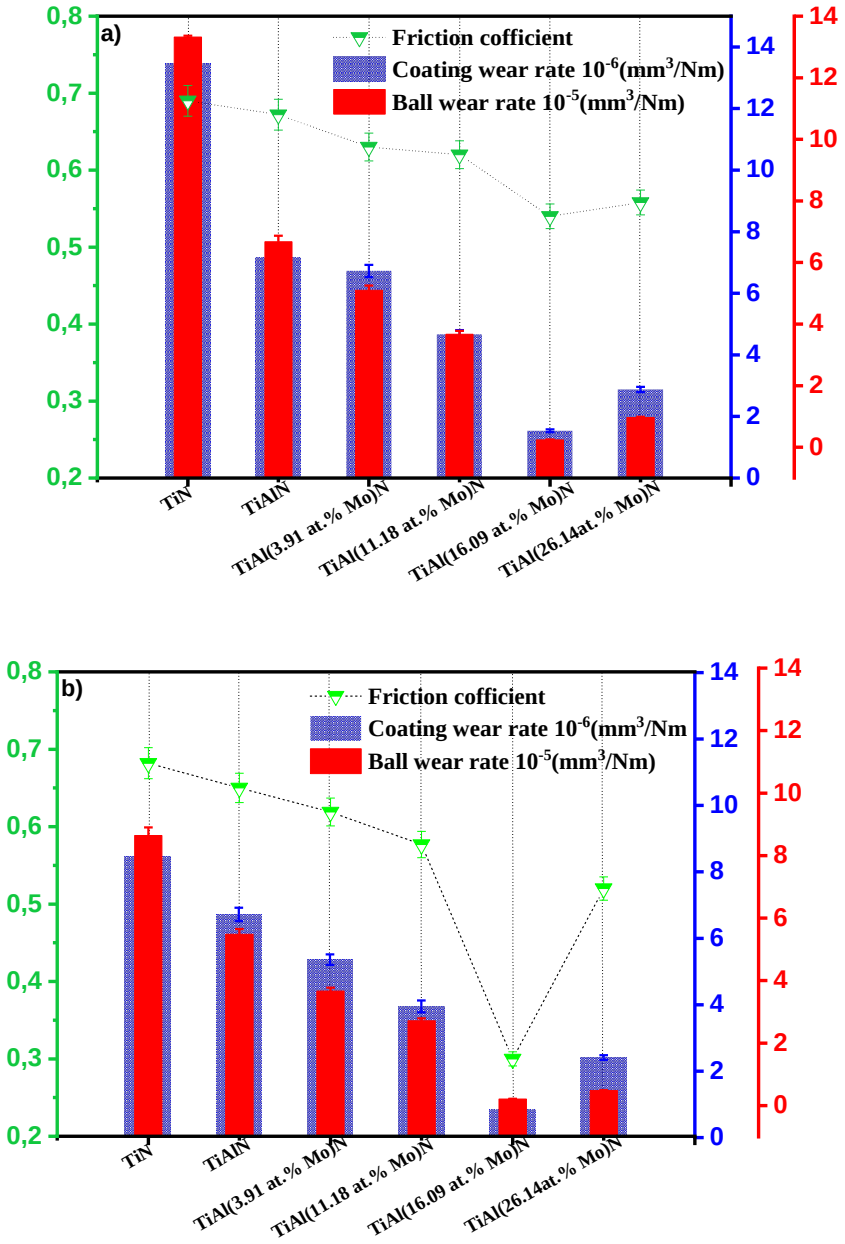

Fig. IV.15. Wear rates of TiAlMoN coatings and steel balls tested under: a) 2N and b) 5N normal loads.

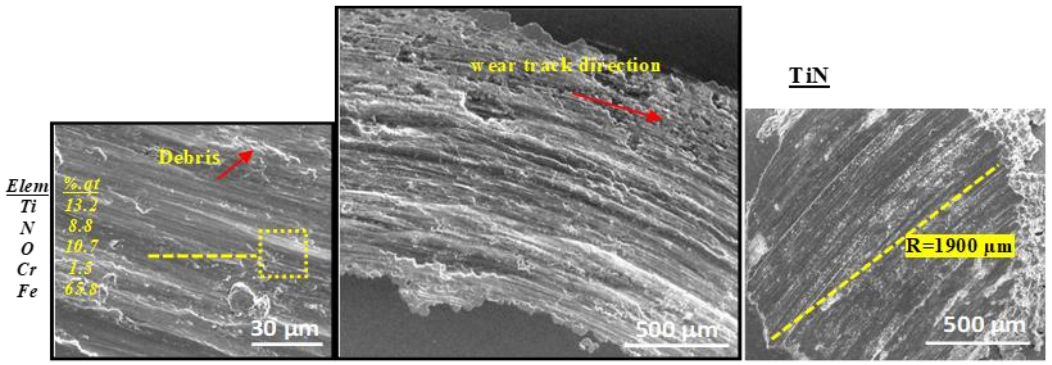
Debris
Elem %.at
Ti 13.2
N 8.8
O 10.7
Cr 1.3
Fe 65.8
30 µm
wear track direction
500 µm
TiN
R=1900 µm
500 µm

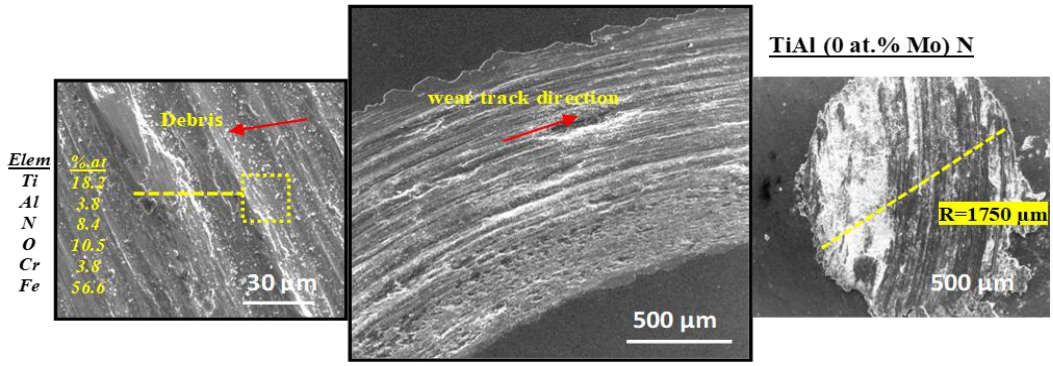
Debris
Elem %.at
Ti 18.7
Al 3.8
N 8.4
O 10.5
Cr 3.8
Fe 56.6
30 µm
wear track direction
500 µm
TiAl (0 at.% Mo) N
R=1750 µm
500 µm

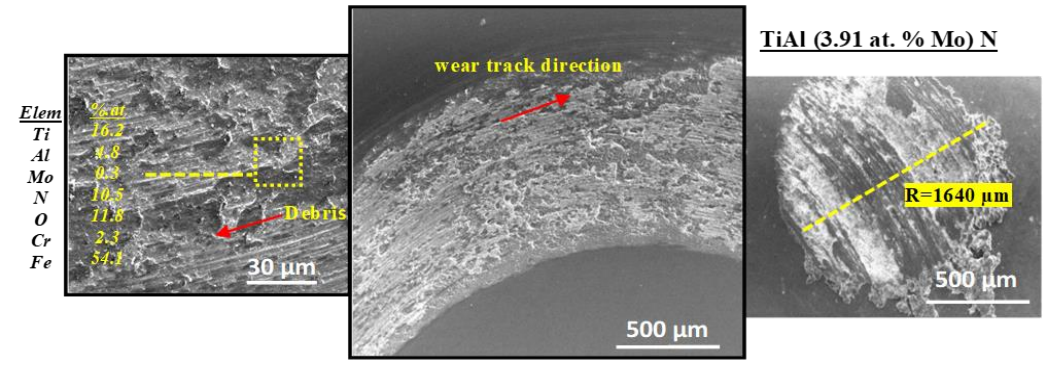
Elem %.at
Ti 16.2
Al 4.8
Mo 0.3
N 10.5
O 11.8
Cr 2.3
Fe 54.1
Debris
30 µm
wear track direction
500 µm
TiAl (3.91 at. % Mo) N
R=1640 µm
500 µm

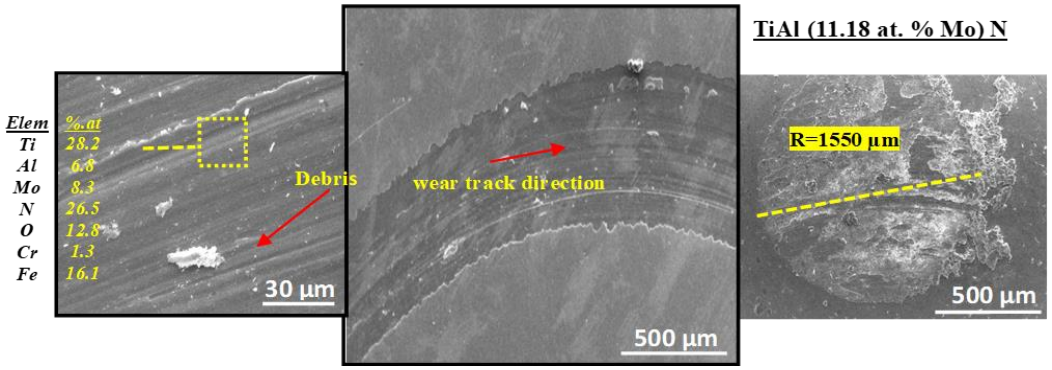
Elem %.at
Ti 28.2
Al 6.8
Mo 8.3
N 26.5
O 12.8
Cr 1.3
Fe 16.1
Debris
30 µm
wear track direction
500 µm
TiAl (11.18 at. % Mo) N
R=1550 µm
500 µm

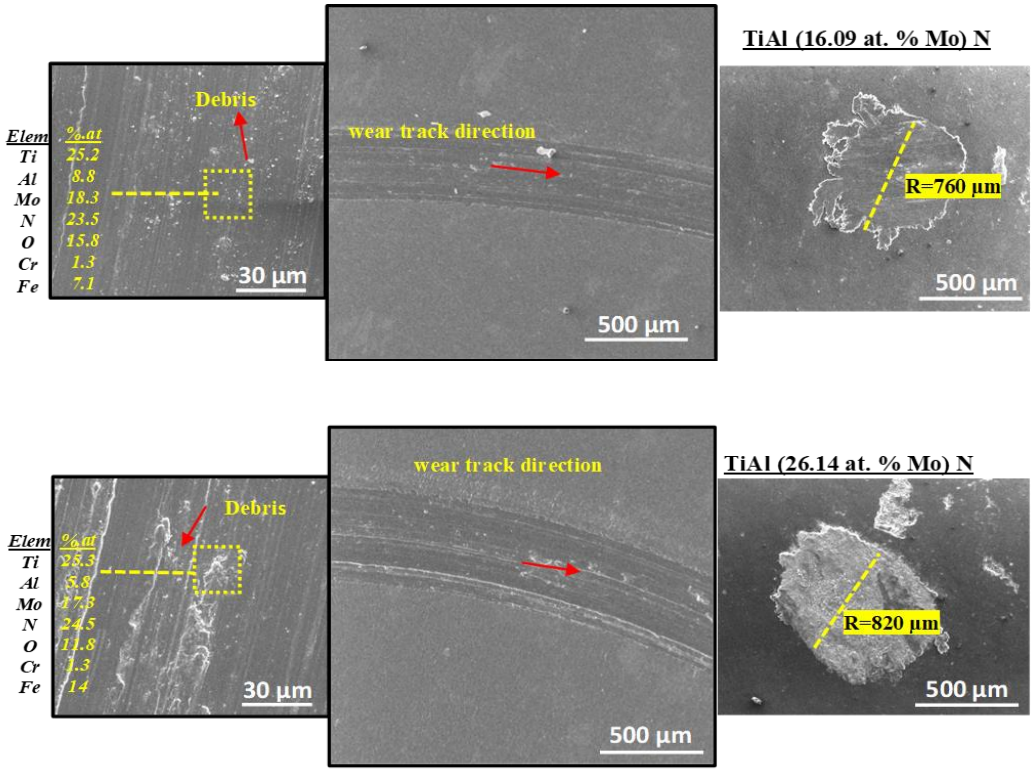

Fig. IV.16. EDS elemental compositions and SEM images of wear tracks of TiN(Mo, Al) coatings tested under 2N normal load (images on the right show the worn zones occurred on steel balls).

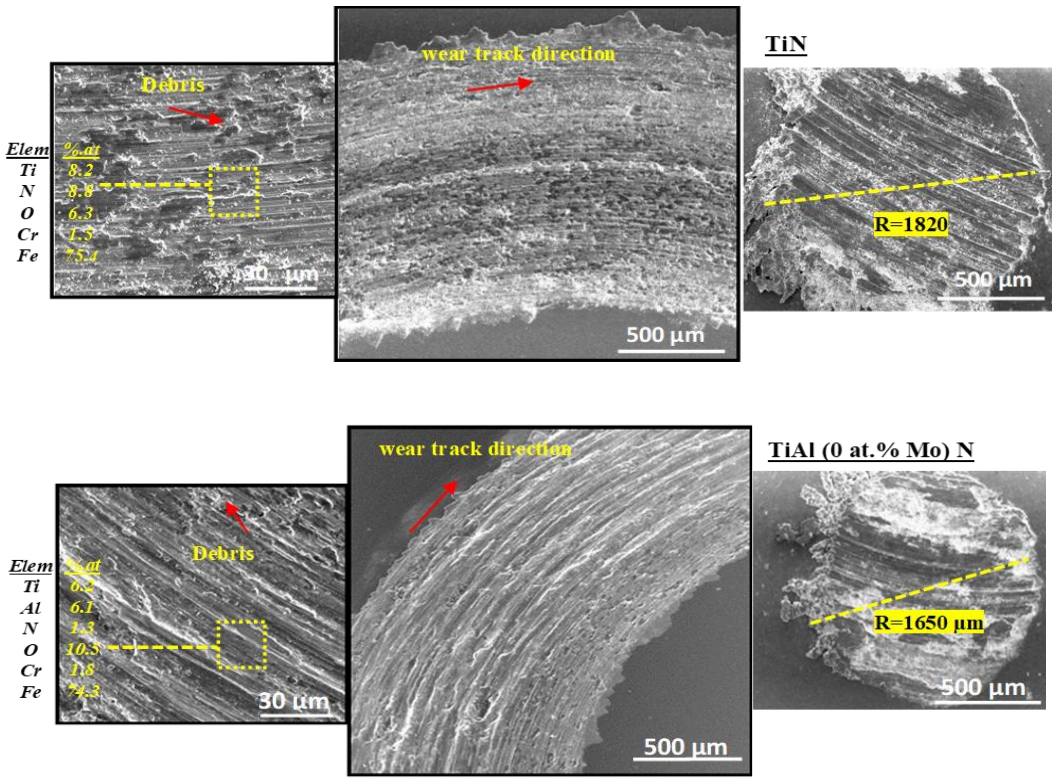

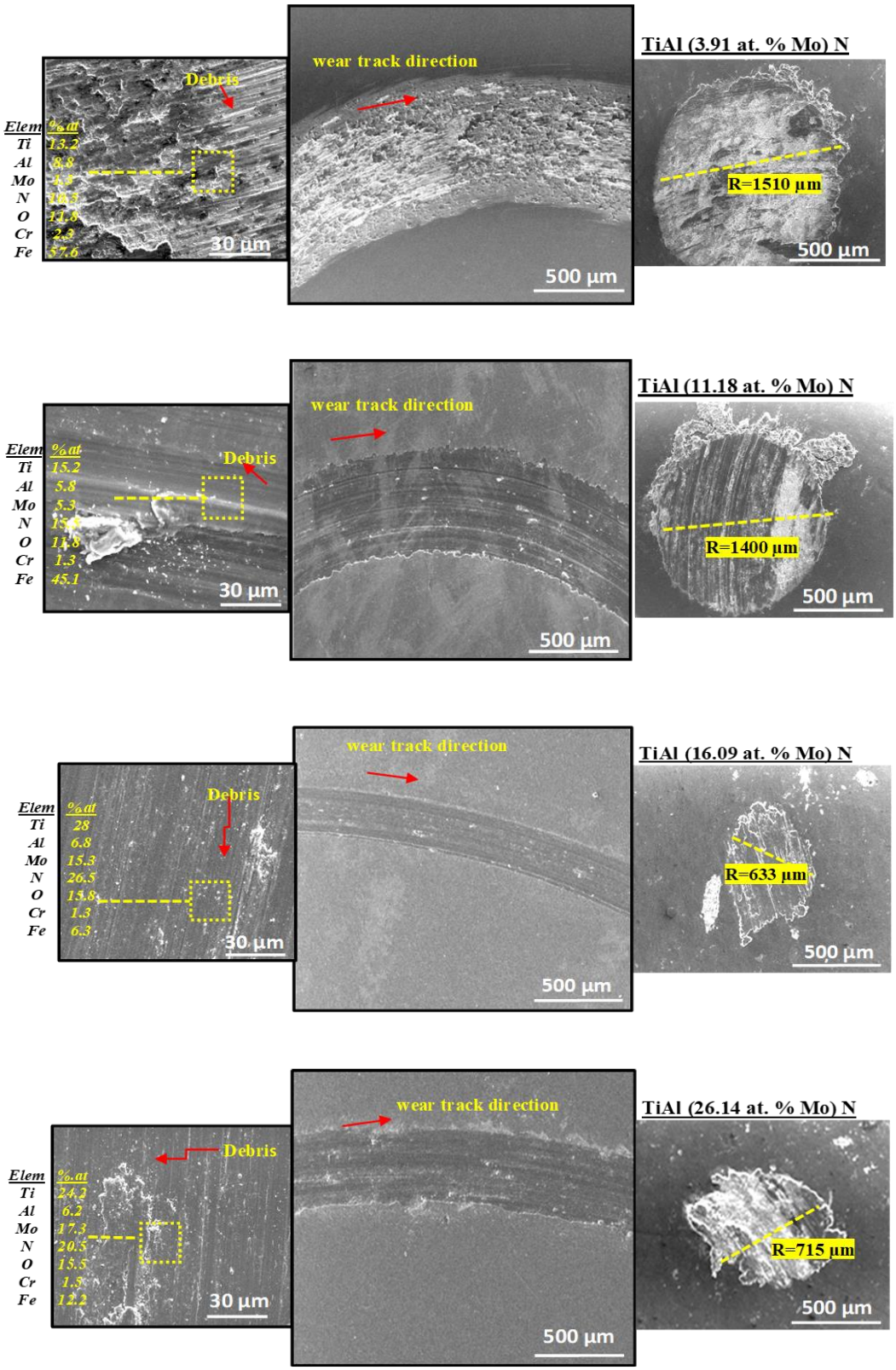

Fig. IV. 17. EDS elemental compositions and SEM images of wear tracks of TiN(Al, Mo) coatings tested under 5N normal load (images on the right show the worn zones occurred on steel balls).

The changes in the phases and elemental composition of the wear tracks of TiAlN and TiAl (16.09 at. % Mo)N films were investigated by Raman analysis (*Fig. IV.18*). We can notice that wear track of the TiAlN film exhibited a distinct metallic bonding character of TiN (458.7 cm^{-1}) with small TiO_2 amount (532.1 cm^{-1}). Raman spectra of the scanned worn zones of TiAl(16.09 at. % Mo)N coating tested under 2N and 5N shows, in addition to TiN and Mo_2N, a significant MoO_3 phase (peaks at 186.1, 640.1 and 789.2 cm^{-1}) able to act as a solid lubricant. This pattern also shows peaks corresponding to TiO_2 and it is consistent with the oxygen acting as a catalyst with the formation of lubricious molybdenum oxides [32].

Thus, molybdenum addition led to maintain a low friction coefficient during sliding test with the formation of MoO_3 phase, which is formed easily by the reaction between the molybdenum and oxygen/moisture at room temperature [33-34]. *Sergevnin et al.* [35] explained the improvement of wear resistance and the COF reduction of the molybdenum-based nitride films by the formation of Mo oxide in the friction zone after local heating, which acts as a good solid lubricant.

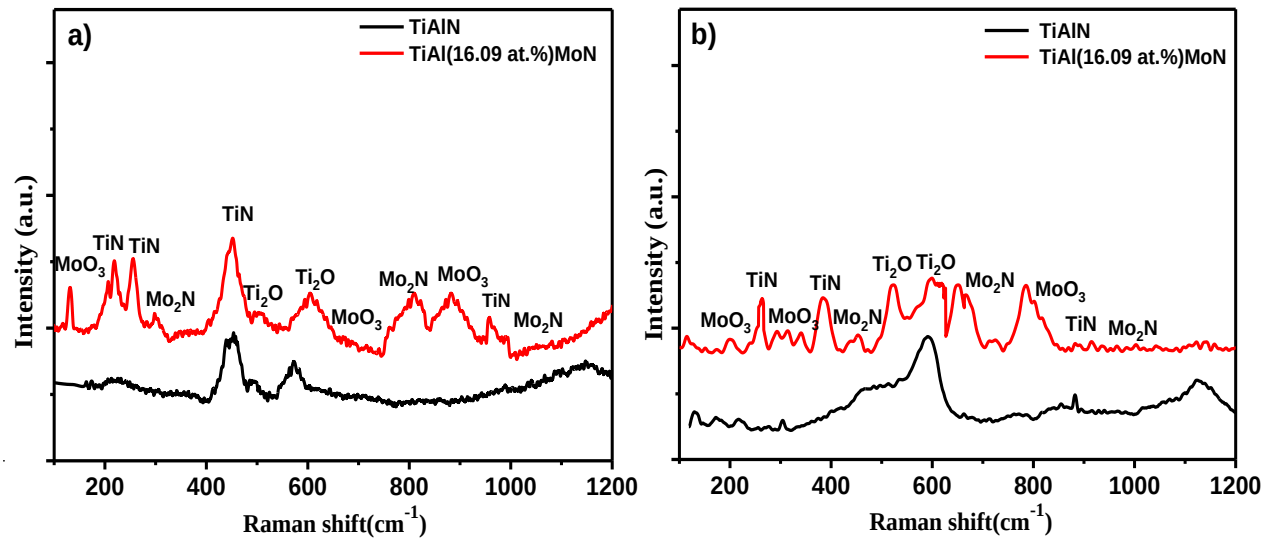

Fig. IV.18. Raman analysis of wear tracks of TiAlN and TiAl (16.09 at. % Mo)N coatings tested under: a) 2N and b) 5N normal loads.

IV. 7 Corrosion resistance

Open circuit potential curves (OCP) of cold sprayed SS316L substrate and TiN(Al, Mo) coatings were obtained by exposing the samples' surfaces to a simulated sea water for 1 hour. These curves are shown in *Fig. IV.19*. As shown from this figure, the OCP of the SS316L

substrate was -137 mV. The deposition of TiN, TiAlN and TiAlMoN coatings containing 3.19, 11.18, 16.09 and 26.14 at.% Mo on the substrates increased the OCPs to -88, -68, -54, -29, -7 and -12 mV, respectively.

The OCP values rapidly increased in the first 15 min for the SS316L, TiN- and TiAlN-coated samples. However, the TiAlMoN-coated samples stabilized after 5 min to higher values. With increasing the Mo content, the OCP shifted to more positive value and the coated sample behavior tended to a noble one. This indicates the formation of a passive layer on the surface that enhanced the corrosion resistance.

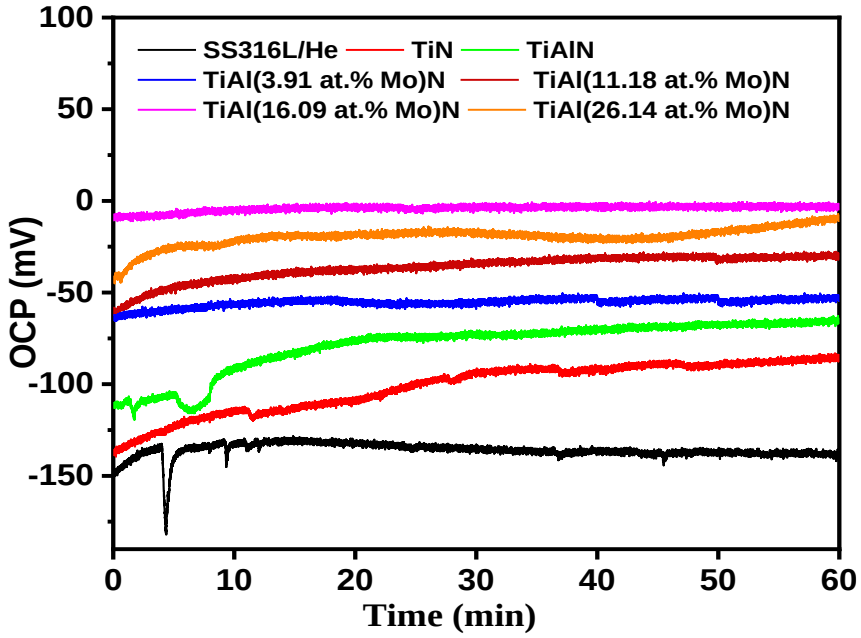

Fig. IV.19. Open circuit potential (OCP) of the cold sprayed stainless steel and the coated samples.

The results of corrosion tests are shown in *Fig. IV. 20* and the main corrosion parameters are listed in *Table IV. 3*. The cold sprayed SS316L had the worst corrosion resistance with the lowest noble potential of -157 mV and the highest corrosion current density (741.31 $nA.cm^{-2}$). With increasing Mo content in TiAlMoN coating, the corrosion potential and current density gradually improved to reach better values of -16 mV and 1.41 $nA.cm^{-2}$ (for the film containing 16.09 at.% Mo) providing the highest polarization resistance Rp of $78.73\times10^{2}(K\Omega.cm^{2})$. The same trend was reported by *Jia et al*. [36] for ZrMoN coatings doped with different Mo contents and tested in a 3.5 wt.% NaCl solution. However, a further increase in Mo content (26.14 at.%) led to decrease the corrosion potential.

The polarization curves indicate that a passive transition region was observed for all tested samples, suggesting that both cold sprayed SS316L and coated samples were spontaneously passivated in the 3.5% NaCl solution. When the applied potential reached Epit value, a sharp increase in the current density occurred as shown in *Fig. IV.20*, suggesting the growth of pitting corrosion [37]. *Table IV. 3* shows that the Epit value increased with the increasing of the Mo content in the TiAlMoN coating to a maximum value of 1268 mV (for the film containing 16.09 at.% Mo) corresponding to the largest passivation region ΔE (949 mV). This can be explained by the low susceptibility to pitting corrosion by the formation of Mo_2N phase which has a better self-corrosion potential in sea water (solution with 3.5 wt.% NaCl) than TiN and ZrN [36, 38]. On the other hand, the dense structure, the low surface roughness and the low wettability of TiAl (16.09 at. % Mo) N film can contribute to the enhancement of its corrosion resistance.

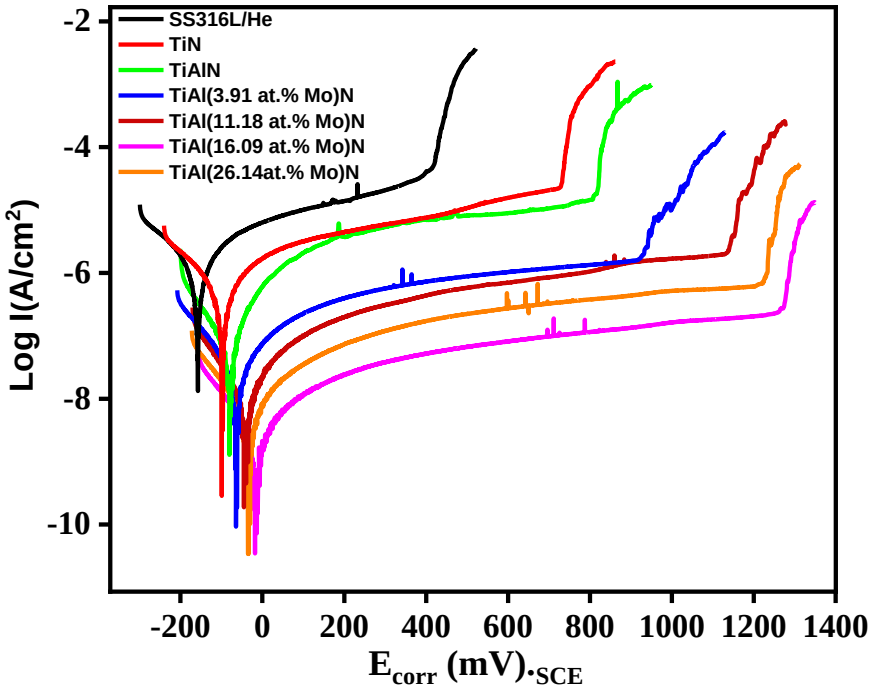

Fig. IV.20. Polarization curves of the cold sprayed stainless steel and the coatings immersed in a 3.5 wt % NaCl solution.

Table IV.3. Electrochemical parameters of the cold sprayed stainless steel and the coatings immersed in a 3.5 wt % NaCl solution.

	Ecorr(mV)	**Icorr(nA/cm^2)**	**Epit(mV)**	**ΔE(mV)**	**Rp(KΩ.cm^2)**
SS316L	-157	741.31	413	453	0.25×10^2
TiN	-98	281.83	728	587	1.00×10^2
TiAlN	-79	52.48	808	632	2.47×10^2
TiAl(3.91 at.%Mo)N	-63	11.22	915	723	9.37×10^2
TiAl(11.18 at.%Mo)N	-42	6.31	1130	850	16.98×10^2
TiAl(16.09 at.%Mo)N	-16	1.41	1268	949	78.73×10^2
TiAl(26.14 at.%Mo)N	-34	3.63	1219	924	37.07×10^2

Conclusion

In this chapter, we presented the TiN (Al, Mo) films elaborated by a RF reactive magnetron sputtering on stainless steel 316L cold-sprayed substrates. The effect of Mo content on the TiAlMoN coatings can be summarized as follows:

- TiN and TiAlN coatings exhibited a columnar growth and Mo addition to the TiAlN led to grain refinement.
- With increasing Mo content in TiAlN coatings, their Single-TiN phase (cubic structure) was transformed to TiN and Mo_2N mixed phases. This led to slightly increase the lattice parameters with high microstrain.
- A high Mo content in coating (≥ 16 at.%) led to obtain a dense morphology and smooth surface, high compressive stress, high contact angle (> 100°) and low surface energy.
- The high residual stress acting as obstacles against further dislocations movement in the TiAlMoN coatings resulted in a high increase in hardness, Young's modulus, H/E andH^3/E^2 ratio which are the important parameters for the wear resistance improvement.
- The tribological behavior was significantly improved with the Mo addition. Wear rate of the film containing 16.09 at.% of Mo was reduced to 1.534×10^{-6} and 0.849×10^{-6} mm^3/N under 2N and 5N loads, respectively. The enhancement of wear resistance is due to the smooth surface, high H/E ratio and the formation of TiO_2 and MoO_3 lubricating phases.
- The corrosion resistance of the cold-sprayed SS316L was enhanced by the protective deposited films. The best anticorrosion behavior was found for the film containing 16.09 at.% Mo.

This study confirms the great potential of hybrid process (Cold spray and Magnetron sputtering) to enhance the product properties. The stainless steel 316L cold-sprayed and then coated with TiAl(16.09 at.% Mo)N film presented the best tribo-mechanical behavior and corrosion resistance performance. It could be qualified as a good surface protection coating for different industrial applications, particularly recommended to be used for bearing, high-speed machining.

References

[1] A. Belgroune, A. Alhussein, L. Aissani, M. Zaabat, A. Obrosov, C. Verdy, C. Langlade. Effect of He and N_2 gas on the mechanical and tribological assessment of SS316L coating deposited by cold spraying process. J Mater Sci, 57 (2022) pp. 5258–5274.

[2] H. Jiménez, D. M. Devia, V. Benavides, A. Devia, Y. C. Arango, P. J. Arango, and J. M. Velez, Thermal protection of H13 steel by growth of (TiAl)N films by PAPVD pulsed arc technique, Materials Characterization, 59 (2008) pp. 1070–1077.

[3] S.P. Pemmasani, K. Valleti, R.C. Gundakaram, K.V. Rajulapati, R. Mantripragada, S. Koppoju, S.V. Joshi, Effect of microstructure and phase constitution on mechanical properties of Ti1−xAlxN coatings, Applied Surface Science, 313 (2014) pp. 936-946.

[4] K. E. Batista, J. L. Da Silva, M. J. Piotrowski, Ab Initio Investigation of the Role of Atomic Radius in the Structural Formation of Pt n TM55–n (TM= Y, Zr, Nb, Mo, and Tc) Nanoclusters. The Journal of Physical Chemistry C, 122(13) (2018) pp. 7444-7454.

[5] F. Salhi, L. Aissani, M. Fellah, A. Chadli, A. Cheriet, A. Belgroune, C. Nouveau, A. Obrosov, M.A. Samad, A. Alhussein, Experimental investigation of structural, wetting, mechanical and Tribological properties of TiZrN thin films deposited by magnetron sputtering, Surfaces and Interfaces, 27 (2021) 101519.

[6] L. Yu, H. Zhao, J.Xu, Mechanical, tribological and corrosion performance of WBN composite films deposited by reactive magnetron sputtering, Applied surface science, 315 (2014) pp. 380-386.

[7] H.C. Barshilia, K.J.J.o.a.p. Rajam, A Raman-scattering study on the interface structure of nanolayered Ti Al N⁄Ti N and Ti N⁄Nb N multilayer thin films grown by reactive dc magnetron sputtering, Journal of applied physics, 98 (2005) 014311.

[8] B. Ma, X. Wang, K. Lin, J. Li, Y. Liu, H. Zhan, W. Liu, A novel ultraefficient non-noble metal composite cocatalyst Mo_2N/Mo_2C/graphene for enhanced photocatalytic H_2 evolution, International Journal of Hydrogen Energy, 42 (2017) pp. 18977-18984.

[9] L. Lan, H. Yao, G. Li, X. Fan, M. Li, T. Qiu, Structural engineering of transition-metal nitrides for surface-enhanced Raman scattering chips. Nano Res. (2021).

[10] Y.W. Lin, H.A. Chen, G.P. Yu, J.H. Huang, Effect of bias on the structure and properties of TiZrN thin films deposited by unbalanced magnetron sputtering Thin Solid Films, 618 (2016) pp. 13-20.

[11] B. Touati, A. Gassoumi, N.K. Turki, Structural, optical and electrical properties of Ag doped PbS thin films: role of Ag concentration, J Mater Sci: Mater Electron, 28 (2017) pp. 18387–18395.

[12] J.C. Moreira, N.R. Demarquette, Influence of temperature, molecular weight, and molecular weight dispersity on the surface tension of PS, PP, and PE. I. Experimental J. Appl. Polym. Sci., 82 (2001) pp. 1907-1920.

[13] K.Y. Law, H. Zhao, Surface wetting: characterization, contact angle, and fundamentals, MRS Bull., 41 (2016) pp. 635-637.

[14] Z. Tang, H. Li, D.W. Hess, V. Breedveld, Effect of chain length on the wetting properties of alkyltrichlorosilane coated cellulose-based paper. Cellulose, 23 (2016) pp1401–1413.

[15] P. Xu, T.W. Coyle, L, Pershin, J, Mostaghimi, Fabrication of micro-/nano-structured super hydrophobic ceramic coating with reversible wettability via a novel solution precursor vacuum plasma spray process, Mater & Des, 160 (2018) pp. 974-984,

[16] Y. Tian, L. Jiang Wetting: intrinsically robust hydrophobicity Nat. Mater., 12 (2013), pp. 291-292.

[17] X. Pang, L. Zhang, H. Yang, K. Gao, A.A. Volinsky, Residual Stress and Surface Energy of Sputtered TiN Films, J. Mater. Eng. Perform., 24 (2015) pp. 1185-1191.

[18] C. Körber, J. Suffner, A. Klein Surface Energy Controlled Preferential Orientation of Thin Films J. Phys. D Appl. Phys., 43 (2010) 055301.

[19] M. Woydt, A. Skopp, I. Doerfel, K. Witke, Wear engineering oxides/anti-wear oxides, Wear, 218 (1998) pp. 84-95.

[20] L. Aissani, A. Alhussein, A. Ayad, C. Nouveau, E, Zgheib, A. Belgroune, M. Zaabat, R. Barille, Relationship between structure, surface topography and tribo-mechanical behavior of Ti-N thin films elaborated at different N_2 flow rates, Thin Solid Films,724 (2021) 138598.

[21] L. Aissani, A. Alhussein, C. Nouveau, L. Ghelani, M. Zaabat, Influence of film thickness and Ar-N2 plasma gas on the structure and performance of sputtered vanadium nitride coatings. Surf. Coat. Technol. 378 (25) (2019) 124948.

[22] P. Carvalho, F. Vaz, L. Rebouta, L. Cunha, C-J. Tavares, C. Moura. Structural, electrical, optical, and mechanical characterizations of decorative ZrOxNy thin films. Journal of applied physics 98 (023715) (2005) 1-8.

[23] M. Sarraf, B. Abdul Razak, A. Dabbagh, B. Nasiri-Tabrizi, N.H. Abu Kasim, W.J. Basirun, E. Bin Sulaiman, Nanomechanical properties, wear resistance and in-vitro characterization of Ta2O5 nanotubes coating on biomedical grade Ti-6Al-4V, Journal of the Mechanical Behavior of Biomedical Materials, 66 (2017) pp. 159-171.

[24] Q. Yang, Wear resistance and solid lubricity of molybdenum-containing nitride coatings deposited by cathodic arc evaporation, Surf. Coat. Technol, 332 (2017) pp. 283–295.

[25] K. Yang, G. Xian, H. Zhao, H. Fan, J. Wang, H. Wang, H. Du, Effect of Mo content on the structure and mechanical properties of TiAlMoN films deposited on WC–Co cemented carbide substrate by magnetron sputtering, Int. Journal of Refractory Metals and Hard Materials, 52 (2015) pp. 29–35.

[26] J. Hao, Y. Zhang, P. Ren, K. Zhang, J. Chen, S. Du, M. Wang, M. Wen, Spinodal decomposition in the Ta-Mo-Al-N films activated by Mo incorporation: toward enhanced hardness and toughness, Ceram. Int. 44 (2018) pp. 21358-21364.

[27] B. Tian, W. Yue, Zh. Fu, Y. Gu, Ch. Wang, J. Liu, Surface properties of Mo-implanted PVD TiN coatings using MEVVA source, Appl. Surf. Sci. 280 (2013) pp. 482–488.

[28] T. Suszko, W. Gulbinski, J. Jagielski, The role of surface oxidation in friction processes on molybdenum nitride thin films. Surf. Coat. Technol, 194 (2005) pp. 319–324.

[29] Q. Yang, L.R. Zhao, P.C. Patnaik, X.T. Zeng, Wear resistant TiMoN coatings deposited by magnetron sputtering, Wear, 261 (2006) pp. 119–125.

[30] S. Du, K. Zhang, M. Wen, P. Ren, Q. Meng, C. Hu, W. Zheng, Tribochemistry dependent tribological behavior of super hard TaC/SiC multilayer films, Surf. Coat. Technol. 337 (2018) pp. 492–500.

[31] Xu. Junhua, Ju. Hongbo, Yu. Lihua, Microstructure, oxidation resistance, mechanical and tribological properties of Mo–Al–N films by reactive magnetron sputtering, Vac, 103 (2014) pp. 21–27.

[32] P.H. Mayrhofer, C. Mitterer, L. Hultman, H. Clemens, Microstructural design of hard coatings, Prog. Mater. Sci., 51 (2006) pp. 1032-1114.

[33] V.S. Sergevnin, I.V. Blinkov, A.O. Volkhonskii, D.S. Belov, A.V. Chernogor, Structure formation of adaptive arc-PVD Ti-Al-Mo-N and Ti-Al-Mo-Ni-N coatings and their wear-resistance under various friction conditions, Surf. Coat. Technol. 376 (2019) pp. 38–43.

[34] S. Zhou, W. Zhao, Y. Wu, Z. Qiu, S. Lin, Z. Zheng, D.C. Zeng, Fabrication and characterization of high-performance Mo-doped TiN coatings Vac, 190 (2021) 110311.

[35] V.S. Sergevnin, I.V. Blinkov, A.O. Volkhonskii, D.S. Belov, D.V. Kuznetsov, M.V. Gorshenkov, E.A. Skryleva, Wear behaviour of wear-resistant adaptive nano-multilayered Ti-Al-Mo-N coatings, App. Surf. Sci, 388 (2016) pp. 13–23

[36] P. Ji, L. Yu, T. Sh, H. Ju, J. Xu, F. Gao, The effect of molybdenum content on microstructure, mechanical, tribological and corrosion behavior of Zr-Mo-N composite films. Materials Today Communications, 26 (2021) 101720.

[37] X. Hao, Q. Fan, Y. Li, R. Miao, J. Ma, H. Chen, X. Zhao, C. Wang, Structural, mechanical and corrosion behaviors of the homogeneous and gradient CrAlSiN coatings in 3.5% NaCl solution. Journal of Materials Research and Technology, 15 (2021) pp.2781-2791.

[38] J. Yang, Z. Yuan, G. Zhang, et al., Manufacture, microstructure and mechanical properties of Mo–W–N nanostructured hard films, Mater. Res. Bull. 44 (10) (2009) pp.1948-1953.

Chapter V

Elaboration and characterization of innovative TiMoON and TiMoON-Ag thin films for biomedical applications

Introduction

This chapter presents the development of a TiON-based thin film with more enhanced properties such as bacterial inactivation kinetics, stability, efficiency and adhesive properties. Innovative TiMoON and TiMoON-Ag films were prepared by RF magnetron sputtering in a N_2/O_2 gas atmosphere and subsequently annealed under vacuum at 400 °C.

The films were characterized by an atomic force microscopy (AFM), a scanning electron microscopy (SEM), a transmission electron microscopy (TEM), an X-ray photoelectron spectroscopy (XPS), an X-ray fluorescence (XRF) and contact angle (CA) measurements. The bacterial inactivation study was performed under simulated solar light irradiation.

The results of this chapter are presented and discussed in details. They were published as a research paper entitled "***Bacterial inactivation on sputtered TiOMoN and TiOMoN-Ag thin films under solar simulated light****" in the Chemical Engineering Journal, 2023.*

V. 1. Coating deposition and annealing treatment

TiMoON and TiMoON-Ag films were sputtered on glass (76×26×1 mm^3) and Si (100) wafers (10 mm×10 mm×480 μm) using magnetron sputtering technique with high purity Ti, Mo and Agtargets. The substrates were cleaned in acetone and subsequently ethanol by an ultrasonic bath for 10 min, then washed with distilled water and dried in air. The substrates were placed on a holder at 10 cm from the targets and sputtered with Ar gas for 15 min at 200 W to remove impurities and surface oxides. The three targets were sputter cleaned inAr for 15 min (100 sccm and 0.4 Pa) at powers: Ti (220 W, 1 A), Mo (239 W, 1 A), and Ag (280 W, 1 A). Once the substrates and targets were cleaned, the TiMoON-Ag coatings were deposited at floating temperature employing a total working pressure of 0.4 Pa in an $Ar/N_2/O_2$ atmosphere. The gas flow rates of (70 sccm Ar), (15 sccm N_2) and (5 sccm O_2) were monitored by flow controllers HORIBASTEC (Ether CAT, N100). Subsequently, the TiON(Mo, Ag) films were deposited at the powers applied to the targets: Ti (600 W, 2 A), Mo (57 W, 0.3 A),and Ag (2, 4, 6, 8, 10) W corresponding respectively to (0.02, 0.03, 0.04, 0.05, 0.06) A. The rotation of the substrate-holder was set at 10 rpm.

The annealing process was carried out at low pressure of 10^{-3} mbar at 400 °C. The heating ramp was adjusted to 2 °C/min up to the target temperature, at which the sample was kept for

80 min. The samples were pre-heated at 200 °C for 20 min. A pressure of 10^{-5} Pa was set by a diffusion pump. Finally, the sample cooling was carried out at a -10 °C/min rate.

V. 2 Antibacterial procedure

V. 2.1 Monitoring of the bacterial inactivation

Escherichia coli (*E. coli K12*) bacterium was obtained from the Deutsche Sammlung von Mikroorganismen und Zellkulturen GmbH (DSMZ), Braunschweig, Germany. Each sample was placed into a glass Petri dish then inoculated with bacteria. The 100 µL culture aliquots with an initial concentration of 4.3×10^{6} colony-forming unit per milliliter (CFU mL^{-1}) in NaCl/KCl were placed on coated and uncoated (control) samples. After preselected times, the samples were transferred into a sterile tube containing 900 µL autoclaved NaCl/KCl saline solution. This solution was subsequently mixed thoroughly using a Vortex for 2 min. Serial dilutions were made in NaCl/KCl solution. A 100 µL sample of each dilution was pipetted onto a nutrient agar plate and then spread over the surface of the plate using the standard plate method. Agar plates were incubated lid down to prevent evaporation for a period of 24 h before the colonies counting. Experiments were carried in triplicates and statistical analysis show standard deviation error bars (± SD, n = 5 %). Solutions and samples were autoclaved before use at 121 °C.

V. 2.2 Genetically modified bacteria for intracellular bacterial inactivation testing

Genetically modified *E. coli* mutant strains deficient in OmpF and OmpCporins (*Outer membrane Channel Proteins F, C*) were prepared according to protocols previously reported [1]. This approach allowed comparing the bacterial inactivation kinetics induced by: (i) the ions able to penetrate inside the cell, or (ii) by contact of the bacteria with the coated/sputtered surface. The genetically modified porinless *E. coli* TK 821 is is ogenic with K12 ATCC (American Type Cell Culture) bacterial strain. Both bacteria contain genotypes that reproduce indefinitely and remaining stable for many generations. The culture conditions used for the *E. coli* and the genetically modified *E. coli* were identical to limit the differences in growth of both strains.

V. 2.3 Irradiation procedures and methodology

The irradiation of the *E. coli* on the TiON(Mo, Ag) samples was performed under solar simulated light (*CPS Suntest System, Atlas GmbH, Hanau, Germany*) with an emission between 320 and 800 nm with light dose of 50 mW/cm^2. This solar simulator was equipped with a quartz glass light tube, a filter E and an IR screen. In this way neither the UVC (Ultraviolet C) nor the IR (Infrared radiation) could reach the samples during the preset irradiation time. The samples were placed in the closed cavity of the solar simulated at 22 cm from the light source. The irradiance was measured by a radiometer/pyranometer (ILT-900-R). The global light irradiance reaching the samples was estimated to be ~0.5% UVB (Ultraviolet B), ~5% UVA (Ultraviolet A) and ~94.5% visible wavelengths. The temperature inside the light cavity was < 35 °C using an integrated ventilation system.

V. 2.4 Determination of the reactive oxidative radicals (ROS) leading to *E. coli* inactivation

Photocatalytic inactivation of bacteria in aerobic conditions proceeds by highly oxidative radicals $^{\bullet}OH$, $HO_2^{\bullet}/O_2^{-}$ and the photogenerated holes (h^+). The scavenging experiments by dimethyl-sulfoxide (DMSO, 2 mM), superoxide dismutase (SOD, 2 mM) and Ethylene tetra-acetic acid di-sodium salt (EDTA-2Na, 2 mM) were carried out to detect/identify the $^{\bullet}OH$, O_2^{-} and $v_b(h^+)$ generated in solution during the bacterial inactivation process.

V. 3. Structure and Composition

The chemical composition of TiMoON-Ag films determined by EDS is shown in *Table V. 1*. This Table shows that the increase of Ag concentration from zero to 13 at. % led toa concomitant decrease in the (Ti/Mo/N) concentrations. The Ti-content changed from 44.2 to 31.7at. %, and the content of Mo from 8.8 to 5.3 at.%. The total pressure Ar/(P_{N2} + P_{O2}) in the sputtering chamber was maintained constant during all depositions. The decrease of Ti and Mo concentration in the films is attributed to the replacement of (Ti, Mo) by Ag. When Ag was added to the TiMoON films, the progressive increase of the (N+O)/(Ti+Mo) ratio suggests the formation of hyper-stoichiometric films.

Annealed TiMoON-Ag films at 400 °C showed an accumulation of Ag on the film surface at the expense of other elements (see *Table V. 1*). Similar results were reported for annealed

TiSiAgN films deposited by RF magnetron sputtering [2]. According to Table1, the (N+O)/(Ti + Mo) ratio for the annealed TiMoON-Ag films is < 1. This means that the annealed TiMoON-Ag films present nitrogen/oxygen interstitial vacancies responsible for lower N-stoichiometry and higher metal stoichiometry. The high metal stoichiometry is due to the vacancies in the film topmost layers by Ag. XRD and EDS analyses showed the increase of Ag on the topmost layers of the film after annealing. This observation was further confirmed by the TEM images analysis of the TiMoON-Ag films presented in section V.4.

Fig. V. 1 shows grazing X-ray diffraction spectra of TiMoON films with different Ag contents before and after annealing at a temperature of 400 °C. TiMoON and TiMoON-Ag films containing low Ag concentration (3-5.3 at. %), the XRD patterns reveal four distinct peaks (111), (200), (220) and (311) at 25.3, 48.1, 55.0 and 62.7°, respectively, corresponding to a cubic-TiON structure (ICDD card no. 01-087-0633) with a (111) preferred orientation [3]. An increase in the Ag content up to 7.4 at. % led to a decrease of (111)/(200) peak intensity and the appearance of (111) and (200) of Ag planes. This observation suggests the formation of TiON and Ag-mixed phases. The diffraction peaks shift to higher angles of TiON peaks due to the substitution of Ti by Ag-atoms. The lattice parameter of the cc-TiON gradually decreased from 0.441 to 0.422 nm with a concomitant increase of Ag content due to the incorporation of Ag in the TiON. However, the crystallite size decreased with the incorporation of Ag then increased at a higher Ag content, as seen in *Table V. 2*. The annealing of the TiMoN-Ag films at 400 °C led to the formation of overlapping peaks of Ag and TiON with the (111) TiON preferential peak. This suggests that a part of silver was partially incorporated in the TiON lattice. No molybdenum phases were identified by XRD in agreement with *Juet al.* [4].

TableV. 1. Chemical composition of TiMoON-Ag films determined by (EDS).

Chemical composition (at. %)												
Coatings	As-deposited films						After annealing treatment at 400 °C					
	Ti	N	O	Mo	Ag	N-O/Me	Ti	N	O	Mo	Ag	N-O/Me
TiMoNO	44.2	29	18	8.8	-	0.88	44	29.2	18.2	8.6	-	0.88
TiMoNO-(3at.%Ag)	41.6	28.7	18.3	8.3	3	0.89	41.6	28.7	18.2	8.5	3	0.88
TiMoNO-(5.3at.%Ag)	39.4	28.6	19.4	7.27	5.3	0.92	38.4	28.3	19.4	7.1	6.72	0.91
TiMoNO-(7.4at.%Ag)	36.6	28.4	21.4	6	7.4	1.0	37.2	28.3	20.4	6.0	8.1	0.95
TiMoNO-(9 at. %Ag)	35.2	27.5	22.4	5.8	9	1.01	37.5	27.2	18.4	6.4	10.4	0.97
TiMoNO-(13at. %Ag)	31.7	27.2	22.8	5.3	13	1.0	31.5	26.4	22.5	5	14.6	0.96

Table V. 2. Lattice parameter, crystallite size and RMS roughness of TiMoON-Ag films.

Coatings	As-deposited films			After annealing treatment at 400 °C		
	Lattice Parameter (nm)	Crystallite size (nm)	RMS roughness (nm)	Lattice Parameter (nm)	Crystallite size (nm)	RMS roughness (nm)
TiMoNO	0.441	67	13.5	0.442	75	13.2
TiMoNO-(3 at. %Ag)	0.438	65	13.7	0.437	67	13.9
TiMoNO-(5.3 at. %Ag)	0.435	38	19.2	0.436	45	20.5
TiMoNO-(7.4 at. %Ag)	0.427	24	20.1	0.428	28	20.3
TiMoNO-(9 at. %Ag)	0.427	31	15.8	0.424	31	14.5
TiMoNO-(13 at. %Ag)	0.422	35	9.9	0.421	32	13.8

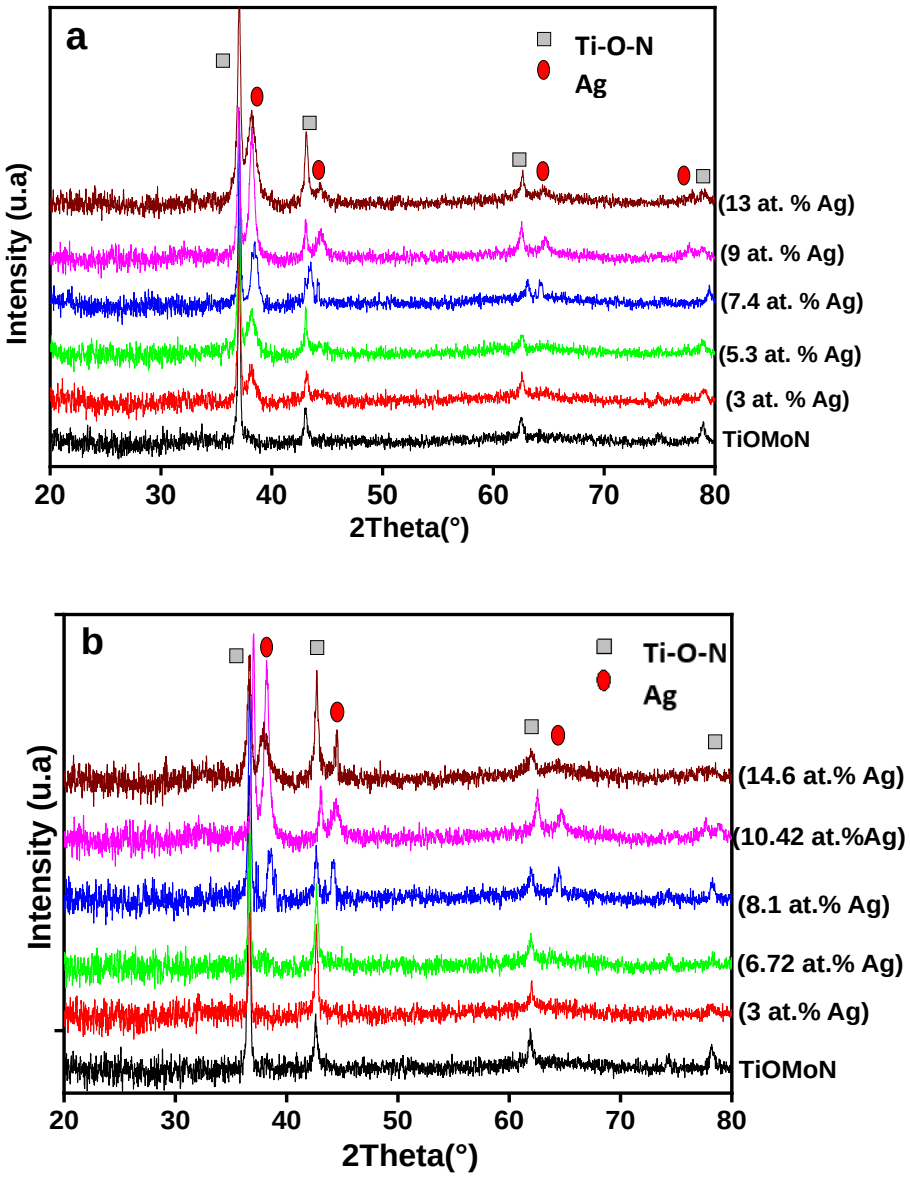

Fig. V.1. XRD diffraction patterns acquired in grazing incidence mode for TiMoON-Ag films deposited with different Ag contents: a) before and b) after annealing at 400 °C.

V. 4 Morphology of the prepared TiMoON-Ag thin films

The surface morphology of the TiMoON films with different Ag contents was observed by a scanning electron microscope (SEM). The metal ions (Ti^+, Mo^+ and Ag^+) in the plasma react with nitrogen and oxygen. The results are shown in *Fig. V. 2*. TiMoON film exhibits a uniform pyramidal-like structure with few pinholes and defects. With increasing Ag content, the surface morphology of the TiMoON-Ag films became denser with fine grain and white spherical particles of Ag appeared on the film surface. After annealing at 400 °C, the Ag particles became larger as shown by the white spots below in *Fig. V. 3*.

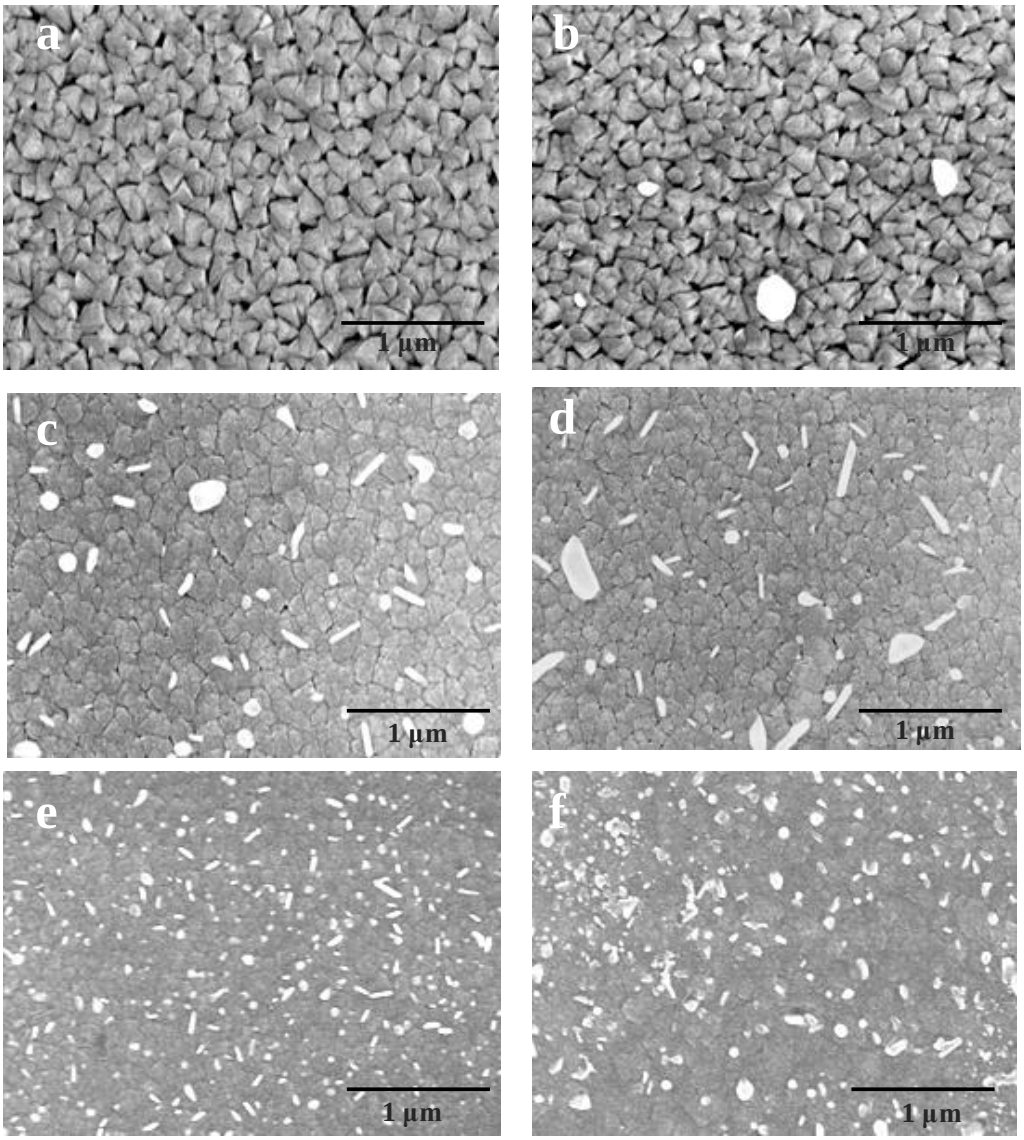

Fig. V.2. SEM images of surface morphology ofthe films: a) TiMoON, b) TiMoON-(3 at. %Ag), c) TiMoON-(5.3 at. %Ag), d) TiMoON-(7.4 at. %Ag), e) TiMoON-(9 at. %Ag), and f) TiMoON-(13 at. %Ag).

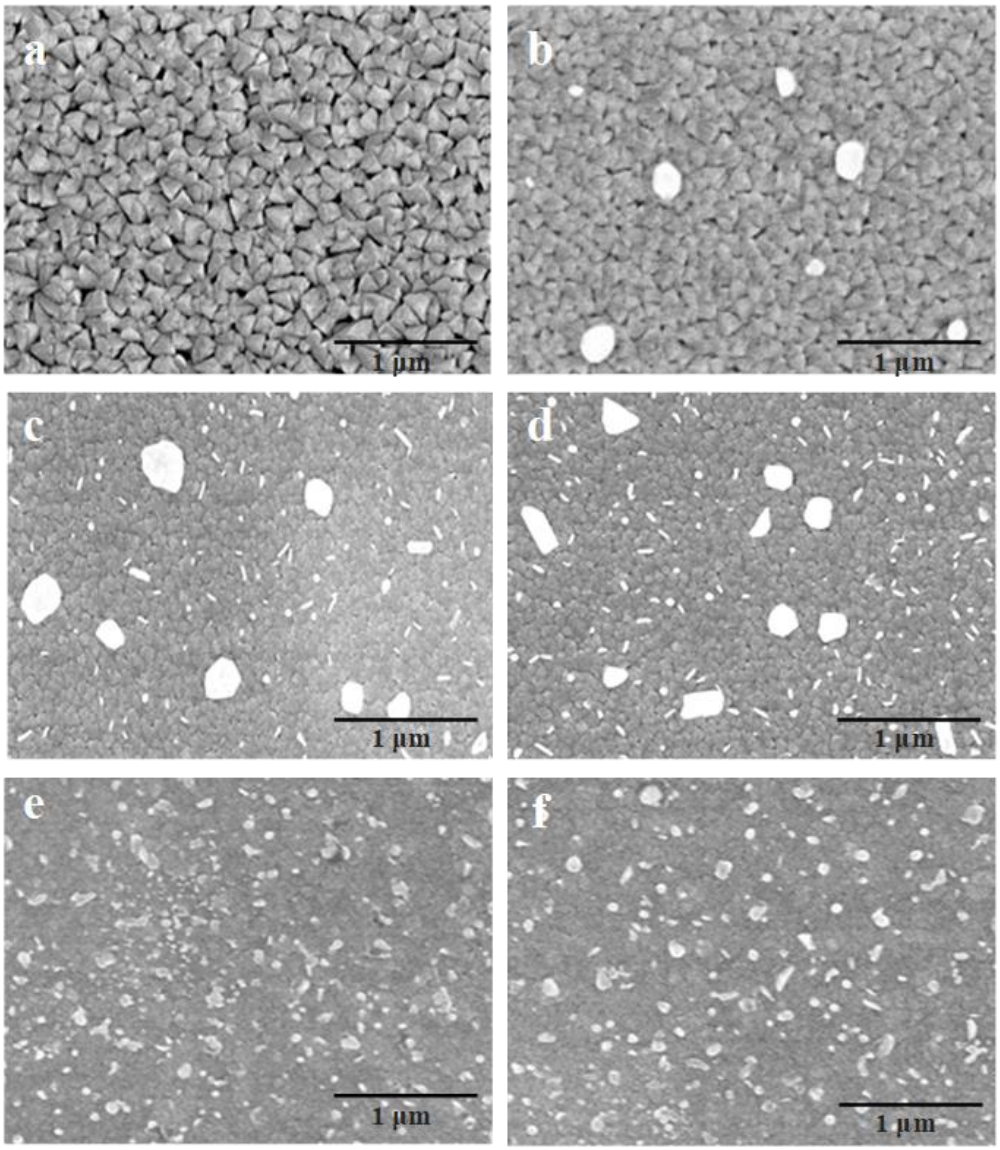

Fig. V. 3. SEM images of surface morphology of the films annealed at 400 °C: a) TiMoON, b) TiMoON-(3 at. %Ag), c) TiMoON-(6.72 at. %Ag), d) TiMoON-(8.1 at. %Ag), e) TiMoON-(10.42 at. %Ag), and f) TiMoON-(14.6 at. %Ag).

Fig. V. 4 shows the transmission electron microscopy (TEM) images of TiMoON-Ag film containing 7.4 at. % of Ag. *Fig. V. 4c, d* shows Ag-agglomerated nanoparticles of 40 nm distributed in film annealed at 400 °C. Nanotube shaped spots were observed on the film surface. According to TEM image of *Fig. 4a*, the size of the pure TiOMoN particles is in the range of 24–28 nm as obtained by *Scherrer* equation (*Table V. 2*).

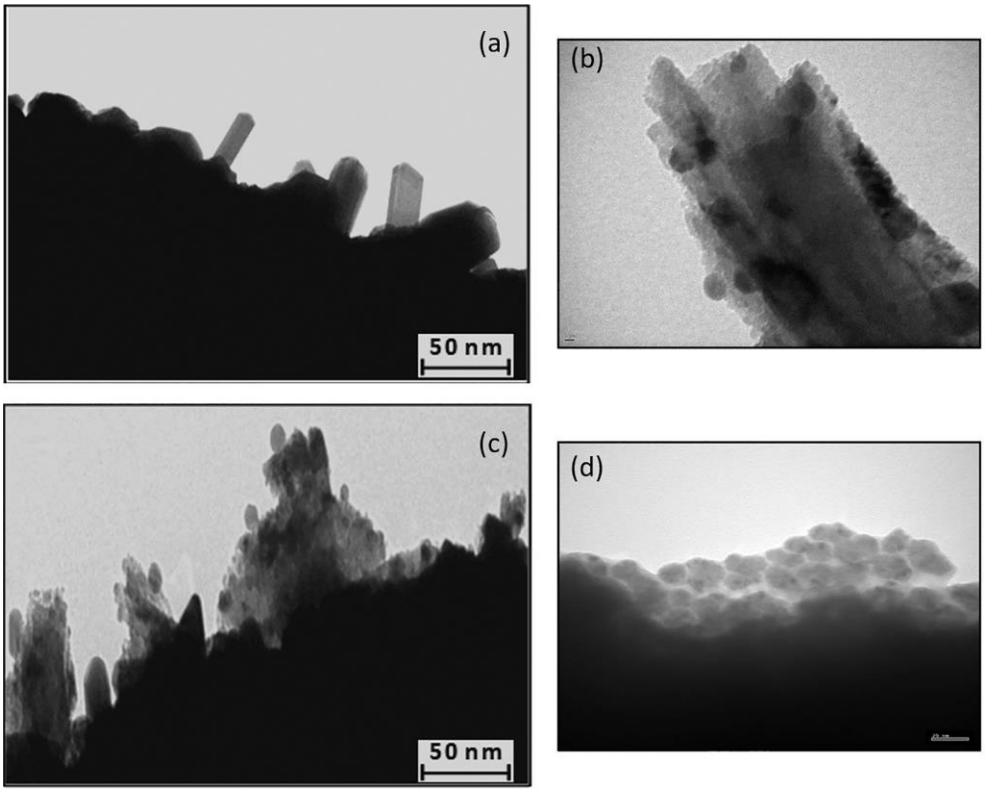

Fig. V.4.TEM cross section morphology of TiMoON-(7.4 at. %Ag) film: a + b) before annealing, and c + d) after annealing at 400 °C.

Fig. V. 5 presents the XPS spectra of Ti2p, O1s, Ag3d and Mo3d of TiMoON-(7.4 at. % Ag) film before and after annealing at 400 °C. Peaks deconvolution was performed for the peaks of each element. The Ti $2p_{3/2}$ and $Ti2p_{1/2}$ peaks indicate binding energies of 457.55 and 465.48 eV, respectively in *Figure V. 5a*. After deconvolution, the Ti $2p_{3/2}$ spectrum consists of three distinct peaks at 455.8, 457.6 and 460.2 eV corresponding to TiN, TiON and TiO_2, respectively [5]. After annealing at 400 °C (*Fig. V.5b*), a small shift to lower binding energy confirms an increased oxygenation of the TiON lattice. The deconvoluted O1s spectrum shows the Ti-O, Ti-O-N and N-O binding energies at 529.9, 531.1 and 533.9 eV in *Fig. V.5c* [6]. After annealing treatment, the Ti-O peak becomes stronger with a decrease in the Ti-O-N peak intensity due to the bonding of oxygen atoms with titanium atoms. The Ag $3d_{5/2}$ spectra show a high peak located at 368.54 eV corresponding to the binding energy of the AgO along with appear small peaks at 368.5 eV (Ag) and 370.3 eV (Ag_2O) (*Fig. V.5e*) [7]. The transformation of Ag to an oxide after annealing was confirmed by XPS analysis. *Fig. V.5f* presents film annealed at 400 °C showing the AgO peak of high intensity significantly shifted with respect to the Ag peak position.

The Mo3d deconvoluted peaks in *Fig. V.5g* showed the presence of three multi-components: Mo_2O_5 at 230.1 eV, Mo_3O at 231.17 eV and MoN at 232.8 eV. After annealing treatment, the atomic ratio Mo_2O_5/Mo_3O slightly increased while that of MoN decreased as compared before annealing treatment. This suggests that the nitrogen in the TiMoON-(7.4 at. %Ag) film was replaced by oxygen leading to molybdenum oxide (MoO_2) but without changing the oxidation state of Mo [8].

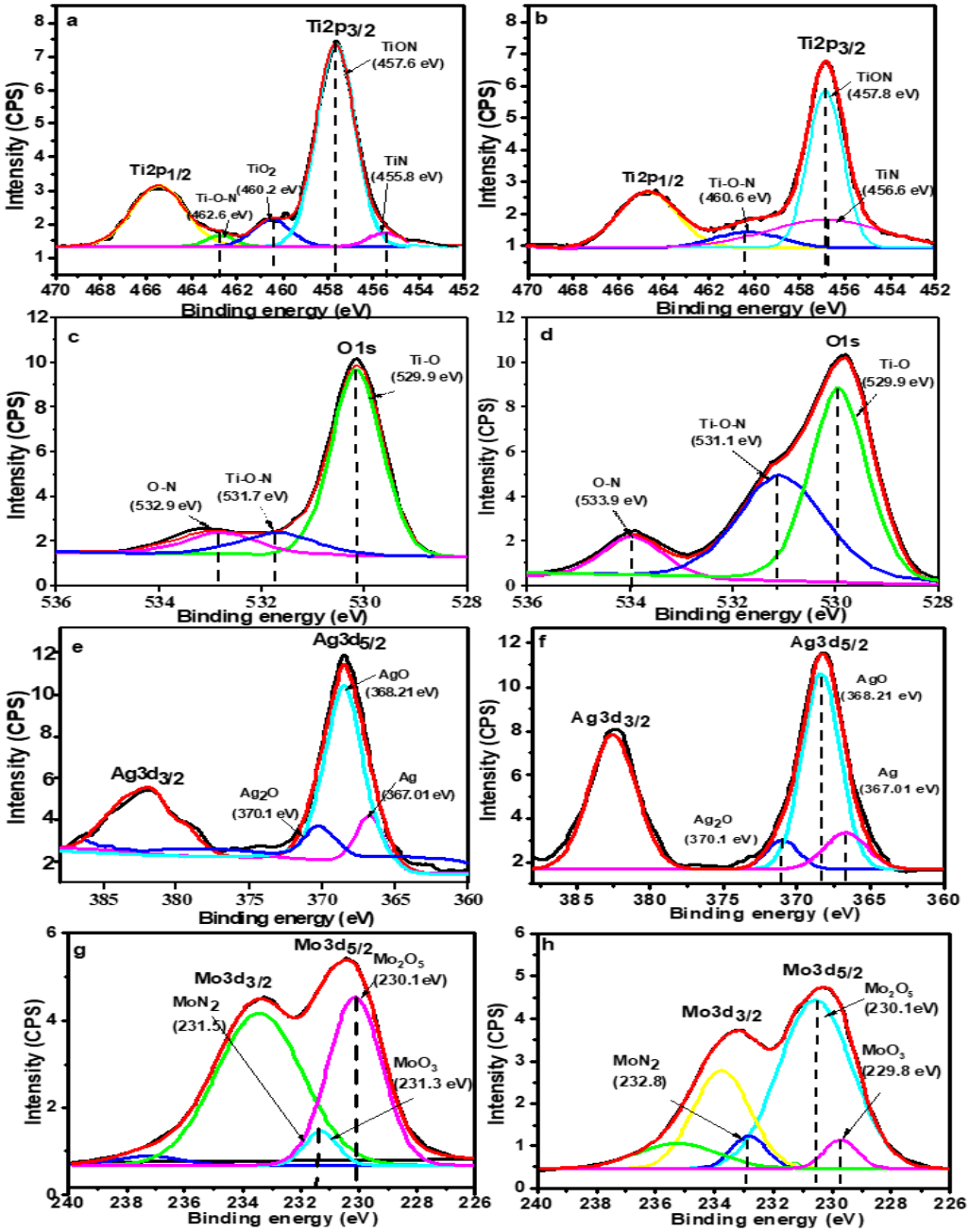

Fig. V.5. XPS spectra of: a) Ti2p, c) O1s, e) Ag3d, and h) Mo3d of the as-deposited TiMoON-(7.4 at. %Ag) film, and b) Ti2p, d) O1s, f) Ag3d, and g) Mo3d after annealing at 400 °C.

V. 5 Wetting Property

Fig. V.6 shows dynamic water contact angle measurements on TiMoON-Ag films deposited on glass before and after annealing treatment at 400 °C. Wetting is higher on TiMoON-Ag films (*Fig. V. 6a*) than in the case of the annealed films (*Fig. V. 6b*). Ag addition and increasing its content in TiMoON film to 7.4 at. % increased the contact angle from 98° to 121°. Films showing a higher contact angle present increased antimicrobial properties/surface roughness [9]. This angle decreased to 115° and 108° for the films containing 9 at. % and 13 at.% of Ag, respectively. Ag-based films are predominantly hydrophobic [10] and the root mean square (RMS) values of the films increase with Ag content as observed for the TiOMoN films. Annealing treatment led to diffuse the Ag through the TiMoON films. Ag particles agglomerate during the film annealing resulted in higher RMS value. The higher hydrophobicity of films will help to prevent water droplets permeation on the film surface [11].

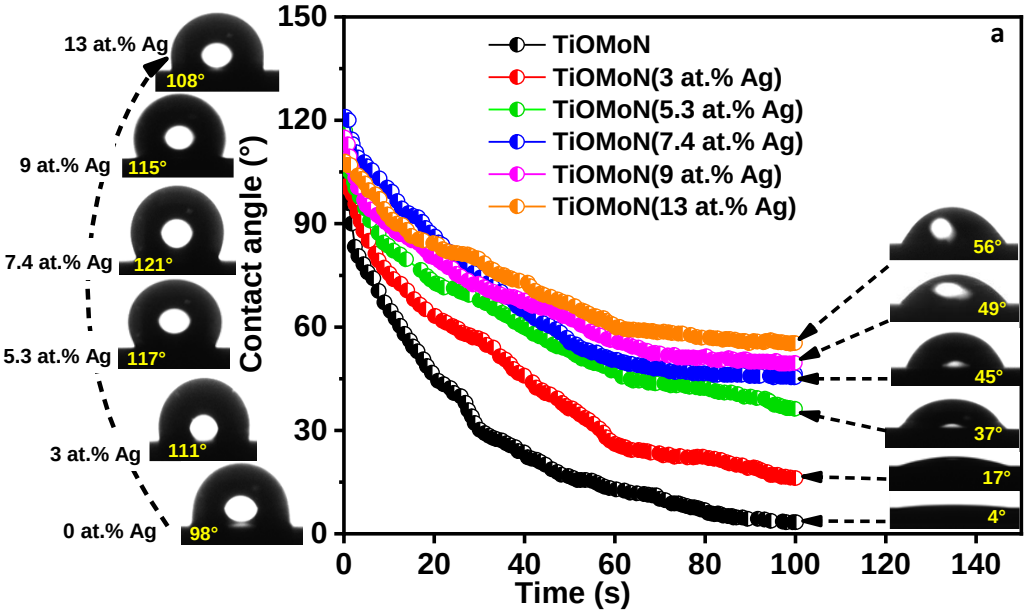

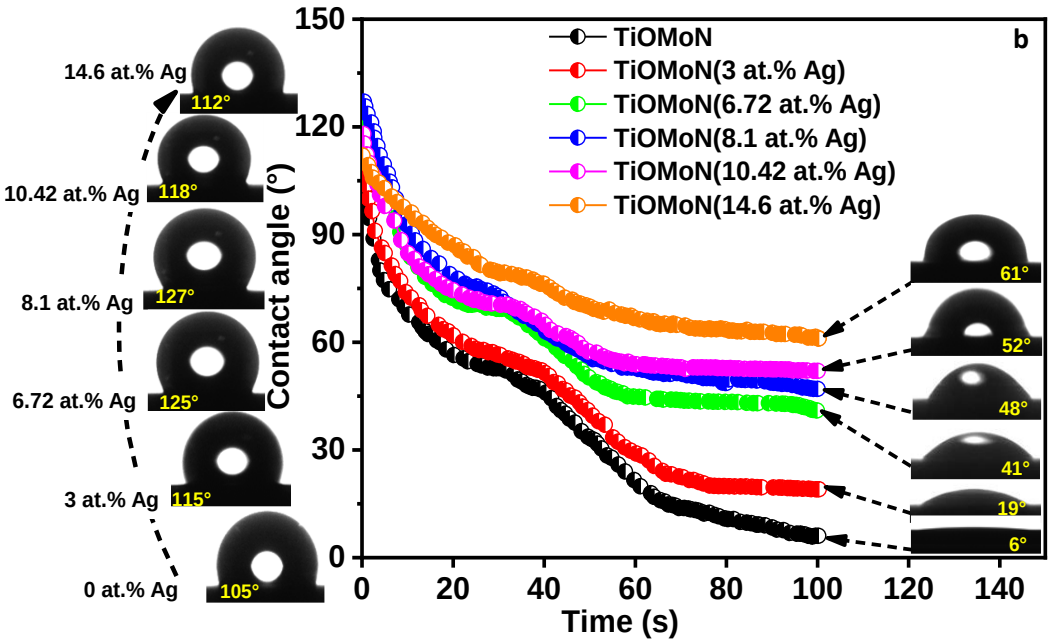

Fig. V. 6. Contact angles of water droplets on TiMoON films deposited with different Ag contents: a) before and b) after annealing treatment at 400 °C.

V. 6 Inactivation kinetics of *E. coli* on TiOMoN-Ag sputtered films

Fig. V.7 shows *E. coli* inactivation on TiOMoN-Ag films under solar simulated light (50 mW/cm^2, 320–800 nm). The addition of Ag to the TiOMoN films led to an acceleration of the bacterial inactivation kinetics in the samples TiOMoN-Ag with 5.3 at. % and 7.4 at. % Ag. These samples presented crystallite sizes (38-24 nm) and RMS roughness of 19.2 nm and 20.1 nm, respectively (*Table V. 2*). High RMS surface roughness means that the film surface presents a high peak density enabling to interact with *E. coli* [12].

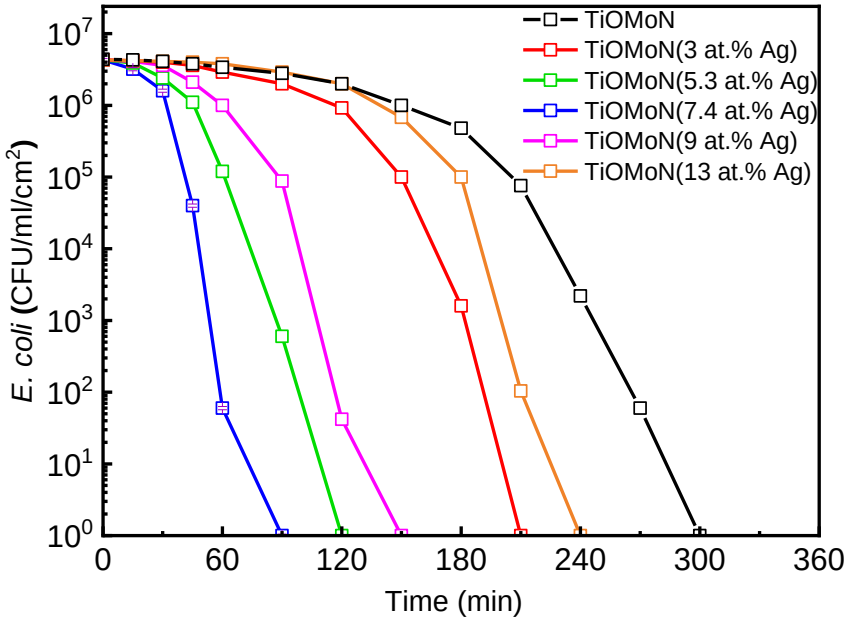

Fig. V.7. Bacterial inactivation on TiOMoN and TiOMoN-Ag coatings under solar simulated light.

V. 6.1 Mechanism suggested for TiOMoN-Ag films leading to bacterial inactivation

Four considerations may be taken into account to rationalize the TiOMoN-Ag mediated bacterial inactivation:

a) The residual H_2O ($\sim 10^{15}$ molecules/cm^2) in the sputtering chamber with a residual pressure of 4×10^{-4} Pa decomposes leading to the evolution of O_2,

b) The TiOMoN-Ag films further oxidize after sputtering when exposed to air,

c) The autoclaving at 121°C used during sterilization prior to the use leads to surface oxidation,

d) The Ag^+ positive charge on the film interacts with the -COO^- and other negatively functional groups of the bacterial envelope.

In the presence of air (O_2) and air humidity, Ag in the film leads to AgOH. The later species decomposes spontaneously to Ag_2O:

$$2AgOH \rightarrow Ag_2O + H_2O \qquad (pk= 2.87) \qquad (V.\ 1)$$

Ag_2O generates of Ag^+ and $HO^{\cdot -}$-ions as shown by *Eq. V. 2*.

$$2Ag_2O + 2H_2O \rightarrow 4Ag^+ + 4HO^{\cdot -} \qquad (V.\ 2)$$

Ag_2O is thermodynamically stable in the region of pH (6–8), which is required for the survival of *E. coli* [13] and absorbs light in the range of the solar spectrum [14-17] generating holes and electrons as shown below:

Ag_2O^+ light (solar simulated light) → $Ag_2O(h^+) + Ag_2O(e^-)$ (V. 3)

$Ag_2O + e^- \rightarrow 2Ag^\bullet + ½O_2{}^{-v}$ (V. 4)

The O_2 in *Eq. V. 4* promotes reactions:

$2e^- + 2H_2O + O_2 \rightarrow 2OH^\bullet + 2OH^{\bullet-}$ (V.5)

$e^- + O2 \rightarrow O_2^{\bullet-}$ (V. 6)

$h^+ + H_2O \rightarrow OH^\bullet + H^+$ (V. 7)

TiO_2 in the films also leads to $OH^{-\cdot}$ radicals [18-22]:

TiO_2+ light (solar simulated light) → $TiO_2(h^+) + TiO_2(e^-)$ (V. 8)

$h^+ + H_2O \rightarrow OH^\bullet + H^+$ (V. 9)

$h^+ + OH^- \rightarrow OH$(V. 10)

$e^- + O_2 \rightarrow O_2^{\bullet-}$ (V. 11)

$O_2^{\bullet-} + H^+ \rightarrow H_2O^\bullet$ (V. 12)

$2H_2O^\bullet \rightarrow O_2 + H_2O_2$ (V. 13)

$H_2O_2 + O_2^{\bullet-} \rightarrow HO^\bullet + OH^- + O_2$ (V. 14)

$HO^\bullet$+ bacteria → cell death (V. 15)

The third bacterial inactivation mechanism is due to MoO_3 leading to formation of H_3O^+ through surface acidic reactions which subsequently reacts with H_2O:

$MoO_3 + H_2O \rightarrow H_2MoO_4$ (V. 16)

$H_2MoO_4 + H_2O \rightarrow MoO_4^- + 2H_3O^+$ (V. 17)

The *E. coli* inactivation mechanism is presented graphically in *Fig. V.8*. The Ag^+ cations anchor on the cellular membrane, which is coordinated with H_3O^+ ions. The later species enters the cell wall affecting the respiration cycle of *E. coli* [23-24]. MoO_3 presents a similar pattern to inactivate bacteria [25-26]. *Bogdan et al. [27] and Nesic et al.* [28] presented the experimental evidence for electrons in the conduction band reacting with the adsorbed O_2 on TiO_2 to yield $HO_2^{\bullet-}$radical anions and highly oxidative radicals attacking the inner cell wall membrane and leading to cell death.

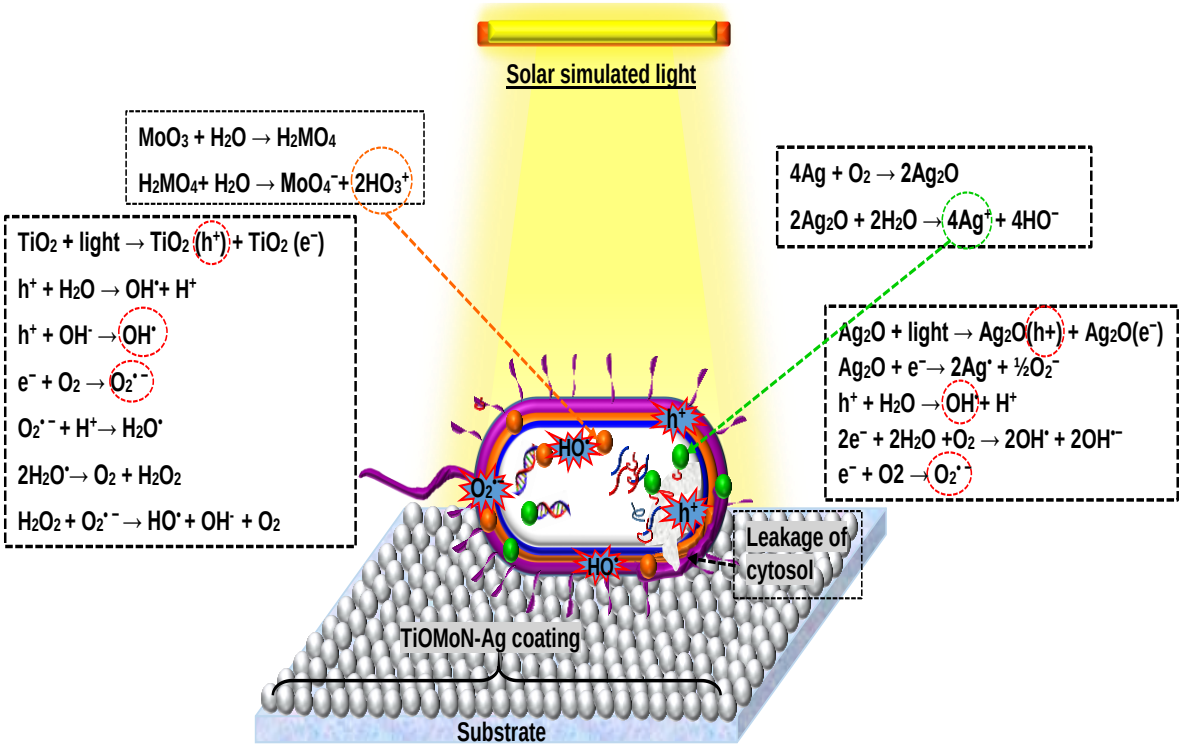

Fig. V. 8. Schematic diagram illustrating the bactericidal inactivation mechanism of TiOMoN-Ag films.

V. 6.2 Effect of film annealing on the bacterial inactivation

Fig. V.9 shows the *E. coli* inactivation on annealed TiOMoN and TiOMoN-Ag films under solar light (50 mW/cm^2, 320–800 nm). During annealing at 400 °C, Ag immigrates to the film surface as seen in SEM surface and TEM images (*Figs V. 2-4 and Table V. 1*). The film with 3 at. % Ag with a smoother surface (RMS = 13.9 nm) presented a lower bacterial

inactivation of *E. coli* as compared to TiOMoN-6.72 at. % Ag with a higher RMS value of 20.5 nm (*Fig. V. 9 and Table V. 2*).

The Ag agglomeration in the films with higher Ag content (10.42 and 14.6 at. % Ag) led to the degradation of inactivation kinetics on films presenting RMS values of 14.5 nm and 13.8 nm, respectively (*Figs V. 3 e-f and V.9, Tables V.1 et V. 2*).

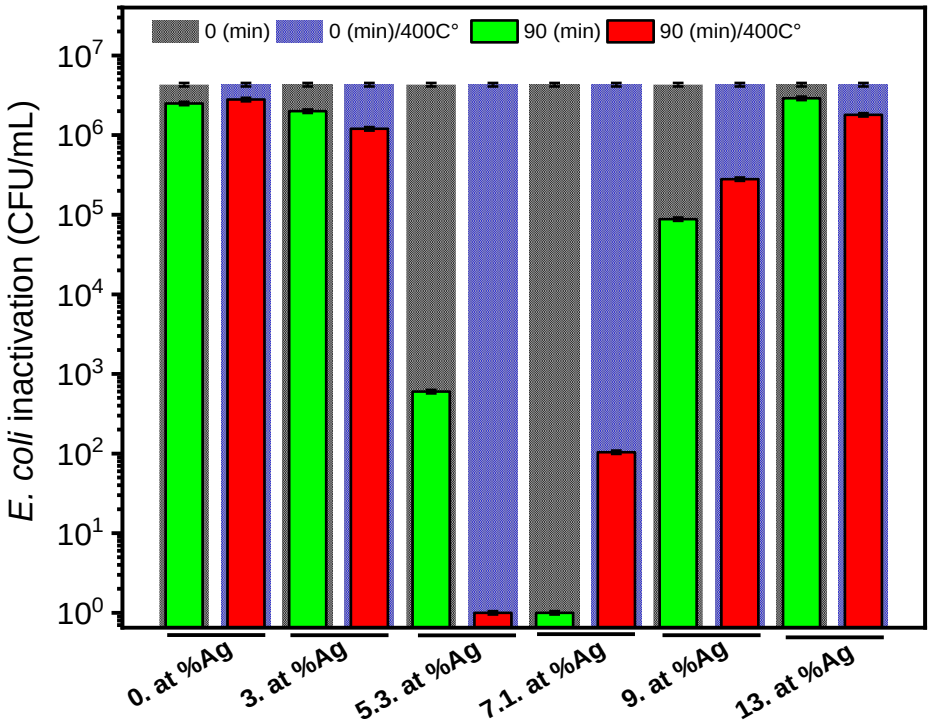

Fig. V. 9. Effect of the annealing treatment on the bacterial inactivation on TiMoON-Ag films containing different Ag contents.

V. 6.3 Bacterial inactivation of normal and porinless E. coli on TiMoON-7.4 at. %Ag films

Fig. V. 10 presents the bacterial inactivation results under solar simulated light (50 mW/cm^2, 320–800 nm) for normal and porinless *E. coli* on the TiOMoN-7.4 at. % Ag film. *Fig. V.10* shows that the bacterial inactivation took 90 minutes for normal *E. coli* and 150 min for porinless *E. coli*. In the case of normal *E. co*li, the Ag^+ diffuse through the *E. coli* cell wall porins from the first contact (time zero) due to Ag^+-ions associated with $Ag/Ag_2O/AgO$-oxides. This leads to a fast bacterial inactivation compared to porinless *E. coli* (*Fig.V. 10*). In the case of the porinless bacteria, the $Ag/Ag_2O/AgO$-oxides in a first stage process damage the outside cell wall integrity and only after this initial stage is completed, Ag^+-ions translocate through the

cell wall into the cell cytoplasm leading to bacterial death [24-30]. In the later process, the damage of the cell envelope was due to the change in local pH, denaturation of the cell functional groups, cell size and shape and changes in the surface cell potential [29].

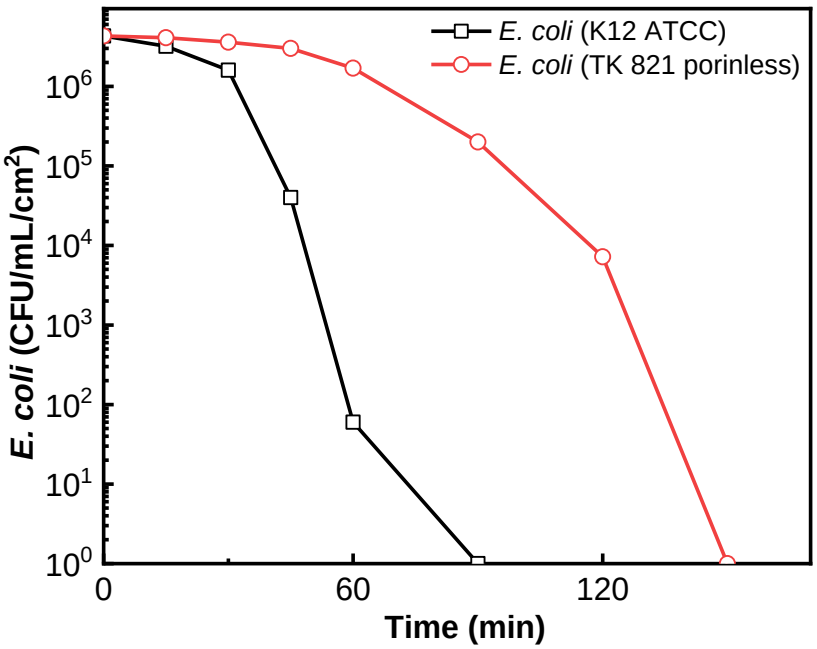

Fig. V.10. Bacterial inactivation of normal and porinless *E. coli* on TiMoON-7.4 at. %Ag film.

V. 6.4 Stereomicroscopy of E. coli on Stained Bacteria Samples

Fig. V. 11 presents the stereomicroscopy images captured on the TiOMoN-7.4 at. % Ag film in the dark and under light as a function of the disinfection time. The green dots represent the living bacteria, while the red dots present dead bacteria. The red color is due to the fluorochrome that enters the cell and stains the DNA-cytoplasm, when the cell wall membranes are damaged [31]. After 15 min in the dark, only green dots were observed. Under light irradiation after 60 min, red dots with some of the green cells are seen in *Fig. V. 11*, indicating partial bacterial inactivation that is completed afterwards beyond 90 min.

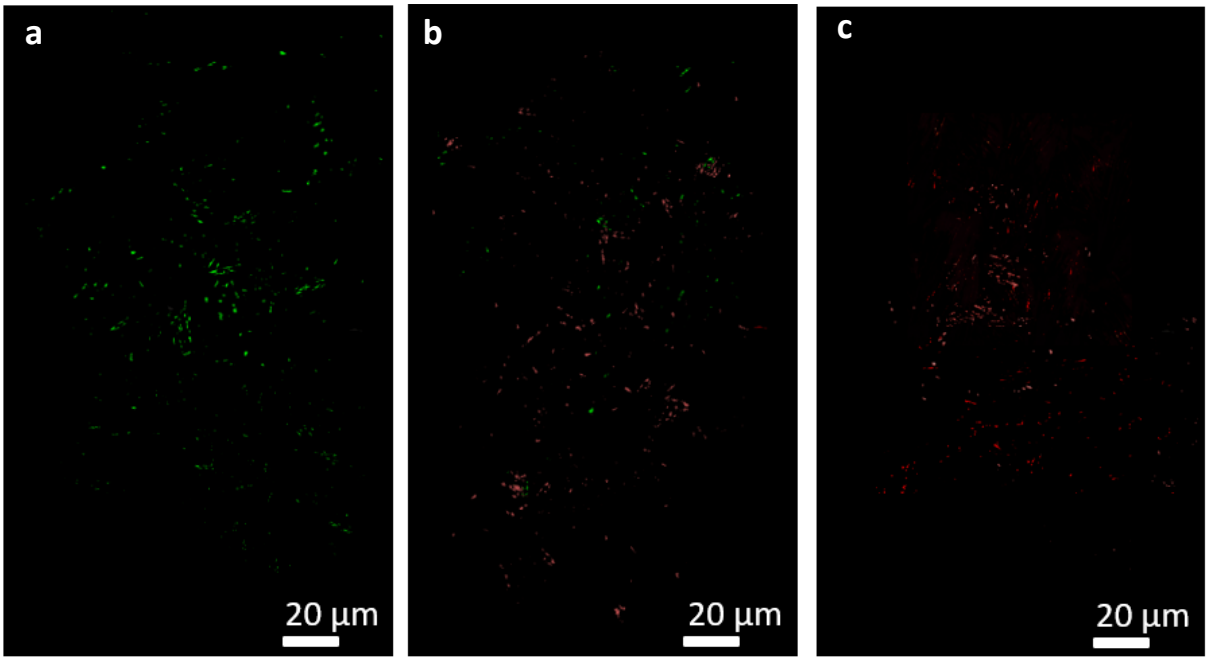

Fig. V. 11. Fluorescence stereomicroscopy of *E. coli* on TiOMoN-7.4 at. % Ag film for: a) time zero (15 min in the dark), after b) 60 min and c) 90 min under solar simulated light.

V. 6.5 Contribution of the ROS in the bacterial inactivation at the interface of TiOMoN-7.4 at. % Ag film under solar simulated light

Reactive oxygen species (ROS) are the species that lead to bacterial inactivation in solution. To identify these species dimethylsulfoxide (DMSO, 2 mM), superoxide dismutase (SOD, 2 mM) and ethylene tetra-acetic acid disodium salt (EDTA-2Na, 2 mM) were used to identify the $^{\bullet}OH$, $O_2^{-}$and $v_b(h^+)$. The photocatalytic bacterial inactivation in *Fig. V.12*was suppressed by addition of dimethylsulfoxide (DMSO) and ethylene tetra-acetic acid disodium salt (EDTA-2Na). The $^{\bullet}OH$ and h^+ species intervene jointly leading to the bacterial inactivation. The SOD ($O_2^{\bullet-}$ scavenger) in *Fig. V. 12* inhibits bacterial inactivation to a small degree compared to $v_b(h^+)$ and the $^{\bullet}OH^-$ radical.

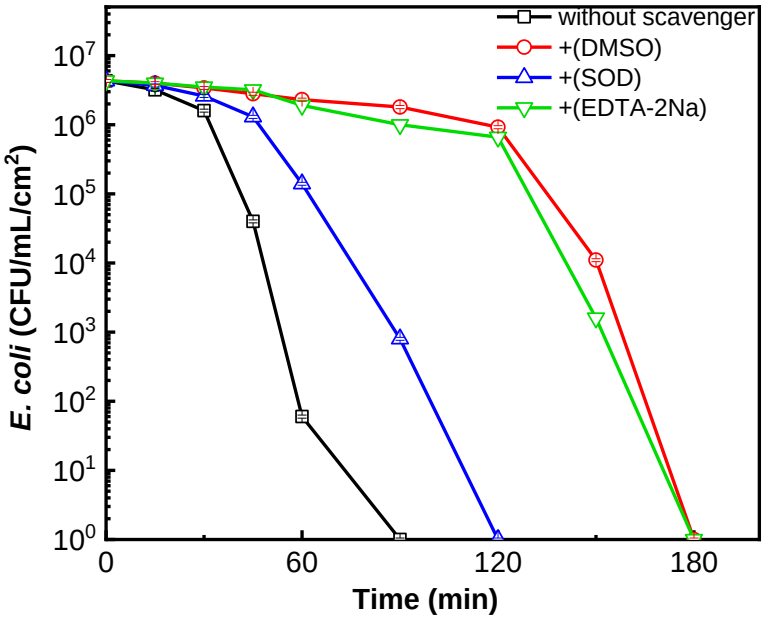

Fig. V.12. Contribution of the reactive oxygen species (ROS) in the bacterial inactivation at the interface of TiOMoN-7.4 at. % Ag film under solar simulated light.

Fig. V.13a presents the UV–Vis absorption plots of TiMoON and TiMoON-7.4 at.% Ag films. The spectra of the films were registered in the 250 – 800 nm range. The spectrum of TiOMoN shows a high absorption < 400 nm with a very little absorption in the visible region. XPS results indicated that doping by 7.4 at.% Ag leads to the formation of Ag_2O. Ag_2O induces a red shift in the spectrum of the TiOMoN–(7.4 at. % Ag) film. According to *Liu et al.* [31] TiO_2 and MoO_3 also contribute to the red shift in the films shown in *Fig. V. 13*.

Fig. V.13b shows the spectra of the films used to calculate the bandgap (bg) by Tauc's equation:

$$(\alpha h\nu)^n = K(h\nu - Eg) \qquad (V.\ 18)$$

K, α, and h*ν* present the constant value, absorbance coefficient, and photon's energy, respectively, n is the transition category (n = 0.5 for indirect and n = 2 for direct transition). The intercept from the extrapolation of the linear portion of the (αhν)1/2~hν plot gives the bandgap. The Eg value of the TiOMoN film reduced from 2.88 eV to 2.11 eV after doping by 7.4 at. % Ag.

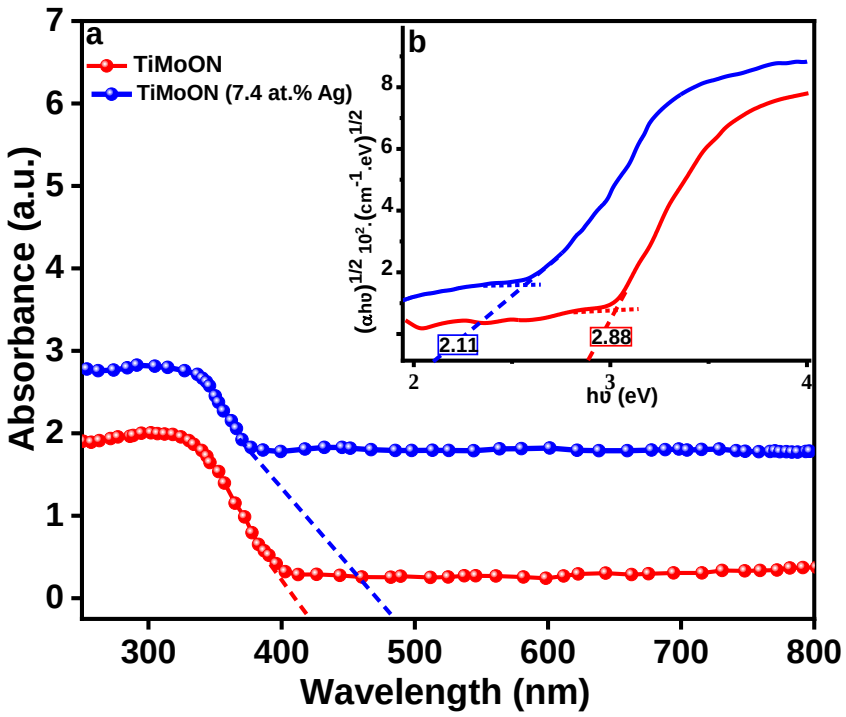

Fig. V. 13. (a) Optical absorption spectra and (b) Tauc plots of fabricated samples.

A simplified scheme for the intervention of the TiOMoN-Ag film for bacterial inactivation is suggested next in *Fig. V.14*. Visible light absorption has been reported for MoO_3 [32-33]. *Fig. V.14*suggests that electrons move from the Ag_2O to the heterojunction TiO_2 /MoO_3. These TiO_2/MoO_3/Ag_2O electrons can be trapped by O_2 to yield $O_2^{\bullet-}$ and $^{\bullet}OH$ when intervening in the bacterial inactivation process.

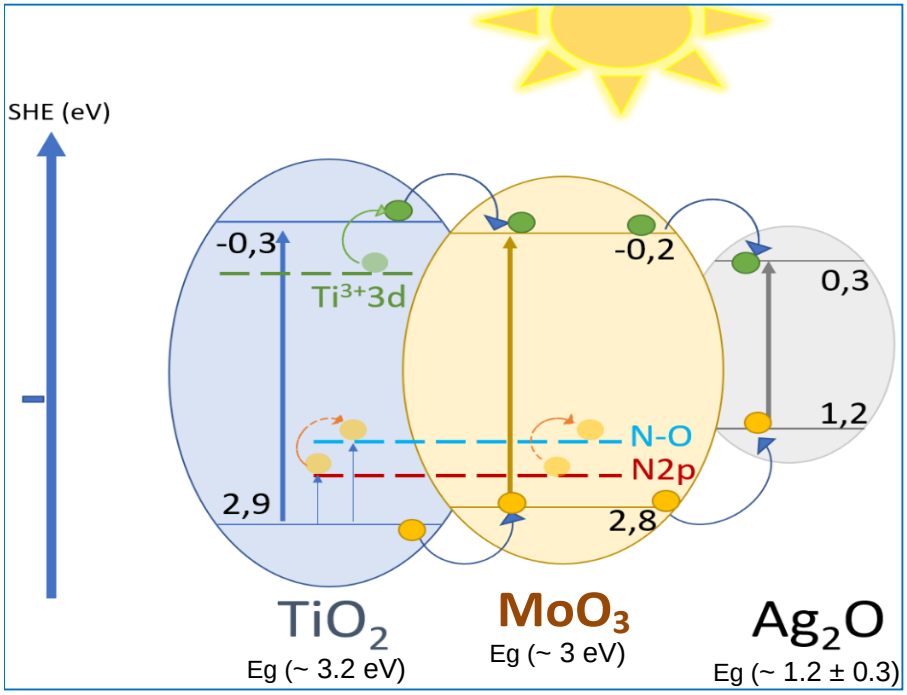

Fig. V.14. Suggested mechanism under solar simulated light leading to bacterial inactivation/death.

Conclusion

In this chapter, TiMoON and TiMoON-Ag films deposited with different Ag contents by RF magnetron sputtering presented dense and rough structure with heterogeneous distribution of Ag nanoparticles. Differentiated *E. coli* bacterial inactivation process by extracellular and intracellular processes is investigated by the genetically modified bacteria and the effect of different concentrations of various chemicals (scavengers, oxidants, holes) on the photocatalytic process was also reported in details:

- *With increasing Ag content, the surface morphology of the TiMoON-Ag coatings became denser with a very fine grain size with the appearance of white spherical particles due to Ag precipitation on the film surface. The annealing treatment at 400 °C led to a bonding of more Ag-nanoparticles on the film surface compared to the as-deposited films. The hydrophobic property of the TiMoON increased with the increasing of the Ag content getting the highest values of 121° and 127° for 7.4 % Ag before and after annealing, respectively.*
- *There is no reaction for bacterial inactivation in dark and the faster inactivating photocatalysts were obtained for TiOMoN-7.4 at. % Ag and TiOMoN-6.72 at. % Ag films with the highest RMS of 20.1 nm and 20.5 nm for the as-deposited and annealed films, respectively.*
- *An extracellular mechanism is suggested in the initial stages for porinless E. coli, followed by a second stage intracellular process.*
- *Identification of the ROS in solution showed that hydroxyl radicals played the main role in the bacterial degradation.*
- *The films hydrophobicity increased with the film Ag-content and led to an acceleration of the bacterial inactivation process.*

References

[1] S. Rtimi, S. Konstantinidis, N. Britun, M. Bensimon, I. Khmel, V. Nadtochenko, Extracellular bacterial inactivation proceeding without Cu-ion release: Drastic effects of the applied plasma energy on the performance of the Cu-polyester (PES) samples, Appl. Catal. B 239 (2018) 245–253.

[2] A. Al-Rjoub, A. Cavaleiro, F. Fernandes, Influence of Ag alloying on the morphology, structure, mechanical properties, thermal stability and oxidation resistance of multilayered TiSiN/Ti (Ag) N films. Materials&Design, *192* (2020) 108703.

[3] A.A. Mosquera, J.M. Albella, V. Navarro, D. Bhattacharyya, J.L. Endrino, Effect of silver on the phase transition and wettability of titanium oxide films. Scientific reports, 6(1) (2016), pp. 1-14.

[4] H. Ju, L. Yu, D. Yu, I. Asempah, J. Xu, Microstructure, mechanical and tribological properties of TiN-Ag films deposited by reactive magnetron sputtering. Vacuum, 141(2017), pp. 82-88.

[5] N.R. Mucha, J. Som, J. Choi, S. Shaji, R.K. Gupta, H.M. Meyer, C.L. Cramer, A.M. Elliott, D. Kumar, High-performance titanium oxynitride thin films for electrocatalyticwater oxidation, ACS Appl. Energy Mater, 3(9)(2020), pp. 8366–8374.

[6] S. Rtimi, R. Sanjines, M.Andrzejczuk, C. Pulgarin, A. Kulik, J. Kiwi, Innovative transparent non-scattering TiO_2 bactericide thin films inducing increased E. coli cell wall fluidity. Surface and Coatings Technology, 254(2014), pp. 333-343.

[7] O. Baghriche, S. Rtimi, C. Pulgarin, C. Roussel, J. Kiwi, RF-plasma pretreatment of surfaces leading to TiO2 coatings with improvedoptical absorption and OH-radical production, Applied Catalysis B: Environmental, n 130–131(2013), pp. 65– 72

[8] E. Vernickaitė, M. Lelis, N. Tsyntsaru, V. Pakštas, H. Cesiulis, XPS studies on the Mo oxide-based coatings electrodeposited from highly saturated acetate bath, CHEMIJA. 31(2020), pp. 203–209.

[9] S. Calderon Velasco, A. Cavaleiro, S. Carvalho, Functional properties of ceramic-Ag nanocomposite coatings produced by magnetron sputtering, Progress in Materials Science, 84 (2016), pp.158–191.

[10] L. Wang, Y.Wang, P. Shum, Y. Hou, T. Fu, Sputter-Deposited Cr–Ag Films for Environmental Antimicrobial Applications, Coatings, 11(2021)1153.

[11] P. Navabpour, S. Ostovarpour, J. Hampshire, P. Kelly, J. Verran, K. Cooke, The effect of process parameters on the structure, photocatalytic and self-cleaning properties of TiO_2 and Ag-TiO_2coatings deposited using reactive magnetron sputtering, Thin Solid Films, 571(2014), pp. 75–83.

[12] A. Alhussein, S. Achache, R. Deturche, F. Sanchette, C. Pulgarin, J. Kiwi, S.Rtimi, Beneficial effect of Cu on Ti-Nb-Ta-Zr sputtered uniform/adhesive gum films accelerating bacterial inactivation under indoor visible light. Colloids and Surfaces B: Biointerfaces, 152(2017), pp. 152-158.

[13] S. Rtimi, J. Kiwi, Update on interfacial charge transfer (IFTC) processes on films inactivating viruses/bacteria under visible light: mechanistic considerations and critical issues. Catalysts, 11(2) (2021), 201.

[14] S. Rtimi, D.D. Dionysiou, S.C. Pillai, J. Kiwi, Advances in catalytic/photocatalytic bacterial inactivation by nano Ag and Cu coated surfaces and medical devices, Applied Catalysis B: Environmental 240 (2019), pp. 291–318.

[15] H. Foster, I. Ditta, S. Varghese, A. Steele, Photocatalytic disinfection using titanium dioxide: spectrum and mechanism of antimicrobial activity, Appl. Microbiol. Biotechnol. 90 (2011), pp. 1847–1868.

[16] N. Reidy, A. Haase, A. Luch, K. Dawson, I. Lynch, Mechanisms of silver nanoparticle release, transformation and toxicity: a critical review of current knowledge and recommendations for future studies and applications, Materials 6 (2013), pp. 2295–2950.

[17] H. Shi, G. Li, H. Sun, T. An, P. Wong, Visible-light-driven photocatalytic inactivation of *E. coli* by Ag/AgX-CNTs (X = Cl, Br, I) plasmonicphotocatalysts: Bacterial performance and deactivation mechanism, Applied Catalysis B: Environmental, 158–159(2014), pp. 301-307.

[18] S. Rtimi, C. Pulgarin, M. Bensimon, J. Kiwi, Evidence for TiON sputtered surfaces showing acceleratedantibacterial activity under simulated solar irradiation, Solar Energy 93 (2013), pp. 55–62.

[19] A. Mills, C. Hill, P. Robertson, Overview of the current ISO testsfor photocatalytic materials. J. Photochem. Photobiol. A 237(2012), pp. 7–23.

[20] S. Rtimi, O. Baghriche, C. Pulgarin, R. Sanjines, J. Kiwi, Design, testing and characterization of innovative TiN–TiO_2 surfacesinactivating bacteria under low intensity visible light. RSC Adv. 2(2012), pp. 8591–8595.

[21] B. Subramanian, C. Muraleedharan, R. Annanthakumar, M. Jayachandran, A comparative study of TiN, TiON and TiAlNassurface coatings for bioimplants. Surf. Coat. Technol. 205(2011) pp.5014–5020.

[22] L. Heefner,Transport of H+, K+, Na+ and Ca2+ in spretococcus, Moll. Cell. Biochem. 44 (1982), pp.81-89.

[23] S. Ciuca, M. Badea, E. Pozna, I. Pana, A. Kiss, L. Floroian, A. Semenescu,C.M.Cotrut, M. Moga, A. Vladescu, Evaluation of Ag containing hydroxylapatitecoatings to the Candida albicans infection, J. Microbiol. Methods 125 (2016) 12–18.

[24] V.H. Matsubara, F. Igai, R. Tamaki, P. TortamanoNeto, A.E. Nakamae, M. Mori, Use of silver nanoparticles reduces internal contamination of external hexagon implants by Candida albicans, Braz. Dent. J. 26 (5) (2015), pp.458–462.

[25] K. Lorenz, S. Bauer, K. Gutbrod, J.P. Guggenbichler, P. Schmuki, C. Zollfrank,Anodic TiO_2 nanotube layers electrochemically filled with MoO_3 and their antimicrobialproperties, BiointerphasesJ. 6 (1) (2011) 16–21.

[26] Y. Zhao, J. Xu, Z. Li, T. Fu, S. Jiang, In vitro antibacterial properties of $MoO_3/SiO_2/Ag_2O$ nanocomposite coating prepared by double cathode glow discharge technique, Surface & Coatings Technology 397 (2020) 125992.

[27] J. Bogdan, J. Zarzynska, J. Plawinska-Czarnak, Comparison of infectiousagents susceptibility to photocatalytic effects of nanosized titanium and zinc oxides: a practical approach, Nanoscale Res. Lett. 10 (1) (2015) 1023.

[28] J. Nesic, S. Rtimi, D. Laub, G.M. Roglic, C. Pulgarin,J. Kiwi, New evidence for TiO_2uniform surfaces leading to complete bacterialreduction in the dark: Critical issues, Colloids and Surfaces B: Biointerfaces 123 (2014) 593–599.

[29] S. Rtimi, R. Sanjines, C. Pulgarin, J. Kiwi, Microstructure of Cu-Ag Uniform Nanoparticulate Films on Polyurethane 3D Catheters: Surface Properties, ACS-Applied Materials and Interfaces 8 (2016) 56 - 63.

[30] S. Rtimi, V. Nadtochenko, I. Khmel, M. Bensimon, J. Kiwi, First unambiguous evidence for distinct ionic and surface-contact effects during photocatalytic bacterial inactivation on Cu–Ag films: Kinetics, mechanism and energetics, Materials Today Chemistry, 6(2017), pp. 62-74.

[31] C. Gunawan, W. Teoh, C. Marquis, R. Amal, Induced Antimicrobial Resistance to Nanosilver. Small, 9(2013), pp. 3554−3560.

[32] H. Liu, T. Lv, C. Zhu, Z. Zhu,Direct bandgap narrowing of TiO_2/MoO_3heterostructure composites for enhanced solar-driven photocatalytic activity, Solar Energy Materials and Solar Cells,153(2016), pp. 1-8

[33] D. Chen, Z. Xie, Y. Zeng, W. Lv, Q. Zhang, F. Wang, G. Liu, H. Liu, Accelerated photocatalytic degradation of quinolone antibiotics over Z-scheme MoO_3/g-C_3N_4heterostructure by peroxydisulfate under visible light irradiation: mechanism, kinetic and products. Journal of the Taiwan Institute of Chemical Engineers, 104(2019), pp. 250-259.

GENERAL CONCLUSION AND PERSPECTIVES

GENERAL CONCLUSION AND PERSPECTIVES

GENERAL CONCLUSION

The main purpose of this thesis was to study and ameliorate the tribo-mechanical properties, anticorrosion behavior and anti-bacterial performance of the cold-sprayed 316L stainless steel coated with binary (TiN), ternary (TiAlN), quaternary (TiAlMoN) and (TiMoONAg) coatings deposited by magnetron sputtering technique.

First, the cold spray process parameters were simulated by using a Kinetic Spray Solutions (KSS) software and many experiments were carried out to evaluate the effect of process parameters on the tribo-mechanical behavior and electrochemical corrosion performance of the cold-sprayed SS316L coating.

→ *The one-dimensional model showed that the increase of carrier gas temperature with a fine size particle led to a larger particle velocity.*

→ *The SS316L coating cold-sprayed under He with high particle velocity presented a dense and smooth coating, leading to enhanced hardness and tribological performance and the best corrosion resistance in sea water (3.5 wt. % NaCl solution).*

Then, TiN, TiAlN and TiAlMoN coatings with different molybdenum contents were successfully produced on SS316L using the magnetrons sputtering technique.

→ *With increasing Mo content in TiAlN coatings, their single-TiN phase was transformed to TiN and Mo_2N mixed phases. This led to slightly increase the lattice parameters with high microstrain.*

→ *The $Ti_{33}Al_3N_{47}Mo_{16}$ coating showed a dense morphology and smooth surface, high compressive stress, high contact angle (104°) and low surface energy (32.22 mN/m).*

→ *The tribological behavior was significantly improved with the Mo addition. Wear rate of the film containing 16.09 at.% of Mo was reduced to 1.534 $\times 10^{-6}$ and 0.849$\times 10^{-6}$ mm^3/N under 2N and 5N loads, respectively. The enhancement of wear resistance is due to the smooth surface, high H/E and H^3/E^2 ratio and the formation of TiO_2 and α-MoO_3 lubricating phases.*

→ *The corrosion resistance of the cold-sprayed SS316L was enhanced by the protective deposited films and the best anticorrosion behavior was found for the film containing 16.09 at. % Mo.*

The innovative TiMoON and TiMoON-Ag films deposited with different Ag contents on glasses by RF magnetron sputtering presented dense and rough structure with heterogeneous

distribution of Ag nanoparticles. The antibacterial performance of these films was investigated.

→ *With increasing Ag content, the surface morphology of the TiMoON-Ag coatings became denser with a very fine grain size with the appearance of white spherical particles due to precipitation of Ag on the film surface. The annealing treatment at 400 °C led to a bonding of more Ag-nanoparticles on the film surface compared to the as-deposited films.*

→ *The hydrophobic property of the TiMoON increased with the increasing of the Ag content getting the highest values of 121° and 127 for 7.4 at. % Ag before and after annealing, respectively.*

→ *There was no reaction for bacterial inactivation in dark and the faster inactivating photocatalysts were obtained for TiOMoN(7.4 at. % Ag) and TiOMoN (6.72 at. % Ag) films with the highest RMS of 20.1 nm and 20.5 nm for the as-deposited and annealed films, respectively.*

→ *An extracellular mechanism was suggested in the initial stages for porinless E. coli, followed by a second stage intracellular process.*

→ *Identification of the ROS in solution showed that hydroxyl radicals played the main role in the bacterial degradation and the films hydrophobicity increased with the film Ag-content and led to an acceleration of the bacterial inactivation process.*

→ *The bacterial inactivation on TiOMoN (7.4 at. % Ag) film was completed in short time (within 90 min) which presents a more advancement of disinfection of film surfaces showing a potential for practical applications in the biomedical field.*

As a point of view to improving more the coatings developed in this work and taking into account the results obtained in this study, several perspectives can be suggested:

- It seems interesting to study the other parameters of magnetron sputtering process (like substrate temperature) to enhance the coatings and improve their resistance to wear and corrosion also analyze the adhesion of coatings.
- We have seen that the TiOMoN (7.4 at. % Ag) film has an effective anti-bacterial performance under solar simulated light. In next step, it would be interesting to test this coating in other environments like in the case of coated hip implant inserted in human body.

Appendix A : Résumé en Français

Tenue à l'usure et à la corrosion des revêtements à base de titane déposés sur des aciers inoxydables 316 L

Introduction générale

Les principaux défis dans le domaine industriel sont de concevoir et de produire des composants avec des films durs ayant un faible coefficient de frottement (COF) et une forte résistance à la corrosion pour l'utilisation dans des environnements sévères [1-2]. Cold Spray (CS) est l'un des techniques de revêtements qui ont rapidement progressé en présentant une nouvelle technologie future et émergente. Le dépôt d'acier inoxydable par CS a un fort potentiel dans différents domaines en raison de ses caractéristiques telles que la facilité de fabrication, la bonne résistance mécanique, la résistance raisonnable à la corrosion, la biocompatibilité et le faible coût [2].

Cependant, la dureté de surface de l'acier inoxydable(SS) 316L et la résistance à l'usure sont médiocres [3, 4]. Si on prend l'exemple de prothèses d'hanche, on estime qu'environ 10 % des prothèses ont seulement été changées. Après 10 à 15 ans du fait, la corrosion et l'usure localisée se sont produits à cause de la forte concentration des ions Cl^- dans les fluides physiologiques [5]. De plus, la faible propriété antibactérienne est l'une des principales limitations de l'acier inoxydable 316L qui est principalement utilisé dans la fabrication d'instruments chirurgicaux.

Afin d'améliorer les propriétés mécaniques, tribologiques, anticorrosion et la performance antibactérienne de l'acier inoxydable 316L, il est nécessaire d'appliquer des revêtements protecteurs. La pulvérisation magnétron s'est rapidement développée et fait aujourd'hui partie des techniques préconisées pour le dépôt de divers revêtements industriels.

L'objectif de ce travail est de développer une nouvelle génération de revêtements à base de titane de bonnes propriétés tribo-mécaniques, électrochimiques et antibactériennes. Nous développons un traitement DUPLEX qui s'articulera en deux étapes à savoir une première partie la réalisation et la caractérisation de l'acier inoxydable 316L par Cold Spray puis le traitement de surface par l'application et la caractérisation des couches minces à base de nitrure de titane (TiN). Différents dépôts ternaires (TiAlN), quaternaires TiAlMoN et un innovant revêtement

quinaires (TiMoONAg) ont été déposés par la technique de pulvérisation cathodique magnétron.

Ce manuscrit s'articule autour de cinq chapitres.

- ***Le premier chapitre*** est consacré à la synthèse bibliographique de l'acier inoxydable 316L constituant le substrat élaboré par cold spray puis le traitement de surface par application des couches minces quaternaires de système TiAlMoN et de l'innovant quinaire TiMoONAg.
- ***Le deuxième chapitre*** constitue une présentation des techniques d'élaboration (cold spray et pulvérisation cathodique magnétron), conjointement aux nombreuses méthodes de caractérisations physico-chimiques des revêtements (DRX, MEB, XPS, RAMAN, UV-visible…) et de leurs propriétés d'usage (étude mécanique, tribologique, corrosion et activité antibactérienne).
- ***Le troisième chapitre*** est dédié d'abord à l'identification des paramètres optimaux de l'élaboration de revêtements de 316L par la technique de cold spray. L'effet des gaz utilisés d'hélium et d'azote a été étudié. Le comportement tribologique a été évalué sous différentes charges appliquées dans des conditions sèches et nous avons étudié le comportement électrochimique (résistance à la corrosion) dans une solution d'eau salée de 3,5% massique de NaCl.
- ***Dans le quatrième chapitre***, nous proposons une technique hybride combinant la technique de cold spray (CS) et la pulvérisation magnétron (MS) pour fabriquer des composants hybrides CS-MS. Nous étudions des revêtements TiAlMoN déposés par MS sur l'acier inoxydable 316L pour l'objectif d'améliorer le comportement tribologique et la résistance à la corrosion des composants hybrides développés.
- ***Dans le cinquième chapitre***, nous présentons des films innovants de TiMoON et TiMoON-Ag préparés par la pulvérisation magnétron dans un mélange de gaz (Ar /N_2/O_2). Ces revêtements sont suivi par un traitement thermique de recuit sous vide à 400 °C et leurs comportements antibactériens ont été évalués sous une irradiation de lumière solaire simulée.

Enfin, la thèse est terminée par une conclusion générale et des perspectives pour nos futurs travaux de recherche.

Chapitre I: Etude bibliographique sur les matériaux étudiés

I. 1. L'acier inoxydable 316L

Dans le cadre de cette étude, nous nous intéresserons aux aciers austénitiques, en particulier la nuance 316L qui se relève de la catégorie des aciers Cr-Ni-Mo à base carbone. Cette nuance appartient à la famille des aciers inoxydables 316, 321, 347 et 304. Ils ont une faible limite d'élasticité inférieure à 300 MPa, une résistance mécanique inférieure à 650 MPa et une dureté de (250-400) HV [6]. Le dépôt d'acier inoxydable par Cold Spray (CS) a un fort potentiel dans différents domaines. Les études des propriétés tribologiques de l'acier 316L dans la littérature sont limitées à cause de ductilité et sa faible résistance à l'usure [2-4]. L'inflammation et l'infection, qui sont généralement dues à l'adhérence et à la colonisation de bactéries sur les biomatériaux causent les principales limitations de cet acier [7].

I. 2. Système quaternaire de revêtement TiAlMoN

Une attention importante a été apportée au développement des matériaux dits adaptatifs, ce qui implique de travailler avec succès dans diverses conditions et de s'adapter aux facteurs externes variantes [8]. Plusieurs chercheurs ont démontré que les revêtements durs sont généralement caractérisés par de bonnes propriétés tribologiques grâce à l'oxydation pendant le frottement et la formation d'un lubrifiant solide [9]. Il a été observé que l'introduction du molybdène (Mo) dans le système TiAlN a conduit à l'augmentation de la dureté et du module d'élasticité en raison de l'effet de renforcement de la solution solide par le molybdène [10].

Un coefficient de frottement faible et une excellente résistance à l'usure ont été constatés dans divers revêtements de nitrures dopés par Mo, tels que TiN/MoN [11] et TiMoN [12]. Par conséquent, on peut conclure que le molybdène a un potentiel comme un élément de dopage qui peut former des oxydes et des phases Magnélli, où l'ordre spécifique des lacunes en oxygène conduit à la formation de plans de cisaillement à faible propriété d'usure [13]. Il est bien admis que le faible frottement des revêtements contenant du molybdène est attribué à la formation d'une couche superficielle lubrifiante de MoO_3 due au mécanisme de tribo-oxydation. Néanmoins, dans la littérature, les études des revêtements quaternaires dopés en molybdène sont très limitées [14, 15]. Le molybdène peut être un bon candidat pour améliorer la résistance à l'usure et à la corrosion. A notre connaissance, il n'y a pas des études antérieures déjà réalisées sur la mouillabilité et la résistance à la corrosion par piqûres des revêtements TiAlMoN.

I. 3. Système quinaire de revêtement TiOMoN-Ag

A notre connaissance, il n'y a pas d'études précédentes sur le revêtement TiOMoNAg. Nous sommes les premiers qui avons élaboré ce type de revêtement par pulvérisation magnétron et nous avons étudiés la performance antibactérienne sous une lumière solaire simulée dans différentes conditions. Selon notre hypothèse qui est basée sur la combinaison entre les différents composants (TiO_2, MoO_3 et Ag_2O), nous avons conçu le revêtement TiOMoNAg pour l'application biomédicale.

Des travaux de recherche récents ont exploré l'utilisation d'oxydes métalliques binaires pour diminuer l'infection grâce à la génération d'espèces réactives de l'oxygène (ROS) à partir des semi-conducteurs photo-activés qui peuvent tuer efficacement les bactéries [16]. Parmi ces semi-conducteurs, le dioxyde de titane (TiO_2) est le photocatalyseur le plus utilisé et qui présente un grand potentiel dans la purification des eaux compte tenu de sa non-toxicité, son faible coût et sa forte oxydation [17]. L'efficacité antibactérienne de photocatalyseur TiO_2 est attribuée à la génération des trous (h+) et les électrons réagissent (e-) conduisant à des radicaux hydroxyles (·OH), l'oxygène (O^{-}) et le peroxyde d'hydrogène (H_2O_2). Sous la lumière, TiO_2 ne peut répondre que dans la région ultraviolette (UV), ce qui limite son utilisation dans le domaine d'énergie solaire [18].

De plus, des films à base de Mo ont été testés sur des bactéries Gram positives et Gram négatives, présentant des propriétés bénéfiques. Tétault et al. [19] ont découvert que l'activité antibactérienne de MoO_3 provient de la formation d'ions (H_3O^{+}). Son mécanisme est basé sur la diffusion de ces ions dans les membranes cellulaires qui détruit l'équilibre de pH et les systèmes de transport enzymatique, détériorant ainsi la prolifération des bactéries. Cependant, les deux semi-conducteurs TiO_2 et MoO_3 sont limités par leur large gap. Récemment, Ag_2O s'est avéré être un photocatalyseur de lumière visible auto-stable et très efficace avec un gap d'énergie d'environ 1,2 eV [20]. Il a été démontré que l'hétérojonction d'Ag_2O avec d'autres semi-conducteurs pourrait efficacement améliorer l'activité photocatalytique induite par la lumière visible, comme Ag_2O/TiO_2 [21] et $MoO_3/SiO_2/Ag_2O$ [22]. Cette combinaison donne une très bonne capacité de photo dégradation et d'activité antibactérienne.

Chapitre II. Méthodes et techniques expérimentales

Dans notre travail, le logiciel « Kinetic Spray Solutions (KSS) » a été utilisé pour simuler le processus de cold spray (CS) afin d'estimer les conditions optimales d'élaboration avant la réalisation de dépôt d'acier inoxydable 316L.

II. 1. Techniques de l'élaboration

Un traitement DUPLEX a été développé en deux étapes :

- Déposition de l'acier inoxydable 316L par le procédé CS, en utilisant He et N_2 comme gaz propulseurs. Des dépôts d'environ 2 mm d'épaisseur ont été réalisés en appliquant les paramètres idéaux déterminés par la simulation.
- Déposition des revêtements à base de TiN par la technique de pulvérisation magnétron : TiAlN, TiAlMoN et TiMoONAg.

Les dépôts CS ont été réalisés à l'aide d'un système CGT K3000 en projetant les poudres d'acier 316L type H.C. Starck 0717-074. La Fig. II.1 illustre le principe de dépôts CS où on peut remarquer la buse convergeant utilisée de type dé-lavale. Un bras de robot industriel est utilisé pour effectuer le mouvement du pistolet de projection afin d'obtenir un chemin de pulvérisation contrôlable et précis. Les paramètres utilisés pour les dépôts CS sont présentés dans le Tableau III. 1.

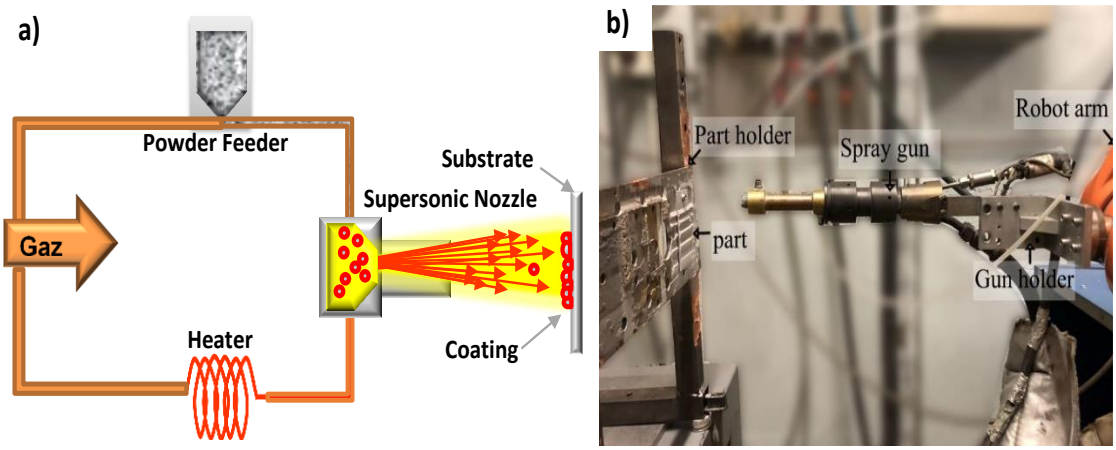

Fig. II.1. a) Illustration schématique de principe du dépôt CS, b) la machine de dépôt utilisée [23].

Tableau III. 1. Conditions d'élaboration de l'acier inoxydable 316L par cold spray.

Conditions de projection	N_2	He
Débit massique de poudre (g/min)	40	75
Vitesse de balayage (mm/s)	300	200
Distance de standoff (mm)	25	25
Pression de gaz (bar)	30	21.8
Température du gaz °C	650	480
Distance de la gorge de l'injecteur (mm)	-50	-18
Pas de balayage (mm)	2	1

La machine (*Dephis, France*) a été utilisée (Fig. II. 2) pour l'élaboration des revêtements (TiN(Al, Mo) et TiMoON-Ag) par pulvérisation cathodique magnétron. Le choix de cette technique a été fait en raison de ses nombreux avantages par rapport aux autres techniques de revêtement sous vide telles que la vitesse de croissance de dépôt élevée, la facilité de pulvérisation, la haute pureté, la haute densité et l'uniformité des films, etc. Les paramètres utilisés dans la déposition de nos couches minces sont présentés dans les Tableaux III. 2 et III.3.

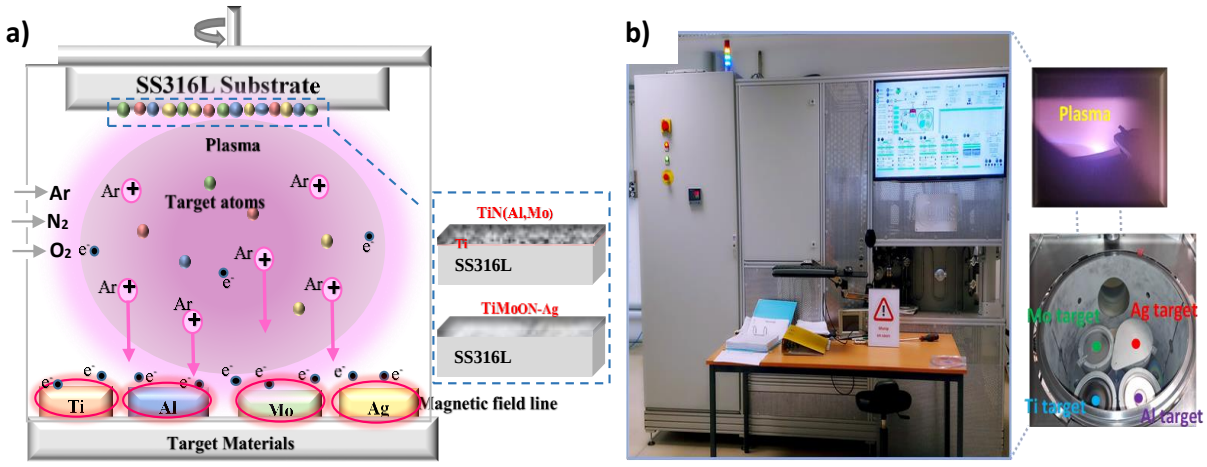

Fig. II.2. (a) Illustration schématique du principe de dépôts réalisés par pulvérisation cathodique magnétron et (b) la machine de dépôt utilisée.

Tableau III. 2. Tableau récapitulatif des paramètres de dépôt du TiN(Al, Mo)

Substrat (Elaboré par CS)	Acier inoxydable 316L
Pression de vide	6×10^{-4} Pa
Pression de travail	0.4 Pa
N_2/Ar	0.25
Courant de pulvérisation de Ti et Al (A)	Ti(2.5), Al(0.5)
Courant de pulvérisation de Mo (A)	Varié entre 0 et 0.7
Température du substrat	Température flottante
Vitesse de rotation du porte-substrat	10 rpm

Tableau III. 3. Tableau récapitulatif des paramètres de dépôt du TiMoON-Ag

Substrat	Verre
Pression de vide	6×10^{-4} Pa
Pression de travail	0.4 Pa
Début de gaz Ar, N_2 et O_2(sccm)	Ar(70), N_2(15) et O_2(5)
Courant de pulvérisation de Ti et Mo (A)	Ti(2), Al(0.3)
Courant de pulvérisation de Ag (A)	Varié entre 0.02 et 0.06
Température du substrat	Température flottante
Vitesse de rotation du porte-substrat	10 rpm

II. 2. Techniques de caractérisations

Nous avons utilisé plusieurs techniques de caractérisations physicochimiques et d'usage. La fig. II.3 présente la liste de ces techniques utilisées.

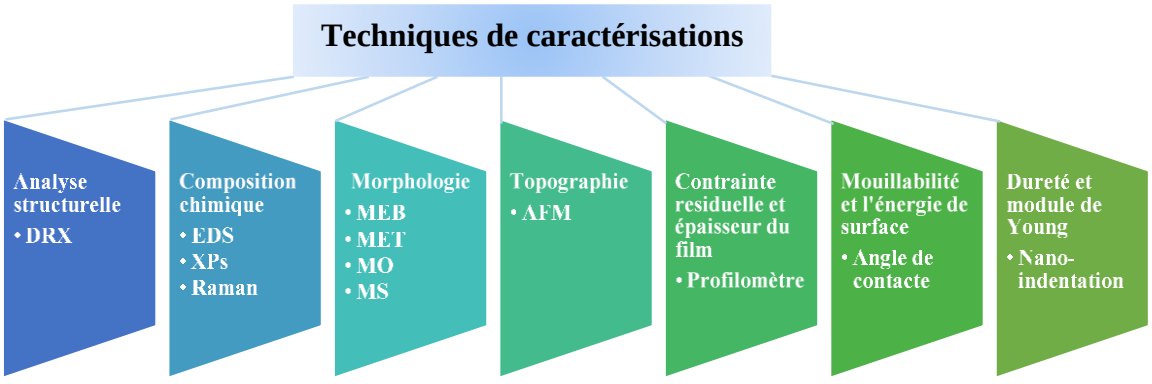

Fig. II.3. (a) Schéma de techniques de caractérisations utilisées.

II. 3. 1. Performance tribologique

Des tests de frottements et d'usure ont été effectués dans notre étude à l'aide d'un tribomètre (CSM, Anton Paar) (Fig. II.4). Nos revêtements ont été testés contre des billes en acier 100C6 (6 mm de diamètre). Les tests ont été réalisés à température ambiante en appliquant deux charges (2 et 5 N) pendant une distance parcourue de 50 m.

Les courbes des coefficients de frottement ont été automatiquement enregistrées par le logiciel du tribomètre. La perte (volume usé) a été mesurée à l'aide d'un profilomètre (Altisurf 500), puis les taux d'usure (W en $mm^3.N^{-1}m^{-1}$) des revêtements ont été évalués en utilisant l'équation suivante (Eq. II.1):

$$W = \frac{V}{LF} \quad \text{(II. 1)}$$

Où V est le volume usé en mm^3, L est la distance de glissement totale en m, et F est la charge appliquée en N. Après les tests de frottement, les traces d'usures ont été analysées par un MEB, EDX et Spectroscopie Raman.

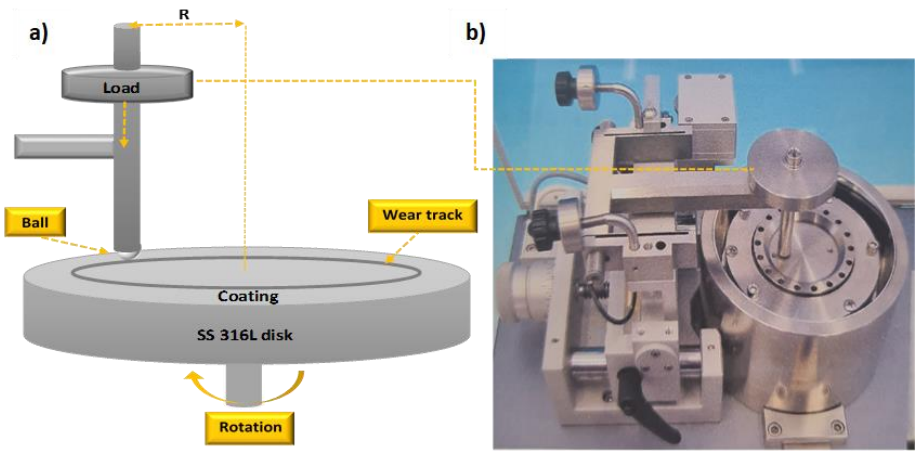

Fig. II.4. (a) Illustration schématique d'un test de frottement, et (b) le tribomètre utilisé.

II. 3. 2. Comportement électrochimique

Les propriétés électrochimiques de nos échantillons ont été évaluées à l'aide d'un potentiostat Origalys et d'une cellule de corrosion Biologic (Fig.II.5). Des tests de corrosion par piqûres ont été effectués sur une surface d'exposition de 1 cm^2 à température ambiante dans une solution de 3,5% massique de NaCl (PH~6,3). Trois électrodes ont été utilisées : une électrode au calomel saturée SCE (Hg/Hg_2Cl_2-Sat.KCl) comme électrode de référence, un maillage de

platine comme une contre-électrode et les éprouvettes avec et sans revêtement comme une électrode de travail. Afin d'assurer la stabilité du système, le potentiel de circuit ouvert (OCP) a été mesuré pendant 60 min. La vitesse de balayage a été fixée à 0,5 mV/sec Les principaux paramètres de corrosion ont été déterminés en utilisant des courbes de polarisation.

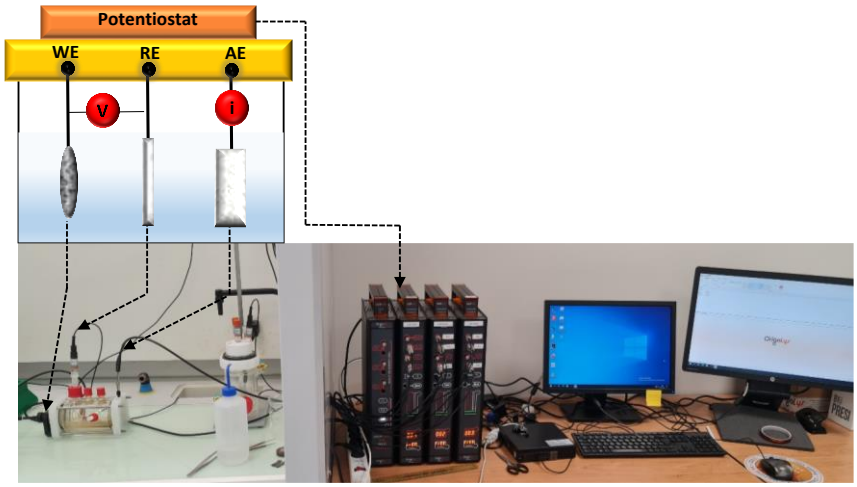

Fig. II.4. Montage expérimental pour les essais de corrosion.

II. 3. 3. Tests antibactériens

Nous avons évalué le comportement antibactérien des films de TiMoON et TiMoON-Ag déposés par pulvérisation magnétron et suivis par un recuit sous vide à 400 °C. Nous avons étudié leur cinétique d'inactivation, leur stabilité, leur efficacité et leurs propriétés adhésives à l'aide de bactéries Escherichia coli (E. coli K12). Les tests ont été effectués sous une lumière solaire simulée (50 mW/cm^2, CPS Suntest System, Atlas GmbH, Hanau, Allemagne) avec une émission entre 320 et 800 nm.

Nous avons également utilisé des souches mutantes de bactérie E. Coli génétiquement modifiées déficientes en porines OmpF et OmpC. Cette approche a permis de comparer la cinétique d'inactivation bactérienne induite par : (i) le contact des bactéries avec la surface des films déposés et (ii) les ions capables de pénétrer à l'intérieur des cellules de bactéries. Enfin, les essais de piégeage réalisés par le diméthylsulfoxyde (DMSO, 2 mM), la super oxydedismutase (SOD, 2 mM) et le sel disodique de l'acide éthylène tétraacétique (EDTA-2Na, 2 mM) ont été utilisés pour détecter/identifier le •OH, O_2^-et vb (h^+) générés en solution lors du processus d'inactivation bactérienne.

Chapitre III. Préparation et caractérisation de l'acier inoxydable 316L projeté à froid

Les paramètres du procédé de cold spray, simulés par le modèle unidimensionnel, ont montré que :

→ *La vitesse des particules diminue avec l'augmentation de sa taille. Les particules les plus fines sont plus chauffées au col, mais elles se refroidissent plus rapidement dans la partie divergente de la tuyère.*
→ *La température maximale est atteinte au col et la vitesse maximale est au point d'impact.*
→ *La vitesse d'He (2200 m/s) est deux fois plus élevée de celle de N_2 (1000 m/s).*

Les résultats obtenus par la simulation de jet à froid, nous ont permis d'identifier les principaux paramètres idéaux à utiliser pour l'élaboration des acier. Dans ce chapitre, nous présentons les revêtements en acier inoxydable austénitique 316L déposés sur des substrats en aluminium par jet à froid (Cold Spray) sous gaz He et N_2.

La Fig. III. 1 présente les spectres DRX des revêtements d'acier inoxydable 316L projetés à froid en utilisant d'azote et d'hélium comme des gazes propulseurs. On constate que seule la phase austénitique (γ) a été détectée présentant une structure cfc. Nous avons remarqué que le revêtement 316L déposé avec He était plus dense avec une teneur en oxygène plus faible et une surface plus lisse et homogène par rapport à celui déposé avec N_2[24]. D'autre part, les mesures de porosité confirment que le revêtement 316L projeté avec He présentait une valeur inférieure à (0,5 ± 0,01 %) par rapport à celui projeté avec N_2 (1,06 ± 0,03 %), ce qui est dû à la grande vitesse d'impact des particules associées à une grande déformation plastique résultant un revêtement plus dense.

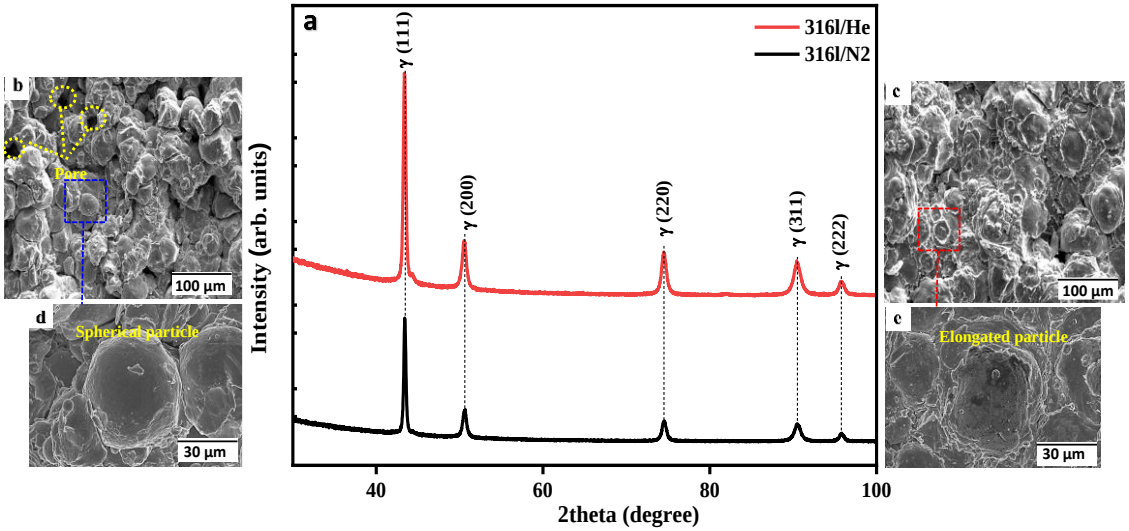

Fig. III.1. Diffractogrammes DRX des revêtements 316L réalisés par cold spray en utilisant He et N_2(a), et images MEB de morphologie de surface des revêtements projetés par : N_2 (b, d) et He (c, e).

Le revêtement 316L déposé avec He avait une dureté et un module d'élasticité plus élevés (7,5± 0.5 et 164 ± 10) GPa en comparaison avec celui de N_2(6.8 ± 0.5 et 152 ± 10) GPa(Fig. III.2). Ceci est lié à l'effet d'écrouissage pendant le processus de dépôt avec une vitesse de particules plus élevée en utilisant de l'hélium, comme rapporté *par Mangour et al.* [25].

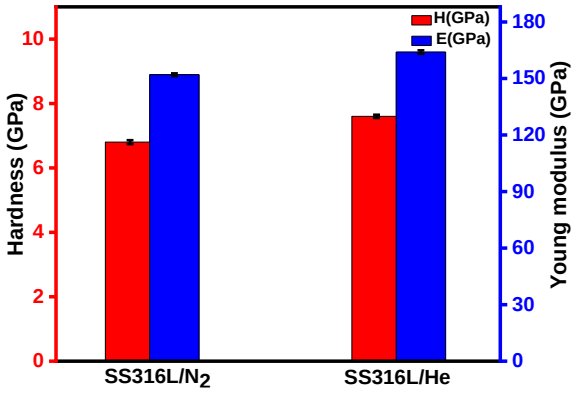

Fig. III. 2. Dureté et module de Young des revêtements 316L projetés à froid avec He et N_2.

Les taux d'usure des revêtements et des billes ont augmenté avec la charge appliquée de 2 à 5 N (Fig. III. 3). Avec une charge appliquée plus élevée (5N), la profondeur de pénétration de la bille 100C6 est de l'ordre de (22,5 et 15) µm pour les revêtements projetés avec d'azote et d'hélium, respectivement. Les coefficients de frottement sont de (0,65 - 0,70) pour l'acier 316L projeté avec He et (0,69 - 0,73) pour l'acier projeté avec N_2 mesurés sous charge appliquée de 2N et 5N, respectivement. L'augmentation du taux d'usure a conduit à l'augmentation du

coefficient de frottement du revêtement, mais comparativement il est plus faible pour le revêtement 316L projeté avec l'hélium, pour les deux charges, grâce à sa densité et surface dure [26].

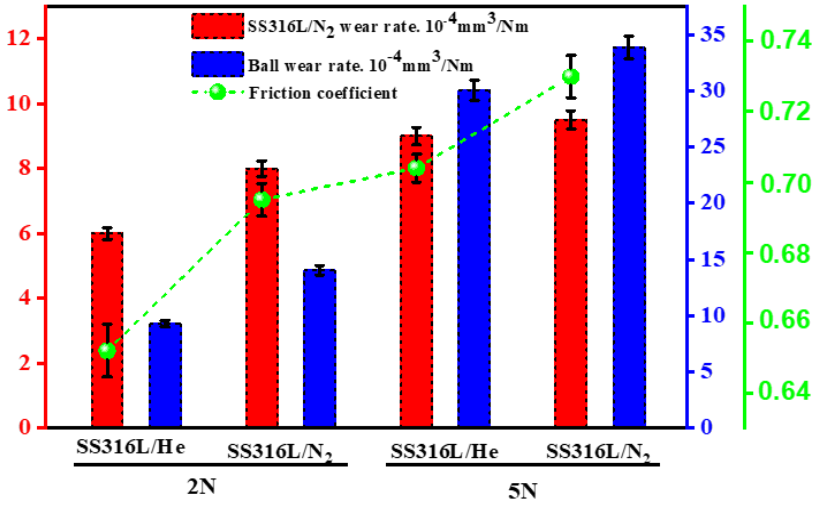

Fig. III. 3. Coefficients de frottement et taux d'usure des revêtements d'acier inoxydable 316L et des billes testés sous différentes charges (2 et 5 N).

Les traces d'usure des revêtements de 316L projetés avec He et N_2 (Fig. III. 4) présentent un mélange de débris d'usure et de déformation plastique avec l'apparition de nombreux types de défauts de surface tels que des micro-piqûres, délaminage, et des sillons qui sont plus apparents sur la surface de revêtement testé à 5 N. De plus, l'existence d'oxygène a entraîné une augmentation du taux d'oxydation de surface et la formation d'oxydes de fer [27]. Les taux d'usure des surfaces de contact des billes 100C6 ont été augmentés avec l'augmentation de la charge appliquée due à l'augmentation de la température entre la bille et le revêtement 316L [28].

D'autre part, les résultats des tests de corrosion, réalisés dans une solution de 3,5% massique de NaCl, sont présentés dans la Fig. III. 5. L'acier inoxydable 316L/N_2 projeté à froid (avec l'azote) a un potentiel de (-170 mV) et une densité de courant de corrosion de (1,20 µA.cm^{-2}). Le potentiel de corrosion et la densité de courant du l'acier 316L déposé avec He sont clairement améliorés pour atteindre de meilleures valeurs de (-157 mV et 0,74 µA.cm^{-2}, respectivement) correspond à la meilleure résistance à la corrosion (15.67 to 21.66) KΩ.cm^2. Les courbes de polarisation montrent la formation des régions de transition passive sur les deux échantillons testés, ce qui indique que l'acier 316L projeté à froid présente un comportement de passivation spontanée.

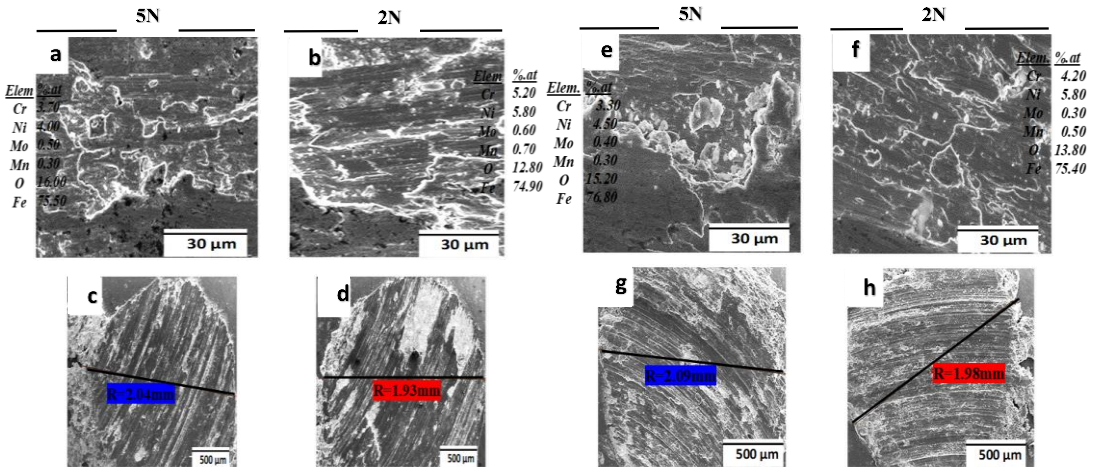

Fig. III. 4. Images MEB et composition chimique des traces d'usure sur les revêtements 316L projetés à froid avec He(a,b,) et N_2 (e, f,). (c, d, g, h) présent les surfaces usées sur les billes 100C6 après 50 m de glissement.

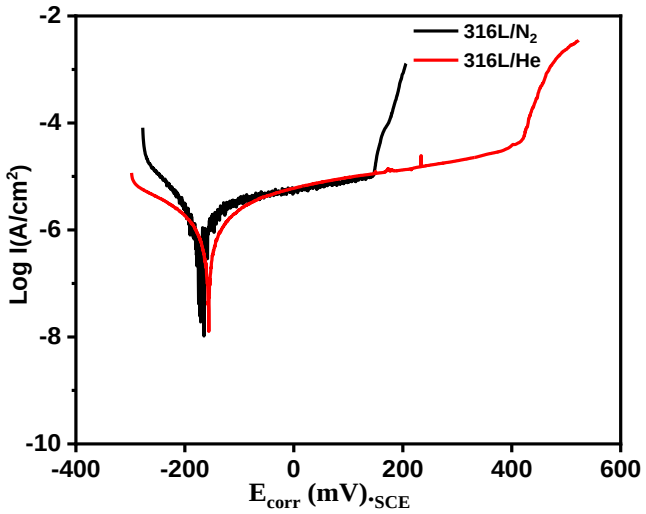

Fig. III. 5. Courbes de polarisation du 316L projeté à froid avec He et N_2 dans une solution de 3,5 % massique de NaCl.

La Fig. III. 5 montre que le potentiel de piqûration de 316L/He Epit = 413 mV correspondant à une plus grande région de passivation ΔE (393 mV). Ces valeurs sont bien meilleures que celles de 316L/N_2 (Epit = 146 mV, ΔE = 195 mV). En fait, la faible oxydation, la surface dense avec une faible rugosité contribuent à l'optimisation de la bonne résistance à la corrosion [29].

Chapitre IV. Élaboration et caractérisation des couches minces de TiN(Al,Mo) déposées par pulvérisation magnétron

Pour les films TiAlMoN, nous avons remarqué la présence de deux phases TiN et Mo_2N et le changement d'intensité des pics DRX (200) et (111) avec la variation de la quantité de Mo dans les films (Fig. IV. 1.a). On peut constater l'évolution du coefficient de texture : augmentation de I(111)/[I(111) +I(200)] et diminution de I(200)/[I(111)+I(200)] (Fig. IV.1.b). En fait, l'incorporation par substitution de Mo avec un grand rayon atomique (1,41 Å) dans la maille TiAlN provoquant une distorsion de la maille cristalline et un changement de ces paramètres (Fig. IV.1.b) [30]. L'augmentation de la teneur en Mo a conduit aussi à la diminution de la taille des cristallites à 38 nm (avec 16.09 at. % Mo, Fig. IV. 1.c).

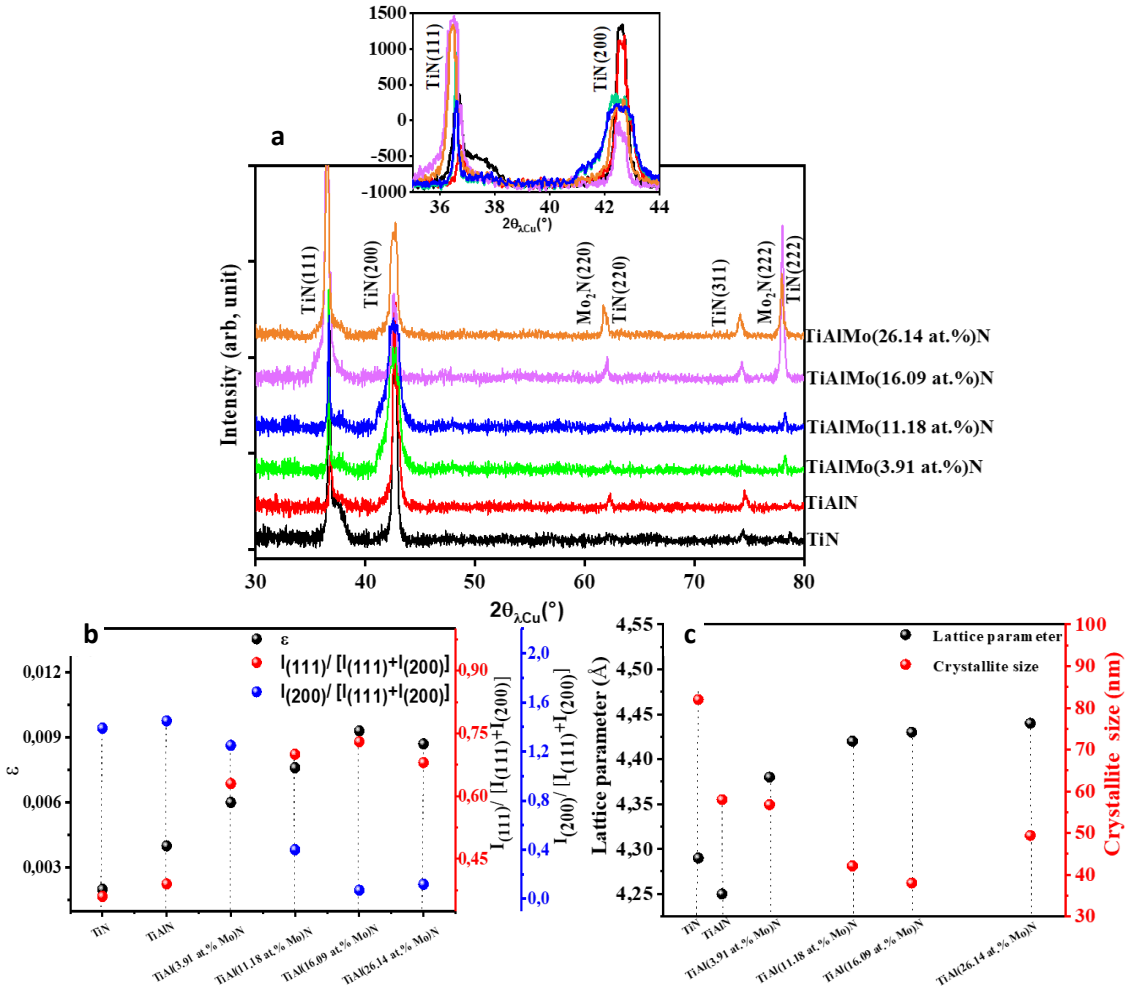

Fig. IV. 1.(a) Spectres DRX, (b) coefficients de texture et microdéformation, (c) paramètre de maille et taille des cristallites des revêtements Ti(Al,Mo)N.

Les revêtements TiN et TiAlN ont présenté une structure colonnaire avec une certaine porosité entre les grains globulaires. L'augmentation de la teneur en Mo dans le revêtement (16,09 at. % de Mo) a conduit à une amélioration de la qualité de surface : film plus dense avec une surface lisse et homogène correspondant à la zone T selon le modèle ASZM [31] (Fig. IV. 2). Ceci est dû à la mobilité des adatomes l'apparition de l'orientation préférentielle (111) conduisant à la densification de la structure. Avec une teneur élevée en Mo (26,14 at. %), la structure de revêtement TiAlMoN deviens colonnaire [31].

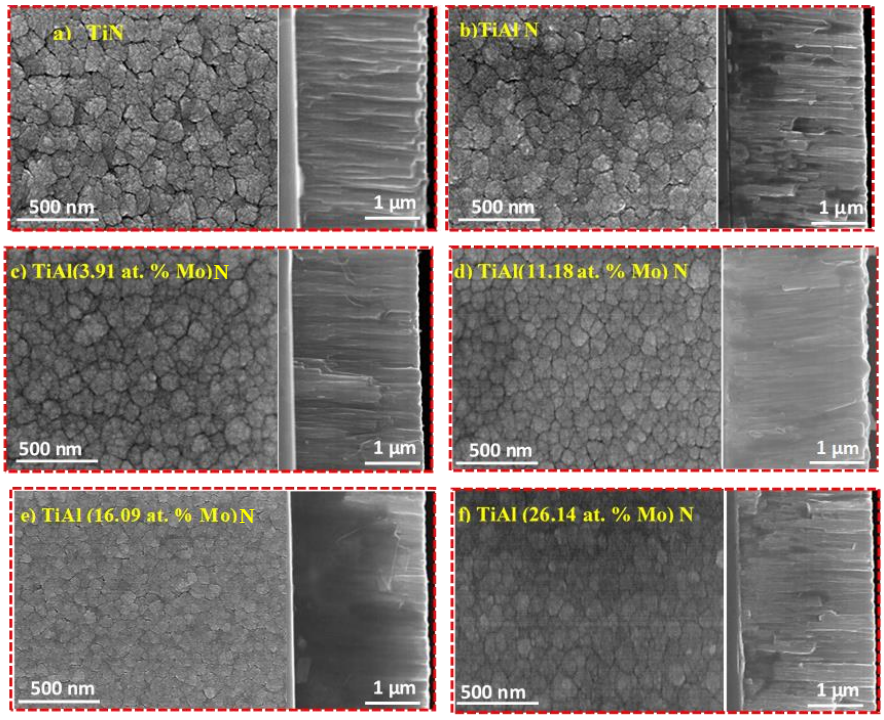

Fig. IV. 2. Images MEB de surface et coupe transversale des revêtements Ti(Al, Mo)N.

Les images TEM du revêtement TiAlN-(16,09 at.% de Mo) ont montré une structure mixte de grains denses et colonnaires (Fig. IV.3). Nous avons remarqué deux zones différentes : la zone (I) présentant une structure dense avec deux orientations (111) et (200) de la phase cubique (TiN), et la zone (II) riche en Mo correspondant à la phase Mo_2N avec une orientation préférentielle (111).

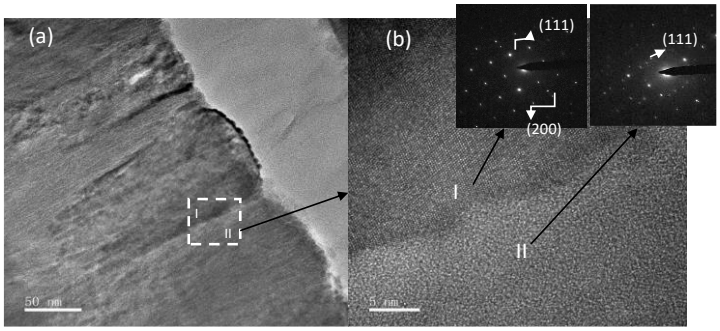

Fig. IV. 3. Images de: a) BFTEM et b) HRTEM et SAED de film TiAlN-(16.09 at.% Mo).

La Fig. IV.4 présente les valeurs moyennes des angles de contact entre les films et les gouttes d'eau. Les valeurs mesurées étaient de 65,4°, 73,5°, 91,4°, 94,4°, 104,4° et 100,2° pour les revêtements TiN, TiAlN et TiAlMoN contenant 3,91, 11,18, 16,09 et 26,14 at. % de Mo, respectivement. Le revêtement TiAlMoN contenant 16,09 at. % Mo montre un angle de contact plus élevé correspondant à sa faible mouillabilité et sa grande hydrophobicité par rapport aux autres revêtements. Nous pouvons également remarquer que l'énergie de surface totale diminue avec l'augmentation de la teneur en Mo et la valeur la plus faible de 32,22 mN/m a été obtenue pour le film mentionné. Dans notre étude, nous avons trouvé que la rugosité de surface a eu un impact direct sur l'angle de contact et l'énergie de surface. D'autres facteurs affectant l'énergie de surface ont été mentionnés tels que l'orientation préférentielle (111) qui entraîne une énergie de surface inférieure à celle de l'orientation (200) ce qui est cohérent avec d'autres études [32].

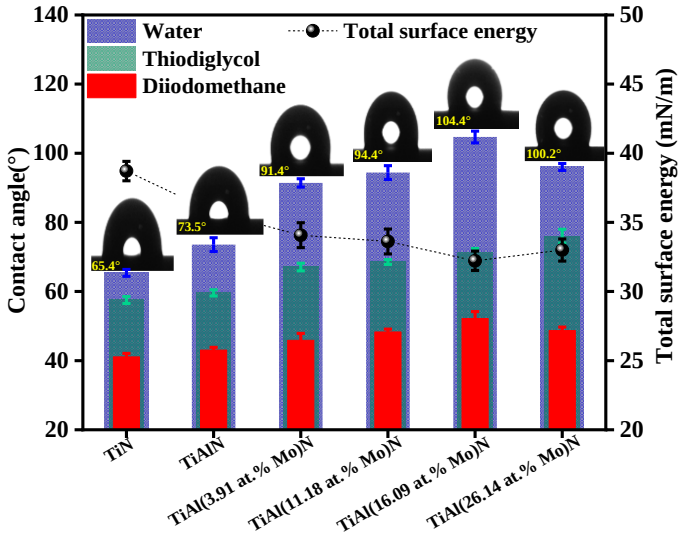

Fig. IV. 4. Angle de contact et énergie de surface totale des revêtements Ti(Al, Mo)N.

Fig. IV.5 présente les propriétés mécaniques des revêtements Ti(Al, Mo)N. Nous pouvons remarquer que les valeurs de dureté des revêtements TiN et TiAlN étaient respectivement de 20,05 et 21,4 GPa. Avec l'augmentation de la teneur en Mo de 3,91 à 26,14 at. %, une augmentation progressive des valeurs de la dureté et du module de Young a été observée, respectivement de (23,40, 278,5) à (29,50, 334,50) GPa. Cela est dû à l'effet de renforcement avec la présence de la phase Mo_2N, l'affinement du grain et les contraintes résiduelles en compression [24]. De plus, la dureté élevée des films TiAlMoN est également due au plan dense de TiN(111) [33].

Les rapports H/E et H^3/E^2 généralement liés respectivement à l'indice de plasticité et à la résistance à la déformation plastique qui donnent une bonne prédiction sur le comportement tribologique des revêtements [34]. Les valeurs maximales d'H/E et H^3/E^2 de 0,092 et 0,237 respectivement ont été obtenues pour le film contenant 16,09 at. % de Mo qui devrait présenter la meilleure résistance à l'usure.

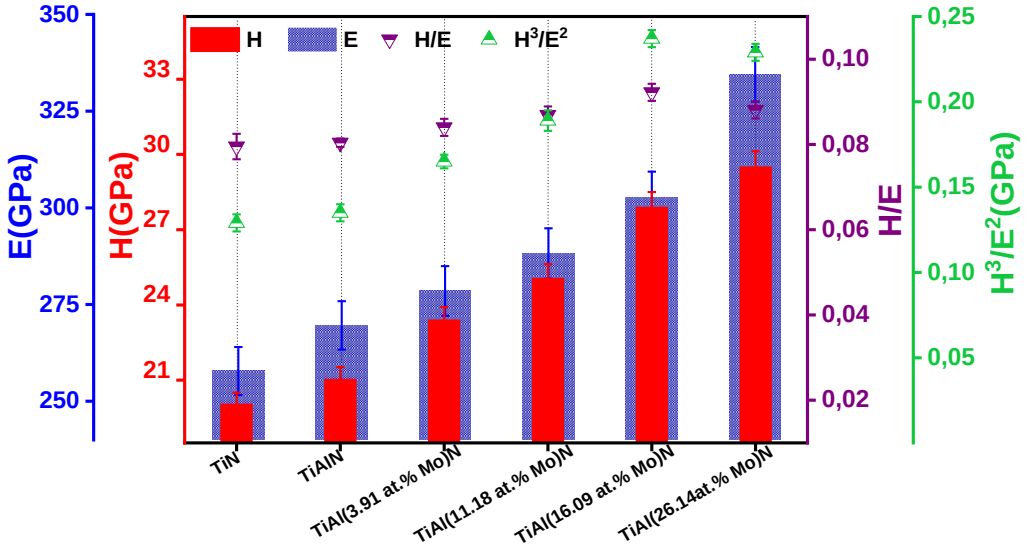

Fig. IV. 5. Dureté, module de Young et rapport H/E des revêtements Ti(Al, Mo)N.

Les revêtements TiN et TiAlN ont présenté des coefficients de frottement(COF) et taux d'usure élevés en raison de leur faible dureté et l'intensité de TiN (200) qui est relativement supérieure à celle de TiN (111). Avec l'augmentation de la teneur en Mo, le COF a diminué à 0,3 et le taux d'usure devient plus faible ($0,849\times10^{-6}$ mm^3/Nm) pour le film contenant 16,09 at. % Mo. Ce taux d'usure a légèrement augmenté pour le film contenant 26,14 at.% de Mo. Ces résultats indiquent que la performance tribologique du film TiAlMoN s'est considérablement améliorée avec l'incorporation de Mo et la formation d'une solution solide très dure et des

phases mixtes (Figs. IV.1.a et IV.3). De plus, le faible COF peut être attribué à la structure dense et la formation des oxydes de molybdène qui servent comme un milieu lubrifiant entre les deux surfaces en contact [35].

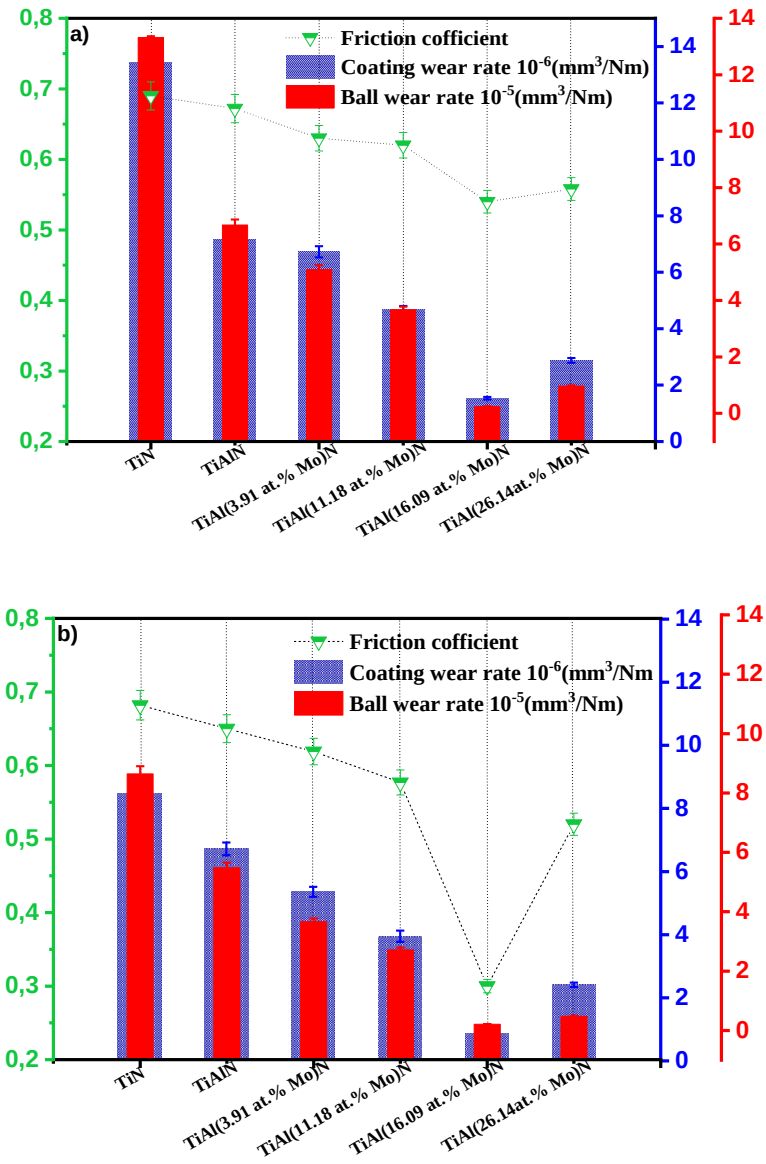

Fig. IV. 6. Taux d'usure des revêtements Ti(Al, Mo)N et des billes d'acier 100C6 testés sous charges : a) 2N et b) 5N.

La fig. IV.7 présente l'analyse Raman et les images MEB des traces d'usure sur les revêtements TiAlN et TiAl(16,09 at.% Mo)N. Nous remarquons que la trace d'usure du film TiAlN présente des multiples signes d'usure et des rayures proéminentes. En revanche, le film TiAl(16,09 at.% Mo)N présente des traces d'usure plus étroites. L'analyse Raman de TiAlN montre un caractère de liaison métallique distinct de TiN (458,7 cm^{-1}) avec une petite quantité de TiO_2 (532,1 cm^{-1}). Les revêtements TiAl(16,09 at. %Mo)N testés sous 2N et 5N montrent,

en plus de TiN et Mo_2N, la formation de la phase lubrifiante d'oxyde MoO_3 (pics à 186,1, 640,1 et 789,2 cm^{-1}).

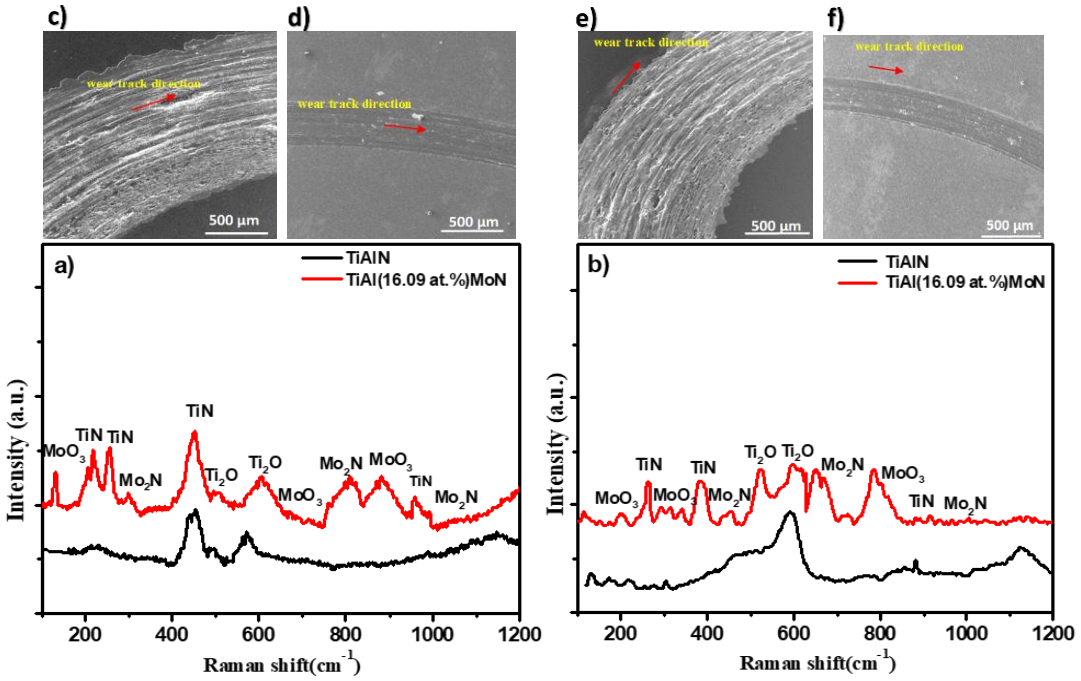

Fig. IV. 7. Analyse Raman etimages MEB des traces d'usure apparues en appliquant a) 2N et b) 5N sur les revêtements TiAlN (c,e) etTiAl(16,09 at.% Mo)N (d,f).

La Fig. IV.8 présente les courbes de polarisation de l'acier inoxydable 316L et les revêtements TiAlMoN. Nous constatons que l'acier 316L a une résistance à la corrosion la plus basse avec un potentiel plus bas de -157 mV et une densité de courant de corrosion plus élevée (741,31 $nA.cm^{-2}$). Avec l'augmentation de la teneur en Mo dans le revêtement TiAlMoN, le potentiel de corrosion et la densité de courant progressivement améliorent pour atteindre de meilleures valeurs de -16 mV et 1,41 $nA.cm^{-2}$ (pour le film contenant 16,09 at.% Mo) offrant la résistance de polarisation la plus élevée Rp de 78,73 × 102 ($K\Omega.cm^2$).

Les courbes de polarisation indiquent que la région de transition passive a été observée pour tous les échantillons testés, suggérant que l'acier 316L et les dépôts ont été spontanément passivés dans la solution de NaCl. La valeur maximale de potentiel de piqûration Epit= 1268 mV obtenue pour le film contenant 16,09 at.% Mo correspond à la plus grande région de passivation (ΔE = 949 mV) avec des petites piqûres indiquant le meilleur comportement anticorrosion. Cela peut s'expliquer par la faible sensibilité à la corrosion par piqûres avec la formation de phase Mo_2N qui a un meilleur potentiel d'auto-corrosion dans l'eau salé (solution

à 3,5% massique de NaCl) [36]. D'autre part, la structure dense, la faible rugosité de surface et la faible mouillabilité peuvent contribuer à l'amélioration de la résistance à la corrosion.

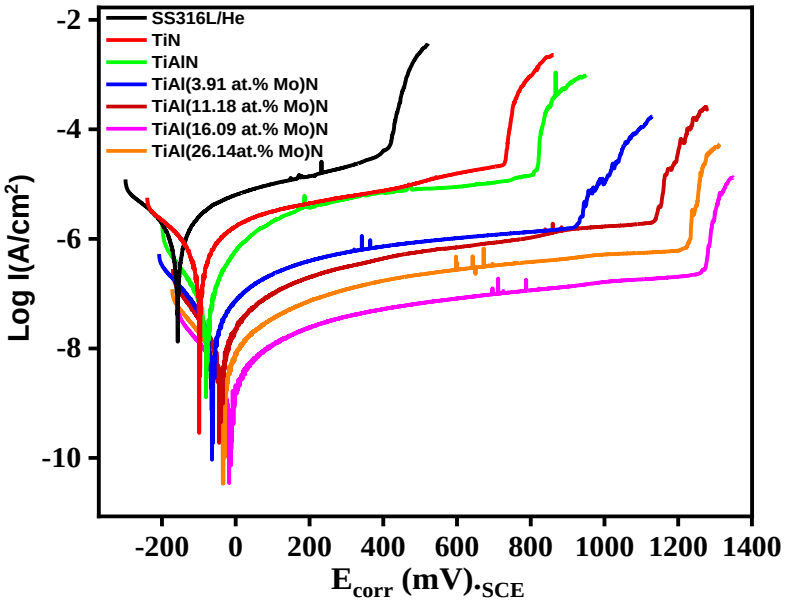

Fig. IV. 8. Courbes de polarisation de l'acier inoxydable 316L et lesrevêtements Ti(Al, Mo)N.

Chapitre V : Élaboration et caractérisation de couches minces innovantes TiMoON et TiMoON-Ag pour des applications biomédicales

Dans ce chapitre, nous présentons un nouveau revêtement développé à base de TiMoON dopé en Ag. Le Tableau V.1 présente la composition chimique de ces films avant et après recuit à 400 °C. L'analyse des spectres DRX (Fig. V.1) suggère la formation des phases mixtes TiON et Ag. Cependant, il est difficile de détecter des phases à base de Mo à cause de sa faible teneur dans les films et le chevauchement entre les pics de TiN et MoN qui peut entraver l'apparition des pics de phases à base de Mo. Les pics de diffraction de TiON sont déplacés vers des angles plus élevés en raison de la substitution de Ti par des atomes d'Ag. Le paramètre de maille et la taille des cristallites du cc-TiON ont diminué avec une augmentation concomitante de l'Ag jusqu'à 7,4 at.% en raison de l'incorporation d'Ag dans la structure de TiON. Le recuit des films TiMoON-Ag à 400°C a conduit à un chevauchement des pics d'Ag et TiON avec une orientation préférentielle (111) TiON. Ceci suggère qu'une partie de l'argent a été partiellement incorporée dans le réseau de TiON et aucune phase de molybdène n'a été identifiée par DRX.

Tableau. V .1. Composition chimique des films TiMoON-Ag déterminée par EDS et WDS.

Composition chimique(at. %)												
Revêtement	Avant traitement thermique						Après traitement thermique à 400 °C					
	Ti	N	O	Mo	Ag	N-O/Me	Ti	N	O	Mo	Ag	N-O/Me
TiMoNO	44.2	29	18	8.8	-	0.88	44	29.2	18.2	8.6	-	0.88
TiMoNO-(3 at. %Ag)	41.6	28.7	18.3	8.3	3	0.89	41.6	28.7	18.2	8.5	3	0.88
TiMoNO-(5.3 at. %Ag)	39.4	28.6	19.37	7.27	5.3	0.92	38.4	28.3	19.4	7.1	6.72	0.91
TiMoNO-(7.4 at. %Ag)	36.6	28.4	21.4	6	7.4	1.0	37.2	28.3	20.4	6.0	8.1	0.95
TiMoNO-(9 at. %Ag)	35.2	27.5	22.4	5.8	9	1.01	37.5	27.2	18.4	6.4	10.4	0.97
TiMoNO-(13 at. %Ag)	31.7	27.2	22.8	5.3	13	1.0	31.5	26.4	22.5	5	14.6	0.96

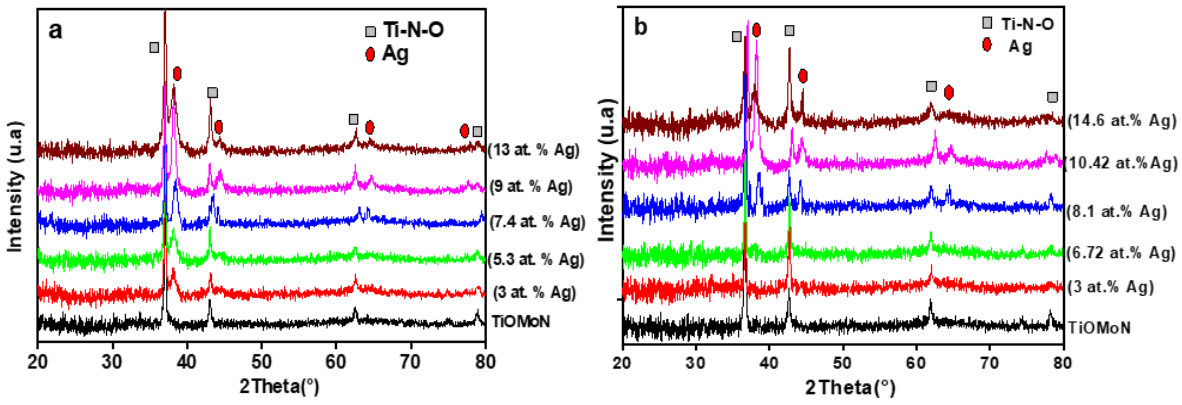

Fig. V.1. Spectres DRX acquis en mode d'incidence rasante pour les films TiMoON-Ag déposés avec différentes teneurs en Ag : a) avant et b) après recuit à 400 °C.

Le film TiMoON a présenté une structure pyramidale uniforme avec peu de pores et de défauts (Fig. V.2). Avec l'augmentation de la teneur d'Ag dans le film, la morphologie du film TiMoON-Ag est devenaient plus dense avec l'apparition des particules sphériques blanches de granules d'Ag sur la surface du film. Après recuit à 400 °C, les particules d'Ag sont devenues plus gros (Fig.V.2). La même morphologie a été observée par *Pedrosa et al.* [37] dans son étude sur les films à base de TiN dopés en Ag.

La Fig.V.3 présente des images MET de la coupe transversale du film TiMoON-(7,4 at. % Ag) avant et après recuit à 400 °C. Nous avons observé des nanoparticules agglomérés d'Ag de 40 nm de diamètre répartis dans le film recuit à 400 °C. Des taches en forme de nanotubes ont été observées sur la surface du film. La taille des particules de TiMoON pur est de l'ordre de 24-28 nm obtenues par l'équation de Scherrer (Tableau V.1).

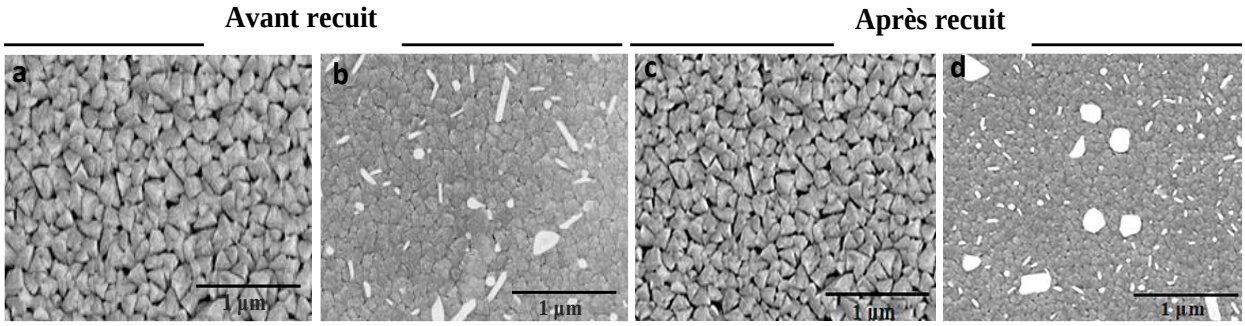

Fig. V.2. Images MEB de la surface de TiMoON(a, c) etTiMoON-(7.4 at. %Ag) (b,d)avant etaprès recuit à 400 °C, respectivement.

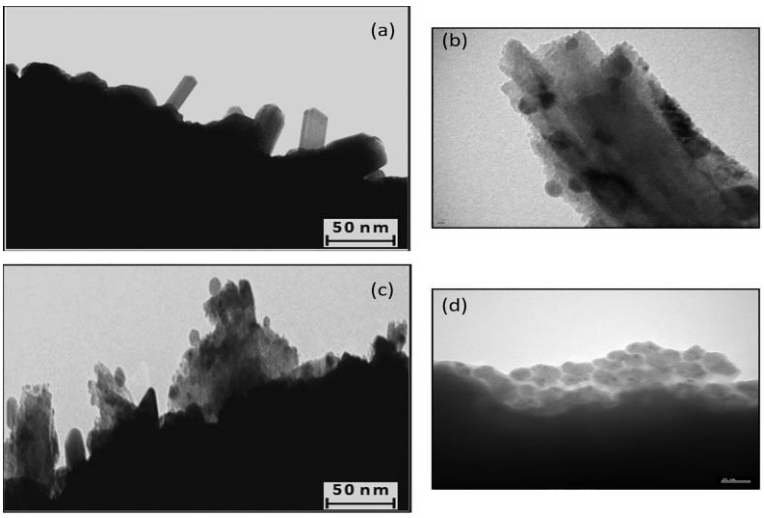

Fig. V.3. Images MET de la coupe transversale du film TiMoON-(7,4 at. % Ag) : a) avant et b) après recuit à 400 °C.

La Fig. V.4 présente la variation d'angle de contact en fonction du temps des films TiMoON-Ag. Nous constatons que la mouillabilité est plus élevée dans le cas des films non recuits (Fig. V.4a). L'augmentation de la teneur en Ag à 7,4 at.% a augmenté l'angle de contact de 98° à 121°. Les films représentant des angles de contact plus élevés montrent des propriétés antimicrobiennes/rugosité de surface accrues [38]. Cet angle a diminué à 115° et 108° pour les

films avec une teneur d'Ag de 9 et 13 at.%. Les films contenant d'Ag sont principalement hydrophobes et rugueuse, ce qui était observé précédemment par Calderon et al. [39].

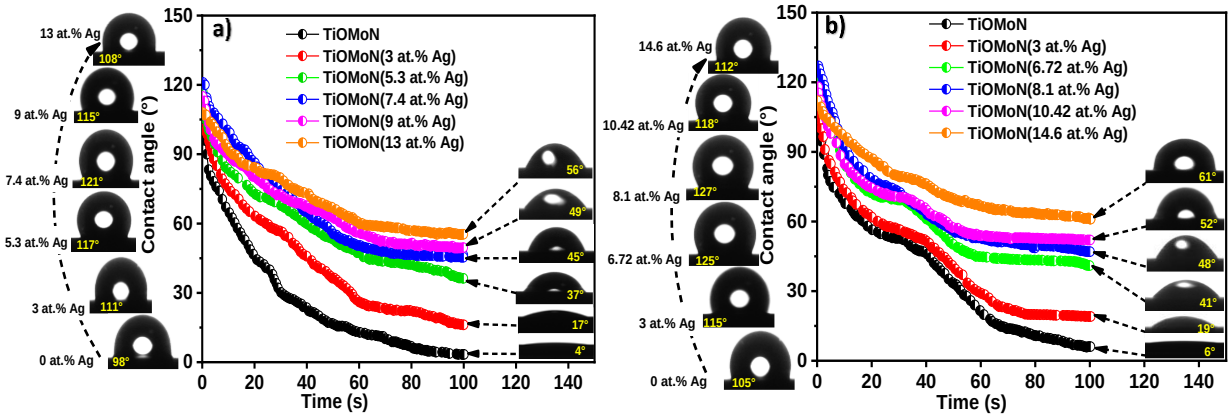

Fig. V.4. Angles de contact en fonction du temps mesurés sur les films TiMoON-Ag (a)avant et (b) après traitement thermique.

D'après la Fig. V.5, l'addition d'Ag aux films de TiOMoN a conduit à l'accélération de la cinétique d'inactivation bactérienne sur les revêtements de TiOMoN-Ag avec 5,3 et 7,4 at. %d'Ag. Ces deux films présentent des tailles de cristallites de (21-28) nm et des rugosités RMS de (20,1 nm et 19,0 nm), respectivement. Une rugosité de surface élevée signifie que la surface de film présente une densité de pic élevée permettant d'interagir avec les bactéries [40].

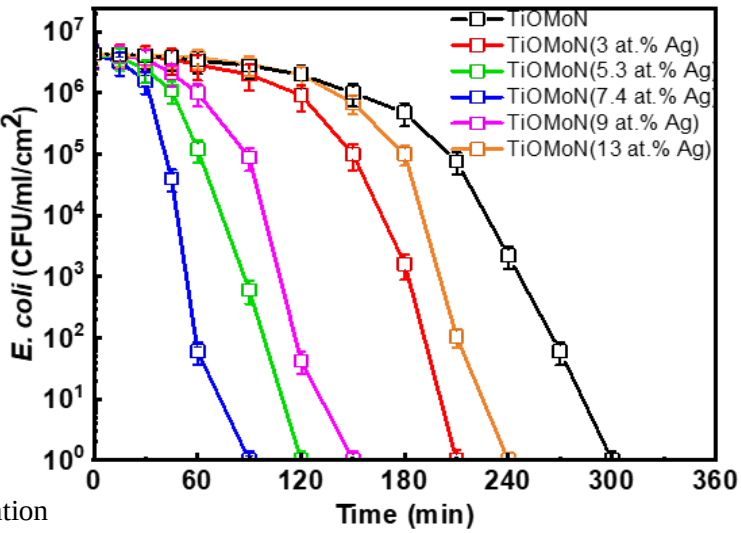

Fig. V.5. Inactivation bactérienne sur les revêtements TiOMoN-(Ag) sous lumière solaire simulée (50 mW/cm^2, 320–800 nm).

La Fig. V.6 montre que l'inactivation bactérienne a pris 90 minutes pour E. coli normal et 150 minutes pour E. coli modifié génétiquement. Cela suggère que le mécanisme de

l'inactivation est extracellulaire dans les étapes initiales puis suivi d'un processus intracellulaire en deuxième étape. Dans le processus ultérieur, les endommagements de l'enveloppe cellulaire étaient dus au changement du pH local, à la dénaturation des groupes fonctionnels cellulaires, la taille des cellules et aux changements du potentiel cellulaire de surface.

La figure V.6b montre quel 'inactivation bactérienne photocatalytique a été supprimée par l'ajout de diméthylsulfoxyde (DMSO) et de sel disodique de l'acide éthylène tétraacétique (EDTA-2Na). Les espèces $^{\bullet}OH$ et h^{+} interviennent conjointement et entraînent l'inactivation bactérienne. La SOD (capteur d'$O_2^{\bullet-}$) inhibe l'inactivation bactérienne à un faible degré par rapport à vb(h^{+}) et le radical $^{\bullet}OH^{-}$. Des résultats similaires ont été constatés par Karbasi et al.[41].

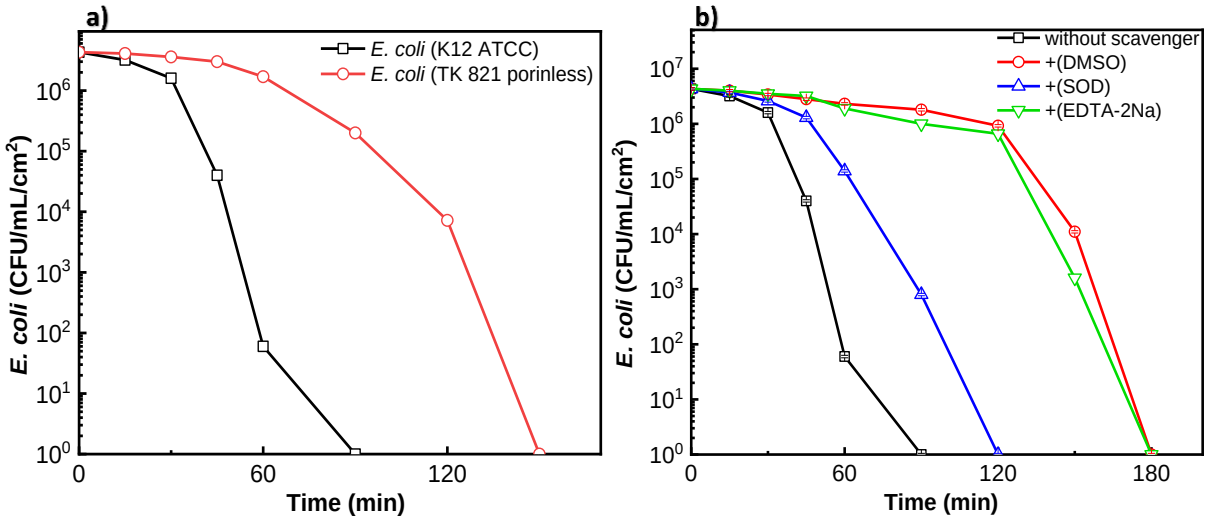

Fig. V.6.a) Inactivation bactérienne d'E. Coli normaux et sans porines sur le film TiMoON (7,4 at. %Ag), et b)la contribution des espèces réactives de l'oxygène (ROS) sur son comportement.

Les spectres d'absorption UV-Vis et les courbes de Tauc des films TiMoON et TiMoON-(7,4 at. %Ag) sont présentés dans la Fig.V.7. Les spectres de TiOMoN montrent une forte absorption dans le cas < 400 nm et avec une faible absorption dans le domaine visible. Le dopage par 7,4 at. %d'Aga conduit à la formation d'Ag_2O qui entraine un décalage vers le visible. La bande interdite d'énergie (Eg) a été évaluée à partir du spectre d'absorption enregistré en utilisant l'équation de Tauc. La valeur de l'Eg du film TiOMoN passe de 2,88 eV à 2,11 eV après dopage de 7,4 at. % Ag, de sorte que le transfert de charges devient facile entre les oxydes TiO_2, MoO_3 et Ag_2O sous irradiation lumineuse solaire simulée, ce qui est également bénéfique pour leurs performances photocatalytiques.

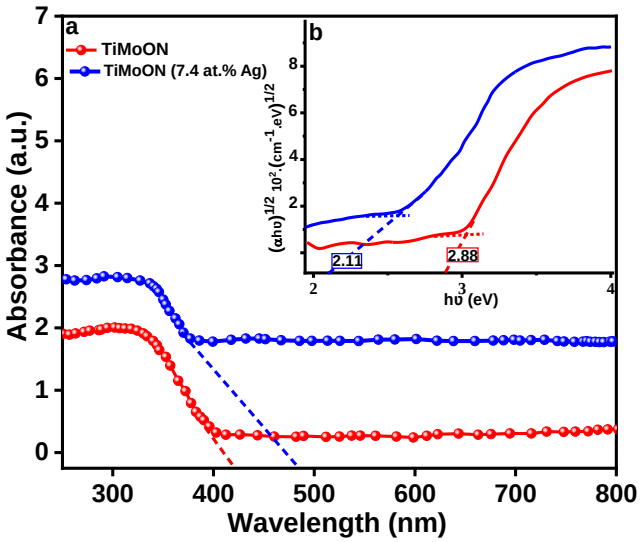

Fig. V.7.a) Spectres d'absorption optique et b) Courbes de Tauc des films TiMoON et TiMoON-(7,4 at. %Ag).

La Fig. V.8 présente une illustration schématique simplifiée de l'intervention du film TiOMoN-Ag sur l'inactivation bactérienne. On propose que les électrons se déplacent de l'Ag_2O vers l'hétérojonction TiO_2/MoO_3. Ces électrons de $TiO_2/MoO_3/Ag_2O$ peuvent être piégés par O_2 pour donner $O_2^{\bullet-}$et $^{\bullet}OH$ lorsqu'ils interviennent dans le processus d'inactivation bactérienne.

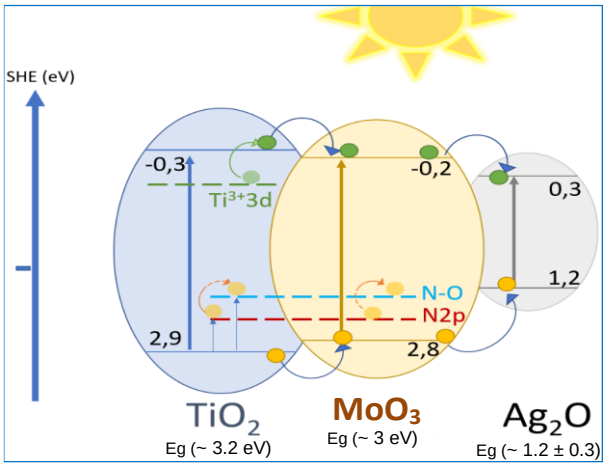

Fig. V.8. Mécanisme suggéré de l'inactivation/mort des bactéries sous lumière solaire.

Conclusion générale

L'objectif principal de cette thèse est d'étudier et d'améliorer les propriétés tribo-mécaniques, le comportement anticorrosion et la performance antibactérienne de l'acier inoxydable 316L projeté à froid suivi d'un traitement de surface par dépôt de nouveaux revêtements à base de nitrure de titane par PVD dans un mélange gazeux (Ar, N_2 et O_2).

L'étude numérique et expérimentale de l'acier inoxydable 316L projeté à froid montre que:

→ Le modèle unidimensionnel a révélé que l'augmentation de la température du gaz porteur avec des particules fines de petite taille entraînaient une vitesse de particule plus grande.

→ L'acier 316L projeté à froid avec He (une vitesse de particules élevée) a présenté un revêtement dense et lisse, conduisant à une bonne dureté et une performance tribologique améliorée avec une meilleure résistance à la corrosion.

L'état de l'art que nous avons réalisé nous a permis de sélectionner les revêtements de TiN, TiAlN, TiAlMoN, TiMoON et TiMoAgON comme objets de l'étude. Les résultats de cette étude montrent que :

→ L'addition de Mo au système TiAlN conduit à une réelle amélioration des propriétés structurales et morphologiques. En effet, les couches colonnaires denses deviennent mieux cristallisées avec la formation des phases TiNet Mo_2N.

→ Les films de TiAlMoN ont présenté des contraintes résiduelles en compression et un comportement hydrophobique (un angle de contact élevé supérieur à 90°et une faible énergie de surface).Le film $Ti_{33}Al_3N_{47}Mo_{16}$ a montré des valeurs élevées de dureté et module d'Young (27.9 et 302.7 GPa), respectivement.

→ Ainsi, nous avons alors démontré que l'addition du Mo au film TiAlN améliore leur résistance au frottement à sec contre de l'acier 100Cr6. Le taux d'usure du film contenant 16,09 at.% de Mo a été réduit à $1{,}534\times10^{-6}$ et $0{,}849\times10^{-6}$ mm^3/Nm sous charges appliquées de 2N et 5N, respectivement. L'amélioration de la résistance à l'usure est due à la surface lisse, au rapport H/E élevé et à la formation des phases lubrifiantes TiO_2 et α-MoO_3.

→ La résistance à la corrosion de l'acier 316L projeté à froid a été améliorée par des films protecteurs déposés et le meilleur comportement anticorrosion a été trouvé pour le film contenant 16,09 at.% de Mo.

De nouveaux revêtements innovants TiMoON-(Ag) avec différentes teneurs en Ag ont été déposés sur des verres par pulvérisation magnétron. Les propriétés physicochimiques et biomédicales ont été évaluées.

→ Avec l'augmentation de la teneur en Ag, la morphologie des revêtements TiMoON-Ag devient plus dense avec une granulométrie très fine et l'apparition des particules sphériques blanches est due à la précipitation d'Ag sur la surface du film. Les films denses et rugueux ont été distingués par une distribution hétérogène de nanoparticules d'Ag.

→ Le caractère hydrophobe du TiMoON s'est amélioré avec l'augmentation de la teneur en Ag. Les valeurs les plus élevées de 121° et 127°ont été trouvées pour le film contenant 7,4 at.% d'Ag avant et après recuit, respectivement.

→ Un mécanisme antibactérien extracellulaire est suggéré dans les étapes initiales pour E. coli sans porine, suivi d'un processus intracellulaire en deuxième étape.

→ L'identification des ROS en solution a montré que les radicaux hydroxyles jouent un rôle principal dans la dégradation bactérienne et que l'hydrophobicité des films augmente avec la teneur en Ag conduisant à une accélération du processus d'inactivation bactérienne.

→ L'inactivation bactérienne la plus rapide (90 min) a été obtenue sur le film TiOMoN-(7,4 at.% d'Ag). Le développement de ce nouveau revêtement présente un potentiel tres important dans le domaine de désinfection des surfaces et pour les applications biomédicales.

Références

[1] L. Wang, D.O. Northwood, X. Niea, J. Housden, E. Spain, A. Leyland, A. Matthews, Corrosion properties and contact resistance of TiN, TiAlN and CrN coatings in simulated proton exchange membrane fuel cell environments, Journal of Power Sources, 195 (2010) pp. 3814–3821.

[2] K. Taube, K. Bewilogua, Encyclopedia of Materials: Science and Technology. (2001) pp. 9286–9293.

[3] M. Guemmaz, A. Moser, J. Grob, R. Stuck, Sub-surface modifications induced by nitrogen ion implantation in stainless steel (SS 316L) correlation between microstructure and nanoindentation results, Surf. Coat. Technol, 100-101 (1998) pp. 353-357.

[4] P. Wei, S.Lein, S. Chin, S. Jinn. Boron- ϕ doped Si grown by ultra-high vacuum chemical vapor deposition, Mater Chem&Phy, 767 (2002) pp. 426-429.

[5] H.A. Zaman, S. Sharif, M.H. Idris, A. Kamarudin, Metallic biomaterials for medical implant applications: A Review, Applied Mechanics and Materials, 735 (2015) pp. 19-25.

[6] S. Grosso, Revêtements architecturés de Ti, TiN et TiO élaborés par pulvérisation cathodique au défi lé sur des fils en acier inoxydable : relation entre la composition chimique, la microstructure et les propriétés d'usage. Energieélectrique. Université Grenoble Alpes, 2017. Français. NNT : 2017GREAI083. tel-01725382.

[7] W.J. Leong, H. Hasan, Z. Zakaria, M.Z.H. Ghazali, S.A. Ab Hamid, S.A. Hassan Risk factors and etiologies of clean and clean contaminated surgical site infections at a tertiary care center in Malaysia, Southeast Asian Journal of Tropical Medicine and Public Health, 48 (6) (2017), pp. 1299-1307.

[8] S. Aouadi, Y. Paudel, B. Luster, S. Stadler, P. Kohli, C. Muratore, C.J. Hager, A. Voevodin, Adaptive Mo2N/MoS2/Ag tribological nanocomposite coatings for aerospace applications, Tribology Letters, 29(2008), pp. 95-103.

[9] L. Tomaszewski, W. Gulbinski, A. Urbanowicz, T. Suszko, A. Lewandowski, W. Gulbinski, TiAlN based wear resistant coatings modified by molybdenum addition. Vac. 121(2015), pp. 223-229.

[10] F. Regent, J.Musil,Magnetron sputtered Cr–Ni–Nand Ti–Mo–N films: comparison of mechanical properties, Surface and Coatings Technology. 142–144 (2001), pp. 146-151.

[11] V. M. Beresnev, O. V. Bondar, B. O. Postolnyi, M. O. Lisovenko, G. Abadias, P. Chartier, D. A. Kolesnikov, V. N. Borisyuk, B. A. Mukushev, B. R. Zhollybekov, A. A. Andreev Comparison of tribological characteristics of nanostructured TiN, MoN, and TiN/MoN Arc-PVD coatings. Journal of Friction and Wear, 35(2014), pp. 374-382.

[12] J. Xu, H. Ju, L. Yu, Effects of Mo content on the microstructure and friction and wear properties of TiMoN films, ActaMetall Sin. 48 (2012), pp. 1132-1138.

[13] M. Woydt, A. Skopp, I. Doerfel, K. Witke, Wear engineering oxides/anti-wear oxides, Wear, 218 (1998), pp. 84-95.

[14] V. S. Sergevnin. I. V. Blinkov. D. S. Belov. N. I. Smirnov. A. O. Volkhonskii. K. A. Kuptsov, Wear and erosion of arc-PVD multilayer Ti-Al-Mo-N coatings under various conditions of friction and loading, The International Journal of Advanced Manufacturing Technology, 98 (2018), pp. 593-601.

[15] B. Yi, S. Zhou, Z. Qiu, D.C. Zeng, The influences of pulsed bias duty cycle on tribological properties of solid lubricating TiMoCN coatings, Vacuum, 180 (2020)109552.

[16] S. Rtimi, C. Pulgarin, M. Robyr, A. Aybush, I. Shelaev, F. Gostev, V. Nadtochenko, J. Kiwi, Insight into the catalyst/photocatalyst microstructure presenting the same composition but leading to a variance in bacterial reduction under indoor visible light,Applied Catalysis B: Environmental,208(2017), pp. 135-147.

[17] M.D. Hernández-Alonso, F. Fresno, S. Suárez, J.M. Coronado, Development of alternative photocatalysts to TiO_2: challenges and opportunities. Energy & Environmental Science, 2(12)(2009), pp. 1231-1257.

[18] R. Levinson, P. Berdahl, H. Akbari, Solar spectral optical properties of pigments— part I: model for deriving scattering and absorption coefficients from transmittance and reflectance measurements, Solar energy materials and solar cells, 89 (2005), pp. 319-349.

[19] N. Tetault, H. Gbaguidi-Haore, X. Bertrand, R. Quentin, N. van der Mee-Marquet, Biocidal activity of metalloacid-coated surfaces against multidrug-resistant microorganisms, Antimicrobial resistance and infection control,1(1)(2012), pp.1-6.

[20] Y. Du, D. Tang, G. Zhang, X. Wu, Facile synthesis of Ag_2O-TiO_2/sepiolite composites with enhanced visible-light photocatalytic properties. Chinese Journal of Catalysis, 36 (2015), pp. 2219-2228.

[21] B. Liu, L. Mu, B. Han, J. Zhang, H. Shi, Fabrication of TiO_2/Ag_2O heterostructure with enhanced photocatalytic and antibacterial activities under visible light irradiation, Applied Surface Science, 396(2017), pp. 1596-1603.

[22] Y. Zhao, J. Xu, Z. Li, T. Fu, S. Jiang, In vitro antibacterial properties of MoO_3/SiO_2/Ag_2O nanocomposite coating prepared by double cathode glow discharge technique. Surface and Coatings Technology, 397(2020), 125992.

[23] H. Wu. Process Modeling and Planning for Robotic Cold Spray Based Additive Manufacturing. Material chemistry. University of Bourgogne Franche-Comté, France (2020).

[24] M. Amiri, G.A. Crawford, J.C. Earthman, Quantitative percussion diagnostics for evaluating porosity and surface roughness of cold sprayed and laser deposited materials, Journal of materials research and technology, 14(2021), pp. 312-323.

[25] B. AL. Mangour, P. Vo, R. Mongrain, E. Irissou, S. Yue, Effect of heat treatment on the microstructure and mechanical properties of stainless steel 316L coatings produced by coldspray for biomedical applications, Journal of thermal spray technology,23 (2014), pp. 641-652.

[26] J. Zhou, K. Ma, C.X. Li, M. Yasir, X.T. Luo, C.J. Li, Microstructures of aluminum surfaces reinforced with 316L stainless steel particles via high-speed particle injection and the resulting double strengthening mechanism, Surface and Coatings Technology, 385 (2020) 125380.

[27] Q. Li, P. Song, Q. Ji, Y. Huang, D. Lia, R. Zhaia, B. Zhenga, J. Lu, Microstructure and wear performance of arc-sprayed Al/316L stainless-steel composite coating, Surface and Coatings Technology, 374 (2019), pp. 189-200.

[28] Ş. Ürdem, E. Duru, H. Algül, M. Uysal, H. Akbulut, Evaluation of high temperature tribological behavior of electroless deposited NiB–Al_2O_3 coating,Wear, 482–483(2021), 203960.

[29] S.G. Rodríguez, B. Torres, N.P. González, E. Otero, J. Rams, Corrosion behavior of 316L stainless steel coatings on ZE41 magnesium alloy in chloride environments. Surface and Coatings Technology, 378(2019), 124994.

[30] K. E. Batista, J. L. Da Silva, M. J. Piotrowski, Ab-initio investigation of the role of atomic radius in the structural formation of PtnTM55–n (TM= Y, Zr, Nb, Mo, and Tc) Nanoclusters. The Journal of Physical Chemistry C, 122(13) (2018) pp. 7444-7454.

[31] Y.W. Lin, H.A. Chen, G.P. Yu, J.H. Huang, Effect of bias on the structure and properties of TiZrN thin films deposited by unbalanced magnetron sputtering Thin Solid Films, 618 (2016) pp. 13-20.

[32] X. Pang, L. Zhang, H. Yang, K. Gao, A.A. Volinsky, Residual stress and surface energy of sputtered TiN films, J. Mater. Eng. Perform., 24 (2015) pp. 1185-1191.

[33] J. Hao, Y. Zhang, P. Ren, K. Zhang, J. Chen, S. Du, M. Wang, M. Wen, Spinodal decomposition in the Ta-Mo-Al-N films activated by Mo incorporation: toward enhanced hardness and toughness, Ceram. Int. 44 (2018) pp. 21358-21364.

[34] B. Tian, W. Yue, Zh. Fu, Y. Gu, Ch. Wang, J. Liu, Surface properties of Mo-implanted PVD TiN coatings using MEVVA source, Appl. Surf. Sci. 280 (2013) pp. 482-488.

[35] Q. Yang, L.R. Zhao, P.C. Patnaik, X.T. Zeng, Wear resistant TiMoN coatings deposited by magnetron sputtering, Wear, 261 (2006) pp. 119-125.

[36] P. Ji, L. Yu, T. Sh, H. Ju, J. Xu, F. Gao, The effect of molybdenum content on microstructure, mechanical, tribological and corrosion behavior of Zr-Mo-N composite films. Materials Today Communications, 26 (2021) 101720.

[37] P. Pedrosa, C. Lopes, D. Machado, E. Alves, N.P. Barradas, N. Martin, F. Macedo, C. Fonseca, F. Vaz, Nanocomposite Ag: TiN thin films for dry biopotential electrodes. Applied surface science, 285 (2013), pp. 40-48.

[38] L. Wang,Y.Wang,P. Shum, Y. Hou, T. Fu, Sputter-deposited Cr–Ag films for environmental antimicrobial applications, Coatings, 11(2021),1153.

[39] S. Calderon Velasco, A. Cavaleiro, S. Carvalho, Functional properties of ceramic-Ag nanocomposite coatings produced by magnetron sputtering, Progress in Materials Science, 84 (2016), pp. 158-191.

[40] A. Alhussein, S. Achache, R. Deturche, F. Sanchette, C. Pulgarin, J. Kiwi, S.Rtimi, Beneficial effect of Cu on Ti-Nb-Ta-Zr sputtered uniform/adhesive gum films accelerating bacterial inactivation under indoor visible light. Colloids and Surfaces B: Biointerfaces, 152(2017), pp. 152-158.

[41] M. Karbasi, F. Karimzadeh, K. Raeissi, S. Rtimi, J. Kiwi, S. Giannakis, C. Pulgarin, Insights into the photocatalytic bacterial inactivation by flower-like Bi2WO6 under solar or visible light, through in situ monitoring and determination of reactive oxygen species (ROS). Water, 12(4) (2020), pp. 1099.

Appendix B

Publications and communications

I. Scientific publications

Papers in international peer-reviewed journals

1. **A. Belgroune**, L. Aissani, A. Alhussein, M. Zaabat, J. Kiwi, S. Rtimi, "*Bacterial inactivation on sputtered TiOMoN and TiOMoN-Ag thin films under solar simulated light"*. Chemical Engineering Journal, Vol. 460, (2023),141590.
2. **A. Belgroune**, A. Alhussein, L. Aissani, M. Zaabat, A. Obrosov, C. Verdy, C. Langlade, "*Effect of He and N_2 gas on the mechanical and tribological assessment of SS316L coating deposited by cold spraying process"*. Journal of Materials Science, 57(8) (2022),pp. 5258-5274.
3. **A. Belgroune**, L. Aissani, F. Salhi, C. Nouveau, A. Alhussein, "*Mechanical and Tribological Behaviors of Nanocomposite Titanium Nitrides Coatings"*. In Defect and Diffusion Forum, Trans Tech Publications Ltd. 406(2021), pp. 312-318 (conference article).
4. L. Aissani, **A. Belgroune**, A. Saoudi, A. Hmima, M. Fellah, A. Obrosov, A. Alhussein, "*Tribo-mechanical performance and antibacterial activity in (Cu, Zr)-alloyed Ti (Al) N coatings synthesized by reactive magnetron sputtering"*. Journal of Materials Science, 57(41) (2022), pp. 19612-19630.
5. L. Aissani, A. Alhussein, **A. Belgroune**,C. Nouveau, E. Zgheib, R. Barille, A. Montagne, "*Effect of carbon content on structural, mechanical and tribological properties of CrVCN coating"s*. Thin Solid Films, 732(2021), 138782.
6. L. Aissani, M. Fellah, **A. Belgroune**, A. Obrosov, M.A. Samad, A. Alhussein, "*Effect of O_2 flow rate on the structure, wettability and tribo-mechanical behaviour of Zr-O-N thin films"*. Surfaces and Interfaces, Vol. 26 (2021), 101441.
7. F. Salhi, L. Aissani, M. Fellah, A. Chadli, A. Cheriet, **A. Belgroune**, C. Nouveau, A. Obrosov, M.A. Samad, A. Alhussein, "*Experimental investigation of structural, wetting, mechanical and Tribological properties of TiZrN thin films deposited by magnetron sputtering"*. Surfaces and Interfaces, 27(2021), 101519.
8. L**.** Aissani, A. Alhussein, A. Ayad, C. Nouveau, E. Zgheib, **A. Belgroune**, M. Zabbat, R. Barille, "*Relationship between structure, surface topography and tribo-mechanical*

behavior of Ti-N thin films elaborated at different N_2 flow rates". Thin Solid Films, 724(2021), 138598.

II. International communications

1. **Ahlam Belgroune**, Linda Aissani, Akram Alhussein, "*Physical and Mechanical Properties of Cr-Al-N and Cr-V-N Ternary Systems";* The 47th International Conference On Metallurgical coatings and thin films (USA, virtual conference), April 26-30, 2021.
2. **Ahlam Belgroune**, Linda Aissani, Corrine Nouveau, AkramAlhussein, Abdelaziz Aboudi, "*Mechanical and tribological behaviors of nanocomposite titanium nitrides coatings";* the 1st International Conference on Materials, Energy and Environment (MEE'2020), El Oued (Algeria), January 20-21, 2020.
3. L. Aissani, **A. Belagroune**, F. Salhi, S. Khenchoul, A. Cheriet, C. Nouveau, A. Alhussein. « *Nitrogen doping to improve the mechanical and tribological properties of vanadium coating";* the 1st International Conference on Materials, Energy and Environment (MEE'2020), El Oued (Algeria), January 20-21, 2020.
4. L. Aissani, **A. Belgroune**, L. Radjhi, C. Nouveau, A. Alhussein. « *Study of Structural and Mechanical Properties of Hard Thin Films";* 2ème workshop international de mécanique des structures et des matériaux. Université de Batna (Algeria). 17-18 décembre 2018.
5. **Ahlam Belgroune**, Linda Aissani, Ghilani Laala, Mourad Zaabat, Akram Alhussein, Farid Lakmine, *Résistance à la corrosion des revêtements composite Ni-P dans un mulieu agressif (3.5 NaCl)*. 2nd International Symposium on Mechatronics & Renewable Energy (ISMRE), El-Oued University (Algeria), December 10-11, 2018.
6. Linda Aissani, Corinne Nouveau, Laala Guilani, **Ahlam Belgroune**, Akram Alhussein, « *Influence de la diffusion de chrome sur la dureté des aciers à base de carbone* ». 2nd International Symposium on Mechatronics & Renewable Energy (ISMRE), El-Oued University (Algeria), December 10-11, 2018.
7. **Ahlam Belgroune**, Linda Aissani, Mourad Zaabat, Farid Lakmine, Nassima Bouaziz, "*Elaboration and characterization of nickel phosphorus composite coatings to study the phenomenon of corrosion";* International conference on materials science (ICMS), Setif 1 University (Algeria), September 12-14, 2018.

III. National communications

1. **Ahlam Belgroune**, Linda Aissani, Mourad Zaabat, Farid Lakmine, Nassima Bouaziz, L'étude de l'efficacité anticorrosive des revêtements composite Ni-P sur l'acier au carbone X52'', 1ere Journée en Energies Renouvelables et Matériaux avancés -JNERMA-OEB 2018-Algerie.
2. **Ahlam Belgroune**, Linda Aissani, Mourad Zaabat, Farid Lakmine, Akram ALHESSEIN, Nassima Bouaziz, « Analyse électrochimique pour examiner le comportement de la corrosion de l'inhibiteur pour l'acier API 5LX52 », 1er séminaire national de physique et chimie des matériaux (SNPCM'2018) Université 20 aout 1955-Skikda. 28-29 Novembre 2018-Algerie.
3. Aissani Linda, **Belgroune Ahlam**, Radjhi Lamia, Alhussein Akram, « Structural and mechanical properties of CrN coatings »; 1er séminaire national de physique et chimie des matériaux (SNPCM'2018) Université 20 aout 1955-Skikda. 28-29 Novembre 2018-Algérie.
4. Aissani Linda, **Belgroune Ahlam**, Radjhi lamia, Alhussein Akram, « Elaboration et caractérisation de couches minces de vanadium déposées par pulvérisation magnétron radiofréquence » ; 1er séminaire national de physique et chimie des matériaux (SNPCM'2018) Université 20 aout 1955-Skikda, Algérie.
5. Aissani Linda, Ghilani Laala, **Belgroune Ahlam**, « Etude du comportement structural et mécanique des dépôts à base de Vanadium » ; 1er Journée nationale en énergies renouvelable et matériaux avances (JNERMA2018) Université Larbi BEN MHIDI-OEB, Algerie. 13 November 2018.
6. Aissani Linda, Fellah Mamoun, **Belgroune Ahlam**, Radjhi Lamia, Lamraoui Hanane, Alhussein Akram, « Caractérisation avec rayonnement X des nitrures de chrome déposés par pulvérisation cathodique magnétron » ; 1er séminaire national de physique et chimie des matériaux (SNPCM'2018) Université 20 aout 1955-Skikda, Algérie.
7. Aissani Linda, **Belgroune Ahlam**, Ghilani Laala, Radjhi Lamia, Alhussein Akram, « Influence de l'épaisseur de film sur les propriétés des couches minces à base de chrome » ; The first days on 'Science and Engineering JSSE 18', ENP Constantine 2018- Algérie.
8. **Belgroune Ahlam**, Aissani Linda, Mourad Zaabat, « Tenue au frottement et à la corrosion de revêtements à base de Titane déposés sur des pièces en Acier inox 316L fabriquées par cold spray », Journée doctoriale LCAM 2018 Université Larbi BEN MHIDI-OEB-Algérie.

Appendix C

Abstract

Wear and corrosion resistance of titanium based coatings deposited on cold spray 316l stainless steel

Abstract

In this work a duplex treatment was developed in two steps. The first part was based on the elaboration and characterization of stainless steel 316L performed by cold spray. The second step was devoted to the application and characterization of TiN-based thin films. TiAlN, TiAlMoN and TiMoONAg films were deposited by magnetron sputtering and the effects of different deposition parameters on the microstructure and coating properties were evaluated.

The objective of this work was to develop a new generation of optimized titanium-based coatings that can be proposed with improved tribo-mechanical properties, electrochemical behavior and antibacterial performance. The results obtained showed a great potential of hybrid process (Cold spray and Magnetron sputtering) to enhance the product properties. The stainless steel 316L cold-sprayed and then coated with TiAl(16.09 at.% Mo)N film presented the best tribo-mechanical behavior and corrosion resistance. It can be qualified as a good surface protection coating for different industrial applications.

The TiOMoN (7.4 at. % Ag) thin film had the best bacterial inactivation, which presents an advancement for surface disinfection showing agreat potential in the biomedical field.

***Keywords**: Thin films, Surface preparation, Titanium, Stainless steel, Friction, Mechanical wear, Corrosion, Bacteria.*

Résumé

Tenue à l'usure et à la corrosion des revêtements à base de titane déposés sur des acier inoxydable 316L

Résumé

Dans ce travail nous avons réalisé un traitement duplex qui s'articule en deux étapes à savoir une première partie ; la réalisation et la caractérisation de l'acier inoxydable 316L élaboré par jet froid puis l'application et la caractérisation des couches minces à base de TiN. TiAlN, TiAlMoN et TiMoONAg ont été déposées par pulvérisation magnétron et les effets de différents paramètres de dépôt sur la microstructure et les propriétés du revêtement ont été évalués.

L'objectif de ce travail est de développer une nouvelle génération de revêtements optimisés à base de titane qui peuvent être proposés avec des bonnes propriétés tribo-mécaniques et électrochimique, et de performance antibactérienne améliorée. Les résultats obtenus ont montré un grand potentiel du procédé hybride (jet froid et pulvérisation magnétron) pour améliorer les propriétés d'un produit. L'acier inoxydable 316L pulvérisé à froid puis recouvert d'un film de TiAl (16,09 at.% Mo)N a présenté le meilleur comportement tribo-mécanique et anticorrosion. Il pourrait être qualifié comme un bon revêtement de protection de surface pour différentes applications industrielles.

Le revêtement TiOMoN (7,4 at. % Ag) a montré le meilleur comportement antibactérien, ce qui présente un avancé dans la désinfection des surfaces et présente un potentiel dans le domaine biomédical.

Mots clés : *Couche minces, Traitements de surface, Titane, Acier inoxydable, Frottement, Usure (mécanique), Corrosion, Bactéries.*

ملخص

مقاومة التآكل للطلاءات التي أساسها التيتانيوم المترسبة على الفولاذ المقاوم للصدأ 316L

ملخص

في هذا العمل قمنا بتطوير مواد جديدة من اجل تحسين خصائص السطوح على مرحلتين; بداية قمنا بتصنيع وقياس خصائص الفولاذ 316L وفي المرحلة الثانية تم طلاء هذا الفولاذ بمواد مبتكرة جديدة بتقنية الرش المغناطيسي بالاستناد على نتريدات التيتانيوم والألمنيوم قمنا بترسيب طلاءات جديدة ثم دراسة تأثير المعاملات المختلفة على بنية وخواص هده الطلاءات.

إن الهدف من الدراسة هو تطوير جيل جديد من الطلاءات التي أساسها التيتانيوم مضادة للبكتيريا وذات خواص ميكانيكية وكهر وكيميائية محسنة.

أظهرت النتائج التي تم الحصول عليها أهمية استخدام التقنية المزدوجة (الرش البارد الرش المغناطيسي) من اجل تحسين خصائص المنتج ;لقد وجدنا بان الطلاء TiAl (16.09 at.% Mo)N كان الأفضل من حيث السلوك الميكانيكي و مقاومة الاحتكاك و التآكل هدا الطلاء يمن استخدامه من اجل حماية المعادن المستخدمة في التطبيقات الصناعية .

إن الطلاء TiOMoN (7.4 at. % Ag) الذي تم تطويره في هدا العمل اثبت فعالية كبيرة و سلوكا مميزا مضادا للبكتيريا إن هدا الطلاء المبتكر يمكن استخدامه للأجهزة و الأدوات المستخدمة في المجال الطبي.

الكلمات المفتاحية: طلاء، طبقة رقيقة، معالجة سطحية، تيتانيوم، فولاذ مقاوم للصدأ، احتكاك، تآكل، بكتيريا.